An investigation regarding cellular, synaptic and glial processing in the inferior colliculi

S D WEBB

PHD 2019

An investigation regarding cellular, synaptic and glial processing in the inferior colliculi

SAMUEL DAVID WEBB BSc. (Hons)

A thesis submitted in partial fulfilment of the requirements of Manchester Metropolitan University for the degree of Doctor of Philosophy

Department of Life Sciences, Manchester Metropolitan University

2019

Declaration

I hereby declare that I have personally undertaken all the work described in this thesis.

Abstract

The inferior colliculus (IC) is an integral centre of auditory processing. Neuronal processing of sound within IC is well established, as are its afferent and efferent projections. The IC is a complex structure that can be divided into sub-regions that undertake different aspects of processing. The central nucleus (CNIC) - a primary central auditory processing sub-region, the lateral cortex (LCIC) which is involved in polysensory integration, and the dorsal cortex (DCIC) which is involved in plasticity and processing descending signals from the auditory cortex. How processing is regulated within these sub-regions, and how non-neuronal cells, such as glia, contribute to local processing, is unclear. In other regions of the brain, astrocytes and microglia contribute to synaptic processing, but little is known of their morphology or variability throughout IC. Therefore, this thesis combines anatomical, physiological and molecular biological approaches to investigate astrocytic and microglial interrelationships with neuronal somata and synapses. Specifically, the morphology and colocalisation of microglial and astrocytic processes have been contrasted between sub-regions of IC in young guinea pig. Interestingly, analysis revealed that *Iba1+* microglia, not *GFAP+* astrocytes, make numerous abutments with *GAD67+* somata (putative inhibitory neurons) throughout the IC parenchyma, and microglia were more ramified and interacted with more putative excitatory synapses (colocalised with *synaptophysin* and *Homer1*) in DCIC than other sub regions. As the IC was hypothesised to be an unexplored locus of pathology in neurodegeneration, a measurement of how markers of microglia, astrocytes and neurons were modified in theTgF344-AD (Tg) rat model of Alzheimer's disease, from 6- to 18-months was conducted. This produced evidence for little neuronal loss up to 18-months in CNIC and other brain regions, but there was a considerable increase in *GFAP+* expression, which mirrored results observed in the CA3 region of hippocampus. However, astrocytes in hippocampus demonstrated age-dependent increases in astrocyte ramification length and number, but this was not found in any sub-region of IC. Furthermore, there were increased maximal respiration rates in isolated synaptosomes from 15-month Tg IC, which matched findings from hippocampus. Scanning electron microscopy revealed putative synaptosomes were reduced in size in 15-month Tg IC and hippocampus. QRT-PCR found a trend for a reduction in the expression of *GAD65, SV2a, Iba1* and *synaptophysin* mRNA in the 15-month Tg model, suggesting loss of synapses and microglia precedes loss of neurons in this model. These findings show that microglia differentially contribute to processing between sub regions of young adult IC, and multiple hallmarks of hippocampal dysfunction in Alzheimer's disease are found at the same time points in the Tg model. Collectively, these findings reveal novel roles for glia in the IC and suggest potential links between IC dysfunction and Alzheimer's disease.

Acknowledgments

First and foremost, I would like to thank my parents, I am who I am because of you and if it was not for you, I would never have made it to where I am today. You have always supported me (I can certainly think of many low points…) and have made endless sacrifices/contributions that I will never forget. I hope that having a doctor in the family somewhat repays all that you have given me. I could not have asked for better parents and I hope that this message communicates my appreciation better than I do in person.

Next I would like to thank Anya White, as I can honestly say that you have supported me in more ways than you could possibly imagine. Particularly at the earlier stages of my PhD, being with you opened up a new way of interpreting life and more importantly the way I understand scientific research, and these are skills that have shaped, and will continue to shape who I am, and I hold this more dear than anything else.

I would like to take time to thank Stuart Fielding as our constant philosophical conversations helped me develop as a person quicker than I could have possibly imagined, I only hope that I have had the same effect. I would also like to thank Glenn Ferris, my molecular work/understanding would be very limited if it was not for your help, give me shout if there is anything I can do for you? Friday football lot, I haven't forgotten you, my PhD was definitely made better by all of you so a big shout out to all of you.

Finally, I would like to thank my supervisor Llwyd Orton. Unfortunately, I don't have the space to convey my gratitude to you. I owe you everything that I have become. I couldn't have asked for a better supervisor, you pushed me in every aspect of my life making me an overall better person. My dream was to become a neuroscience researcher before university, you have facilitated that. I can only hope that you gained a fraction from me of what I gained from you.

Keep it going…

List of Abbreviations

IC: inferior colliculus

AD: Alzheimer’s disease

CN: cochlear nucleus

DCN: dorsal cochlear nucleus

VCN: ventral cochlear nucleus

PVCN: posterior ventral cochlear nucleus

AVCN: anterior ventral cochlear nucleus

SOC: superior olivary complex

CNIC: central nucleus of the inferior colliculus

LSO: lateral-superior olive

MSO: medial-superior olive

MNTB: medial nucleus of the trapezoid body

LL: lateral lemniscus

VNLL: ventral nucleus of the lateral lemniscus

DNLL: dorsal nucleus of the lateral lemniscus

MGB: medial geniculate body

mMGB: medial division of the medial geniculate body

dMGB: dorsal division of the medial geniculate body

vMGB: ventral division of the medial geniculate body

LCIC: lateral cortex of the inferior colliculus

DCIC: dorsal cortex of the inferior colliculus

GABA: gamma-Aminobutyric acid

CA: Cornu ammonis

GFAP: glial fibrillary acidic protein

S100B: S100 calcium-binding protein B

F4/80: EGF-like module-containing mucin-like hormone receptor-like 1

Aβ: amyloid beta protein

APP: amyloid precursor protein

Tg: transgenic Fischer 344 Alzheimer’s disease

PBS: phosphate buffered saline
PFA: paraformaldehyde
GAD67: glutamic acid decarboxylase 67
NeuN: hexaribonucleotide binding protein-3
CD11b: cluster of differentiation molecule 11B
HyD3: hybrid detector
TIFF: tagged image file format
Iba1: ionized calcium binding adaptor molecule 1
VCNIC: ventral central nucleus of the inferior colliculus
GSL1: Griffonia (Bandeiraea) Simplicifolia Lectin 1
ROI: region of interest
ROC: receiver operating characteristic
SR101: Sulforhodamine 101
PSEN1: Presenilin 1
DAB: diaminobenzidine
ANOVA: analysis of variance
FDG: fludeoxyglucose
PET: positron emission tomography
OCR: oxygen consumption rate
ATP: adenosine triphosphate
FCCP: Carbonyl cyanide-4-phenylhydrazone
SEM: scanning electron microscopy
PCR: polymerase chain reaction
GAD65: glutamic acid decarboxylase 65
SV2A: synaptic vesicle glycoprotein 2A
OCT: optimal cutting temperature
BCA: bicinchoninic acid assay
DNTB: 5′-Dithiobis 2-nitrobenzoic acid
CSA: citrate synthase activity
Cyc1: cytochrome C1

EIF4A2: eukaryotic translation initiation factor 4A2

GAPDH: glyceraldehyde 3-phosphate dehydrogenase

Contents

Chapter 1 – General introduction

Chapter 2 – General methodology

Chapter 3 – *Iba1+* microglia interact with neuronal somata and synapses in the inferior colliculus

Chapter 4 – Increased labelling of astrocytic *GFAP+* in the ageing TgF344-AD rat inferior colliculus is similar to CA3 in hippocampus

Chapter 5 – Age-dependent synaptic dysfunction in the inferior colliculus and hippocampus of Tg-F344AD rats

Chapter 6 – General discussion

Chapter 1 – General introduction

1.1 – Overview

After centuries of neuroscientific study and technological advancements, substantial discoveries have been made into understanding brain anatomy and physiology. It is well established that the regions of the brain are made up of neurons, synapses, microglia and astrocytes. However, the individual and interdependent roles each of these components play from region to region across the brain is far from clear. One of these brain regions is an integral nucleus within the auditory pathway, the inferior colliculus (IC), of which there is a particular paucity of study regarding the glial cells therein, and is consequently the main target of this thesis.

There is emerging evidence that hearing loss is associated with the development of dementia. Therefore, this Chapter will first lay the foundation of how sounds are processed along the auditory pathway, with a focus on how they project to the IC, as this is the model auditory nucleus employed in this thesis to identify mechanisms between hearing loss and dementia. This will be followed by contextualising background on astrocytes, microglia and synapses, and an introduction to each of the brain regions studied in this thesis, with particular focus on the IC, setting the stage for the findings presented in Chapter 3. This will be followed by an outline of the physiological effects of aging, dementia, Alzheimer's disease (AD) and the link between hearing loss and dementia, which are of direct relevance to the studies presented in Chapters 4 and 5. To this end, the two animal models used in this thesis will be discussed. Finally, this Chapter will culminate by highlighting pertinent gaps in our understanding that are addressed in this thesis.

1.2 – The auditory pathway

The auditory pathway is a complex system that can be divided into the peripheral and central components. The peripheral pathway processes sound stimuli outside the head, along the external, middle and inner ear (Figure 1.1), detecting changes in air pressure waves and mediating transfer of these signals toward the central component, where auditory signals enter the brain and are processed by the central auditory pathway (Figure 1.2). Structures along the central auditory pathway are based on a tonotopic organisation - i.e. a frequency place map, first established in the inner ear, and found throughout the auditory system. The numerous structures along the central auditory pathway allow the determination of fundamental parameters of auditory perception, such as sound level (perceived as loudness) and azimuthal/vertical position (perceived as location). This section will provide a brief outline of the structures along the peripheral and central auditory pathways.

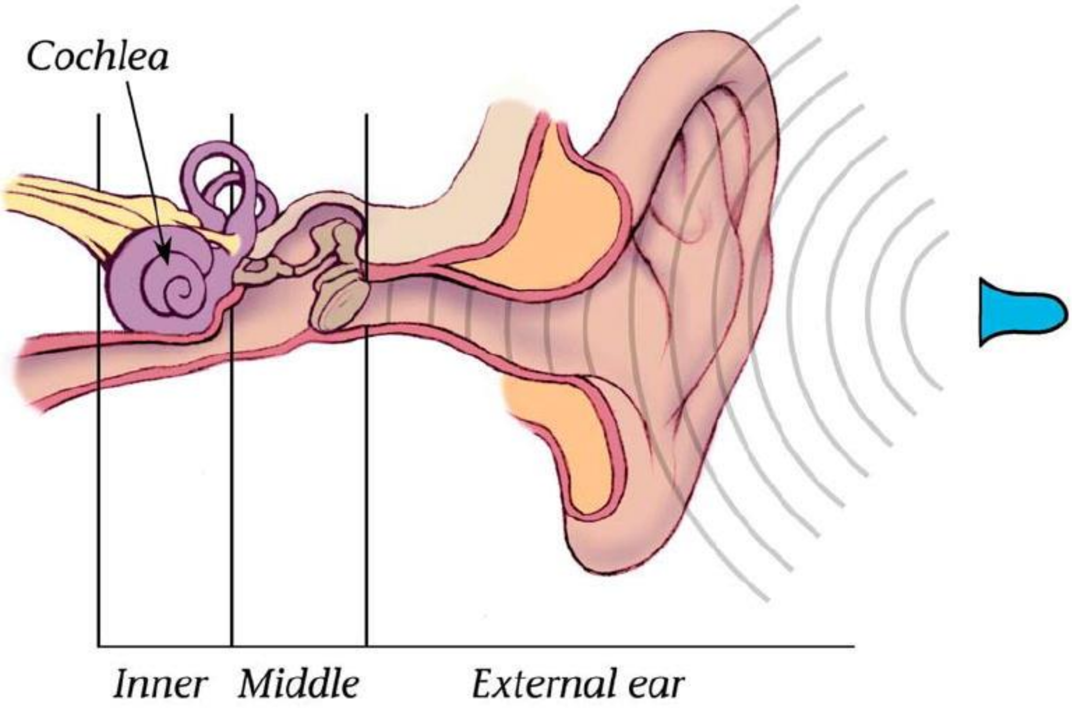

Figure 1.1. Image displaying the location of the cochlea in the inner ear with respect to the structures of the middle and extrnal ear the peripheral auditory pathway from Brownell (1997).

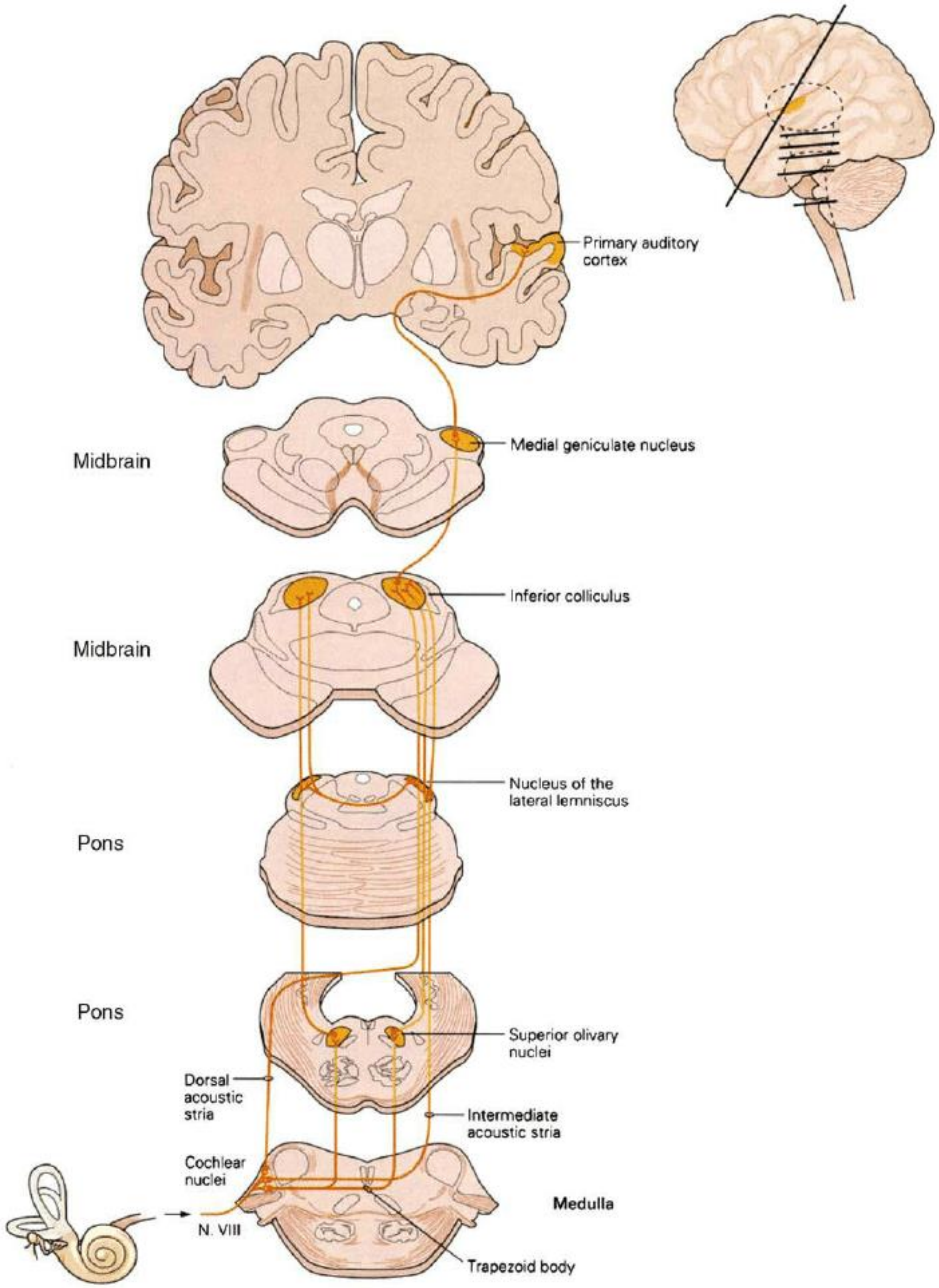

Figure 1.2. Image displaying the structures that make up the central auditory pathway and their location within the brain from Graven and Browne (2008). Note the key location of the IC within the ascending and descending pathwys.

1.2.1 – External ear

The external ear is comprised of the pinna, concha and auditory canal and is the first point of contact for air pressure along the auditory pathway. The pinna is a corrugated structure, which directs the air molecules based on their elevation, amplitude and frequency through the concha towards the auditory canal. Sound molecules oscillate down the length of the auditory canal and impinge upon the tympanic membrane. Depending on the elevation, amplitude and frequency of the air molecules determines the angle at which they interact with the tympanic membrane (eardrum).

1.2.2 – Middle ear

The middle ear is composed of an air-filled environment, separated from the external environment by the tympanic membrane (Sade *et al.*, 1995). Figure 1.3 provides a representation of the anatomy of the middle ear. The tympanic membrane is composed of the *pars flaccida* and *pars tensa,* which are involved in maintaining the pressure within the middle ear and converting air molecules into specific vibrations respectively (Stenfors *et al.*, 1979, Milazzo *et al.*, 2017). Attached to the *pars tensa* is the malleus, which transduces vibrations of the tympanic membrane (Mason, 2016). These vibrations then pass to the incus, then the stapes. These three bones are the smallest in the body and collectively form the ossicles.

The stapes is attached to a footplate that connects to the membrane of the oval window. Here, the vibrations displace the fluid within the inner ear. The malleus incus and stapes form the ossicular chain, which together amplify the pressure exerted upon the tympanic membrane and result in increased detection of signals.

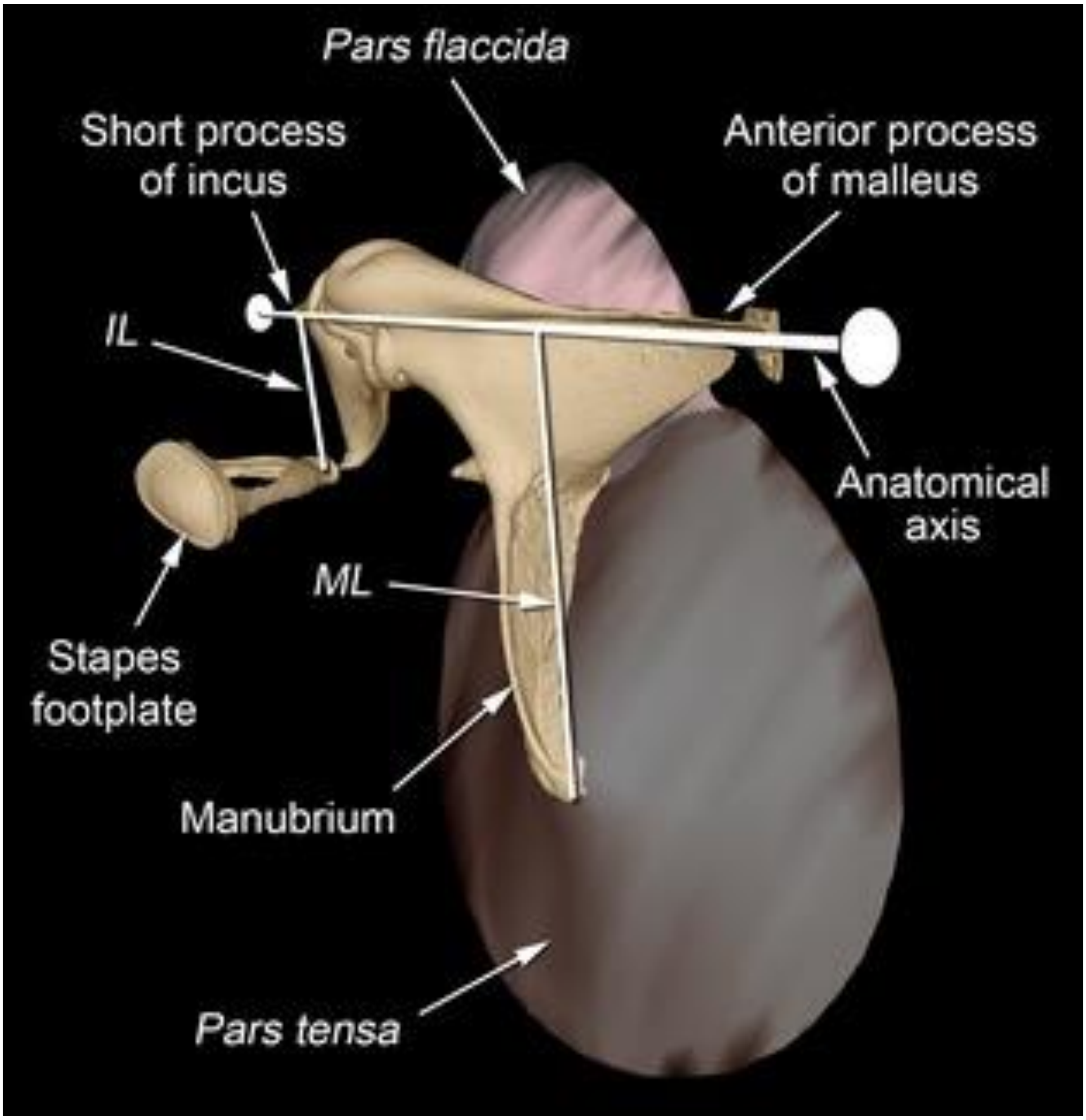

Figure 1.3 Image depicting the structures of the middle ear (Mason, 2016). Sound waves directed from the outer ear impinge upon the fibrous *pars flaccida* and *pars* tensa. At the *pars tensa* the sounds waves are converted into vibrations which are passed to the malleus. The malleus then directs the vibrations through the incus, then stapes. The vibrations are then directed across the stapes footplate, which is attached to the oval window of the bony labyrinth.

1.2.3 – Inner ear

The inner ear consists of the bony labyrinth and within it the membranous labyrinth, which are composed of three main constituents, including the cochlea, vestibule and the three semi-circular canals (Figure. 1.4A). The membranous labyrinth is surrounded by perilymphatic fluid and filled with endolymphatic fluid. Vibrations across the oval window disrupt the endolymph within the vestibule and here signals diverge into the cochlea and semi-circular canals. Signals that traverse the semi-circular canals are important in vestibular processing and the cochlea is important in auditory processing. The vestibular system is beyond the scope of this thesis, but has been reviewed by Angelaki and Cullen (2008).

The membranous structures within the cochlea include the *scala vestibuli* and *scala tympani* which are separated by the cochlear duct (Figure 1.4B). Along the *scala tympani* lies the basilar membrane, which forms part of the organ of Corti, and lies in opposition to the tectorial membrane. The basilar membrane enlarges along the axial border, and resonates according to its size, producing a frequency dependent map of maximal displacement in response to sound stimuli. The organ of Corti is populated by inner and outer hair cells, with protruding stereocilia. The displacement of the basilar membrane in opposition to the tectorial membrane causes mechanotransduction of the vibrations to an electrical signal by disrupting the stereocilia of hair cells, which in turn innervate spiral ganglion fibres (Hudspeth, 1989).

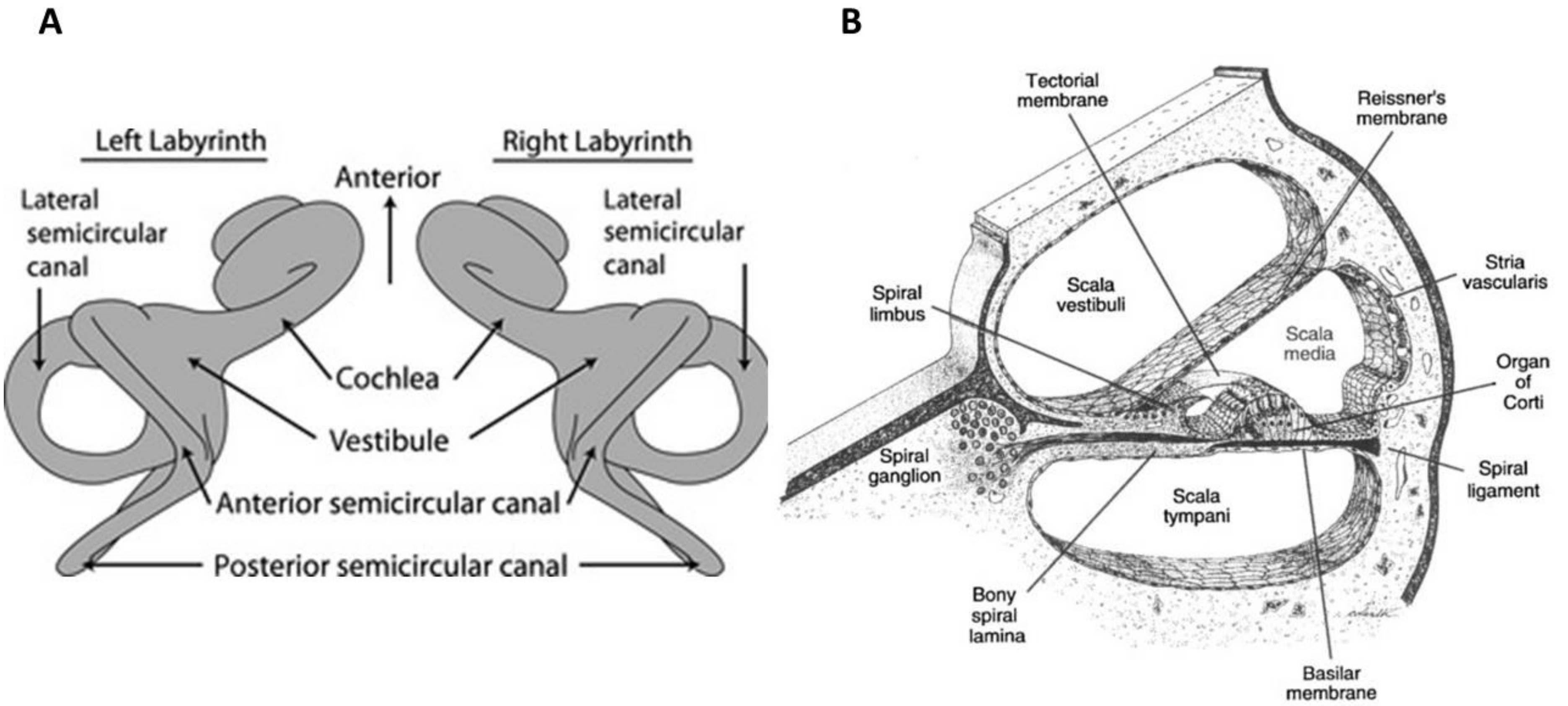

Figure 1.4 (A) Composition and bilateral anatomical positioning of the bony labyrinth from each ear. The bony labyrinth is subdivided into three semi-circular canals, the cochlea and the vestibule from Ekdale (2016). (B) An example image illustrating the composition within the cochlea from Jenison (2001). The cochlea is where mechanical signals are converted into electrical signals in spiral ganglion fibres. This transduction process occurs at the organ of corti, which is located above the basilar membrane and below the tectorial membrane. These structures are encased within the scala tympani and scala vestibule, which surround, and are sealed from, the scala media.

1.2.4 – Cochlear nucleus

Auditory spiral ganglion nerve fibres enter the brain and branch to innervate divisions of the cochlear nucleus (Benson and Brown, 2004). Two main divisions that comprise the cochlear nucleus include the dorsal cochlear nucleus (DCN) and ventral cochlear nucleus (VCN). The VCN can be further sub-divided into posterior (PVCN) and anterior (AVCN) regions (Figure 1.5). Spiral ganglion fibres from the cochlea tonotopically innervate neurons within the cochlear nucleus and these signals bifurcate and innervate the AVCN and PVCN. Neurons are innervated in line with their source of innervation from hair cells on the basilar membrane (Lorente de Nó, 1979, De No, 1981, Osen and Roth, 1969). Low frequency signals relayed into the CN are processed ventrally, while higher frequency signals are processed dorsally (Evans and Nelson, 1973, Rose *et al.*, 1959).

The PVCN is made up of stellate and octopus neurons and stellate neurons can be further classified as T and D stellate cells (Oertel *et al.*, 1990). T stellate cells signal through the nucleus of the trapezoid body and project to the contralateral IC, while D stellate cells signal with the DCN. Octopus cells are found within the most caudo-medial region of the PVCN and are found perpendicular to auditory nerve fibres. T stellate neurons in PVCN are tonotopically arranged, in line with the AVCN. T and D stellate cells also populate the AVCN, in addition to bushy cells. Here, T stellate and bushy cells in parallel form the tonotopic pathway, whereby bushy cells project to the superior olivary complex and the T-stellate cells project to the IC, forming a major source of afferent input (Blackburn and Sachs, 1990, Frisina *et al.*, 1990, Joris *et al.*, 1994, Cant and Benson, 2003).

The DCN has three layers, including the molecular, fusiform and deep layers. The DCN is predominantly composed of fusiform neurons with apical dendrites protruding to the *glia*-

limtans border with basal dendrites directed towards the deep layer (Blackstad *et al.*, 1984). The apical dendrites of the fusiform neurons extend into the molecular layer. Fusiform cell bodies populate the fusiform layer and their basal dendrites enter the deep layer. Other neuronal cell types that populates the deep layer are giant cells (Ryugo and Willard, 1985) and unipolar brush cells (Bauer *et al.*, 2013). These two cell types are involved in projecting to the contralateral IC (Adams, 1979, Ryugo and Willard, 1985). The DCN receives afferent projections from the PVCN and the present fusiform and giant cells are oriented tonotopically. The DCN is involved in filtering self-made sounds (Singla *et al.*, 2017), responding to spectral cues and integrating signals with vestibular and somatosensory systems through parallel fibre inputs similar to cerebellar circuits (Singla *et al.*, 2017).

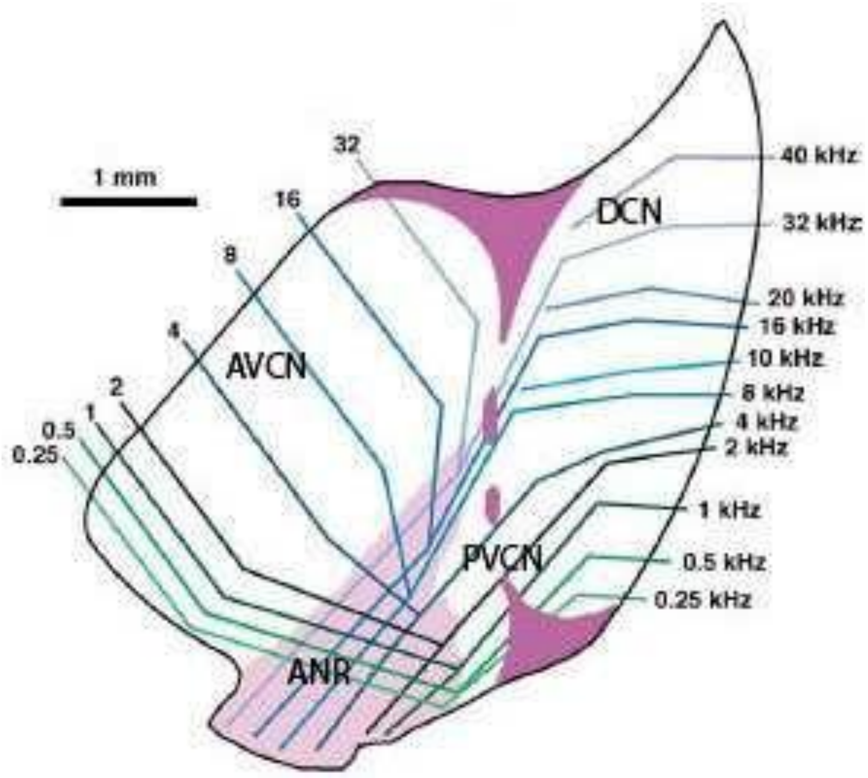

Figure 1.5. The CN is subdivided into the AVCN, PVCN and DCN. Each region of CN is organised tonotopically, with high frequency signals processed dorsally and low frequencies ventrally from Bahmer (2007).

1.2.5 – Superior olivary complex

The superior olivary complex (SOC) is comprised of numerous nuclei that are located in close proximity within the ventral pons. The SOC is the second target in the ascending auditory pathway, receiving afferent tonotopic projections from both sides of the CN. The SOC is a primary source of excitatory projections to the central nucleus of the IC (CNIC) (Oliver *et al.*, 1995). Nuclei of the SOC are the first sites in the auditory pathway where signals from both ears converge. The SOC is subdivided into the lateral-superior olive (LSO), medial-superior olive (MSO), the medial nucleus of the trapezoid body (MNTB) and numerous periolivary nuclei. Schofield and Cant (1991) classified up to eleven different subtypes of periolivary nuclei, including the lateral and ventral nucleus of the trapezoid body, though these are thought to vary between species. Tonotopy is also found throughout SOC, whereby high frequency signals in LSO are processed in the medial portion and low frequency signals are processed laterally. In MSO, high frequency signals are processed ventrally and low frequencies dorsally (Goldberg and Brown, 1968) and in MNTB high frequency signals are processed ventromedially and low frequencies are processed dorsolaterally (Figure 1.5) (Guinan *et al.*, 1972). This tonotopic organisation is reflected in the locations within the IC to which respective neurons project.

The MSO is located centrally within the SOC and receives bilateral projections derived from bushy cells from the cochlear nucleus (Harrison and Irving, 1966, Osen and Roth, 1969). Central MSO is populated by fusiform cells, whereby their dendrites are orientated perpendicular to the plane and protrude towards the lateral borders. In addition, there are a smaller proportion of marginal neurons, with dendrites branching towards the centre of the nucleus, as well as multipolar cells that are distinct from marginal cells. Some marginal neurons are located centrally with others located rostro-caudally (Schwartz, 1977). The MSO receives ascending bilateral projections from both ipsilateral and contralateral AVCN, enabling the integration of signals. The main source of afferent excitatory synaptic endings projected from neurons in the MSO can be found in the CNIC (Oliver *et al.*, 1995).

The LSO has a number of fusiform cells lining the central band, which have polar dendrites oriented perpendicular to the arching nature of the nucleus, and in opposition has a number of marginal cells populating the border. The main sources of afferent auditory signals to the LSO are from the ipsilateral AVCN and MNTB and the LSO projects bilaterally to the lateral lemniscus and IC. Projections to the IC from the LSO are a primary source of glycinergic processing, which is a major source of inhibitory input. This inhibition may modify the representation of interaural level responses, in combination with excitatory projections from other sources (Saint Marie and Baker, 1990). In addition, the LSO has a significant number of excitatory synaptic endings found in the CNIC (Oliver *et al.*, 1995), albeit less than the MSO.

The MNTB is composed predominantly of principal, elongate and stellate neurons and is home to the largest synapses in the mammalian brain, the calyces of Held (Morest, 1968). Principal neurons are the most numerous and anatomically have dense dendrites, which innervate the calyces of Held. The elongated neurons are smaller than principal neurons and have four to five dendritic arbours that protrude dorsoventrally (Morest, 1968). Stellate neurons are located with principal and elongated neurons and have fewer dendrites that protrude in multiple directions. The MNTB is a relay between the AVCN and the LSO and the major projections from the MNTB are relayed tonotopically to the ipsilateral LSO. The MNTB also has ascending connections with the lateral lemniscus and IC. Determination of interaural time differences and interaural level differences are processed across various regions of the SOC. Collectively, these nuclei interact to distinguish binaural interaural time and level differences via excitatory and inhibitory inputs, which are further processed in the IC, after traversing through the lateral lemniscus (Kelly *et al.*, 2009).

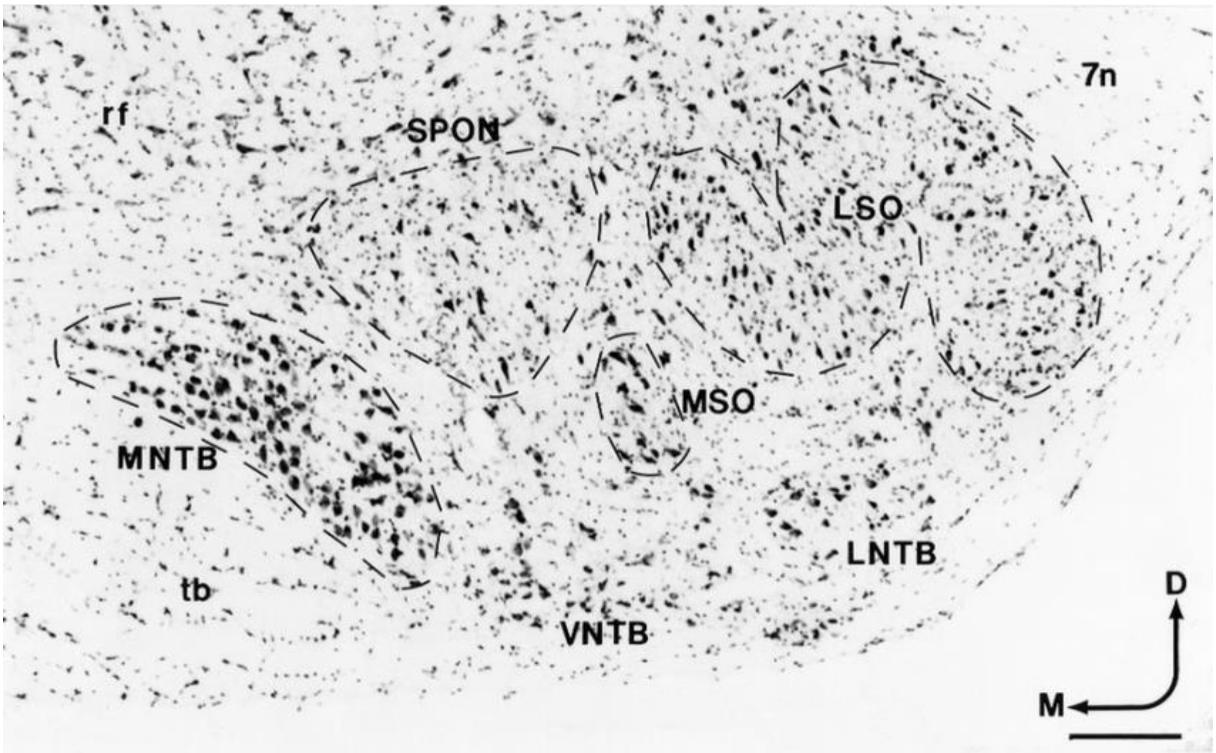

Figure 1.6. The parcellation of the main subdivisions of the SOC from (Kulesza and Berrebi, 2000). Each subdivision is tonotopically organised. The LSO has high frequencies medially and low frequencies laterally. High frequencies in MSO are processed ventrally and high frequencies dorsally. In MNTB, high frequencies are processed ventromedially and low frequencies dorsolaterally.

1.2.6 – Lateral Lemniscus

Afferent projections from neurons in CN and SOC are sent to each side of the lateral lemniscus. The lateral lemniscus is essential in relaying ascending auditory information from the CN and SOC to the IC (Kelly *et al.*, 2009). There is conflicting literature as to how many subdivisions of lateral lemniscus there are. Some research suggest there is three (Adams, 1979, Zook and Casseday, 1982), some suggest two (Brunso-Bechtold *et al.*, 1981, Glendenning *et al.*, 1981) and others one (Saint Marie and Baker, 1990, Willard and Martin, 1983). In rat there is a subdivision termed the intermediate nucleus of the lateral lemniscus that has been found to project to the ipsilateral CNIC (Kelly *et al.*, 2009). However, it is generally considered that there are two different groups of neurons that project to distinct regions. These groups include the ventral nucleus of the lateral lemniscus (VNLL) and the dorsal nucleus of the lateral lemniscus (DNLL) (Figure 1.7). These regions have distinct neuronal types; the VNLL is comprised of oval neurons, multipolar and horizontal cells (Adams, 1979). On the other hand, DNLL is comprised of four types of neurons including, i) ovoid multipolar neurons with dark Nissl labelling, ii) large bipolar with dark Nissl labelling, iii) medium sized ovoid neurons and iv) small round neurons with light Nissl labelling (Bajo *et al.*, 1993).

The VNLL predominantly sends afferent signals to the ipsilateral CNIC (Saint Marie and Baker, 1990, Tanaka *et al.*, 1985) and sends fewer projections to the medial geniculate body of the thalamus, the DNLL (Whitley and Henkel, 1984), the periolivary nuclei and the ventral nucleus of the trapezoid body (Whitley and Henkel, 1984). As a result of the predominant signals projected to the IC, the topographic orientation of VNLL neurons mirror the orientation of projections to the CNIC (Benson and Cant, 2008). Tonotopic organisation of nuclei in the VNLL is a concept of controversy. Guinan *et al.* (1972) suggests in cats that there is no tonotopic organisation, however, Covey and Casseday (1991) showed tonotopically organised neurons in bat. These results may underpin evolutionary differences across species and provide insight into the relationship between frequency hearing ranges and shaping VNLL tonotopy, which will ultimately shape IC structure. Similarly, to VNLL, neurons in the DNLL have been found to project afferent signals to distinct regions of the CNIC, which are organised tonotopically (Kelly *et al.*, 2009). DNLL also sends afferent signals to regions of the contralateral DNLL and superior colliculus (SC), in addition to transmitting descending projections to the periolivary regions of the SOC (Bajo *et al.*, 1993).

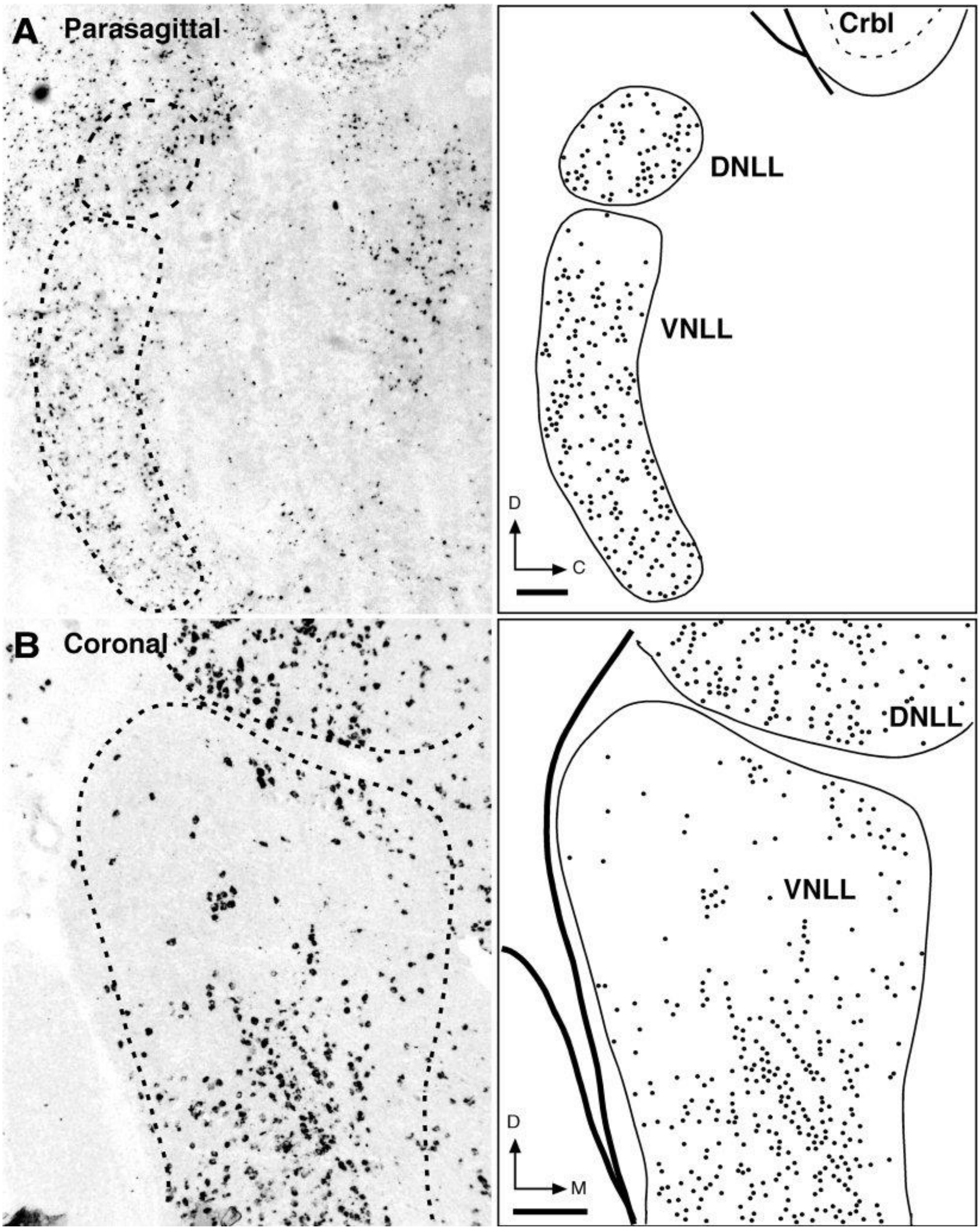

Figure 1.7. Micrographs labelled with the inhibitory *GAD65* mRNA using *in situ* hybridisation (A) sagittal (B) coronal. Subsequent masks of micrographs (located adjacent to respective micrograph) taken from (Riquelme *et al.*, 2001). The DNLL and VNLL can be separated based on neuronal densities.

1.2.7 – Medial geniculate body

Of the structures comprising the auditory pathway, there is the least amount of literature surrounding the medial geniculate body (MGB). What is known is that the MGB is located laterally from the midline, at the caudal end of the thalamus (Winer and Wenstrup, 1994). Anatomically, it is evident that the MGB is an essential relay point along the afferent auditory pathway, receiving projections from the IC. The MGB is subdivided into three subdivisions including the medial division of MGB (mMGB) dorsal MGB (dMGB) and ventral MGB (vMGB) (Morest, 1964).

Afferent tonotopic auditory signals, transmitted from the IC, are processed in the MGB prior to processing in the auditory cortex. Neurons within the mMGB are medium-sized including radiate, tufted elongate dendrites small stellate and large neurons, which are weakly tufted (Winer and Morest, 1983). The ramification of neuronal dendrites within the dMGB are much finer than in the other sub-regions. In addition, the dMGB is involved in projecting descending signals to the lateral cortex of the IC (LCIC) creating a thalamo-collicular connection (Kuwabara and Zook, 2000). The vMGB is defined by tufted neuronal dendrites, and the neurons follow a tonotopic fibrodendritic laminated structure and projections from IC accordingly course in parallel (Morest, 1964, Clerici *et al.*, 1990). This maintained structure between the IC and MGB suggests that if the IC was afflicted, that it would also influence processing in the MGB. to The vMGB is involved in the rapid transmission of afferent signals and is sharply tuned to fast modulations of sounds (Edeline, 1999), in contrast to the dMGB which has slower responsiveness (Bartlett, 2013), demonstrating functional differences related to variations in cellular anatomy.

1.2.8 – Auditory cortex

The auditory cortex is located within the neocortex and is comprised of six layers based from the outermost layer to the deepest layer (Rakic, 2009) at the apex of the auditory pathway. What defines the borders of auditory cortex is challenging, as the anatomy and physiology differ substantially between animals within a species, and more so between species (Kaas, 2010). Winer (1984) characterised in the tonotopically-organised layer IV, a variety of different sub-types of neurons in primary auditory cortex. The majority of neuronal types include small, medium and large tufted neurons, with inward facing axons. Albeit less numerous, there are also sporadically located large multipolar, double bouquet, and spiny stellate cells throughout. In layer V of auditory cortex, projections from the IC comprise large pyramidal neurons that have dendrites that project extensively into layer II (Games and Winer, 1988). The majority of auditory cortex signals have been found to project predominantly to the dorsal cortex of the IC (DCIC), with a significantly lower number being projected to the CNIC (Winer *et al.*, 1998). Auditory cortex receives afferent signals from the vMGB, which terminate in layers III and IV, this information is then relayed to influence non-auditory cortical regions (Webster, 1992). A large proportion of neurons from layers II and III, and to a lesser extend IV and V have been found to relay signals via the white matter tract, the corpus callosum, to the contralateral auditory cortex (Rouiller and Welker, 1991).

1.3 – Brain regions of interest to this thesis

The previous section introduced the auditory pathway as it forms the major sources of afferent and efferent connections of IC to demonstrate its integrative nature. Other brain regions of interest used throughout this thesis were selected as regions independent of the auditory pathway, with important roles pertinent to each Chapter. An overview will be provided here, and their more specific roles will be introduced in each respective results Chapter.

The results Chapters of this thesis focus primarily on IC. The first of these investigates interrelationships of glial cells and putative GABAergic neurons and synapses, and also investigates how these vary across different sub regions of IC (Chapter 3). The next Chapter builds upon Chapter 3, by looking at the interrelationships of glial cells across sub regions of IC and how they compare to other regions of the brain in an ageing transgenic model, in addition to measuring neuronal counts (Chapter 4). The final Chapter investigates synaptic functioning and gene expression, along with measuring glial gene expression, in an ageing transgenic model and how it compares to other regions of the brain (Chapter 5). Therefore, these brain regions will now be introduced, with preeminent focus on the IC.

1.3.1 – The inferior colliculus anatomy and physiology

The IC is located in the midbrain, rostral to the cerebellum, caudal to SC, and ventral to visual cortices (Figure 1.8A). The IC is made up of two egg shaped structures, which are connected by a commissure that is involved in integrating bilateral signals and contribute to the neural representation of azimuthal sound location (Orton and Rees, 2014). Ascending afferent signals reaching the IC are predominantly received from the contralateral DCN and VCN. Fewer, but significant projections to IC originate from the ipsilateral ventral nucleus of the trapezoid body, VNLL and the deep layers of SC. Furthermore, projections from nuclei on both sides of the midline are received from the MSO, DNLL and auditory cortex (Willard and Martin, 1983).

Morest and Oliver (1984) defined each sub-region of IC to be tegmental or tectal based on neuronal dendritic morphology. The tectal regions predominantly receive afferent signals from the auditory pathway and tegmental regions receive input generally from other sources. They classified the three main subdivisions that comprise the IC including, the CNIC, dorsal cortex (DCIC) and lateral cortex (LCIC), which is often referred to in the literature as the external cortex (Coote and Rees, 2008). Recently, Bielefeld *et al.* (2008) expanded upon the work of Morest and Oliver (1984), uncovering that the CNIC predominantly receives ascending input rather than descending. Additionally, they found that neurons in the cortices could be classified into two groups: i) primarily receiving ascending auditory projections and ii) receive a multitude of descending projections, neuromodulatory nuclei and projections from the contralateral IC.

1.3.1.1 – Central nucleus, lateral cortex and dorsal cortex inferior colliculus

The CNIC is defined by its fibrodendritically laminated neuronal layout with the neuropil, mainly populated by disk-shaped neurons, with dendritic fields in parallel with terminating afferent laminated myelinated axons, intermingled with less numerous stellate cells, which have radiating dendritic fields that span across laminae (FitzPatrick, 1975). This is in contrast to the cortices, which are comprised of neurons that are orthogonal to in the CNIC, but lack disc-shaped neurons (Chen *et al.*, 2018). Other methods that allow sub regions to be discerned include implementing histological methods such as using immunohistochemistry for calcium-binding proteins, including parvalbumin, calretinin and calbindin (Tardif *et al.*, 2003). Neurons in CNIC are predominantly parvalbumin positive, with sparse calretinin and calbindin positive neurons; however, this reverses in the cortices, whereby calretinin and calbindin comprise the largest concentration of neurons (Figure 1.8B). Differing densities of calcium-binding proteins provides insight into the signalling properties across the IC sub regions, one feature being that the CNIC is more GABAergic than the cortices which are more glutamatergic (Gritti *et al* 2003). Numerous studies have revealed that the DCIC resembles LCIC with smaller neurons and a fibrous outer layer (Ito *et al.*, 2009, Rockel and Jones, 1973). The border of the DCIC, adjacent to the CNIC is clearly separated by neurons in CNIC, lining the fibrodendritic laminae and neurons within DCIC lack clear orientation (Morest and Oliver, 1984). The LCIC is located relative to the low frequency processing region of CNIC and is defined by a fibrous outer layer and an adjacent layer with a low number of neurons (Morest and Oliver, 1984). More details specific to each sub region are introduced within each results Chapter.

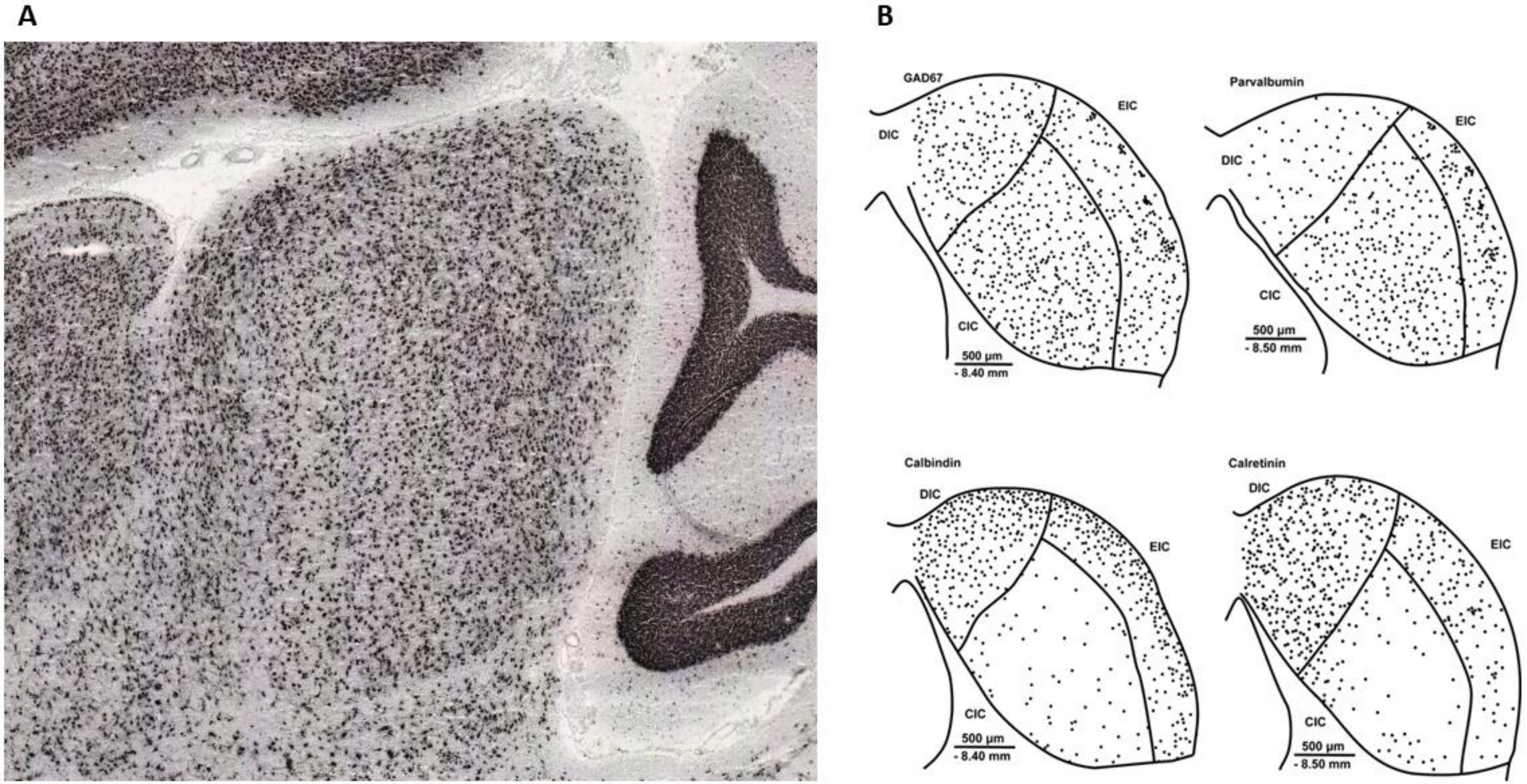

Figure 1.8. (A) Micrograph displaying staining for *NeuN*, which labels nonspecific ubiquitous neurons throughout the IC. (B) Example drawings illustrating the densities of *GAD67*+, *parvalbumin*+, *calbindin*+ and *calretinin*+ neurons across the sub regions of IC, from (Ouda *et al.*, 2012). Contrasting (A) and (B) illustrates the high proportion of GABAergic (*GAD67*+) cells within the IC. How GABAergic neurons are distributed across the sub regions of IC and their interrelations with other cell types is covered in Chapter 3. In addition, notice the higher density *parvalbumin*+ neurons in the CNIC in comparison to the cortical regions. Also, notice the lack of *calbindin*+ and *calretinin*+ neurons within the CNIC.

1.3.1.2 – Inhibitory processing

Inhibition within the IC is mainly regulated by glycinergic and GABAergic transmission (Koch and Grothe, 1998). GABAergic projections to the IC are primarily received from the DNLL (Adams and Mugnaini, 1984) and less so from LSO and the VNLL. Glycinergic projections are received from the VNLL, LSO, periolivary nuclei and CN (Saint Marie and Baker, 1990). Approximately 25% of neurons within IC are GABAergic and these neurons differ in the number of synaptic inputs onto non-GABAergic neurons across subdivisions (Merchán *et al.*, 2005). In addition, GABAergic neurons projecting from the MGB to IC can be classified based on synaptic inputs, or lack thereof (Beebe *et al.*, 2016).

The mechanism in IC that is involved in regulating interaural time differences and enabling signals from both ears to be perceived together is regulated by inhibitory processing (Fujita and Konishi, 1991). The nature of inhibitory processing in IC led (Ingham and McAlpine, 2005) to postulate that GABAergic inhibition is involved in regulating neuronal gain, which is a phenomenon that is hypothesised to be a crucial mechanism involved in the development of tinnitus (Brotherton *et al.*, 2015).

1.3.1.3 – Glial cells

Glial cells will be introduced briefly here regarding the IC. A more in-depth introduction to astrocytes and microglia will be provided in section 1.4. In addition to the high density of GABAergic neurons, Hafidi and Galifianakis (2003) demonstrated that the IC develops a dense oligodendrocyte network in mature gerbil. They also showed that astrocyte cell bodies equidistantly populate the IC sub-nuclei from birth using the marker S100. Using the reactive marker of astrocytes *GFAP* there were no labelled cells throughout. Microglia are widely distributed in IC across all sub regions (Lawson *et al.*, 1990), but little research has been conducted into the anatomy of microglia in IC. A recent study by Rosskothen-Kuhl *et al.* (2018) looking at the role of glial cells in IC auditory processing compared normal hearing to neonatally deafened rats concluded that growth and activity of astrocytes and microglia are essential for regulating excitatory and inhibitory processing, which highlights using the IC as a model for understanding contributions glia make to inhibitory neuronal processing.

1.3.1.4 – Metabolic functioning

Among all other brain regions, the IC is by far the most metabolically active nucleus within the brain (Sokoloff *et al.*, 1977a). Correspondingly, the IC also has the highest blood volume and influx of glucose and amino acids in the brain (Cremer and Seville, 1983) along with the highest levels of cerebral blood flow (Landau *et al.*, 1955, Sakurada *et al.*, 1978). A study by Gross *et al.* (1987) revealed that the capillary density was substantially higher in the CNIC in contrast to the cortices. These findings strongly suggest the possibility of IC being susceptible to metabolic decline. Consequently, Clerici and Coleman (1987) observed remodelling of pure-tone metabolic evoked response detection to compensate for age-related reductions in afferent signals from the cochlea. In addition, during acoustical stimulation of IC, trafficking of glucose, lactate and amyloid-beta results in clearance into the interstitial fluid that could have implications in IC dysfunction (Ball *et al.*, 2010). More details on the IC pertinent to the findings of this thesis will be presented in each results Chapter, as pertinent to the respective data found therein.

1.3.2 – Hippocampus

The hippocampus is one of the most studied parts of the brain, due to it largely being involved in memory and learning (Anand and Dhikav, 2012). The hippocampus is located between the mesencephalon and the medial portion of temporal lobe (Destrieux *et al.*, 2013). Hippocampus is a large sub-cortical brain region that is subdivided into two parts, the Cornu ammonis (CA) and dentate gyrus (Anand and Dhikav, 2012). The regions of the CA are respectively termed CA1, CA2, CA3 and CA4 and are based on a pathway of pyramidal neurons that curve around the hippocampus starting at the dentate gyrus (Parekh *et al.*, 2015) (Figure 1.9A). The subdivisions of hippocampus receive signals from cortical, limbic and sub-cortical regions, specifically from the subiculum and entorhinal cortex (Rajmohan and Mohandas, 2007). Dentate gyrus is the initial site for incoming neuronal activity from the entorhinal cortex via the perforent path, which then projects to the CA3, CA2 and CA1 regions (see Figure 1.9B). Neuronal anatomy differs substantially across hippocampal sub-regions. The dentate gyrus is composed of a dense granule cell layer with mossy fibres that innervate CA3 pyramidal cells (Amaral *et al.*, 2007). The pyramidal cells of the CA3 region, in turn excite the pyramidal neurons of CA1. After passing along the hippocampal pathway, the CA1 region directs efferent signals back to sub-cortical regions, entorhinal cortex and subiculum.

Synapses in hippocampus are primarily glutamatergic (Fonnum, 1984), but also demonstrate extensive local inhibition (Pelkey *et al.*, 2017) and measures of long-term potentiation at synapses have revealed that stimulating the entorhinal cortex results in feedforward stimulation of CA3 and CA1 (Yeckel and Berger, 1990). The ratio of neurons to glia is higher in the hippocampus than in neocortex (Christensen *et al.*, 2007) and glial cells have been shown to directly influence neuronal and synaptic activity by interaction and releasing glutamate (Angulo *et al.*, 2004).

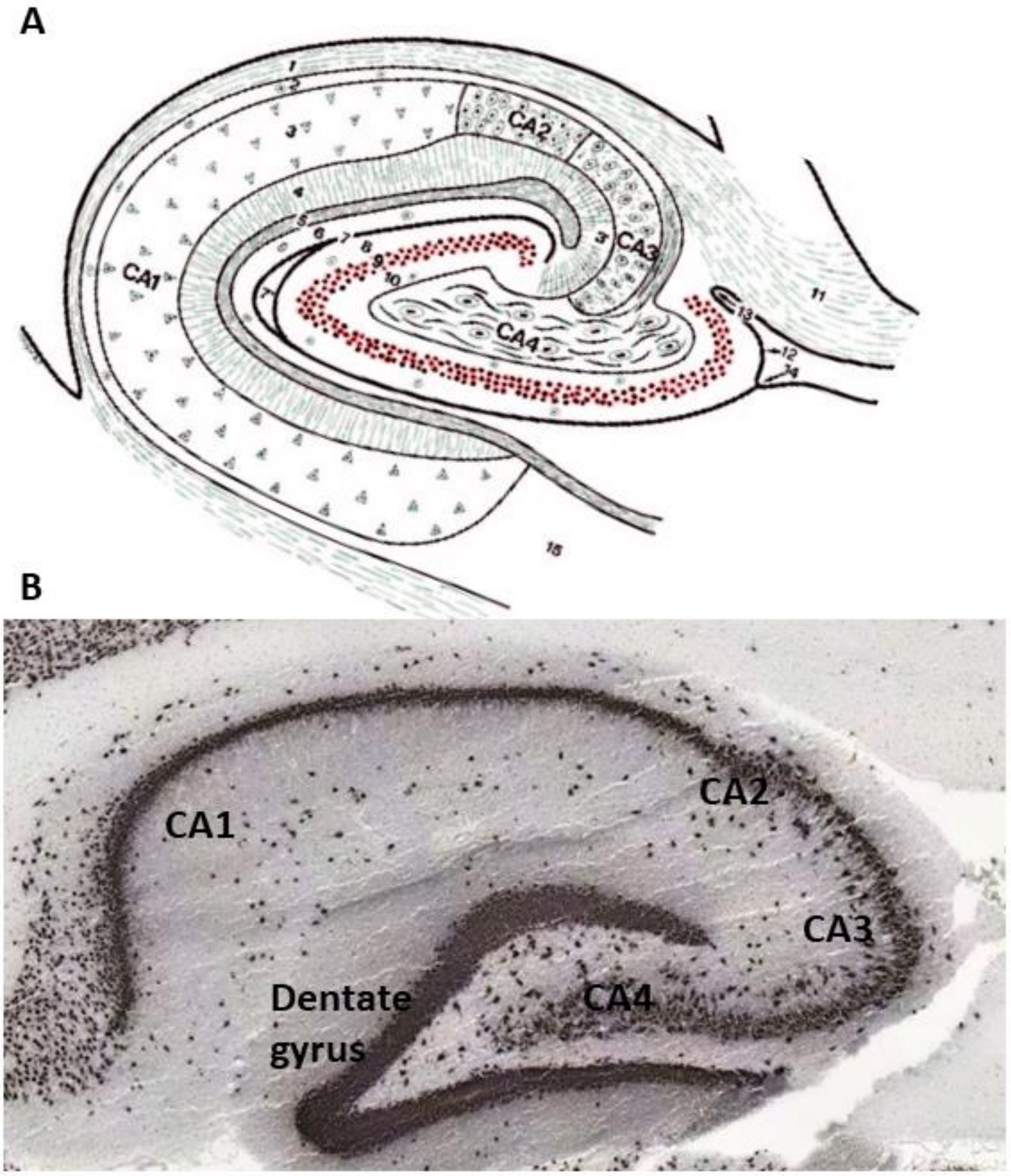

Figure 1.9. (A) Drawing of a sagittal view looking at the anatomy of the hippocampus adopted from (Achten *et al.*, 1995), illustrating the differences between CA1, CA2 , CA3 and CA4 regions and the granule layer of the dentate gyrus is depicted in red. (B) Micrograph labelled with *NeuN* demonstrating the distribution and density of neurons across the different regions of hippocampus. Notice the thick granule layer in dentate gyrus and the transition in neuronal distribution between CA3 and CA1.

1.3.3 – Striatum

Striatum is subdivided into the dorsal striatum and the ventral caudoputamen. The dorsal striatum is pertinent to this thesis, so will be referred to as striatum hereafter. The striatum is a sub-cortical brain region located in the basal ganglia of the forebrain, rostrally adjacent to the lateral ventricle across from hippocampus and ventrally to somatosensory cortex. Striatum is an essential region involved in mediating responses based on reward-circuitry, hence influencing decision-making (Lauwereyns *et al.*, 2002). This is in addition to being involved in motor initiation and motor function (Montgomery and Buchholz, 1991). The predominant neuronal cell type within the striatum are medium spiny GABAergic (Ade *et al.*, 2008) and these cells receive substantial glutamatergic projections from cortical regions and dopaminergic projections from the midbrain (Centonze *et al.*, 2001). Lovinger (2010) reviewed synaptic neurotransmission in striatum and discusses how glutamatergic synaptic long-term potentiation and depression is important in habitual learning. Astrocytes in striatum demonstrate significantly less connections with excitatory synapses than in hippocampus (Chai *et al.*, 2017) and also astrocytes have been found interacting with specific neuronal types, suggestive of heterogeneous astrocyte activity (Martin *et al.*, 2015).

1.3.4 – Prefrontal cortex

The frontal cortex consists of the premotor, primary motor and prefrontal cortices. The prefrontal cortex is the region of the frontal cortex that regulates working memory and this is a critical function that deteriorates as a result of numerous neurological conditions including Alzheimer's disease (Sampath *et al.*, 2017). Therefore, this thesis only focuses on the prefrontal cortex. The prefrontal cortex occupies the most rostral component of the forebrain. Amongst all animals, the prefrontal cortex is the most developed in humans, which hampers the interpretability when experimenting on other mammals (Kolb *et al.*, 2012). This does not however, disrepute studying prefrontal cortex in other mammals, as mammalian prefrontal cortex has evolved from similar ancestors and the cell types are not dissimilar (Teffer and Semendeferi, 2012). There are substantial differences in prefrontal cortex anatomy to understand when comparing rodents to humans. Primates have a lateral prefrontal cortex, which is not as developed in rodents (Preuss, 1995).

The rodent prefrontal cortex is subdivided into the medial and orbital regions, which can be further subdivided into dorsal medial and ventral medial prefrontal cortices that are also present in primates (Ongur and Price, 2000, Cholfin and Rubenstein, 2008). The prefrontal cortex is essential in distinguishing between autonomic functioning and goal-directed responses in humans (Perret, 1974, Cohen and Servan-Schreiber, 1992). Synaptic dendritic spine formation in frontal cortex is higher than in any other region of the brain with the lowest level of corresponding elimination (Elston *et al.*, 2010), which likely relates to cognitive capacity.

1.3.5 – Superior colliculus

The superior colliculus is an integral centre within the visual pathway and is co-member of the *corpora quadrigemina* shared with the IC, located ventrally to the visual cortex in the tectum (Paxinos and Franklin, 2019). Superior colliculus is a layered brain region composed of deep and superficial layers and the number of layers are different across species, which are separated in mammals from other species such as birds and reptiles, in that they signal with cerebral cortex and other sub-cortical regions (Huber and Crosby, 1943, Karten, 2015). The superior colliculus is tasked with integrating visual stimuli into responding with movement (Jay and Sparks, 1987, Marino *et al.*, 2015). The auditory and visual system are linked by specific auditory signals processed in the IC being relayed to the SC, which produces autonomic saccadic eye movements in response to stimuli (Jay and Sparks, 1987). Glial cells in superior colliculus have been found to support neuronal functioning and influence afferent input (Barradas *et al.*, 1989), which is similar to the response observed in IC (Rosskothen-Kuhl *et al.*, 2018).

1.3.6 – Cerebellum

The cerebellum is different from the other brain regions, having a much higher neuronal number and receives significant indirect input from the cerebral cortex (Coffman *et al.*, 2011). It is subdivided into three main regions, consisting of the flocculonodular lobe, anterior lobe and posterior lobe. Cerebellum regulates motor movements, including maintaining posture and balance by regulating muscle activity (Takakusaki, 2017). The cerebellum has five main types of neuronal cells including the main Purkinje cells, granule, Golgi, Lugaro and brush cells, which based on their distribution can provide insight into cross-species cerebellar functioning (Sultan and Glickstein, 2007). Glutamatergic brush cells in cerebellum are also found in the DCN (Kalinichenko and Okhotin, 2005) and are strongly linked to vestibular function, likely being a source of the connection between hearing and balance. Cerebellum is well integrated with cortical regions, whereby its effects are regulated by individual regions and dysfunction could potentially present as forms of learning difficulties (D'Angelo and Casali, 2012). There is a wealth of literature investigating long term synaptic potentiation and depression in cerebellum, all that conclude that synaptic remodelling is essential for learning (Hansel *et al.*, 2001, D'Angelo and Casali, 2012, Ito, 1989, Armano *et al.*, 2000). One type of astrocyte described in cerebellum are called Bregmann glia (Chan-Palay and Palay, 1972), which are involved in granule cell development (Rakic, 1971) and interacting with neurons (Grosche *et* *al.*, 2002). Distributions of microglia are substantially lower in cerebellum and less ramified in morphology in contrast to microglia in cortical regions (Stowell *et al.*, 2018).

1.4 – Roles of astrocytes and microglia in the brain

A major focus of this thesis are glial cells in the IC, particularly astrocytes and microglia. Therefore, these cell types will be introduced here.

1.4.1 – Astrocytes

Astrocytes are one of the most abundant cell types within the brain (Sofroniew and Vinters, 2010). They are important in a large range of roles including facilitating neurotransmission, regulating neuroinflammation and maintaining homeostasis (Matias *et al.*, 2019). They have been recognised as intermediary cells forming tripartite connections between pre- and post-synapses of neurons, underpinning their role in mediating neurotransmission (Perea *et al.*, 2009). Two main types of astrocytes were classified by Miller and Raff (1984) including protoplasmic and fibrous astrocytes.

Protoplasmic astrocytes were described as widely ramified with bushy processes and numerous in grey matter, they have been found to interact with synapses (Rothstein *et al.*, 1996) and line the *glial-limitans* border (Alvarez *et al.*, 2013). Fibrous astrocytes differ from protoplasmic astrocytes substantially in anatomy, as they possess rarely ramified, long processes, and are predominantly found in the white matter. Astrocytes demonstrate different morphologies across the brain (Miller, 2018), which suggests that they could be targeted to provide insight into functioning within separate brain regions.

A common method to identify and investigate astrocytes is by implementing immunohistochemistry. The most widely used marker is anti-glial fibrillary acidic protein

(*GFAP*), which labels intermediate filaments most commonly found in astrocytes (Pekny and Pekna, 2014). The identification of *GFAP*+ astrocytes was first derived from plaques developed in multiple sclerosis (Eng and Dearmond, 1982), but now is used to label astrocytes throughout the brain. Another commonly used astrocyte marker is *S100B*, which is a less specific marker of astrocytes demonstrates high specificity in grey matter regions, but in white matter labels predominantly oligodendrocytes (Streitburger *et al.*, 2012). When labelling regions of the brain with a large proportion of myelinated fibres, *S100B* demonstrates high levels of non-specific labelling, whereas *GFAP* is much more specific (Steiner *et al.*, 2007). In contrast, in the healthy central nervous system, many astrocytes are not detected by *GFAP*, but under pathological conditions all astrocytes are thought to be labelled (Pekny and Pekna, 2004).

Under pathological conditions, astrocytes are key regulators of the immune response as they have been found to become reactive when responding to stress (Pekny and Pekna, 2014). Throughout pathology, astrocytes have been observed to increase in expression and adapt their morphology by becoming more ramified (Dossi *et al.*, 2018). It has also been noted that depending on the stressor, brain region, animal model and a range of different contexts, astrocyte activity can be detrimental and can exacerbate inflammation and damage to tissue (Sofroniew and Vinters, 2010). Therefore, by understanding how astrocytes are distributed across the brain under pathological conditions could provide novel insight into how certain diseases progress.

1.4.2 – Microglia

Microglia are abundantly distributed throughout the brain parenchyma and account for approximately 10% of all cells within the brain (Kettenmann *et al.*, 2011), they are mononucleated cells, which are derived from a mesodermal origin (Rezaie and Male, 2002).

Microglial function is essential to maintain homeostasis within the brain under normal and pathological conditions (Perry *et al.*, 2010). Microglial phenotypes are interdependent with their surrounding environment, changes in the environment can drastically alter microglial morphology. By monitoring and characterising microglial morphology provides insight into the pathological state of the brain. Broadly, microglia have been classified into two types based on extreme changes in morphology. Microglia are generally considered to have a resting and activated state. These states include a healthy 'resting' state, where microglia have widely ramified processes radiating from the somata (Streit, 2001). They also have a pathological 'activated' state, which is when the microglia respond to subsequent stressors, whereby they lose their ramified morphology by withdrawing their processes into the somata (Lynch, 2009). These changes between states is a key component in understanding neurological disease, which is currently poorly understood.

Lawson *et al.* (1990) utilised the macrophage specific plasma membrane glycoprotein marker *F4/80* as a marker of microglial cells identified the distribution of microglia throughout the 'resting' brain. They identified that microglia are distributed differently depending on brain region, but also present various morphologies throughout. This suggests that microglia have different functions depending on where they are situated in the brain under healthy conditions, mirroring astrocytes in this respect. However, there is a paucity of evidence regarding region dependent roles and variations of microglia across the health central nervous system.

Within the healthy brain, microglia are constantly surveying the parenchyma making significant interactions with neurons and synapses (Nimmerjahn *et al.*, 2005, Wake *et al.*, 2009). Microglia have been identified to shape neuronal circuits by phagocytosing synapses with weak connections and injured synapses (Schafer *et al.*, 2012). They have also been found to contribute to the formation of synapses and dendritic spines (Parkhurst *et al.*, 2013, Miyamoto *et al.*, 2016). Not only are microglia involved in regulating neurotransmission, they are also involved in active neurotransmission. Tremblay *et al.* (2010) revealed that microglia adapt their morphology under healthy conditions whereby removing the light exposure to mice for 6-10 days caused microglia within the visual cortex to retract their processes, and when the light exposure was re-introduced for 12-hour light/dark cycles, returned the processes to their previous state. Therefore, identifying regions of the brain with more ramified processes could uncover a sub-discipline of neurotransmission.

Under pathological conditions, microglia are among the first cells to react in the event of an immune response (Rock *et al.*, 2004). Microglia have been observed to increase in number, by activating and responding to the areas of interest (Sarlus and Heneka, 2017). In AD, there is an increased accumulation of activated microglia, which may contribute to neurodegeneration (Solito and Sastre, 2012). Taking into account that microglia demonstrate different morphologies across the brain, one would suggest that their response to neuropathological triggers may be region dependent.

1.5 – Age related changes within the brain

Ageing, the process of passing time (Lopez-Otin *et al.*, 2013) is associated with senescence, a term used to describe the process that living organisms undergo with age (Tchkonia *et al.*, 2013). The extent to the effects that ageing has on the brain are so numerous that it would be unfeasible to cover all aspects. Broadly, ageing in the brain results in declining function of the vasculature, cell morphology, cognitive function, a decrease in neurotransmitter levels and a reduction in metabolism (Peters, 2006). Diseases that have increased in incidence with the older population include cardiovascular disease (Olivieri *et al.*, 2013), hearing loss (Gates and Mills, 2005) and dementia (Bhat *et al.*, 2012). Importantly, these diseases are not solely because of ageing; all involve the interaction of genetic and environmental influences (Rodriguez-Rodero *et al.*, 2011).

A specific mechanism that has been observed as a result of ageing incudes changes in cell morphology. Neuronal morphology, density and subsequent dendrites have been found to change dependent on brain region, and in neurodegenerative diseases such as AD this is accelerated (Flood and Coleman, 1986). Another mechanism associated with age-related cognitive decline includes synaptic dysfunction and subsequent loss, which are particularly prominent in hippocampus and frontal cortex (Morrison and Baxter, 2012). Brain regions that are associated with executive cognitive functions, such as hippocampus and frontal cortex are particularly susceptible to age-related decline (Burke and Barnes, 2006).

Ageing has been found to cause *GFAP*+ astrocytes in the mouse dentate gyrus and CA1 to increase substantially in size from 3-months to 24-months in contrast to entorohinal cortex that did not show any significant changes (Rodriguez-Arellano *et al.*, 2016). These findings demonstrate astrocytes are affected differently depending on brain region as a result of ageing, highlighting the need to uncover how astrocytes are affected in other brain regions. Hippocampus does not demonstrate an age-dependent increase in microglia (Vanguilder and Freeman, 2011), however, the cerebral cortex demonstrates age-related reductions (Sharaf *et al.*, 2013). Overall, the effects of ageing on the brain are not fully understood (Chinta *et al.*, 2015, Govoni *et al.*, 2010), making it a tricky distinction to determine whether or not these signs of dysfunction are associated with pathology, or are signs of 'normal' ageing. The decline associated with ageing can broadly be classified into either a compensatory plastic response, which is characteristic of continued normal cognitive functioning, or can enter a pathological state that results in accelerated decline (Harada *et al.*, 2013). This thesis employs the IC as a target nucleus in different animal models to try and identify specific mechanisms that can provide insight into some of the changes that contribute to this pathological switch.

1.6 – Dementia with a focus on Alzheimer's disease

Coincidently, many of the mechanisms associated with ageing, are also signs of dementia (Whalley, 2002). Therefore, what separates 'normal' ageing from dementia? The prevalence of dementia globally is between 5% and 7% of all adults aged over 60, where the likelihood of developing dementia doubles every 5 years (Prince *et al.*, 2013). There are different forms of dementia, which have significantly different aetiologies and effects, including AD (Qiu *et al.*, 2009), Frontotemporal dementia (Warren *et al.*, 2013), corticobasal degeneration (Svenningsson, 2019), dementia with Lewy bodies (Abe and Chiba, 2019) and Parkinson's disease dementia (Eversfield and Orton, 2019, Jankovic and Aguilar, 2008). Dementia is broadly classified as a disorder of impaired cognitive ability, including memory loss and cognitive dysfunction, which progresses over time (Scott and Barrett, 2007). A stage of ageing commonly associated with ageing is termed mild cognitive impairment (Eshkoor *et al.*, 2015), but is also considered an early stage of dementia (Knopman and Petersen, 2014). Therefore, what causes the transition between mild cognitive impairment and dementia? A focus of this thesis is on AD, so will be introduced in detail to try and understand the switch between mild cognitive impairment and AD.

Around 60% of all dementia cases are attributed to AD (Rizzi *et al.*, 2014). Symptomology of AD is commonly associated with a progressive decline in cognition, and depending on disease stage, can present a wide repertoire of symptoms. Clinical diagnosis of AD is difficult as there is significant overlap between the pathophysiologies across the different forms of dementia (Alves *et al.*, 2012). However, AD is classically characterised by accumulation of insoluble amyloid beta protein (Aβ), tau associated neurofibrillary tangles, glial responses, synaptic loss, the accumulation of senile plaques and neuronal loss (Karantzoulis and Galvin, 2011, Mandelkow and Mandelkow, 1998, Iqbal and Grundke-Iqbal, 2010, Crews and Masliah, 2010). The clinical diagnosis of patients with AD usually surround the later stages of the disease, yet this occurs after a long prior prodromal stage of central mechanisms deteriorating (Petersen *et al.*, 2009). Substantial techniques enable the identification of neuronal atrophy such as magnetic resonance imaging (Johnson *et al.*, 2005). Others target amyloidosis and tauopathy by measuring rates of metabolic decline by utilising the radioactive tracer [18F]fluorodeoxyglucose and positron emission tomography (Nordberg, 2004). These techniques are critical to identifying the earlier stages of AD, yet they do not provide specific insight into components that initiate or drive AD development.

The understanding that certain genes cause the early manifestation of AD led to developing transgenic models that emulate the pathophysiology that can be monitored by more invasive techniques (Spires and Hyman, 2005). This has enabled the monitoring of age-dependent pressures that AD genes exert on the brain and localise subsequent key anatomical and physiological adaptations (Jankowsky and Zheng, 2017). The most common transgenic models of AD are developed in mice (Hall and Roberson, 2012). Most AD models possess the mutant human familial APP gene that has been shown to independently cause the manifestation of AD in humans by causing an overproduction of insoluble Aβ (Goate and Hardy, 2012). Other genes that are expressed in transgenic models that independently cause AD in humans are the mutant presenilin genes (Levy-Lahad *et al.*, 1995). Models based on these genes have provided extensive knowledge into the pathophysiology preceding neuronal loss and cognitive impairment (Hall and Roberson, 2012).

1.7 – Hearing loss and its association with dementia development

Hearing loss is an umbrella term that covers numerous types and can be attributed to dysfunction that occurs at any point along the auditory pathway, which makes it difficult to diagnose (Brownell, 1997). A number of factors contribute to the development of hearing loss including with particular genetic predispositions such as otosclerosis that affects the middle ear (Cureoglu *et al.*, 2010) and Usher's syndrome that causes cochlea dysfunction (Yan and Liu, 2010). Alternatively, hearing loss can be acquired by the effects of environmental stimulus such as noise exposure (Le *et al.*, 2017), certain antibiotics (Richardson *et al.*, 1997), trauma (Zahnert, 2011) and ageing (Fischer *et al.*, 2016). These various causes have informed the categorisation of various hearing loss types.

Conductive hearing loss is defined by damage or defects of the outer ear, or to the ossicles in the middle ear (Smith *et al.*, 1993). Hearing loss associated with spiral ganglion fibres dysfunction is defined as sensorineural hearing loss (Kuhn *et al.*, 2011). Dysfunction within the central auditory pathway is appropriately called, central auditory processing dysfunction (Atcherson *et al.*, 2015). A combination of the above can occur, which is defined as mixed hearing loss. The most common form of hearing loss associated with ageing, is known as presbycusis (Huang and Tang, 2010). The prevalence of individuals with severe to profound hearing loss is 40% to 60% for individuals over the age of 60, which rises to 80% in people over the age of 85 (Humes *et al.*, 2012). Presbycusis is characterised by a shift in audiometric threshold (Liu and Yan, 2007), and specific factors that contribute include mitochondrial damage and metabolic dysfunction (Lee, 2013).

Lin *et al.* (2011a), revealed that hearing loss was independently associated with all-cause dementia. This led to the comparison of risk factors, and it was uncovered that hearing loss has the most substantial effect on early-dementia development (Livingston *et al.*, 2017). Presbycusis is generally associated with cochlea dysfunction resulting in a loss of afferent signals entering the central auditory pathway (Wong and Ryan, 2015). However, the mechanisms contributing to dementia development must occur within the brain (Shen *et al.*, 2018). This hypothesis is consolidated by Idrizbegovic *et al.* (2011) who identified that central auditory dysfunction is prevalent among AD patients. Significant losses of spiral ganglion auditory nerve fibres in the cochlea have been observed in contrast to hair cells in 3xTg-AD mice (Wang and Wu, 2015). Additionally, Omata *et al.* (2016) developed mutant mouse models *Tg(Math1*^{E}*-Aβ42)1Lt, Tg(Math1*^{E}*-Aβ42*^{Arc}*)1Lt, and Tg(Math*^{E}*-MAPT)1Lt*)) to over-produce Aβ and tau in the cochlea and found that overexpression of these genes were correlated with hearing loss. Additionally, Sinha *et al.* (1993) revealed that amyloid plaques and neurofibrillary tangles were distributed predominantly throughout the CNIC and MGB of AD patients, in contrast to the auditory cortex, which exhibited lesser pathology, and the CN that did not show any. These results implicate the IC as a primary target for auditory related AD, that could contribute to dysfunction. This hypothesis will be tested in Chapters 4 & 5 to identify the extensity of changes in the IC as an indirect measure of auditory dysfunction and its relation to AD development. This Chapter has provided indirect evidence for age resulting in cognitive decline, cognitive decline switching to pathological decline and hearing loss contributing to cognitive decline. There is broad evidence linking ageing, hearing loss and cognitive decline, but there are no bona fide mechanisms linking the three. This thesis aims to provide insight into some of the mechanisms characterising the conditions.

1.8 - Models of study employed in this thesis

In this thesis, two different animal models will be used, guinea pigs and rats. Evolutionarily, guinea pigs and rats evolved from a common ancestor, making them closer to each other in phylogenetics than either to humans (Huchon *et al.*, 2002). Therefore, when understanding the comparability between species, there will be substantive crossover. The first is the tricoloured guinea pig, which is used in auditory research due to its similarities in hearing to humans (Shera *et al.*, 2002). Guinea pigs are an apt model to study central auditory processing, as they have a similar hearing frequency range to that of humans (Marquardt *et al.*, 2007). Guinea pigs have recently being found to demonstrate monoaural and binaural integration which are key characteristics of IC processing, but also discriminate low frequency signals more similar to the human hearing range than mouse and rat models (Greene *et al.*, 2018).

Using guinea pigs to model AD genes would have been appropriate to understand auditory related changes. However, there are currently no transgenic guinea pig models that emulate AD. A suitable alternative is the transgenic Fischer 344 Alzheimer's disease (Tg) rat model, which is the first viable AD model in rats. Rats are a good model to use opposed to mice, due to them having a closer number of synteny blocks to humans, which is a measure of similarity between two sets of chromosomes, demonstrating that they are closer in phylogeny (Bourque *et al.*, 2004). The Tg rat model has been proposed to be useful in the studying the effects of causative human-familial AD genes (Cohen *et al.*, 2013) and this thesis is exploring different approaches to try and consolidate this. In addition, the Fischer344 strain has been shown to demonstrate a moderate loss of hearing between 8 and 25 months (Simpson et al 1985), making it a good model to investigate age-dependent hearing loss with the AD genes. The genes include the human amyloid precursor protein Swedish mutation and presenilin-1, excluding the nucleotides on the exon 9, gene mutations, which both independently result in the early manifestation of AD in humans, by producing excess abnormal amyloid beta in conjunction with an inability to cleave the protein into a soluble derivative. The Tg model in conjunction with guinea pigs provide a comprehensive approach to identifying factors associated with auditory processing and AD.

1.9 – Issues this thesis attempts to address

As introduced in the sections above, the different neuronal projections and regions of the brain that sounds undergo are well described. However, there is little to no information regarding the contributions that glial cells make to the processing of sounds. In addition, a correlational link between hearing loss and dementia has been found, with no information providing mechanistic data implicating the two conditions. Therefore, this thesis will address some outstanding questions surrounding neurons, glial cells and metabolic functioning within the IC, by providing data to try and better understand auditory processing and the potential link to dementia.

1.9.1 – Gaps in our understanding

- Astrocytes and microglia are known to be involved in regulating neuronal and synaptic processing in the brain (Sections 1.4.1 and 1.4.2 respectively). However, there is no research identifying how these cells contribute to processing across the sub regions of IC. Therefore, Chapter 3 aims to uncover how these cells contribute to processing in CNIC, DCIC and LCIC.

- Astrocytes and microglia are known to be differentially distributed across different regions of the brain and are involved in regulating the immune response and reacting to stimuli across the brain (Sections 1.4.1 and 1.4.2 respectively). However, there is no research identifying how these cells respond to ageing in the IC of the Tg model. Therefore, Chapter 4 aims to uncover age-dependent changes in the Tg model affects glial distributions across the CNIC, DCIC and LCIC.
- Synaptic dysfunction and a reduction in metabolism are recognised outcomes of AD. However, there is no research identifying age-dependent changes in mitochondrial functioning in presynaptic nerve endings in IC of the Tg model. Therefore, Chapter 5 aims to uncover mechanisms of metabolic synaptic dysfunction in the IC compared to other regions of the brain in the ageing Tg model.

1.9.2 – Hypotheses

- Astrocytes and microglia contribute to sub regional neuronal and synaptic processing across the guinea pig IC (Chapter 3).
- There will be an age-dependent increase in astrocytes and microglia across the sub regions of IC in the Tg model (Chapter 4).
- Age-dependent metabolic synaptic dysfunction will be more prominent in the IC than in other regions of the brain of the Tg model (Chapter 5).

Chapter 2 – General Methodology

2.1 – Overview of Methodology

This Chapter will present the general methodology employed across the Chapters. Full details pertinent to each specific results Chapter will be presented in those respective Chapters, as appropriate.

2.2 – Animal Models

All experiments were approved by the Faculty Research Ethics and Governance Committee at Manchester Metropolitan University. Adult guinea pig (*Cavia porcellus*) brains were provided by Professor Adrian Rees at Newcastle University, following transcardial perfusion with PBS and 4% PFA following regulations at Newcastle University. Wild type (n=and Tg rats were provided by Dr Herve Boutin at The University of Manchester following regulations at the University of Manchester. These rats were culled at The University of Manchester and transported on ice to Manchester Metropolitan University, where the brains were removed and processed (see Chapters 4 and 5).

2.3 – Immunohistochemistry Protocols

All sections were cut using a cryostat (Leica CM3050S) with an operating and chamber temperature of 18°C. Guinea pig sections were cut at 60µm, in the coronal plane and were placed free floating into a 3 x 4 well plates filled with PBS (0.9% NaCl in 0.01M phosphate buffer (ThermoFisher Cat# 003002)). Tg and wild type rat brains were cut into 10µm thick sections in the parasagittal plane and 4 sections were mounted onto Superfrost+ slides (ThermoFisher lot# 0120045). All experiments were conducted using i) no primary (no primary antibody to determine secondary IgG autofluorescence) , ii) no secondary (no IgG control to determine the presence of debris associated with the primary antibody) and iii) no primary or secondary controls (to identify autofluoresce contributed through reagent contamination and/or human error).

2.3.1 – Chapter 3 immunohistochemistry process

Guinea pig tissue sections were labelled free-floating, starting with a wash in PBS (3 x 5 minutes), then permeabilised and blocked in 0.05% Triton X-100 (to improve antibody invasion of desired cells) in PBS and 1% goat serum (to prevent the secondary antibody from binding to non-specific resident tissues or Fc receptors) (Vector cat# S-1000) (blocking solution) for 1 hour at room temperature. The sections were then incubated in a cocktail of primary antibodies and left overnight at room temperature on a shaker plate (see Chapter 3 for specific antibodies). The next day, sections were washed (3 x 5 minutes) in PBS, followed by blocking solution for 1 hour, followed by incubation in the corresponding secondary antibodies for two hours at room temperature and washed (3 x 2-minutes in PBS) (see section 2.4.1 for specific antibody details). Sections were mounted onto positively charged slides, allowed to dry at room temperature followed by the addition of VectaShield H-1000 mounting medium (to minimise fading of the specific fluorophores) with 0.22x60x0.15mm coverslips (ThermoFisher Cat# 24X60-1.5). Once mounted, sections were stored at 4ºC until imaged.

2.3.2 – Chapter 4 immunohistochemistry process

Tg rat sections were washed (3 x 5 minutes) in PBS, then treated with a citrate antigen retrieval buffer (5mM sodium citrate dihydrate, 15mM Citric Acid, 500ml deionised H_20, 6.0pH) at 80°C for 20 minutes. The slides were washed again (3 x 3 minutes), followed by an hour’s incubation in blocking solution at room temperature (as above). Sections were immersed into a cocktail of primary antibodies overnight at 4ºC in a humidified chamber on a shaker to prevent evaporation (see section 2.4.2 for specific antibody details). Slides were then washed (3 x 5 minutes) in PBS and immersed in blocking solution for 1 hour at room temperature. Sections were incubated in the corresponding secondary antibodies and left on a shaker plate at room temperature for 2 hours in a humidified chamber. Slides were washed 3 x 5 minutes and left to dry, then coverslipped in VectaShield H-1000 mounting medium and 0.22x60x0.15mm coverslips (ThermoFisher Cat# 24X60-1.5). Once mounted, sections were stored at 4ºC until imaged.

2.4 – Details of primary antibodies used in this thesis

All antibodies were stored at -20°C, except for when being used where they were kept at 4°C. See table 2.1 for a list of all details used throughout this thesis and sections 2.4.1 and 2.4.2 describe details pertinent to each antibody in respect to each Chapter. Justification of each antibody is elaborated upon through the introduction of each results Chapter.

Antibody ID	Antibody Name	Target Antigen	Clonality	Host Organism	Vendor	Cat #
AB_2278725	*GAD67*	*GAD67* human, mouse, rat	monoclonal antibody	mouse	Millipore	MAB5406
AB_477010	*GFAP*	*GFAP* human, porcine, rat, human, pig, rat	monoclonal antibody	mouse	Sigma-Aldrich	G3893
AB_839504	*Iba1*	*Iba1* human, mouse, rat	polyclonal antibody	rabbit	Wako	019-19741
AB_2068336	*Calbindin D-28K*	*Calb1* human, rat, mouse	polyclonal antibody	rabbit	Millipore	AB1778
AB_477523	*Synaptophysin*	*Synaptophysin* human, porcine, rat, pig	monoclonal antibody	mouse	Sigma-Aldrich	S5768
AB_2631222	*Homer-1*	*Homer 1* human, rat, mouse	polyclonal antibody	chicken	Synaptic Systems	160 006
AB_2336492	GSL-1	N/A	N/A	N/A	Vector Laboratories	RL-1102
AB_2298772	*NeuN*	*NeuN* avian, chicken, ferret, human, mouse, pig, rat, salamander	monoclonal antibody	mouse	Millipore	MAB377
AB_321301	*CD11b*	*CD11b* rat	monoclonal antibody	mouse	Bio-Rad	MCA275G
AB_10013382	*GFAP*	*GFAP* cat, cow, dog, human, mouse, rat, sheep	polyclonal antibody	rabbit	Agilent	Z0334

Antibody ID	Antibody Name	Target Antigen	Clonality	Host Organism	Vendor	Cat #
AB_2810980	Goat Anti-Chicken IgY H&L (Alexa Fluor 405) preadsorbed antibody	IgY H&L chicken	polyclonal antibody	goat	Abcam	ab175675
AB_2630356	Goat Anti-Rabbit IgG H&L (Alexa Fluor 488) antibody	IgG H&L rabbit	polyclonal antibody	goat	Abcam	ab150077
AB_2687594	Goat Anti-Mouse IgG H&L (Alexa Fluor 555) antibody	IgG H&L mouse	polyclonal antibody	goat	Abcam	ab150114
AB_2687948	Goat Anti-Mouse IgG H&L (Alexa Fluor 647) Antibody	IgG H&L mouse	polyclonal antibody	goat	Abcam	ab150115

Table 2.1 – Antibody table

2.4.1 – Chapter 3 antibodies

Mouse anti-*GAD67* (1:500; monoclonal; clone 1G10.2; Cat# MAB5406; Millipore; RRID: AB_2278725) – according to the manufacturer, the immunizing antigen is a recombinant fusion protein containing unique N-terminus regions from amino acids 1-101 of *GAD67*. Immunoblotting detects a 67kDa protein in rat cerebellum and mouse microsomes; immunohistochemistry demonstrated labelling similar in distribution to *in situ* mRNA hybridization (Fong *et al.*, 2005, Kotti *et al.*, 2006, Ramirez *et al.*, 2008). Use of this antibody has been published in guinea pig IC (Nakamoto *et al.*, 2013, Foster *et al.*, 2014, Beebe *et al.*, 2016), as well as rat IC (Ito *et al.*, 2009).

Mouse anti-*GFAP* (1:500; monoclonal; clone G-A-5; Cat# G3893; Sigma; RRID: AB_477010) was used to detect astrocytes. According to the manufacturer, this antibody is raised against an epitope from the C-terminus of *GFAP* purified from pig spinal cord (Latov *et al.*, 1979, Debus *et al.*, 1983). The antibody has been shown to recognize a single band of approximately 50kDa and reacts with homologous, conserved residues across mammals (Lorenz *et al.*, 2005). The use of this antibody has been demonstrated in many species, including mouse (Komitova *et al.*, 2005), rat (Lennerz *et al.*, 2008, Sanchez *et al.*, 2009), tree shrew (Knabe *et al.*, 2008), guinea pig (Kelleher *et al.*, 2011, Kelleher *et al.*, 2013) and human (Toro *et al.*, 2006). Labelling in this thesis was consistent with these studies and the known morphology of astrocytes.

Rabbit anti-Iba1 (1:1,000; polyclonal; 019-19741; lot# WDE1198; Wako; RRID: AB_839504) – according to the manufacturer, this affinity purified antibody was raised against a synthetic peptide corresponding to the C-terminus fragment of rat Iba1. Labelling via western blot was positive for a 17kDa band (Imai *et al.*, 1996). We observed selective labelling of ramified microglia, matching similar reports in mouse (Bulloch *et al.*, 2008), rat (Helfer *et al.*, 2009)

(Fuentes-Santamaría *et al.*, 2012), Japanese quail (Mouriec and Balthazart, 2013), macaque (Stanton *et al.*, 2015) and chimpanzee (Rosen *et al.*, 2008). We observed labelling consistent with these previous reports.

Rabbit anti-calbindin D-28k (1:1,000; polyclonal; Cat # AB1778; Millipore; RRID: AB_2068336) antibody recognises a single band at 28kDa in human, mouse, and rat brain tissues, according to the manufacturer. This antibody does not bind to calretinin and pre-adsorption of diluted anti-serum with calbindin removed all labelling in human brain (Huynh *et al.*, 2000). Previous work demonstrating labelling of mouse olfactory bulb (Kotani *et al.*, 2010), rat piriform cortex (Gavrilovici *et al.*, 2010) and guinea pig enteric nervous system (Liu *et al.*, 2005) all showed highly selective cytoplasmic labelling of neurons. In this thesis, labelling was consistent with previous reports.

Mouse anti-*synaptophysin* (1:500; monoclonal; Cat# S5768; Sigma; RRID: AB_477523) antibody targets a pre-synaptic synaptosome antigen derived from rat retina, producing a 38kDa band in rat brain extracts, according to the manufacturer. Labelling in this thesis demonstrated punctate labelling, as previously reported in mouse (Wiedenmann and Franke, 1985), rat (Zelano *et al.*, 2009), guinea pig (Glueckert *et al.*, 2008), and human (Jaafari *et al.*, 2008).

Chicken anti-homer1 (1:500; polyclonal; Cat# 160026; SySy; RRID: AB_2631222) IgY antibody is specific for residues 1-196 of human homer1, including splice variants a-d (Soloviev *et al.*, 2000). These residues are highly conserved, with reactivity for mouse and rat. Homer1 has been shown to bind selectively to glutamate receptors (Brakeman *et al.*, 1997) and can be considered a marker of glutamatergic synapses when colocalized with *synaptophysin* (Ciruela *et al.*, 2000, Sala *et al.*, 2001, Lee *et al.*, 2019. This antibody has recently been validated in mouse models of Alzheimer's disease via colocalization with synaptophysin {Reichenbach, 2018 #121).

Blood vessels were labelled with rhodamine conjugated Griffonia (Bandeiraea) Simplicifolia Lectin 1 (*GSL1*) (1:100; RL-1102; Vector; lot# S0926RRID: AB_2336492), which binds to glycoproteins lining the inner lumen.

Secondary antibodies included: goat anti-chicken IgY H&L (Alexa Fluor 405) preadsorbed antibody (1:250; polyclonal; Cat# ab175675; Abcam; RRID: AB_2810980), goat anti-rabbit H&L (Alexa Fluor 488) antibody (1:250; polyclonal; Cat# ab150077; Abcam; RRID: AB_2630356), goat anti-mouse IgG H&L (Alexa Fluor 555) antibody (1:250; polyclonal; Cat# ab150114; Abcam; RRID: AB_2687594) and goat anti-mouse IgG H&L (Alexa Fluor 647) antibody (1:250; polyclonal; Cat# ab150115; Abcam; RRID: AB_2687948) – the manufacturer does not disclose information pertinent to the immunogens within for all secondary antibodies. However, each secondary is well cited in the recent literature (Ionescu et al 2019; Goussakov et al 2019; Ding et al 2019; Yi et al 2019).

2.4.2 – Chapter 4 antibodies

Mouse anti-*NeuN* (1:500; monoclonal; Cat# MAB377; Millipore; RRID: AB_2298772) antibody reacts with most neuronal cell types throughout the brain, according to the manufacturer's instructions. This IgG antibody recognizes 2-3 bands in the 46-48 kDa range in mouse brain. Labelling in this thesis demonstrated nuclear labelling similar to as previously reported in rat spinal cord (Kim et al 2006) and motor nucleus (Pang et al 2009) and mouse olfactory bulb (Panzanelli et al 2007) and hippocampus (Litvinchuk et al 2018).

Mouse anti-*CD11b*, clone OX-42 (1:500; monoclonal; Cat# MCA275G; Bio-Rad; RRID: AB_321301) antibody is a 1,151 amino acid single pass type 1 transmembrane glycoprotein possessing a single vWFA domain and multiple FG-GAP repeats. *CD11b* is expressed on most macrophages, including resident and activated peritoneal macrophages and Kupffer cells, and labels dendritic cells, granulocytes and microglia (Robinson et al 1986). Labelling in this thesis demonstrated cellular structures similar to previous reports in rat cochlear nucleus (Fuentes-Santamaria et al 2013) and mouse spinal cord (Jiang et al 2017).

Rabbit anti-*GFAP* (1:500; polyclonal; Cat# Z0334; Agilent; RRID: AB_10013382) – according to the manufacturer the antibody is a 50 kDa intracytoplasmic filamentous protein that constitutes a portion of the cytoskeleton in astrocytes. Labelling in this thesis appeared similar to previous reports in the dorsal vagal complex (Pecchi et al 2007) and striatum of rats (Yang et al 2008) and prefrontal cortex of chimpanzee (Rosen et al 2008), whereby the labelled cells were cellular with protruding processes.

Secondary antibodies included: goat anti-rabbit H&L (Alexa Fluor 488) antibody (1:250; polyclonal; Cat# ab150077; Abcam; RRID: AB_2630356), goat anti-mouse IgG H&L (Alexa Fluor 555) antibody (1:250; polyclonal; Cat# ab150114; Abcam; RRID: AB_2687594) and goat) – the manufacturer does not disclose information pertinent to the immunogens within. However, each secondary is well cited in the recent literature (Ito et al 2018; Hao et al 2018).

2.5 – Confocal Microscopy

All micrograph imaging of immunohistochemical labelling was acquired using a Leica SP5 confocal microscope. Extensive steps of optimisation were taken in the Leica LAS AF software. Species-specific epitopes of interest were bound with complementary secondary antibody fluorophores exciting at the wavelengths 405, 488, 555 and 647 nanometres. Labelled sections were briefly observed using the mercury bulb and anomalous sections were not included (sections with missing brain regions, freezer damage, too many artefacts, abnormal autofluorescence or negligible labelling that would produce unrepresentative results).

Of the included sections, the strongest and the weakest labelled sections were identified, then to produce fair comparisons, settings were optimised in-between and implemented consistently throughout all experiments. This process was the same for images taken using the 40x and 63x objectives. Overall laser power was set at 30% for all experiments. A hybrid detector (HyD3) combining a vacuum tube and a semiconductor was used to reduce the variability of the lasers baseline point of contact, ultimately improving the consistency of the beam intensity and reducing the levels of noise, increasing the clarity of high-powered images. Several modifiable methodological steps were taken in chronological order to ensure optimal signal representation. Initially, the peak of the emission spectrum was localised using the changeable emission spectrum to be detected by the laser and minimised to reduce non-specific labelling and autofluorescence. Next, the minimal laser intensity was set in conjunction with altering the pinhole circumference, identifying the smallest diameter that produced the highest clarity of image (subjectively determined by minimal autofluorescence, clear definition at low resolution and the edges of structures are determinable). The optimal laser intensity was characterised by the lowest pinhole setting without bleaching the image, which provided the clearest representation of images (this was optimised on control tissue). This enabled reuse of the tissue, full representation across the z-plane of zoomed in images and subjective quantification of the quality of immunohistochemistry and specific markers used. Finally, the voltage of the gain setting was kept at its lowest, which kept the image acquisition as stable and clear as possible by minimising laser manipulation as minimal gain reduces beam distortion (High gain images produced high levels of false autofluorescence and false positive readings that could hamper interpretability of micrographs). Optimisation was undertaken for each wavelength of excitation to account for natural wavelength inconsistencies (this further reduced the levels of autofluorescence).

Regions of interest that were included were defined using guinea pig (Voitenko and Marlinsky, 1993) and rat brain (Paxinos and Watson 2007) atlases to ensure similar anatomical positions along the rostro-caudal axis for coronal guinea pig sections and around the medial portion of the right hemisphere for sagittal rat sections. All whole brain region micrographs were taken using the 40x objective. The x- and y-planes were identified and outlined, whereby the whole regions were encapsulated using the tile parameters in the Leica software (LAS AF). The z-plane of the sections were determined by measuring the z-plane extensity for all four corners on the x- and y-axes. High-powered images were taken using the 63x objective and the zoom function (range= a factor of 1.5-4) to best encapsulate individual regions of interest. Details more pertinent to each experiment are outlined in each Chapter.

2.6 – Image analyses

All micrographs were exported as individual monochrome images in the tagged image file format (TIFF), according to the specific wavelength it was taken. Image analysis for all micrographs was undertaken in the software FIJI ImageJ (Abràmoff *et al.*, 2004). Images were initially stacked on the z-plane and then processed using the filters available in the software (specific features are explained in relevant results Chapters). Image stacks were then merged, depending on specific epitopes labelled and designated a colour. Individual slices were analysed, or a maximum intensity projection was rendered then analysed depending on the research question.

Chapter 3 – *Iba1+* microglia interact with neuronal somata and synapses in the inferior colliculus

3.1 – Introduction

3.1.1 – The importance of inhibitory processing in the inferior colliculus

Inhibition is an essential element of neural processing and a defining component of sensory systems. GABAergic inhibition is prevalent in the auditory system, particularly in the principal auditory midbrain nuclei, the IC. Around a quarter of neurons in the IC are GABAergic (Merchán *et al.*, 2005), which may be one reason why the IC is the most metabolically active nucleus in the mammalian brain (Sokoloff *et al.*, 1977a). Understanding how inhibitory cell types vary in different brain regions, to specialise for distinct functions, is a key area of neuroscientific study (Freund and Buzsaki, 1996, Tremblay *et al.*, 2016). Most investigations into sub-types of inhibitory neurons naturally focus on the cells *per se*, including their morphology, electrophysiological firing characteristics, expression of cytoplasmic calcium binding proteins and peptides and RNA transcriptome. Another approach is to characterize and classify GABAergic neurons based on differences in the afferent axo-somatic inputs they receive (Ito *et al.*, 2009, Beebe *et al.*, 2016).

3.1.2 – Each sub region of the IC has distinct functional roles

The IC has a tonotopic topography that can be divided into sub-regions. The CNIC is dominated by neurons sharply tuned to simple auditory stimuli. The DCIC has much broader frequency tuning and receives extensive corticofugal input and is specialised for synaptic plasticity (Herbert *et al.*, 1991, Winer *et al.*, 1998, Bajo and Moore, 2005, Bajo *et al.*, 2010). The other major sub-region is the LCIC which exhibits polysensory tuning (Aitkin *et al.*, 1978). These sub-regions are analogous to the core, belt and para-belt sub-regions found throughout the auditory pathway (Kaas and Hackett, 1999). Despite the essential role of the IC in hearing, little is known of how glial cells contribute to processing therein.

3.1.3 – Microglia are involved in ongoing processing and synaptic functioning

Microglia are an integral cell type present throughout the brain and are one of the most numerous cell types (van Rossum and Hanisch, 2004, Kettenmann *et al.*, 2011, Nayak *et al.*, 2014). In addition to their neuroprotective and phagocytic functions, microglia contribute to ongoing synaptic function by removing unwanted structures in a process termed 'synaptic stripping' (Trapp *et al.*, 2007). The morphology of microglia varies throughout the brain, suggesting adaptation to their surrounding milieu. Furthermore, microglia interact with neurons during 'ongoing' processing and can sense and respond to local chemical signalling (Pocock and Kettenmann, 2007, Wake *et al.*, 2009, Schafer *et al.*, 2012). Certainly, there is evidence for microglial influence on synaptic plasticity (Zhang *et al.*, 2014, Riazi *et al.*, 2015), but the nature of this role remains poorly understood.

3.1.4 – Aims

This Chapter aims to uncover anatomical contributions that glial cells make to auditory neuronal processing within the IC as a basis for future physiological experiments, by measuring the inter-relationships of *Iba1+*microglia, *GFAP+* astrocytes, *GAD67*+ (putative GABAergic) neurons and *homer1*+ (putative excitatory) synapses in guinea pig. Multi-channel fluorescence immunohistochemistry and confocal microscopy have been implemented on adult guinea pig tissue in the DCIC, CNIC, LCIC and the ventral central nucleus (VCNIC) to investigate potential sub-regional differences. In addition, machine learning methods have been utilised to identify inter-relationships between microglia and *GAD67*+ neurons that could not be detected by traditional statistics.

3.2 – Methodology

3.2.1 – Guinea pig tissue processing

Results are described from four adult (one at four months old, three at six months old) outbred, tricolour guinea pigs (*Cavia porcellus*) of both sexes (three male, one female). Animals were culled at Newcastle University in accordance with Schedule 1 (table A section 4) of the Animals (Scientific Procedures) Act 1986. Sections (two per animal; 8 total) through the superior colliculus and the rostral-most third along the rostro-caudal axis through the IC were first used to optimise labelling. Data are presented from sections in the middle third of the IC along the rostro-caudal axis, which contained the CNIC, DCIC and LCIC. The location of each section through the rostro-caudal axis were referenced to an atlas of the guinea pig brainstem (Voitenko and Marlinsky, 1993).

3.2.2 – Immunohistochemical labelling of tissue

The immunohistochemistry labelling protocol used in this Chapter is outlined in Chapter 2.3.1 All steps in the labelling protocol involved continuous gentle agitation of sections at room temperature (See Chapter 2.4.1 for antibody details). For double labelling of *Iba1* and *GAD67*, goat anti-rabbit AlexaFluor 488 and goat anti-mouse AlexaFluor 568 were used. For double labelling of calbindin and *GFAP*, goat anti-rabbit AlexaFluor 488 and goat anti-mouse AlexaFluor 647 were used. For triple labelling of *Iba1*, *GSL1* (pre-conjugated 568nm rhodamine fluorophore) and *GFAP*, goat anti-rabbit AlexaFluor 488 and goat anti-mouse AlexaFluor 647 were used. For triple labelling of *Iba1*, *homer1* and *synaptophysin*, goat anti-rabbit AlexaFluor 405, goat anti-chicken AlexaFluor 568 and goat anti-mouse AlexaFluor 647 were used.

3.2.3 – Image acquisition

Sequentially acquired micrographs were taken with a confocal microscope (Leica SP5) using a wide field stage and zoom function. Images (8 total; 1 per section) were acquired via a 40x objective (NA=1.25) for images of the entire cross-section of the IC, and a 63x objective (NA=1.4) for 5-row x 6-column (432x552µm) region of interest panoramas (see Figure 3.3). Whole IC images (8 total, 1 per section) were taken using 5µm equidistant slices in the Z-plane to produce maximum intensity tiled projections (pixel size; x & y=0.7583µm, z=50-60µm). For *GAD67* and *Iba1* region of interest panoramas, 5-row x 6-column (432x552µm) tiled images were taken using 1µm z-slices until the entirety of the labelling was imaged (pixel size; x & y=0.2406µm, z=40µm). High magnification images of *Iba1* and synaptic marker labelling were imaged (1 per animal) using 0.05µm z-slices through the full cell (pixel size; x & y= 0.1396µm, z=25µm).

3.2.4 – Image analyses

All image analyses were performed using Fiji ImageJ (Abràmoff *et al.*, 2004). For *Iba1*+ cell density estimates, tiled panorama images of the whole IC (8 images) were subject to manual cell counts. The peripheral borders of the IC were delineated, a contour drawn, and each image cropped to its respective contour. To make fair comparisons between cases, 450µm^2 grids were placed across each IC panorama image and centred on the middle pixels of each micrograph in ImageJ (For example see Figure 3.1B). Only those grids which were filled entirely by labelled parenchymal tissue were subject to counts. Comparisons were then made between cases, such that only grids that were present in images from all four animals were included in calculation of group means and standard deviations per grid.

Two-dimensional maximum intensity projection region of interest 5-row x 6-column panoramas of *Iba1* and *GAD67* were analysed for i) cell counts and percentage field of view covered analyses. In addition, each individual 1µm slice was measured to allow three-dimensional reconstruction and analysis of ii) *GAD67*+ cell counts, iii) individual *Iba1*+ cell Sholl (Example in Figure 3.5N) and iv) skeleton analyses (Example in Figure 3.5M). For Sholl and skeleton analyses a total of 256 cells were analysed (32 per section, 8 per subregion), as this was the maximum number of cells that could be consistently measured across the panoramas. All panorama micrographs were first processed by filtering monochrome images using a median pixel (1.5) filter and then thresholded to binary by implementing the IsoData algorithm. Cell counts, and percentage field of view covered analyses were then performed using the 'Analyse Particles' plugin. For volumetric Sholl analyses, individual *Iba1*+ microglia were cropped and a series of equidistant radiating 1µm concentric spheres were plotted from the centre of the cell body to the furthest radiating extent of ramification. Each intersection with a concentric ring was measured. The Skeletonize algorithm was used to display a one-pixel thick framework of each *Iba1*+ microglial cell. The Analyse Skeleton plugin calculated number of branches and branch lengths for each cell. Additional measurements derived from the Sholl and skeleton analyses included, i)the total number of intersections with the plotted concentric circles as a measure of cell ramification from the centre of the soma, ii) the total number of branches defined by a turning point of the skeletonised framework, which indirectly related to the number of branches and iii) the longest path of each branch was measured and defined as the maximum branch length, which is indirectly a measure of the processes of the cell. Whole IC 40x objective images of *synaptophysin* were analysed for labelling (pixel intensity) density between sub-regions using the Measure function.

To measure *Iba1*+ putative-interactions with *GAD67*+ neurons, individual cells were cropped from panoramas, and were measured without filtering. The diameter of *GAD67*+ somata were quantified by measuring the extremes of each *GAD67*+ cell in the z-plane. Only cells that were entirely contained within the full z-range of the section were included (160 total, 20 per section). All other measures of putative interactions between *Iba1*+ and *GAD67*+ labelling were subject to extensive manual counts on a slice-by-slice basis through each z-stack.

Initially, the levels of colocalisation of *Iba1*, *synaptophysin* and *homer1* were determined using the colocalisation plugin in the LAS AF (Leica) software, which provided a measurement of pixel intensity colocalisation. For synaptic colocalisation measurements, z-slices through *Iba1*+ microglia were thresholded using the Itso algorithm to develop a mask of each slice of the cell and then converted into a stack. Synaptic marker labelling (*synaptophysin* and *homer1*) were thresholded using the Moments algorithm to create masks of each slice. To enable comparison of putative excitatory synapses, monochrome image slices of *synaptophysin* were merged with *homer1*+ labelling. These stacks were then respectively merged with the masks of the *Iba1*+ masked stack, enabling visualization of co-localisation between putative excitatory synapses and microglial processes. A three-dimensional Sholl analysis of volume was then conducted using concentric spheres of 0.025μm increments from the centre of each *Iba1*+ soma, which gave a quantitative measurement of co-localisation across the x, y, and z planes. Each point of colocalisation detected was visually inspected and verified before being included in the dataset.

3.2.5 – Statistical analysis

Data were collected in Excel spreadsheets. Statistical hypothesis testing was performed in Prism 7 (GraphPad). Factorial analyses were conducted using the non-parametric Kruskal-

Wallis ANOVA with sub-region as the factor in all cases. Non-parametric testing was implemented due to the assumption of normality being violated. Where appropriate, *post-hoc* tests with Dunn's method were conducted. This *post-hoc* test was chosen as it is a more representative method for comparison of small samples of biological replicates. For *post-hoc* analyses the α was Šidák corrected for multiple comparisons. This correction method was used to control for false type 1 errors. Spearman's rank correlations were used to investigate potential associations between dependent variables. A correlation matrix was implemented as a multivariate measure to identify associations between variables. To plot results from the correlation matrix and visualise the associations between variables, a principal component analysis was implemented. These variables defined the parameters for the principal component and two-step cluster analyses. Principal component and two-step cluster analyses were conducted in SPSS v25 (IBM). This method was used to identify trends that could not be uncovered by conventional statistics. The exploratory two-step cluster analysis employed Euclidean distance measures with Schwarz's Bayesian clustering criterion. These methods were used to classify inter-relationships to potentially inform future physiological testing. ROC analysis was implemented to characterise the reliability of the results derived from the cluster analyses. All 160 cells were successfully classified by this analysis. Chi-squared analysis was implemented to compare the proportions of neurons across sub-regions classified by cluster analysis. The alpha level was set at $P<0.05$ for all statistical comparisons. Significance between factors from *post-hoc* analyses displayed in figures are referred to as stars (*= $P\leq0.05$; **= $P\leq0.005$; ***= $P\leq0.001$; **** $P\leq0.0001$).

3.3 – Results

3.3.1 – *GFAP*+ astrocytes and *Iba1*+ microglia form the *glia limitans externa* and neurovascular unit in IC

Initially, to identify glial distributions throughout the IC, immunohistochemical labelling of *GFAP*+ astrocytes and *Iba1*+ microglia was implemented in adult guinea pig. Coronal, 60µm sections showed pronounced *GFAP*+ and *Iba1*+ labelling of the *glia limitans externa* lining the dorsal and lateral borders of the IC (Figure 3.1A). Extensive labelling was also distributed medially, lining the cerebral aqueduct, with ramified *GFAP*+ astrocytic processes radiating into the periaqueductal grey, as well as the commissure of the IC. Interestingly, no *GFAP*+ astrocytes were present throughout the IC parenchyma, save for sparse labelling of cells in the outermost layers of the DCIC and LCIC. Conversely, ramified *Iba1*+ microglia tiled the parenchyma in non-overlapping domains with similar density throughout the IC, as quantified in Figure 3.1B.

Combining *Iba1* and *GFAP* labelling with the fluorescent-conjugated lectin *GSL1* revealed extensive peri-vascular labelling along putative penetrating arteries and arterioles (Figure 3.1C). Neurons expressing cytoplasmic calbindin or calretinin were distributed in the outermost regions of the cortices of the IC, matching previous reports (Zettel *et al.*, 1997, Ouda *et al.*, 2012) and in close proximity to vessels and *GFAP*+ processes (Figure 3.1D).

These findings demonstrate that many aspects of IC glial organisation mirror those reported in other brain regions, with both *GFAP*+ astrocytes and *Iba1*+ microglia forming the *glia limitans externa* and lining adjacent to blood vessels. However, the observation that *Iba1*+ microglia but not *GFAP*+ astrocytes were found throughout the parenchyma, suggests a more fundamental role for *Iba1*+ microglia in glial-neuronal putative interactions in IC.

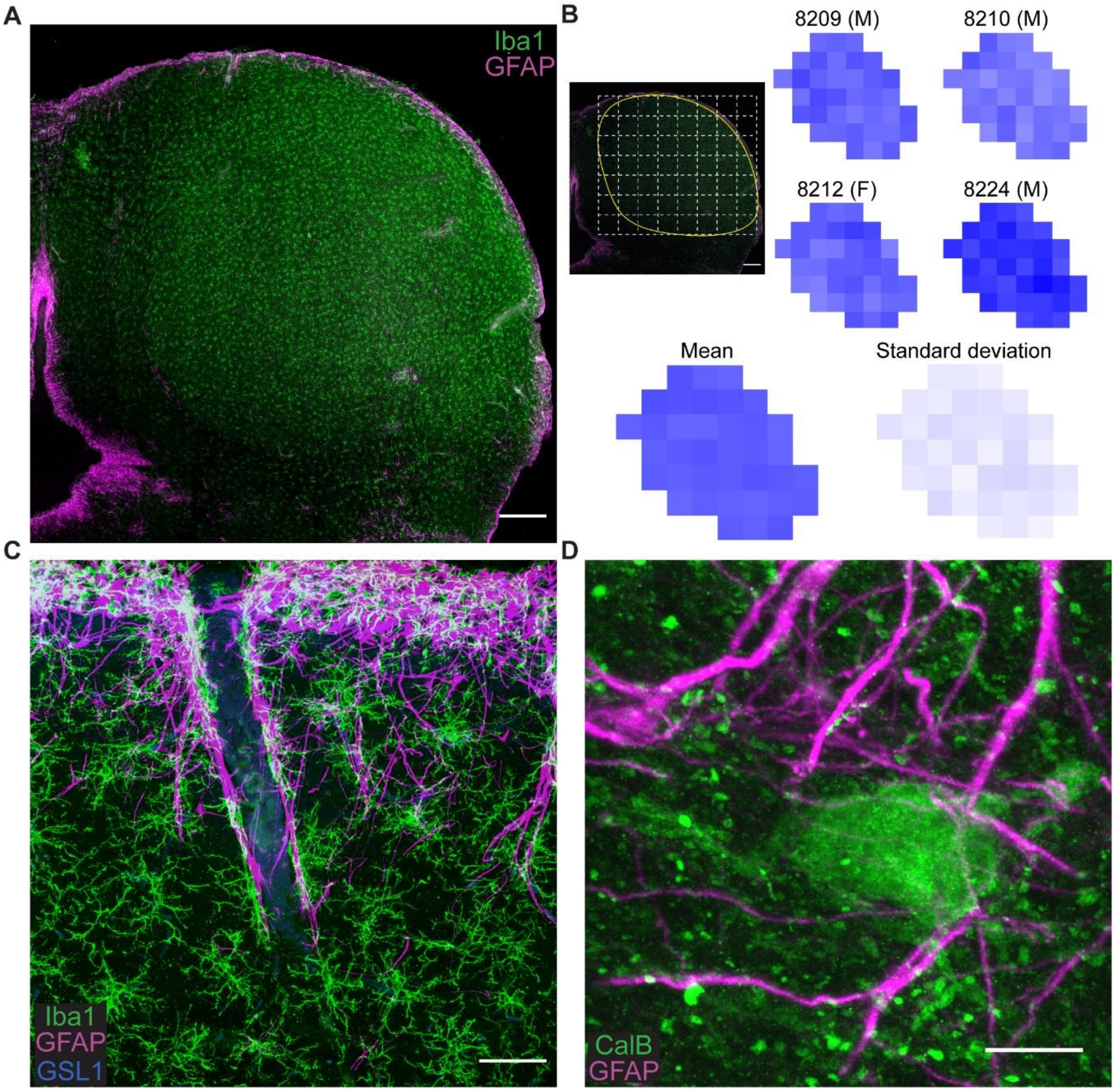

Figure 3.1. Microglia and astrocytes form the *glia limitans externa* and peri-vascular borders but only microglia tile the parenchyma. (A) Tiled maximum intensity projection confocal micrograph of *GFAP*+ astrocytes (magenta) and *Iba1*+ microglia (green) in IC. Scale bar 400µm. Note that *GFAP* labelling is restricted to the peripheral borders and penetrating vessels while *Iba1* is evenly distributed throughout. (B) Quantification of *Iba1*+ somata counts per 450µm^2 grid within the parenchyma across all four cases (see methodology for description). Numbers on top row refer to individual animals. (C) Confocal micrograph showing *GFAP*, *Iba1* and *GSL1* (blue) labelling of a penetrating arteriole coursing into IC. Scale bar 50µm. (D) Confocal micrograph showing a calbindin (green) expressing neuron in the outer layers of the LCIC surrounded by *GFAP*+ axo-somatic processes. Scale bar 10µm.

3.3.2 – Distributions of *Iba1*+ microglia and *GAD67*+ somata vary between sub-regions of IC

To explore the role of parenchymal microglia in IC, tiled confocal micrographs of *Iba1*+ microglia (Figure 3.2A) and *GAD67*+ neurons (Figure 3.2B) across whole coronal IC sections were taken (Figure 3.2C). Dividing the IC into DCIC, LCIC, CNIC and VCNIC based on the criteria of Coote and Rees (2008) allowed definition of regions of interest for comparisons between sub-regions (Figure 3.2D). Specifically labelled colours represent DCIC (orange), CNIC (blue), LCIC (grey) VCNIC (green) for measurements and images throughout.

Next, 5-row x 6-column (432x552µm) micrographs of each IC sub region were taken at higher power to enable representative measurements. Example micrographs can be seen in Figure 3.3. Labelling revealed putative GABAergic neurons throughout the sub regions of IC, with an appeared increased in *GAD67*+ cell density in high-frequency ventral regions, matching previous reports (Figure 3.3K&L) (Ito *et al.*, 2009, Gleich *et al.*, 2014, Beebe *et al.*, 2016). Of note, *Iba1*+ labelling appeared higher in the DCIC compared to the other sub regions (Figure 3.3A&C). These speculative increases in *GAD67*+ cells and *Iba1*+ labelling are quantified in along with cell counts, morphological characteristics and the interactions between *Iba1*+ microglia and *GAD67*+ somata are quantified in sections 3.3.3- 3.3.6 of this Chapter.

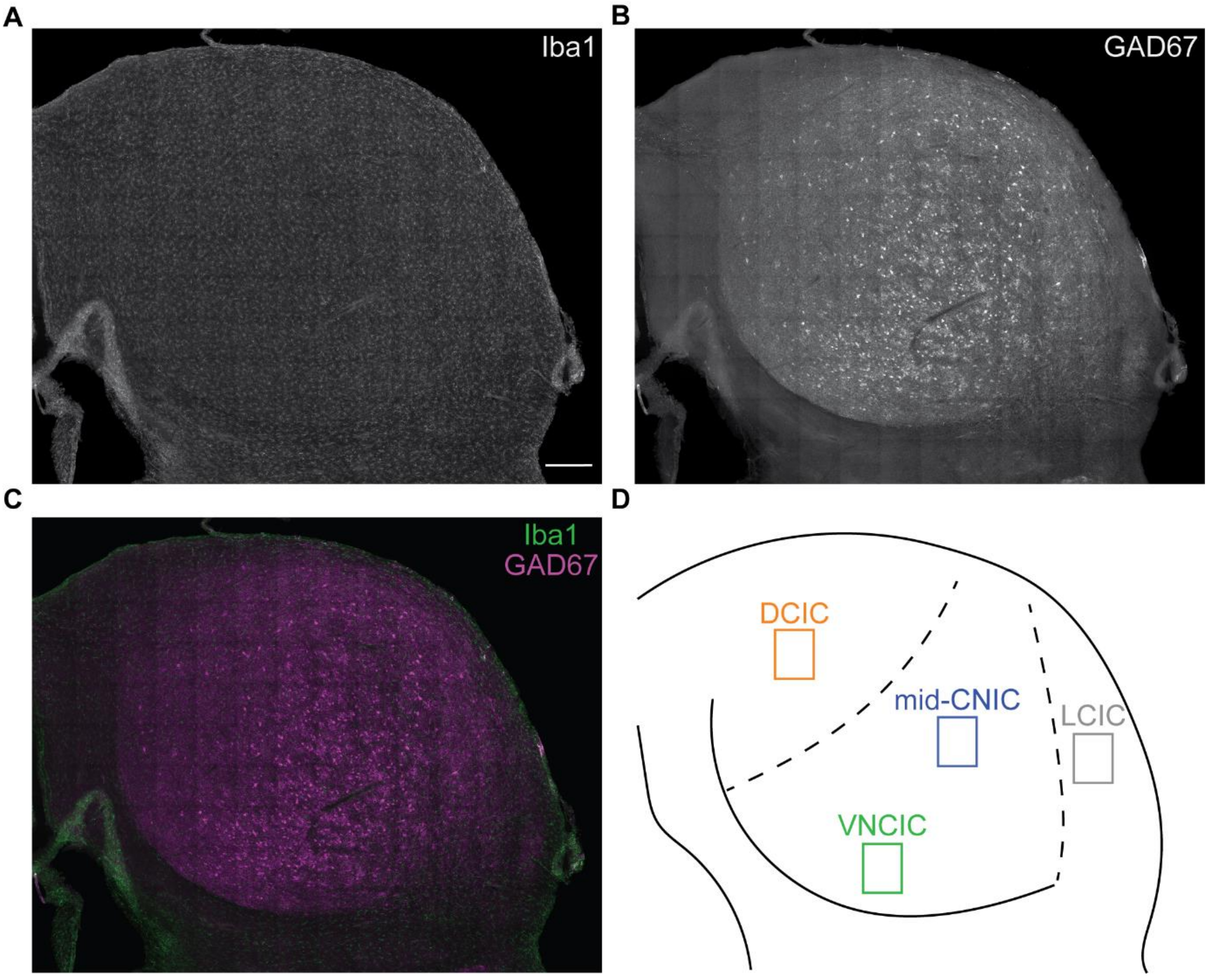

Figure 3.2. *GAD67*+ neurons vary in density between sub-regions of IC. (A) Tiled confocal micrograph showing *Iba1*+ microglia tiling IC parenchyma. Scale bar 400µm. Same scale for panels (B) and (C). (B) *GAD67*+ neuropil can be seen to mark the medial and ventral borders of the IC. *GAD67*+ neurons are found throughout IC but vary in density. (C) Merge of (A) (green) and (B) (magenta). (D) Borders of IC sub-regions were delineated using those defined by Coote and Rees (2008). Regions of interest were located within distinct sub-regions of IC that could be clearly distinguished from one another. See figure 3.3 for high magnification panorama micrographs.

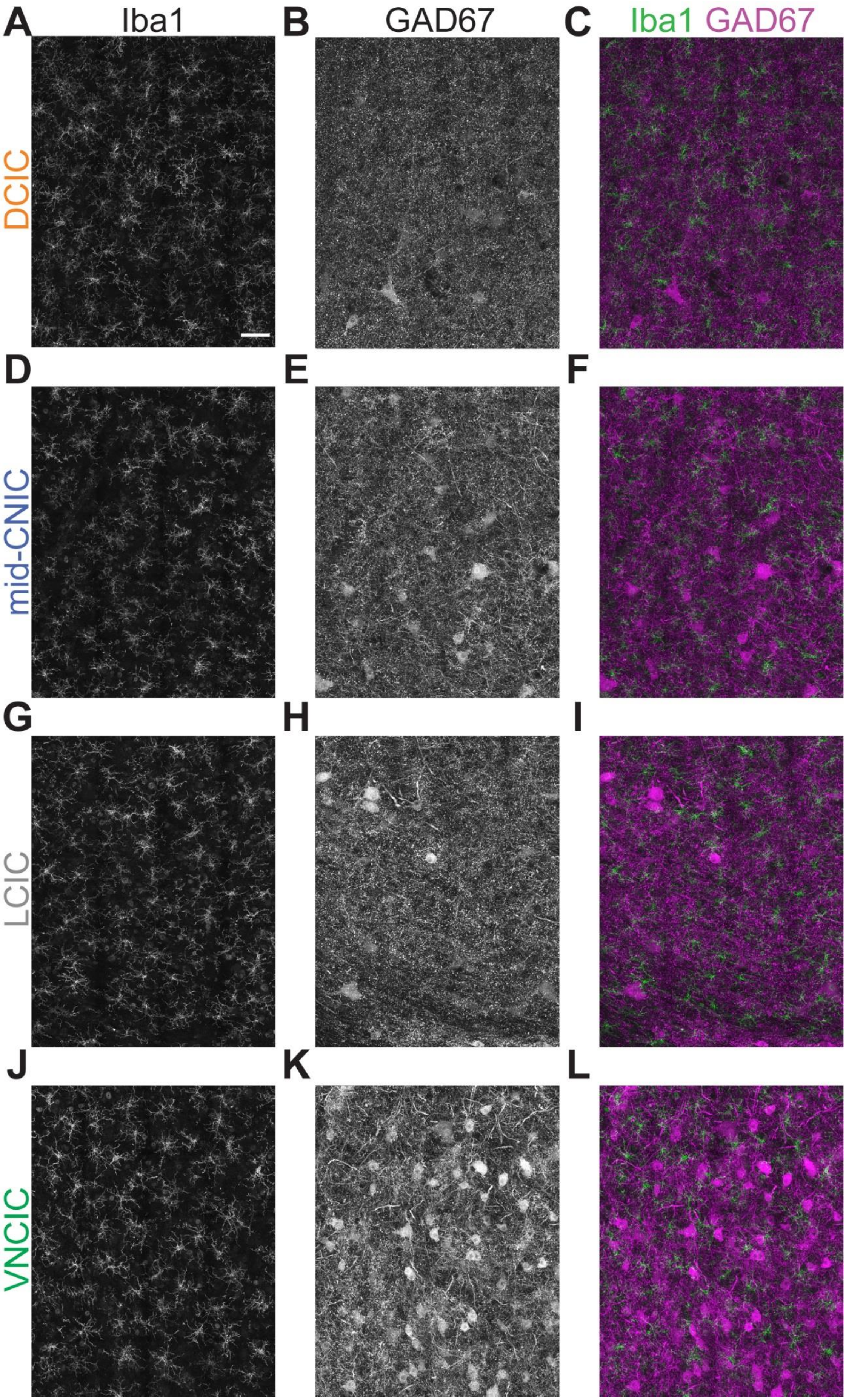
A
Iba1
B
GAD67
C
Iba1 GAD67
DCIC
D
E
F
mid-CNIC
G
H
I
LCIC
J
K
L
VNCIC

Figure 3.3. Representative region of interest panoramas show differences between *Iba1*+ and *GAD67*+ cells in sub-regions of IC. Scale bar in (A) 50µm. Same scale for all panels. Maximum intensity projections of tiled confocal panoramas in all sub-regions show (left column; A,D,G,J) *Iba1*+ microglia tiling the parenchyma with similar density. Conversely, labelling of *GAD67*+ somata (middle column, B,E,H,K) reveals varied cell densities between sub-regions. Merging both labels (right column; C,F,I,L) reveals intercalating of *Iba1*+ processes with *GAD67*+ labelling.

3.3.3 – The highest density of *GAD67* is in VCNIC and *Iba1* in DCIC

Analysis of *GAD67*+ cell counts from 432x552µm regions of interest (Figure 3.4A) revealed that VCNIC had the highest density of cells with a median of 95 (range=66 to 117), followed by 50 in CNIC (range=31 to 74), then 35 in LCIC (range=21 to 44) and 24 in DCIC (range=19 to 38). *Post-hoc* analysis confirmed a greater number of *GAD67*+ neurons in VCNIC (H(3)=24.42; p<0.001) than other sub-regions (*post-hoc* Dunn's tests: VCNIC vs DCIC p<0.0001; VCNIC vs LCIC p=0.0023). CNIC also had a greater number of *GAD67*+ neurons than DCIC (p=0.026) and LCIC (p=0.395), albeit not significant.

Additional analyses of regions of interest confirmed similar densities of *Iba1*+ microglia cell counts between sub-regions of IC, despite the varying density of *GAD67*+ cells (Figure 3.4B). The DCIC had slightly more densely packed *Iba1*+ microglia than other sub-regions, with a median of 88 cells (range=70 to 106) per 432x552µm region of interest. CNIC had a median of 83 (range=76 to 95), while LCIC had a median of 80 (range=63 to 104) and VCNIC had a median of 73 (range=57 to 92). However, a Kruskall-Wallis ANOVA with sub-region as the factor found no detectible difference between groups (H(3)=4.91, p=0.179). Contrastingly, the percentage field of view of *Iba1*+ labelling (see methodology) revealed greater differences in *Iba1*+ labelling between sub-regions (Figure 3.4C). The DCIC (median=14.8%; range=8.7 to 22.5) demonstrated greater *Iba1*+ labelling than CNIC (9.5%; 7.1-13.9), LCIC (8.9% 4.9-12.4) and VCNIC (7.4%; 4.3-12.0). These differences between groups are a real effect (H(3)=12.67; p=0.0034; *post-hoc* Dunn's test between DCIC and VCNIC p=0.002). The greater percentage field of view of *Iba1*+ labelling in DCIC, despite similar soma density between sub-regions, suggests differences in other aspects of *Iba1*+ microglia morphology.

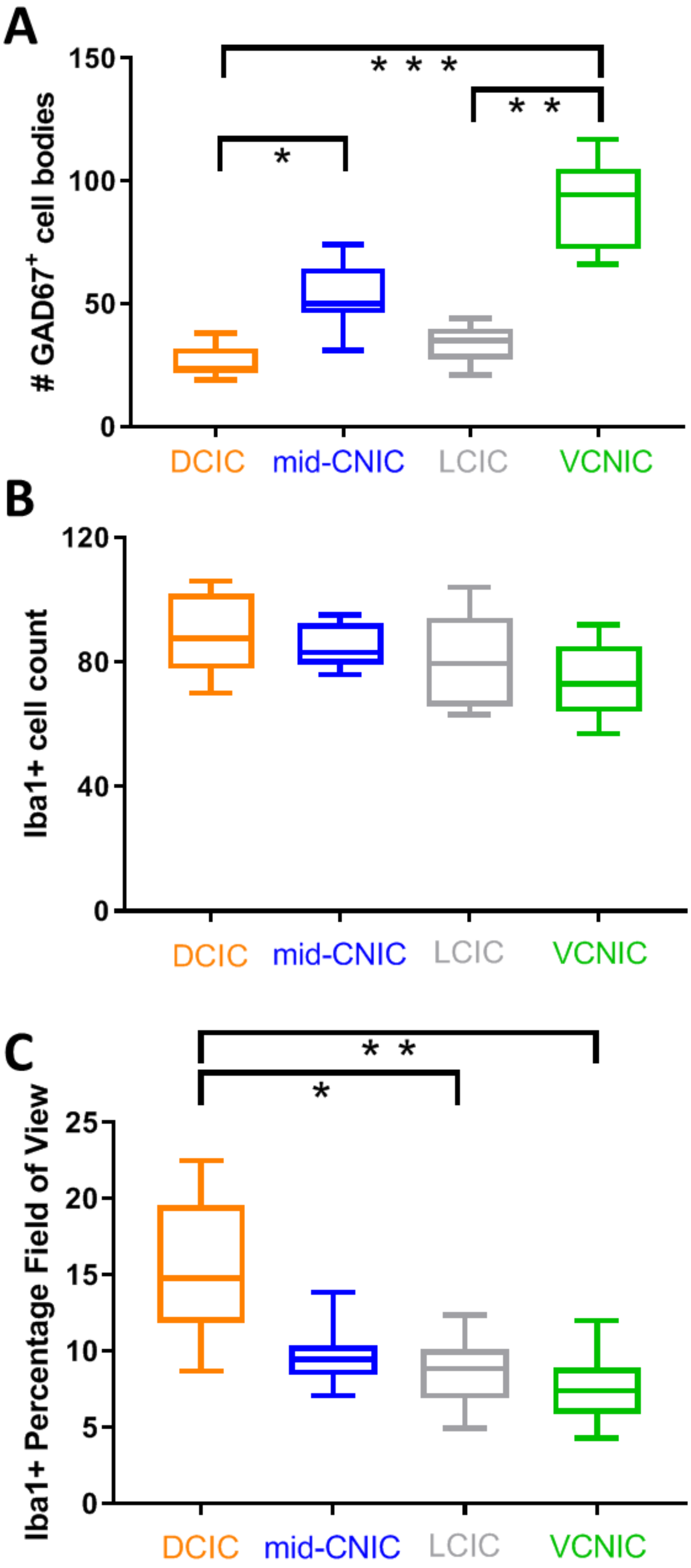

Figure 3.4. (A) Box plot showing *GAD67*+ somata counts in each sub-region of interest, across cases. The VCNIC consistently had the highest number of *GAD67*+ somata while numbers in DCIC and LCIC were lower than CNIC. (B) *Iba1*+ cell counts across sub-regions of interest. DCIC has the highest number across cases, with the lowest in VCNIC contrary to the *GAD67*+ cell counts. (C) Percentage field of view analyses revealed a larger difference between DCIC and VCNIC and LCIC, which suggests further underlying sub-regional differences in morphology.

3.3.4 – *Iba1*+ microglia in DCIC are more ramified than other sub-regions of IC

Iba1+ microglia labelling was better characterised in DCIC by percentage field of view analyses than cell counts, which suggests this was primarily due to a greater number and extent of ramifications compared to other sub-regions of IC. To test this hypothesis, 3D volumetric Sholl analyses were implemented on a total of 64 cells per sub-region (N=256). Individual 1µm slices were quantified for the entirety of each cell to produce a volumetric three-dimensional analysis.

Cells were identified and selected based on whether the entirety of the cell was present across all x, y and z planes of the slices. The slices were projected as a two-dimensional maximum intensity projection to enable a contour to be drawn around the whole cell (Figure 3.5A). The cells were then split into individual slices to remove background/non-cellular labelling (Figure 3.5B-I). Slices were then merged as three-dimensional projections (Figure 3.5J-L) and thresholded to generate binary images (Figure 3.5M). The number of intersections at every micrometre distance radiating volumetrically from the centre of the soma was calculated (Figure 3.5N). Binary thresholded cells were also skeletonized to derive information about the shape and structure of ramifications, including the number of branches and maximum branch length (Figure 3.5O).

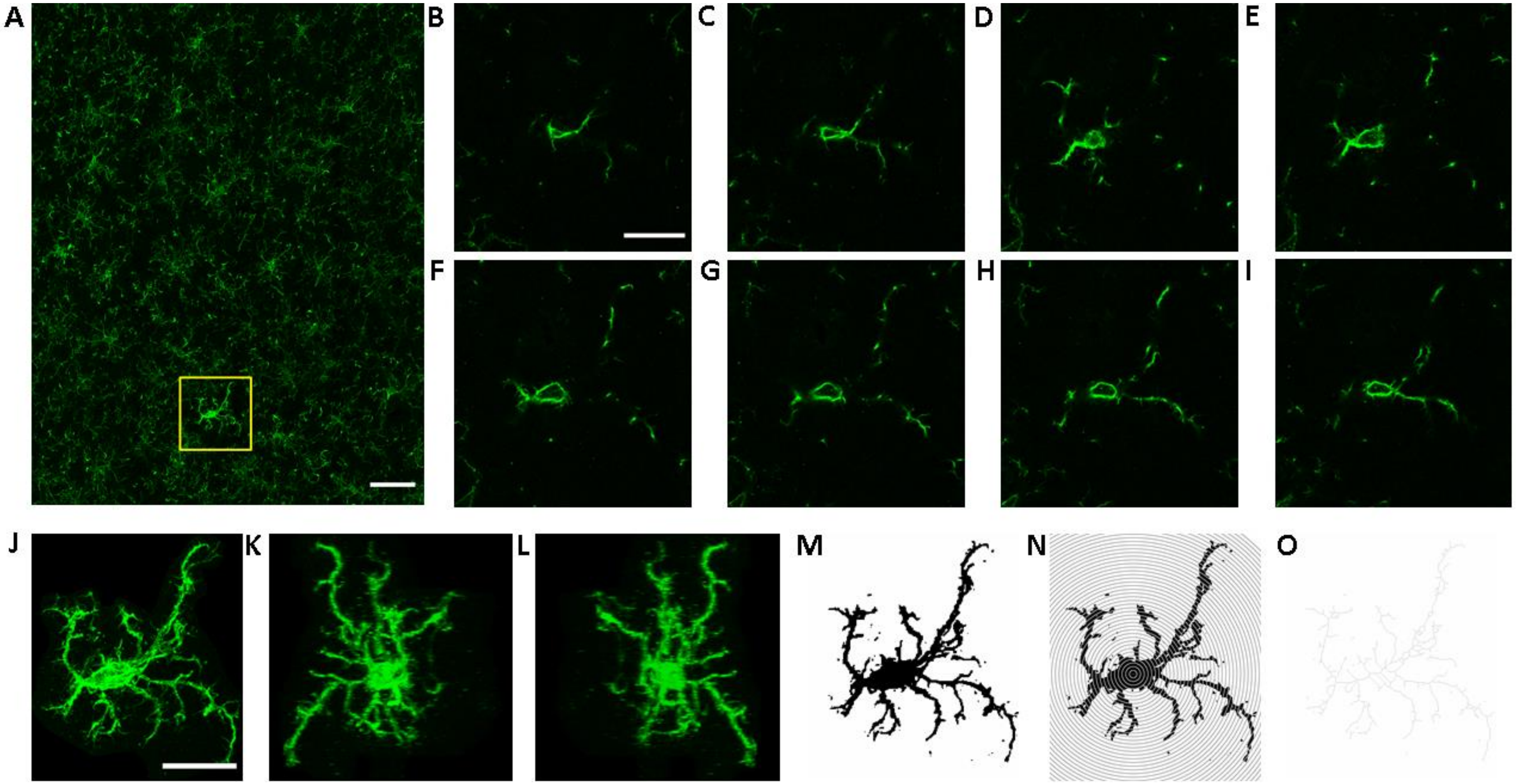

Figure 3.5. Process for volumetric Sholl and skeleton analyses to quantify morphological characteristics of *Iba1*+ microglia. (A) Example of maximum intensity projection of region of interest tiled confocal micrograph showing *Iba1*+ microglia in IC. (A) 6-column x 5-row field of view tiled image was taken using 0.99µm z-slices. Individual cells were subject to Sholl and skeleton analyses (yellow box inset). Scale bar 50µm. (B-I) Examples from 8 extracted slices (of 24 total) from cell in (A) showing high resolution imaging of soma and processes surrounded by non-cellular labelling. Non-cellular labelling was cropped from each individual slice. Scale bar 20µm throughout. (J-L) Three-dimensional projection of the cell at different angles rotating around the x-axis. (M) Each slice was thresholded to binarize cellular processes. (N) Sholl analyses were performed at 1µm resolution throughout x, y and z planes from binarized images. (F) Three-dimensional skeletonized cell framework from (M) to be analysed for number of branches and max branch length. Scale bar 20µm (J) through to (L).

Iba1+ microglia were more ramified in DCIC than CNIC, LCIC or VCNIC at all distances away from the soma (Figure 3.6A). The total number of intersections of every ramification, across cells (independent of distance from the soma) had a median value of 438 in DCIC (IQR=385 to 500). This was significantly greater than in CNIC (332; ±284-399), LCIC (363; ±326-422), or VCNIC (353; ±302-400) (Figure 3.6B). A Kruskal-Wallis one-way ANOVA on ranks, with sub-region as the factor found the differences between sub-regions of IC (H(3)=54.36; p<0.0001). *Post-hoc* analyses via Dunn's tests showed differences between DCIC and the other three sub-regions was a real effect (all p<0.0001).

Analyses of skeletonized *Iba1*+ microglia revealed those in DCIC also had a greater number of branches (Figure 3.6C), with a median of 269 (±222-312). This was greater than CNIC (183; ±150-229), LCIC (193; ±165-224), and VCNIC (165; ±138-201). These greater number of branches in DCIC were also a real effect (H(3)=71.30, p<0.0001; Dunn's tests DCIC vs other sub-regions all p<0.0001).

Conversely, maximum branch length, defined as the longest distance covered by any ramification of skeletonized *Iba1*+ microglia without branching, followed the opposite trend. Longest distances were found in VCNIC (median=14.44µm; IQR=12.76-17.18) (Figure 3.6D). Shorter distances were found in LCIC (14.01; IQR±=11.92-16.16), CNIC (12.86; ±11.22-15.60) and DCIC (11.62; ±11.26-15.01). The difference between VCNIC and DCIC was a real effect (H(3) =12.18, P = 0.0068; *post-hoc* Dunn's test p=0.0079).

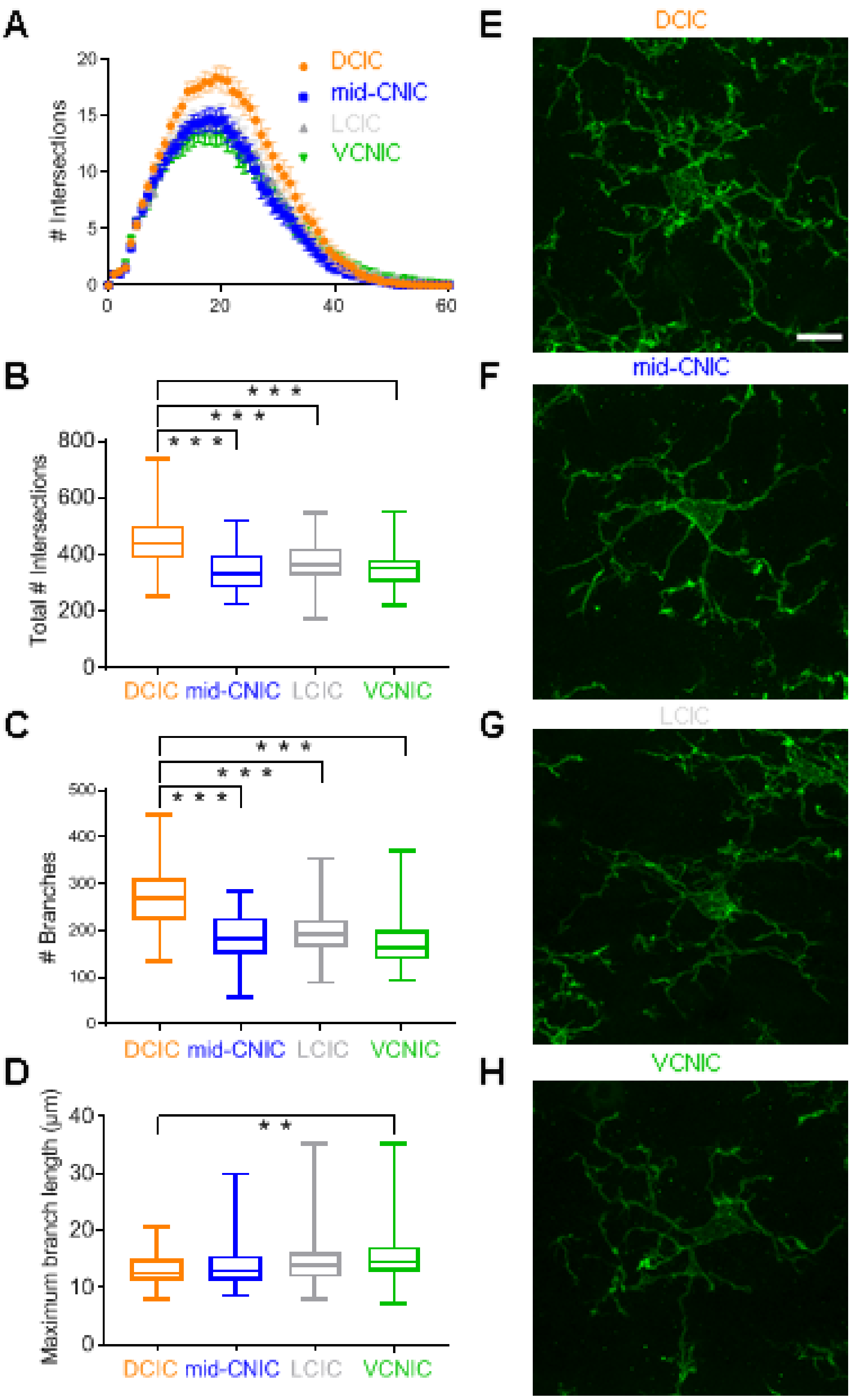

Figure 3.6. *Iba1*+ microglia are more ramified in DCIC than other sub-regions of IC. (A) Sholl analyses (mean ±95% confidence intervals) showing *Iba1*+ microglia in DCIC have greater numbers of ramifications than other IC sub-regions at all distances from the soma. (B) Total number of ramification intersections independent of distance from soma are greater in DCIC. (C) Greater number of intersections in DCIC are due to a greater number of branching ramifications. (D) Maximum branch length, a measure of how long ramifications travel before branching, are longest in VCNIC and shortest in DCIC. Representative examples of *Iba1*+ microglia in (E) DCIC, (F) CNIC, (G) LCIC and (H) VCNIC. Scale bar in (E) 10µm. Same scale bar for panels (F-H).

3.3.5 – *Iba1*+ putative abutments reveal two new types of *GAD67*+ neurons in IC

GAD67+ neurons have been found to receive a variety of presynaptic contacts (Ito *et al.*, 2009, Beebe *et al.*, 2016), but also of interest is whether they also receive different types of *Iba1*+ microglial abutments. To examine the nature of *Iba1*+ putative interactions with *GAD67*+ neurons, five dependent variables from each cell region of interest (n=40 per sub-region) were quantified: (i) *GAD67*+ soma maximum diameter; (ii) percentage of *GAD67*+ soma abutted by *Iba1*+ processes; (iii) number of *Iba1*+ microglia with processes abutting each *GAD67*+ soma; (iv) number of distinct *Iba1*+ processes abutting each *GAD67*+ soma; and (v) total length of *Iba1*+ processes abutting each *GAD67*+ soma (μm). The methods used to calculate these variables are shown in Figure 3.7.

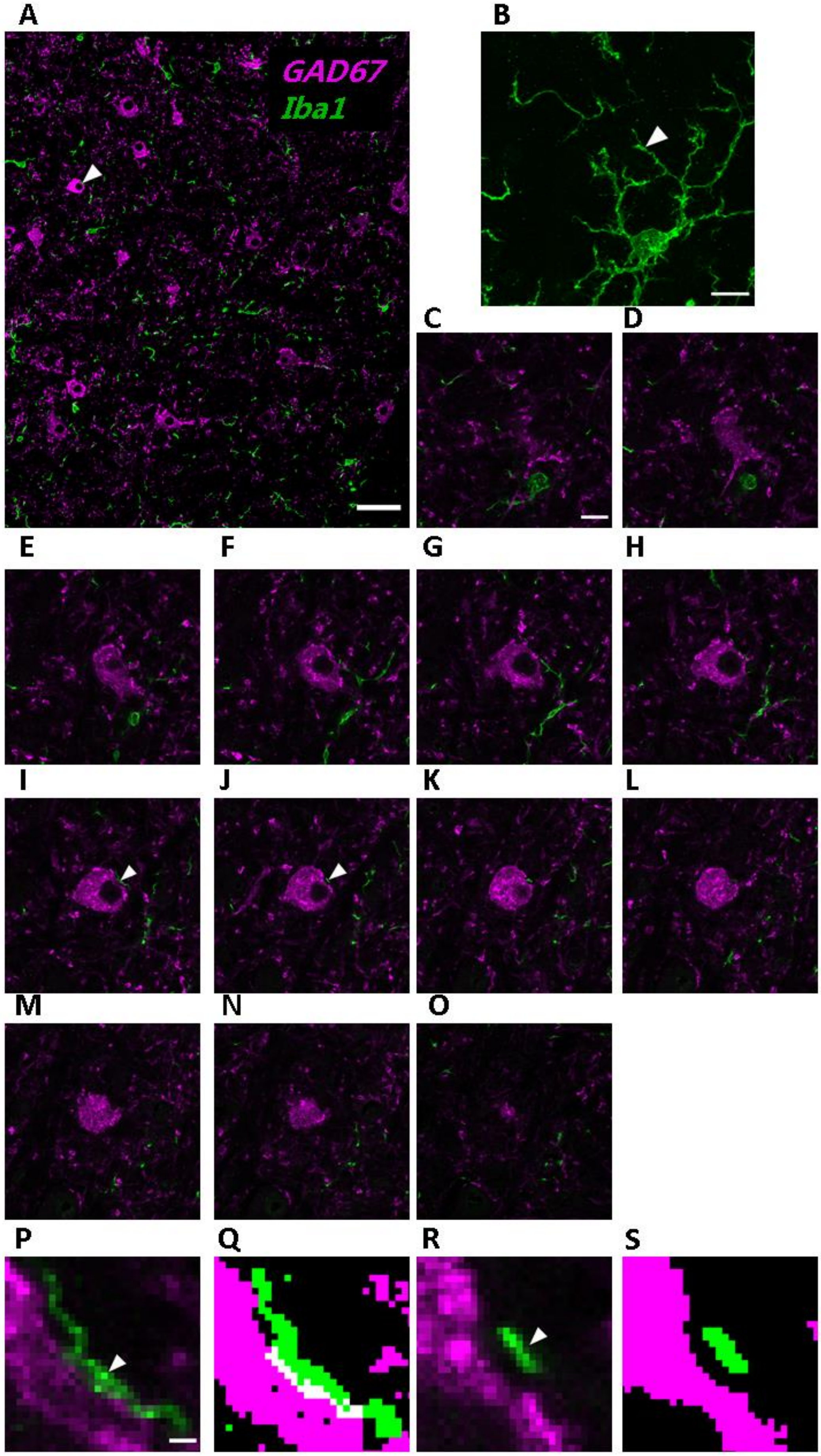
A
GAD67
Iba1
B
C
D
E
F
G
H
I
J
K
L
M
N
O
P
Q
R
S

Figure 3.7. *GAD67*+ cells were selected that were contained entirely within the x, y and z coordinates of the tissue section and region of interest. (A) Example of a 1μm slice of a region of interest panorama in VCNIC, labelled for *GAD67* (magenta) and *Iba1* (green). Example *GAD67*+ cell (white arrow) was selected for analysis. Scale bar 50μm. (B) Maximum intensity projection of *Iba1*+ cell through 13 z-planes in zoomed region around cell selected in (A), allowing visualization of microglial processes and soma. Scale bar 10μm. (C-O) Example 1μm slices though rostro-caudal axis in the z-plane. Soma perimeter length was measured in each slice. White arrows in (I&J) point to magnified region in (P-S). Scale bar 10μm. (P) Magnified region from (I) demonstrating an *Iba1*+ process abutting *GAD67*+ soma. Scale bar 1μm also applies to panels (Q-S). (Q) Thresholding using the Huang algorithm in ImageJ for each label reveals abutment of *Iba1*+ process onto *GAD67*+ soma, with no pixels separation, and a 1-2 pixel thick plexus of double labelling (white), allowing quantification of the location and length of abutment. The distance of abutment was measured along the *GAD67*+ perimeter. Each distinct process abutting the *GAD67*+ cell was counted and the total number of *Iba1*+ cells abutting the *GAD67*+ cell were measured. (R) Magnified region from (J), showing *Iba1*+ process in close proximity to but not abutting *GAD67*+ soma. Thresholding each label reveals clear separation with unlabelled pixels between. This demonstrates that the measures taken facilitated positive and negative identification of abutments at 1μm intervals through the z-plane of all cells analysed.

These features were calculated from micrographs such as the representative example in Figure 3.8A, which shows a *GAD67*+ neuron being abutted by two *Iba1*+ microglia. A correlation matrix was undertaken by correlating each variable against other measured variables, and revealed weak associations between *GAD67*+ soma maximum diameter (i) and the other four dependent variables (ii-v) (Figure 3.8B). There were stronger correlations between the four *Iba1* related variables (ii-v). As these variables were only weakly correlated with *GAD67*+ neuron diameter. These results determined that *GAD67*+ soma maximum diameter was distinct from the other variables and that the other variables are interdependent.

To try to understand the observed distributions, a multivariate analysis was implemented. Initially, a principal component analysis was undertaken for the five variables in all sub-regions of the IC. The data showed a clear dissociation between *GAD67*+ neuron diameter in one cluster and the other four variables, which clustered together (Figure 3.8C). Both clusters were categorized using a standard correlation coefficient of >0.5 as a cut-off value, which showed one cluster was explained by only the *GAD67*+ neuron diameter variable, while the other cluster had significant contributions from all four of the *Iba1*+ related variables. These trends were also true for all sub-region-specific analyses in IC (Figure 3.8Di-iv). Next, a two-step cluster analysis was conducted including all five variables. The parameters included Euclidean distance measures using the Schwarz's Bayesian clustering criterion (Figure 3.8E). Contrasting iterations up to 15 clusters, the analysis found two clusters demonstrated the best explanatory power, displaying good (0.5) silhouette measures of cohesion and separation (Figure 3.8F). Overall, these variables defined the parameters of the clusters based on all the variables and enabled the visualisation of the contribution of each variable, which is not possible using conventional statistics.

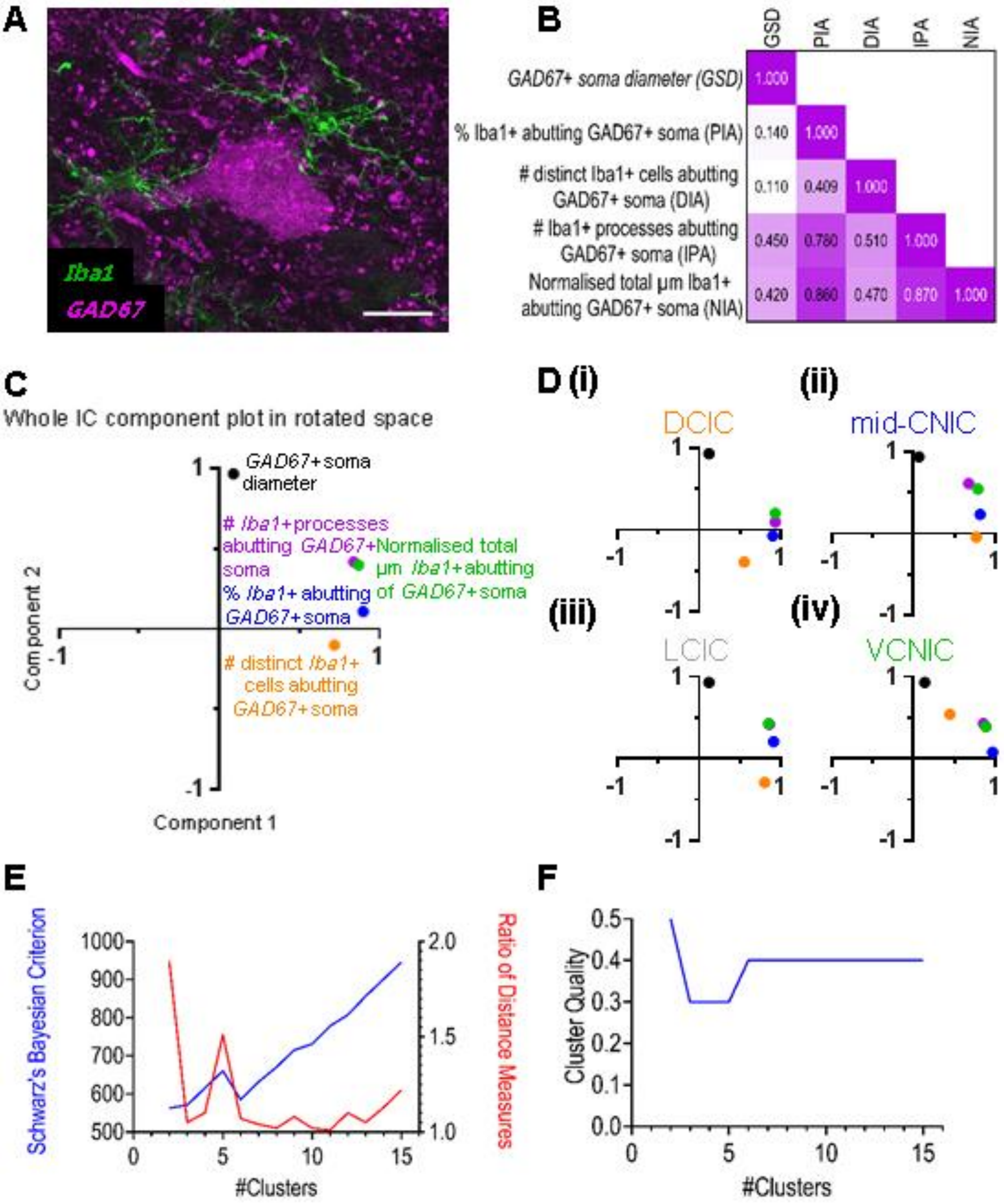

	GSD	PIA	DIA	IPA	NIA
GAD67+ soma diameter (GSD)	1.000				
% Iba1+ abutting GAD67+ soma (PIA)	0.140	1.000			
# distinct Iba1+ cells abutting GAD67+ soma (DIA)	0.110	0.409	1.000		
# Iba1+ processes abutting GAD67+ soma (IPA)	0.450	0.780	0.510	1.000	
Normalised total µm Iba1+ abutting GAD67+ soma (NIA)	0.420	0.860	0.470	0.870	1.000

Figure 3.8. (A) Representative *GAD67*+ cell (magenta) receiving abutting somatic processes from two *Iba1*+ microglia (green). Scale bar 20µm. (B) Correlation matrix showing Spearman's rank correlation coefficient for each combination of measures derived from putative interactions between *Iba1*+ microglia and *GAD67*+ cells. Note lower values in first column. (C) Principal component analysis of the five variables in (B). *GAD67*+ soma diameter separated from the other four variables, which grouped together. (D) As (C) but for each sub-region in IC, showing similar findings in all sub-regions, suggesting robust clustering throughout IC. (E) The largest difference between Schwarz's Bayesian criterion and the ratio of Euclidean distance measures is observed in cluster 2, demonstrating that two clusters display the best explanatory power. (F) Silhouette measures of cohesion and separation were compared from 2-15 clusters, with two clusters demonstrating the highest cluster quality. These data demonstrate that not only did two clusters exhibit the best available explanatory power, but also strong clustering quality, reflecting real underlying differences in *Iba1*+ abutments onto *GAD67*+ neurons between clusters.

All 160 cells were classified into one of the two clusters determined by the two-step analysis. Representative examples of each cluster found in each sub-region are shown in Figure 3.9. There were 23 cases in cluster 1, and 137 in cluster 2. To visualise the contribution of each of the four *Iba1* related variables, each was plotted as a function of *GAD67*+ neuron diameter (Figure 3.10A-D). These scatterplots revealed a dissociation with little overlap between the two clusters using the percentage *Iba1*+ abutting *GAD67*+ somata (Figure 3.10A). There was almost perfect discrimination between the clusters of the normalized total μms of *Iba1*+ abutments onto *GAD67*+ neuron somata (Figure 3.10B). Conversely, the number of *Iba1*+ cells abutting each *GAD67*+ soma had a significant degree of overlap with little difference between clusters (Figure 3.10C). The number of *Iba1*+ processes abutting *GAD67*+ somata had little overlap between distributions (Figure 3.10D). To compare the ability of each of these variables to independently discriminate between the two clusters, ROC analyses were conducted (Figure 3.10E). The high hit rate observed in the ROC analysis demonstrates the reliability of the tests undertaken, a high false alarm rate would indicate a high level of type 1 error rate. These data revealed that while each variable had an area under the curve >0.5, the three variables relating to the nature of *Iba1*+ processes abutting *GAD67*+ neurons had the best discriminatory power. Overall, these results demonstrate that two types of *GAD67*+ cell can be identified based on the interactions with *Iba1*+ microglia, which provides a strong basis exploratory physiological experiments looking at a microglial role in inhibitory processing.

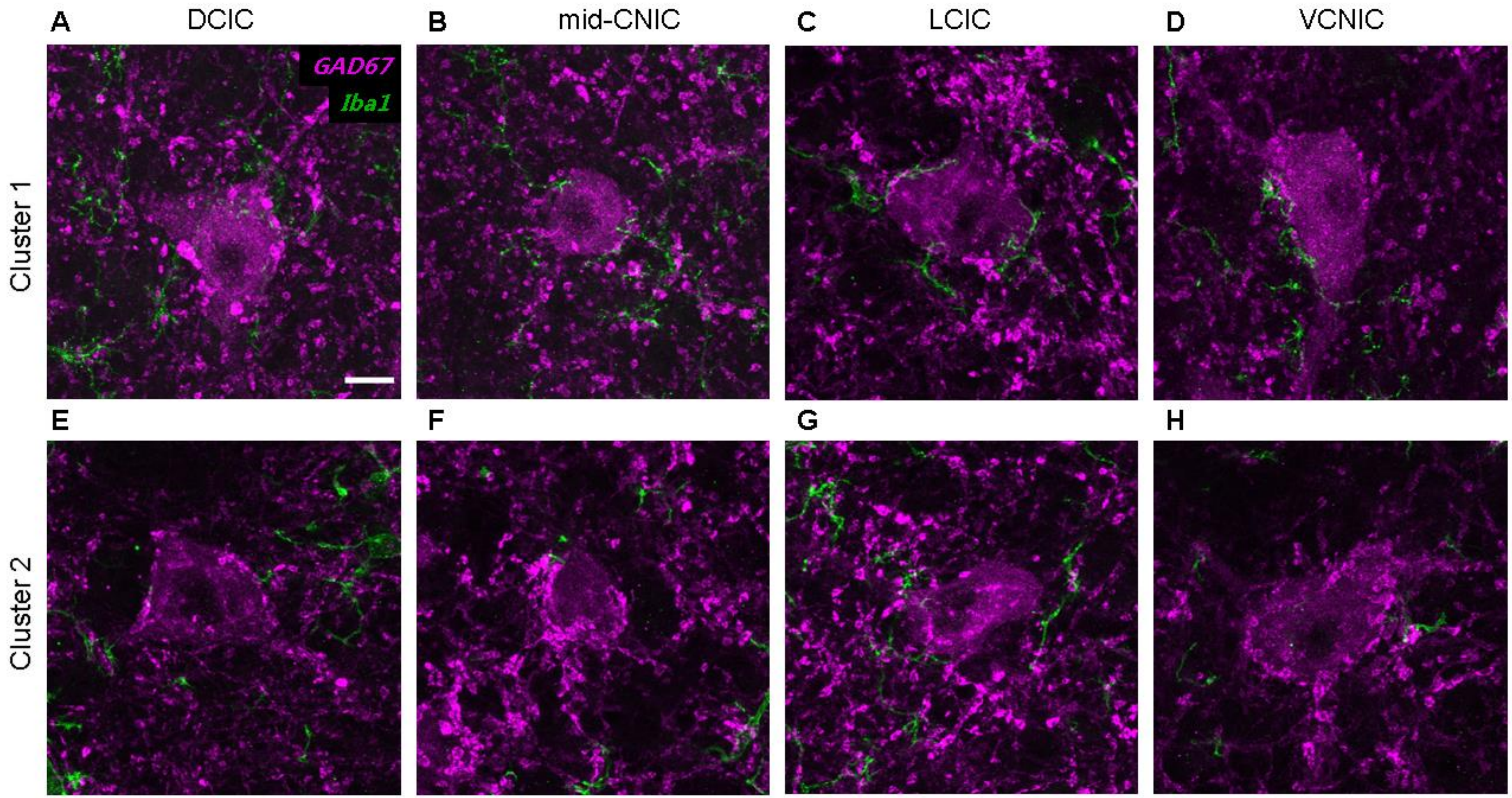

Figure 3.9. Example *GAD67*+ cells taken from each sub-region of IC (maximum intensity projection of five 1µm slices through the centre of each cell in the rostro-caudal z-plane), with one example from each designated cluster from the two-step analysis. Scale bar 10µm applies to all images. Note the greater length of *Iba1*+ abutments surrounding *GAD67*+ somata in cluster 1 (top row), while adjacent *Iba1*+ processes in cluster 2 make few abutments onto the somata (bottom row).

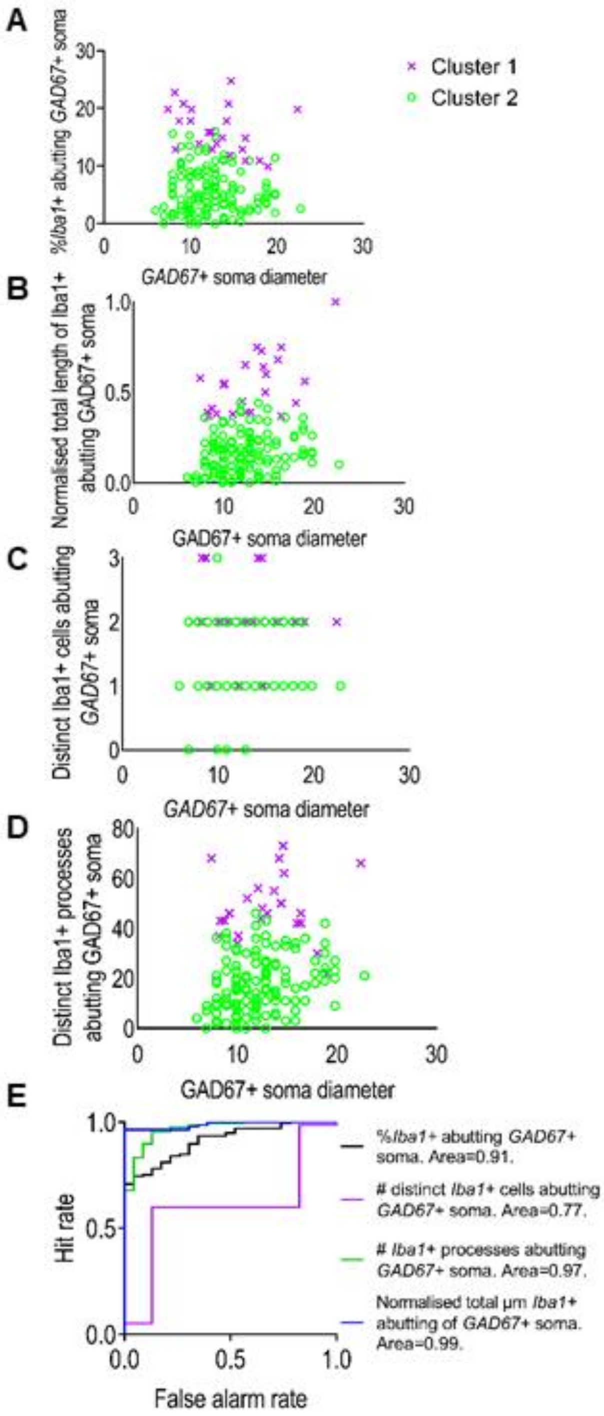

Figure 3.10. *GAD67*+ neurons in IC can be classified into two clusters based on the amount of somatic *Iba1*+ abutments they receive. Scatterplots showing each *GAD67*+ cell from the cluster analysis, classified into either cluster 1 (magenta crosses; n=23) or cluster 2 (green open circles; n=137) for each *Iba1*+ related variable, plotted as a function of *GAD67*+ soma diameter: (A) Percentage *Iba1*+ labelling abutting *GAD67*+ somata; (B) normalized total length of *Iba1*+ labelling abutting *GAD67*+ somata; (C) distinct number of *Iba1*+ cells abutting *GAD67*+ somata; (D) number of *Iba1*+ processes abutting *GAD67*+ somata. (E) ROC analyses showing classifier performance of each variable in discriminating *GAD67*+ cells into cluster 1 or cluster 2. Normalized total μm *Iba1*+ abutting and number of processes of *GAD67*+ somata could almost perfectly discriminate between clusters.

3.3.6 – *Iba1*+ putative interactions with *GAD67*+ neurons show little difference between sub-regions of IC

This section determined whether any of the variables or clusters identified had a relationship to the sub-region of IC in which the cells were located. Diameter of *GAD67*+ somata did not vary between sub-regions (Figure 3.11A) (H(3)=5.3; p=0.151). A small difference was found for the percentage of *GAD67*+ soma abutted by *Iba1*+ processes across all subregions (Figure 3.11B) (H(3)=9.9; p=0.019) and a p*ost-hoc* Dunn's tests revealed that the difference was between DCIC and VCNIC (p=0.012). The number of *Iba1*+ cells abutting each *GAD67*+ somata (Figure 3.11C) (H(3)=6.44; p=0.092), the number of *Iba1*+ abutments onto *GAD67*+ somata (Figure 3.11D) (H(3)=5.55; p=0.141), and the normalised total number of µm covered by *Iba1*+ abutments onto *GAD67*+ somata (Figure 3.11E) (H(3)=4.64; p=0.200) did not differ between sub-regions. However, the number of *GAD67*+ cells abutted by each *Iba1*+ cell was greater in VCNIC (Figure 3.11F) (H(3)=21.32; p=0.0006). *Post-hoc* Dunn's tests revealed a difference between VCNIC and DCIC (p=0.005), which is likely due to the greater density of *GAD67*+ neurons in VCNIC.

Both clusters had similar proportions of regions of interest from each of the four sub-regions of IC (cluster 1: 7 DCIC (30%), 8 CNIC (35%), 6 LCIC (26%), 2 VCNIC (9%); cluster 2: 33 DCIC (24%), 32 CNIC (23%), 34 LCIC (25%), 38 VCNIC (28%)) A Chi-squared test suggested that there was no difference in the relative proportion of each cluster, between sub-regions ($\chi^2(3)=4.21$ p=0.24).

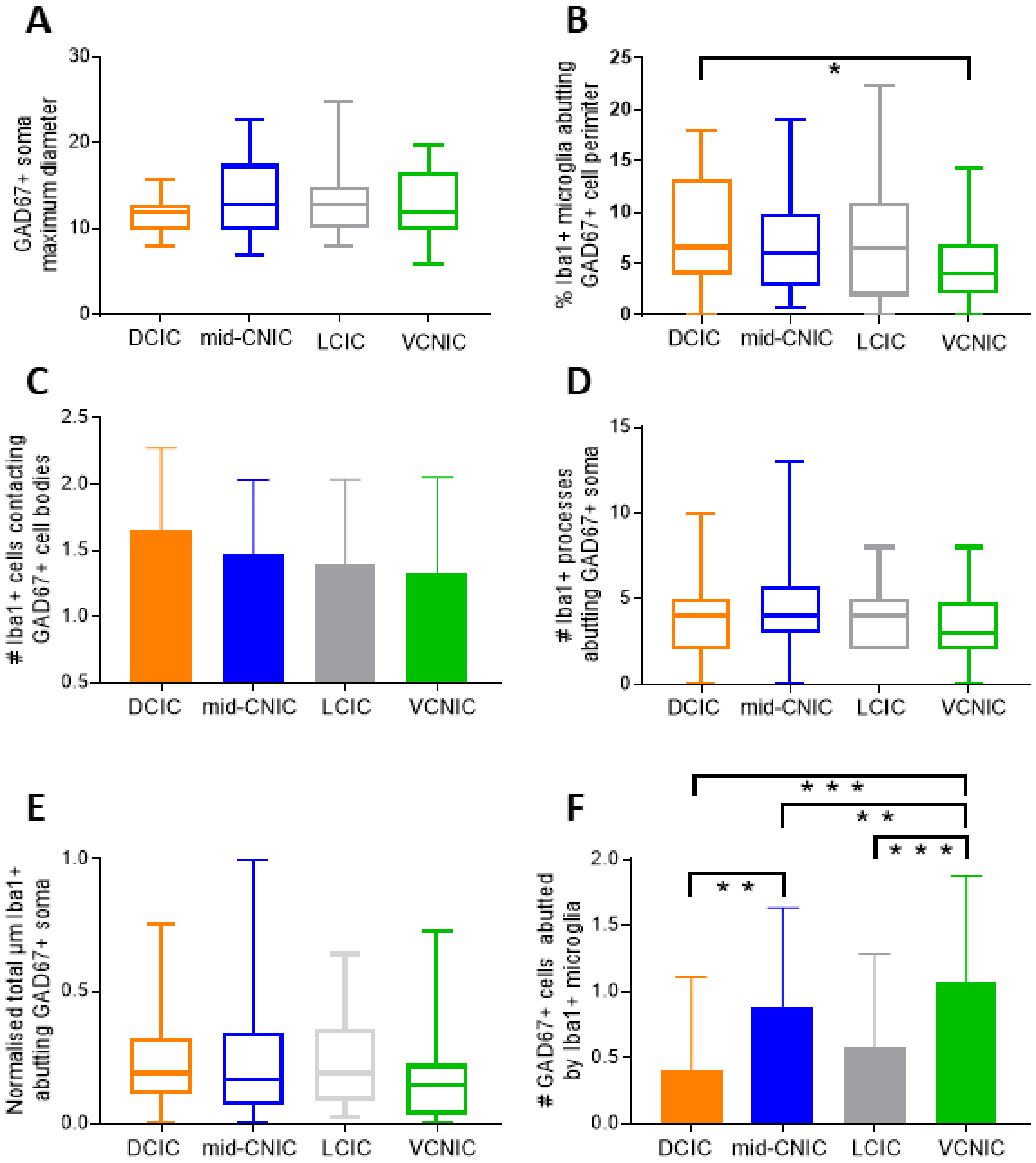

Figure 3.11. No clear relationship between measured variables and IC sub-region. (A) *GAD67*+ soma diameter was similar across sub-regions of IC. (B) The percentage of *Iba1*+ abutting *GAD67*+ somata was lower in VCNIC than the other three sub-regions. (C) The number of *Iba1*+ cells abutting *GAD67*+ somata, (D) the number of *Iba1*+ processes abutting *GAD67*+ somata, and (E) the normalized total µm of *Iba1*+ abutting of *GAD67*+ somata did not differ between sub-regions. (F) There were, on average, a greater number of *GAD67*+ somata abutted by each *Iba1*+ cell, owing to the greater density of *GAD67*+ cells in VCNIC.

3.3.7 – *Iba1*+ microglial processes colocalise at puncta with *synaptophysin* and *homer1* in greater numbers in DCIC

To determine whether *Iba1*+ processes are present at synapses in IC, *Iba1* was co-labelled with the pre-synaptic marker *synaptophysin* and a marker of glutamatergic post-synapses, *homer1*. Figure 3.12A shows a tiled confocal micrograph of *synaptophysin* (magenta) and *Iba1* (green) labelling. A clear shift in *synaptophysin* density can be seen from DCIC to CNIC. Quantification from regions of interest in each sub-region confirmed *synaptophysin* was more densely distributed in DCIC than other sub-regions and mirrored the distributions of *Iba1*+ percentage field of view (Figure 3.12B). Note that these percentage field of view values are calculated from the same animals, but different sections than the analyses presented earlier.

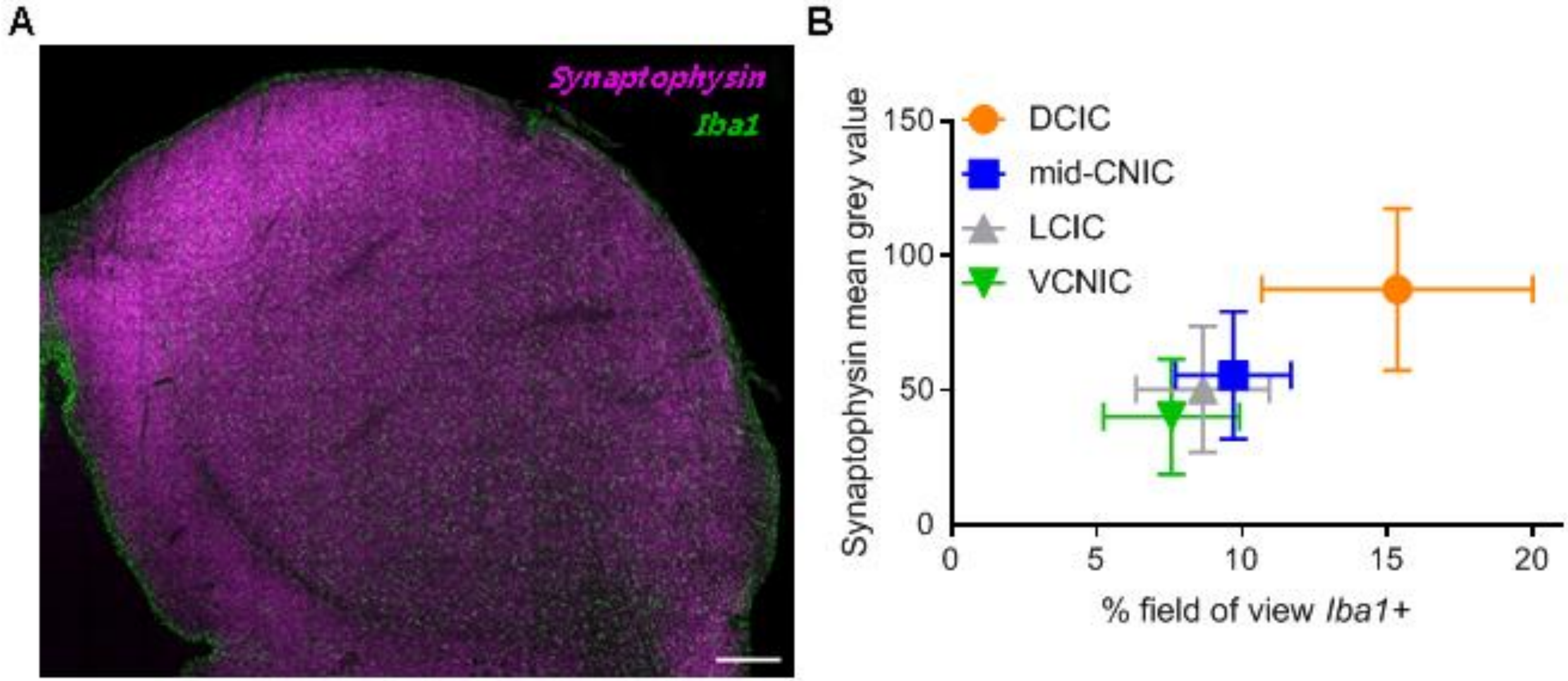

Figure 3.12. Presynaptic marker *synaptophysin* has greater density of labelling in DCIC and correlates with *Iba1* labelling. (A) Tiled confocal micrograph showing representative *synaptophysin* (magenta) and *Iba1* (green) labelling. Note the greater density of *synaptophysin* labelling in DCIC. Scale bar 400µm (B). Quantification from regions of interest in sub-regions (See figure 3.2) showing greater *synaptophysin* puncta density in DCIC which correlates with *Iba1* percentage field of view labelling.

To examine the cellular location of these puncta on *Iba1*+ microglia, three cells were imaged from each sub-region in very fine z-slice steps (0.05µm). A representative image of one z-plane through an *Iba1*+ microglial cell in VCNIC is shown in Figure 3.13A-D, showing a point of colocalisation between *synaptophysin*, *Iba1*, and *homer1* (yellow arrowhead in D). Three-dimensional reconstructions of *Iba1*+ microglia, including all ramifications (Figure 3.13E, green), and points of colocalisation with *synaptophysin* and *homer1* (Figure 3.13H, magenta), allowed visualisation of the locations of these markers. A rectangular region of interest was drawn around colocalized pixels of approximately 0.5µm^2. Plotting spectrographs of pixel intensity for pairwise combination of each of the three labels showed positive relationships (Figure 3.14A-C), with colocalisation rates ranging from 76.5% to 95.0% demonstrating on a slice basis that colocalisation of synaptic labels are in the same anatomical position on microglial processes, which is indicative of microglia interacting with putative excitatory synapses.

Three-dimensional volumetric Sholl analyses (Figure 3.15A) revealed *Iba1*+ microglia in DCIC had a greater number of colocalised puncta. Fitting each sub-region with a LOWESS regression uncovered this trend occurred at all distances from the soma. Quantification of total number of colocalised *Iba1*+, *synaptophysin*+ and *homer1*+ punctum per cell in each sub-region showed that DCIC had a greater number than other sub-regions (Figure 3.15B). The location of each punctum with respect to the branching ramifications of each *Iba1*+ cell was also determined. Puncta were classified as being located on the soma, primary, secondary, tertiary or quaternary branches. Figure 3.15C shows that when normalised, the relative proportion of puncta locations on *Iba1*+ microglia were similar across sub-regions (Table 3.1; χ^2=7.20; p=0.844).

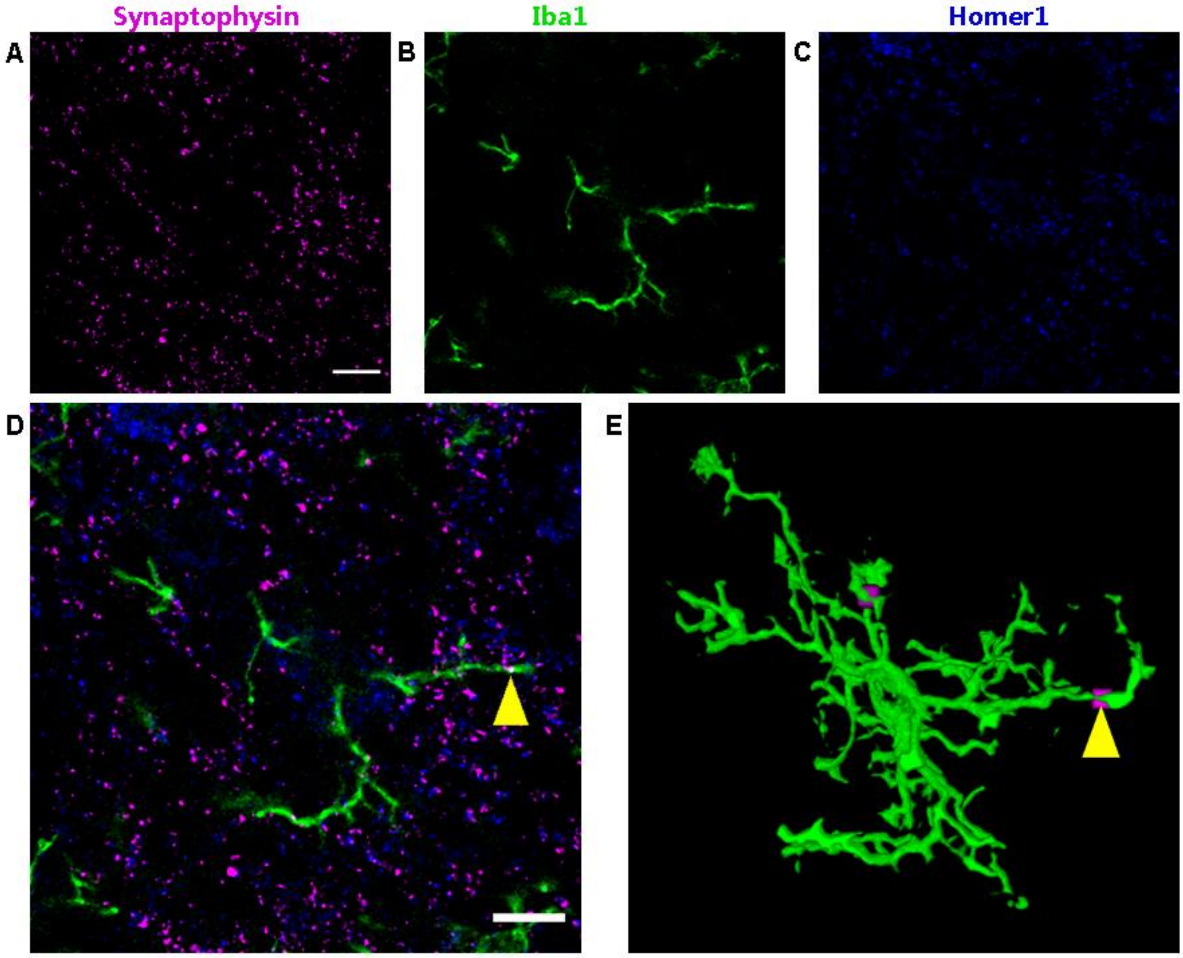

Figure 3.13. Colocalisation of *synaptophysin* and *homer1* on 3D reconstructed *Iba1*+ microglia. Single plane confocal micrograph showing (A) *synaptophysin*, (B) *Iba1*, (C) *homer1* and (D) merged image. Arrowhead shows white pixels, indicating a point of colocalisation of all three labels. All z-planes were thresholded, binarized and pixels containing positive labelling for all three channels were quantified. Scale bars 10µm. (E) 3D reconstruction of *Iba1*+ microglial cell in VCNIC (green, as in (B)) showing two points of *synaptophysin*+ and *homer1*+ colocalisation (magenta; as in (A) and (C), respectively). Green signal to scale in (D) 10µm. Magenta points of colocalisation have been made 13-fold larger for clarity.

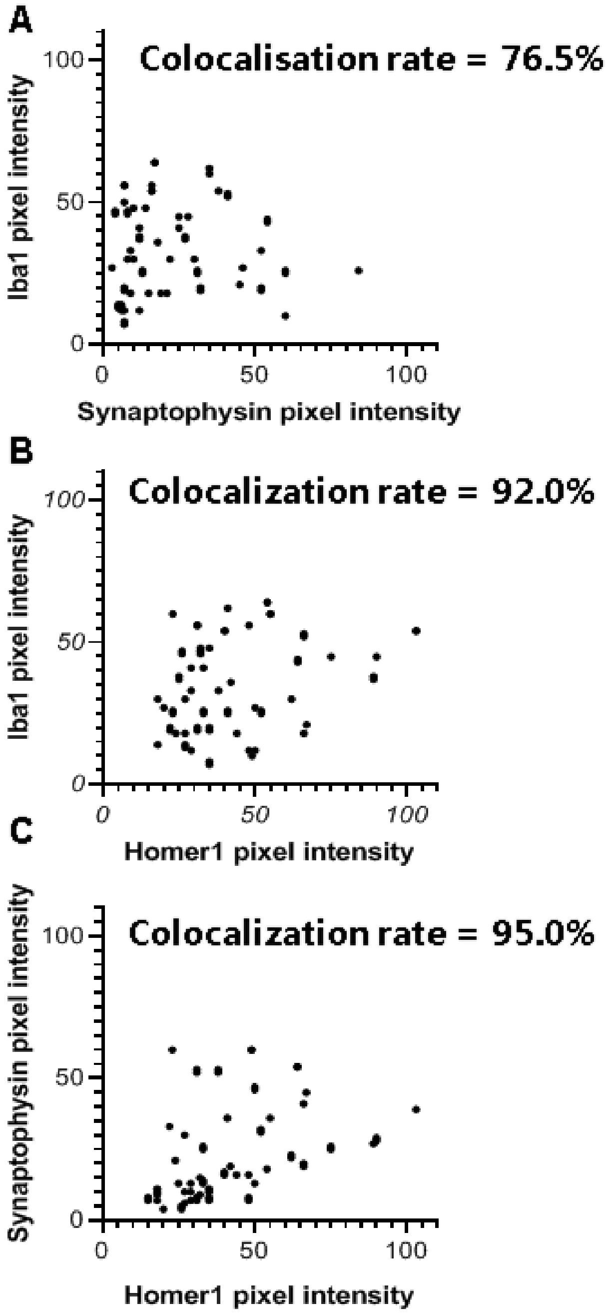

Figure 3.14. Region of interest analysis of point of colocalisation showing pixel intensity from images in Figure 13D&E. (A) *synaptophysin* and *Iba1*, (B) *Iba1* and *homer1* and (G) *synaptophysin* and *homer1*. All combinations showed high rates of colocalisation within region of interest. These results demonstrate the high levels of colocalisation across all three channels at points on an *Iba1* process. Points and positions of colocalisation are quantified in Figure 15. These results clarify the strong level of colocalisation observed between the different markers and justify the representativeness of the results presented in figure 3.15.

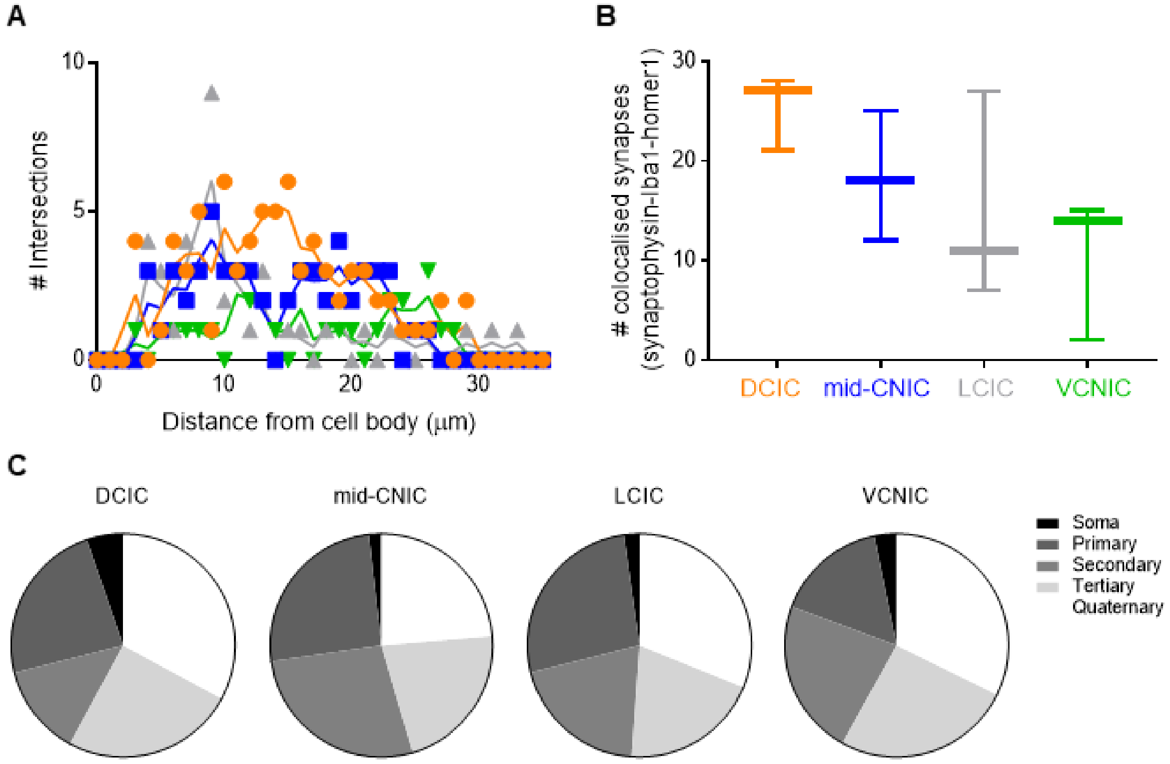

Figure 3.15. *Iba1* colocalises at *synaptophysin*+ and *homer1*+ puncta in greater numbers in DCIC. (A) 3D volume Sholl analysis (plotted in 2D) showing colocalisation of *synaptophysin*+ and *homer1*+ puncta on *Iba1*+ microglia (n=3 per sub-region, colour-coded as in (B). LOWESS regressions highlight greater values in DCIC. (B) Number of colocalized puncta per microglia. The DCIC had a greater number of puncta per microglia. (E) Analyses of puncta location on *Iba1*+ branched ramifications show few puncta are located on somata and similar proportions are found on primary, secondary, tertiary and quaternary branches across sub-regions.

Sub-region	Soma	Primary	Secondary	Tertiary	Quaternary
DCIC	4 (5.3)	18 (23.7)	10 (13.2)	19 (25)	25 (32.9)
CNIC	1 (1.8)	14 (25.5)	15 (27.3)	12 (21.8)	13 (23.6)
LCIC	1 (2.2)	12 (26.7)	9 (20)	9 (20)	14 (31.1)
VCNIC	1 (3.2)	5 (16.1)	7 (22.6)	8 (25.8)	10 (32.2)

Table 3.1. Absolute numbers (and % of the total for that sub-region) of colocalised puncta positive for *synaptophysin*, *Iba1* and *homer1*, as shown in Figure 3.15C. Note similar proportions of puncta both within and between sub-regions.

3.4 – Discussion

The results from this Chapter provide novel anatomical insight into the morphology of microglia and their interactions with GABAergic neurons and synapses. Subsequently, these results can be used as a foundation to inform future physiological investigations. Specifically, these findings reveal *Iba1*+ microglia express morphologies and putative synaptic interactions commensurate with a functional role in activity dependent neurotransmission and synaptic plasticity in the healthy, mature auditory system, which could provide fundamental insight into further understanding how auditory signals are processed. These data show that *Iba1*+ microglia ramifications, but not those of *GFAP*+ astrocytes, interact with *homer1*+ (putative glutamatergic) synapses in IC parenchyma, making the IC a prime model to understand the physiological role of microglia in neuronal processing that could be translated across the brain. Taking advantage of the specialised and functionally diverse sub-regions of IC, a greater number of such synapses in DCIC, an area known to receive a greater proportion of glutamatergic corticofugal contacts than other IC sub-regions were found, potentially suggesting that microglia are more involved in excitatory modulation. This chapter utilises a novel methodological approach to image analyses along with statistical cluster analyses as a way to classify numerous variables and their levels of correlations. This approach has enabled the identification of microglial-neuron interactions, that could not be uncovered by conventional approaches, and could be used as a framework for future researchers investigating other parts of the brain. The cluster analyses revealed two new types of *GAD67*+ neuron defined by the extent of *Iba1*+ microglial contacts onto their soma. These data contribute to the understanding of the role microglia play in 'normal' processing within sensory systems and propose hitherto unexplored avenues of investigation. Similar approaches in other brain areas may produce novel understandings of how microglia contribute to fundamental brain organisation.

3.4.1 – Significance of sub-regional differences

Some aspects of central sensory processing can be interpreted through triad models of organisation. Such models are based on observations that central sub-regions of sensory pathways are dominated primarily by i) ascending innervation producing brisk responses at short latencies to simple stimuli. Located adjacent are at least two regions with longer response latencies - one of which typically receives ii) a diversity of polymodal inputs, while the other is iii) primarily driven by descending, top down afferents (Review Singer (1977)). In the somatosensory system, these have been respectively termed the lemniscal, para-lemniscal and extra-lemniscal pathways (Yu *et al.*, 2006).

In IC, there is longstanding evidence for a triad model of organisation using a diversity of methodologies. These include electrophysiology (Syka *et al.*, 2000) , fMRI (Baumann *et al.*, 2011, De Martino *et al.*, 2013), histology (Faye-Lund and Osen, 1985), immunohistochemistry (Coote and Rees, 2008) and tract tracing of projections (for review of afferent and efferent inputs see Malmierca and Hackett (2010) and Schofield (2010)). The present study provides evidence that *Iba1*+ microglial processes, despite superficially appearing similar throughout IC (Figure 3.1&3.3), also exhibit profound differences between sub-regions (Figure 3.5).

Hafidi and Galifianakis (2003) demonstrated in the IC of gerbil, that *GFAP*+ astrocytes were present surrounding the borders, similar to Figure 3.1, but the marker S100 revealed astrocytes were indeed present throughout all sub regions of IC. This absence of *GFAP*+ labelling may not be indicative of absent astrocytes, but it does open the question to investigate differences in sub-regional astrocyte expression. Chapter 4 investigates differences in *GFAP*+ astrocyte morphology in IC in contrast to other brain regions. The fact that *Iba1*+ microglia present different morphologies across sub-regions still provides insight into transitions in subsequent environments, which may influence auditory processing. The greater density of *Iba1*+ microglial processes at *synaptophysin*+ and *homer1*+ synapses in DCIC indicates that microglia contribute to synaptic processing in IC. Cortical regions of IC exhibit much stronger novelty detection and stimulus specific adaptation than CNIC (Ayala and Malmierca, 2013). This may partly relate to the primary afferent drive to DCIC being descending corticofugal fibres (Herbert *et al.*, 1991, Winer *et al.*, 1998, Bajo and Moore, 2005, Bajo *et al.*, 2006). Projections to DCIC from auditory cortex originate from glutamatergic (Feliciano and Potashner, 1995) pyramidal cells in layer V (Games and Winer, 1988, Winer and Prieto, 2001).

Corticofugal inputs to DCIC primarily target glutamatergic IC neurons (Nakamoto *et al.*, 2013), while large *GAD67*+ neurons in DCIC are a source of tectothalamic inhibition with shorter response latencies than other cells in DCIC (Geis and Borst, 2013). How the greater proportion of *Iba1*+ synapses in DCIC influences auditory processing is unknown, but one might suggest on the basis of greater density of *synaptophysin* labelling in DCIC, that there are a greater number of synapses *per se*. Certainly the DCIC receives a greater diversity of inputs than CNIC, including from auditory cortex, the contralateral IC (Orton *et al.*, 2016), and ascending projections from the brainstem. However, the highly plastic nature of synaptic processing in DCIC leads to the speculation that *Iba1*+ microglial processes may actively contribute to and shape synaptic processing and plasticity therein. Evidence for microglial involvement in such processing has been described in other models, including synaptic stripping and removal of existing synapses (Trapp *et al.*, 2007), or sensing neuronal synaptic activity (Pocock and Kettenmann, 2007) in an activity dependent manner (Wake *et al.*, 2009, Tremblay *et al.*, 2010).

The latter may facilitate microglial influence over synaptic plasticity via modulation of glutamatergic (Hayashi *et al.*, 2006) or purinergic (Tsuda *et al.*, 2010) neurotransmission.

Corticofugal inputs to DCIC have been shown to play an essential role in auditory learning and plastic reweighting of cues (Bajo *et al.*, 2010, Keating *et al.*, 2013). These connections likely underlie elements of human adaptation in unilateral hearing loss (Kumpik and King, 2019), though molecular mechanisms for these observations are underexplored. Intriguingly, *homer1* has recently been shown to mediate behavioural plasticity in association with metabotropic glutamatergic synaptic plasticity in hippocampus (Wagner *et al.*, 2014, Clifton *et al.*, 2017, Gimse *et al.*, 2018). The presence of *Iba1*+ processes at *homer1*+ synapses suggests a microglial role in modulating synaptic function and plasticity in DCIC, potentially in a similar manner to that shown in other brain regions.

3.4.2 – Two novel clusters of GABAergic neurons

As the auditory pathway contains a large proportion of inhibitory neurons, with around a quarter of neurons being GABAergic (Oliver *et al.*, 1994, Merchán *et al.*, 2005), understanding their structure, function, and organisation is a fundamental question. Previous approaches to classifying *GAD67*+ neurons in IC have focused on soma size (Roberts and Ribak, 1987a, Roberts and Ribak, 1987b, Ono *et al.*, 2005) coupled with axo-somatic inputs (Ito *et al.*, 2009), perineuronal nets (Beebe *et al.*, 2016) or cytoplasmic calcium binding protein expression (Ouda and Syka, 2012, Engle *et al.*, 2014). The present analyses show that while there is merit to these approaches, other features of GABAergic sub-types exist. Indeed, *GAD67*+ cells can be classified into two distinct clusters based on the total amount of *Iba1*+ contacts onto their soma (Figure 3.8). That GABAergic neurons in IC can be defined based on *Iba1*+ inputs suggests that microglia are essential to the structure and function of IC processing in the mature, adult auditory system.

Receiver operating characteristic analyses revealed that the two clusters could be distinguished by the three variables that quantified different aspects of *Iba1*+ processes but not by the number of *Iba1*+ microglial cells abutting each *GAD67*+ neuron. This may reflect the highly motile and dynamic nature of microglial processes, even under quiescent conditions (Wake *et al.*, 2009). Other features of GABAergic neurons in IC, such as their discharge patterns and expression of associated ion channels also do not relate to soma size (Ono *et al.*, 2005). Interestingly, the two newly identified clusters of *GAD67*+ neurons did not differ in their relative proportion between the four sub-regions in IC. Future work may investigate the differing afferent neural inputs to and efferent target of these cells, to identify likely physiological and connectional differences between clusters and their relationship to GABAergic signalling in auditory processing.

3.4.3 – Technical Considerations

The use of primary antibodies in less studied species such as guinea pig can be challenging due to potential differences in epitopes and when not adequately controlled for, this may lead to spurious observations (Schonbrunn, 2014). This is particularly important when using exploratory approaches such as in the present study, to ensure all analyses are predicated on specific and selective labelling (Voskuil, 2017). Extensive control experiments were therefore conducted, excluding primary antibody only, secondary antibody only and both antibodies, as well as changing mounting media and solutions throughout optimisation of labelling, to ensure that analyses were based on true labelling.

The lack of *GFAP*+ astrocytes in IC parenchyma was surprising and necessitated numerous confirmatory experiments. However, in all cases, a lack of *GFAP*+ astrocytes in the parenchyma was found alongside extensive labelling in peri-vascular regions and the *glia limitans externa*, demonstrating consistency within and between cases. The lack of *GFAP*+ astrocytes in IC parenchyma does not exclude the possibility that astrocytes reside throughout IC. Indeed, a recent report employing *SR101* as a marker revealed a network of putative astrocytes throughout CNIC (Ghirardini *et al.*, 2018). However, there is some labelling of oligodendrocytes with this marker, which hampers interpretability in studies trying to selectively label astrocytes (Hill and Grutzendler, 2014). Functional differences between astrocytes in CNIC and the outer layers of DCIC and LCIC have been suggested previously via 3-chloropropanediol-induced lesions, which selectively destroyed the former but not the latter (Willis *et al.*, 2003, Willis *et al.*, 2004). The present study leads to the speculation of fundamental gliochemical and physiological differences that may relate to the sub-region specific roles astrocytes and microglia play in their local milieu (Lawson *et al.*, 1990, Olah *et al.*, 2011). Sub-regional differences in *GAD67*+ neurons in the present study suggest that GABAergic and glycinergic signalling released from and received by glial cells may also exhibit such variations throughout IC and perhaps in other structures.

With image analyses, there are inherent problems with using algorithms to threshold immunohistochemical labelling such as a potential loss of data. However, by thresholding the labelling to binary images allows the consistent comparison of the markers across all imaged sections, and also enables the removal of false positive labelling due to the imperfect nature of immunohistochemical labelling. Therefore, this approach is a more reliable and replicable method to comparing specific markers for analysis.

Colocalisation of *synaptophysin* with *Iba1* and *homer1* does not guarantee that this labelling is representative of neuron-neuron chemical synapses. *Homer1* has been shown to localize with metabotropic glutamate receptors on astrocytes (Buscemi *et al.*, 2017). Due to the absence of parenchymal *GFAP* labelling in the present study, one can exclude these astrocytes as potential loci of *homer1*+ labelling, but one cannot rule out non-*GFAP* expressing astrocytes. As astrocytes are known to interact at synapses, this would not exclude the possibility of functional neuron-neuron chemical synapses being identified using this approach. However, the strong weight of probability is that many of the observed loci of colocalisation between *synaptophysin*, *Iba1*, and *homer1* are chemical synapses between neurons, closely abutted by microglial processes. To definitively confirm that *Iba1*+ microglia are interacting with neurons and synapses would need transmission electron microscopy, but the fact that they are located adjacent to the somata or in the same anatomical position, which cannot discredit that they share the same microenvironment.

3.4.4 – Chapter conclusions

There is a wealth of literature that has explored the electrophysiological nature of neurons in sensory systems, but our knowledge of glial cells lags far behind. Based on this research, future work could employ patch-clamp electrophysiology on isolated sections of IC to determine the cellular characteristics of microglia to identify physiological differences between sub types. This Chapter shows that *Iba1*+ microglia, but not *GFAP*+ astrocytes, colocalise at synapses throughout IC, with a greater number in DCIC, a sub-region specialised to mediate top-down plasticity. This finding highlights the role for microglia in mediating different aspects of fundamental auditory processes. Furthermore, two new clusters of *GAD67*+ neurons were discovered which can be distinguished based on the total amount of *Iba1*+ contacts they receive. These data further highlight the fundamental role microglia play in the organisation and function of sensory systems and by future researchers implementing the novel methodology in this Chapter, they could identify more diverse roles for microglia elsewhere in the brain.

Chapter 4 – Increased labelling of astrocytic *GFAP*+ in the ageing TgF344-AD rat inferior colliculus is similar to CA3 in hippocampus

4.1 – Introduction

4.1.1–Importance of investigating Alzheimer's disease

Classic hallmarks associated with the progression of AD include cerebral amyloid angiopathy, the development of parenchymal amyloid plaques, hyperphosphorylated tau protein associated neurofibrillary tangle formation, an upregulated chronic inflammatory mediated glial response, synaptic and neuronal loss and ultimately cognitive disturbances (Serrano-Pozo *et al.*, 2011). In a clinical diagnosis, symptoms are thought to appear after a long prodromal stage (Amieva *et al.*, 2008), highlighting the importance of understanding the early mechanisms leading to AD. A symptom commonly associated with AD is the loss of episodic memory, which is predominantly associated with processing in the hippocampus (Tulving and Markowitsch, 1998). Consequently, the hippocampus is the most common locus in AD studies and has been characterised to undergo 'classic' neuropathological hallmarks of AD, including neuronal loss and gliosis (Amenta *et al.*, 1998, Paduraríu *et al.*, 2012, Navarro *et al.*, 2018). Magnetic resonance imaging of AD patient brains has revealed that the hippocampus demonstrates a large reduction in grey matter volume (Kesslak *et al.*, 1991). Histological analysis has also uncovered in CA1 and CA3 regions of hippocampus, a reduction in neuronal density in AD patients compared to healthy controls (Paduraríu *et al.*, 2012). In addition, numerous studies have characterised age-dependent astrocyte and microglial responses in the hippocampus of transgenic mouse models of AD (Irizarry *et al.*, 1997, Girard *et al.*, 2014) as well as human post-mortem tissue (Griffin *et al.*, 1989, Simpson *et al.*, 2010).

4.1.2 – Hearing loss is associated with early-onset dementia

In humans, increasing levels of hearing loss have been correlated with an increased susceptibility to developing all-cause dementia (Lin *et al.*, 2011b). The manifestation of dementia has multiple components, both non-modifiable such as genetic predispositions (including the expression of mutant human familial genes), and modifiable risk factors that contribute to the development. Numerous studies have uncovered that certain modifiable factors including obesity (Kivipelto *et al.*, 2005), smoking (Zhong *et al.*, 2015), alcohol consumption (Sabia *et al.*, 2018) and a lack of exercise (Laurin *et al.*, 2001) all contribute to increased risk in the early development of dementia. Interestingly, research investigating the aforementioned modifiable risk factors, Livingston *et al.* (2017) has revealed that the risk factor that accounts for more of the variance than any other single, modifiable mid-life risk factor to increased predisposition of dementia, is hearing loss. This link between hearing loss and dementia has highlighted the importance of exploring potential mechanisms in the auditory pathway that are involved/contribute to the development of dementia.

Case-control studies have revealed that age-related hearing loss is associated with a premature development of cognitive dysfunction (Uchida *et al.*, 2019). Cognitive behavioural tests have uncovered a link between hearing loss and cognitive dysfunction in the C57BL/6 mouse model (Park *et al.*, 2016). In addition, anatomical links have correlated that a loss of hair cells precedes a consequent loss of auditory nerve fibres (Hequembourg and Liberman, 2001) and as a result, the central auditory system has been found to compensate by increasing the gain of ascending signals (Salvi *et al.*, 2017). The C57BL/6 mouse model demonstrates early-onset hair cell loss correlating with a decrease in principal neurons in the CNIC and a substantial decrease in synaptic density (Kazee *et al.*, 1995).

Atrophy of grey matter volume is prominent within basal temporal lobe, prefrontal cortex and the hippocampus (Salat *et al.*, 2011). This link with hearing loss however, has uncovered a need for understanding age-related changes within the central auditory pathway that may link central auditory dysfunction to increased dementia risk. The IC is an integral nucleus in the central auditory pathway, that demonstrates mechanistic deterioration associated with age-related hearing loss (Willott, 1986, Kazee *et al.*, 1995, Palmer and Berger, 2018), and also, is the most metabolically active region in the brain (Sokoloff *et al.*, 1977b).

4.1.3 – Neuronal loss and gliosis are critical components in Alzheimer's disease

Gliosis and neuronal loss are fundamental hallmarks in the development of human AD. Microglia and astrocytes are the two main cell types that constitute the glial response. Microglia are resident immune cells present throughout the brain and constitute approximately 10% of all cells (van Rossum and Hanisch, 2004, Kettenmann *et al.*, 2011, Nayak *et al.*, 2014). Depending on the brain region, microglia demonstrate varying functions and are essential in developing neural circuits and related plasticity (Salter and Stevens, 2017). Chronic activation of microglia is considered to exacerbate the symptoms of AD (Solito and Sastre, 2012), but the nature of this activation is unclear. Astrocytes are the most abundant cell type in the brain and are involved in a large repertoire of roles, including regulating neuroinflammation and active inter-cellular signalling (Sofroniew and Vinters, 2010). As a result of their range of functions, the particular role of astrocytes in AD is debated. Neuronal loss is a recognised outcome of AD, following deposition of Aβ peptides and subsequent Aβ plaques (Hardy and Higgins, 1992), yet the exact mechanical pathophysiology preluding this loss is currently unclear (De Strooper and Karran, 2016).

The measurement of anatomical age-dependent cellular changes throughout the development of AD in humans would be insightful in understanding the region of brain and specific mechanisms that cause morbidity. However, there are no techniques that enable age-dependent observations of cell densities in living humans. Using rodents to better understand age-dependent AD progression is an achievable alternative. Animals such as rats are appropriate alternatives, due to the similar conserved phylogeny seen in the genetics that code for almost all cellular processes, which are conserved between species (Gibbs *et al.*, 2004)

An integral aspect of familial AD in humans is the progressive increase in insoluble Aβ, caused by a mutation in amyloid precursor proteins (O'Brien and Wong, 2011). In addition, a mutation of the PSEN1 gene causes the abnormal production of presenilin 1 proteins, which results in an inability to cleave amyloid precursor proteins into soluble derivatives (De Strooper, 2007). The Tg rat model has been developed to analyse changes in AD, via expression of the human amyloid precursor protein Swedish mutation and presenilin 1 genes mutations (Cohen *et al.*, 2013) each of which independently lead to familial AD in humans.

Another interesting feature of the Fischer 344 rat model is the early development of presbycusis, which is appears at 12-months of age (Bielefeld *et al.*, 2008), making this a potentially useful model to investigate age-related hearing loss. The TgF344-AD rat therefore affords the opportunity to investigate potential interactions between age-related hearing loss with activity of mutant human genes that lead to the development of AD. The Tg rat model has been shown to follow similar age-dependent AD development to humans, by demonstrating an active glial response, formation of insoluble Aβ fibrils that comprise extracellular plaques, further development of aggregated tau proteins, subsequent neuronal loss and cognitive disturbances (Cohen *et al.*, 2013). Collectively, the parameters of this model suit the investigation into cellular changes caused by the human familial AD genes and the effects of presbycusis.

4.1.4 – Aims of this Chapter

This Chapter aims to uncover if sub regions of IC (CNIC, DCIC, and LCIC) undergo age-dependent glial adaptations and neuronal loss in the Tg model of AD, and how this compared to other regions of the brain. The time points included in this Chapter were 6-month (~18 years old human), 12-month (~30 years old human) and 18-month (~45 years old human) rats (Andreollo *et al.*, 2012). These time points are important because humans with either familial AD gene mutation would have developed AD by this point (Noguchi et al 1993). Therefore these time points were used to measure age-dependent pathological mechanisms in line with the progression of human AD (Langa and Levine, 2014), to identify if certain regions of the brain demonstrate more pronounced age-dependent glial responses under the pressure of the mutant human familial AD genes. The CA3 region of hippocampus was targeted in addition to the IC as this region has been identified to undergo neuronal loss in AD patients (Padurariu *et al.*, 2012) and profound *GFAP* labelling in 3- and 6-month TgCRND8 mice (Ugolini *et al.*, 2018). Furthermore, the striatum has been investigated due to it demonstrating substantially different astrocyte anatomical and physiological properties to hippocampus (Chai *et al.*, 2017). Finally, white matter tract regions including the corpus callosum and fimbria were used, as white matter varies substantially from grey matter in anatomy and physiology and microglia have been observed commensurate with Aβ deposits in AD (Uchihara *et al.*, 1995).

To identify if these regions underwent age-dependent neuronal loss, the marker *NeuN* was implemented as a neuronal specific nuclear antigen that marks neuronal cell bodies in comparison to other regions of the brain. The label *CD11b* was used in this Chapter as a marker of activated microglia, to identify if there was heterogenous expression across the brain regions as a result of age-dependent changes in the Tg model. In addition to Chapter 3, this Chapter utilised the marker *GFAP* to identify if *GFAP*+ astrocytes became present in the IC of the Tg model and if they are morphologically different in contrast to other regions of the brain.

4.2 – Methodology

4.2.1 – Tissue processing and immunohistochemical labelling

Animals were culled at the University of Manchester in accordance with Schedule 1 (table A section 4) of the Animals (Scientific Procedures) Act 1986. Animal tissue was processed using the methods outlined in Chapter 2. Parasagittal sections were immunohistochemically labelled to report *CD11b*+ activated microglia, *GFAP*+ reactive astrocytes and *NeuN*+ neurons (See Chapter 2.4.2 for antibody details) in CA3, striatum, corpus callosum, fimbria, CNIC, DCIC and LCIC. Sections were cut sequentially at 10μm using a cryostat (Leica CM3050s). Sections were taken from littermate wild type and Tg rats aged 6- (wild type n=4, Tg n=5), 12- (wild type n=10, Tg n=9) and 18-month-old (wild type n=10, Tg n=10). Sections were labelled for *CD11b* (a marker indicative of activated microglia), *GFAP* (intermediate filament protein of reactive astrocytes) and *NeuN* (nuclei of post mitotic mature neurons). Fluorescent labelling of *CD11b*, *GFAP* and *NeuN* (all 1:500 in PBS) were implemented using the methods outlined in Chapter 2.3.2. The Alexa Fluor 488 fluorescent goat anti-rabbit secondary antibody was used to bind to the *GFAP* antibody (1:250). The Alexa Fluor 555 goat anti mouse was used to bind to the *CD11b* and *NeuN* antibodies (both 1:250) on separate sections. *CD11b* and *GFAP* were double labelled while *NeuN* was single labelled.

For chromogenic neuronal labelling, the sections were obtained using the methods outlined in Chapter 2.3. Sections were initially washed 3x5 minutes with PBS. The Sections were then incubated in a citrate 6.0pH antigen retrieval buffer for 20 minutes at 80ºC. The sections were then washed 3x3 minutes in PBS and blocked and permeabilised in 5% normal goat serum and 0.05% Triton X-100 in PBS for one hour at room temperature. After blocking, goat anti-mouse *NeuN* was added to blocking solution and incubated overnight at 4°C in a humidified chamber. The next day, sections were washed 3x5mins in PBS and then immersed in anti-mouse IgG (1:1000) for 1 hour at room temperature, then agitated with an Avidin-Biotin solution (Vector Labs ABC kit) for 30 minutes at room temperature to amplify labelling. Finally, the sections were developed using a Vector DAB peroxidase substrate kit for 10 minutes at room temperature.

4.2.2 – Image acquisition

Fluorescent confocal micrographs were taken using a Leica SP5 confocal microscope. Images were taken from around the lateral ventricle (CA3, striatum, fimbria and corpus callosum) and the IC (CNIC, DCIC and LCIC). The lasers were set up to detect the secondary antibody specific fluorophores and the optimisation procedure and methodology outlined in Chapter 2.5 was implemented to detect signals from secondary antibodies bound to *CD11b*, *GFAP* and *NeuN* respectively. Images from the microscope were taken using the wide-stage function that enabled imaging of the whole IC and desired sub regions around the lateral ventricle in x, y & z dimensions. All images that were quantified were taken using the 40x objective (NA=1.25) and the pixel sizes are x & y=0.7583µm and z=3.8µm across slices. These parameters were optimised to sample a wide enough region to cover all sub-regions. Acquisition parameters were kept the same for all sections, to enable fair between-groups comparisons.

4.2.3 – Image analyses

Methods for acquisition of exported images is outlined in Chapter 2.6. Images were stacked and presented as 2D maximum intensity projections to represent independent brain regions. Each label was acquired as individual monochrome images and a 303x455x10μm region of interest was outlined within each brain region. Regions of interest were utilised to compare labelling density as an indirect representation of cell number, in opposition to measuring whole area counts. This approach was used to consistently compare labelling across numerous sub-regions and develop an understanding of how the various factors influence cell type anatomy. Measurements taken from CA3 incorporated cells external to the principal cell layer. This specific size was used to cover a large enough, but comparable size across each brain region. 303x455x10μm regions of interest were pre-processed prior to analysis: i) contrast was enhanced by 0.005% (note that no specific pixel intensity density analyses were conducted, making this an appropriate method), ii) thresholding using the IsoData algorithm converted the labelling into binary images, iii) parameters in the analyse particles plugin were set to exclude labelling below 30μm^2 with no circularity parameters set. These methods produced cell counts and the percentage field of views for each positively labelled marker.

2D rendered maximum intensity projections of *GFAP*+ labelling from regions of interest in CA3, striatum and CNIC were used to analyse and compare astrocyte morphologies. These regions were selected due to the consistent level of *GFAP*+ cell bodies present that could be quantified. Five cells from each region of interest were selected and 2D Sholl analyses conducted, as this provided a representative sample of cell morphology for each brain region. Parameters of the Sholl analysis were set to measure intersections with process ramifications at 0.76μm equidistantly radiating concentric circles until the furthest intersection was met. This specific distance covered representative measurements of cell process branch points and junctions across brain regions. Sholl quantification in this Chapter included, i) the total number of intersections, ii) longest process span and iii) ramification density, as measurements of cell morphology.

Imaging of chromogenic *NeuN* labelled sections were taken using a 3D Histech Pannoramic 250 slide scanner. Chromogenic *NeuN* analysis was conducted using the 3dhistech CaseViewer software. To consistently and representatively count *NeuN*+ neurons and disregard false positives from cellular debris, manual cell counts were conducted for each *NeuN*+ cell in 303x455x10μm regions of interest in CA3, striatum, CNIC, LCIC and DCIC.

4.2.4 – Statistical analyses

Results from these analyses were recorded in Microsoft Excel and were plotted using Prism (GraphPad) and statistically analysed using SPSS (v24, IBM). For cell counts and percentage field of view, sample size (n) in the text represents individual animals and in the Sholl analyses represents individual cells. Significance was set to $p<0.05$ and determined using 3-factorial between groups ANOVA to measure the effects of brain region, age and genotype. *Post-hoc* Tukey HSD tests were undertaken where appropriate and effect sizes were determined by eta squared and partial eta squared analyses as appropriate. Effect sizes were employed to determine the validity of the significance found between completely different brain regions been contrasted. The effect sizes were used to quantify the strength of the relationship between factors, small effect sizes refer to a weak relationship (<0.01), medium that there is a good relationship (<0.09) and large indicates a strong relationship (>0.25). Weak relationships between factors infer that the probabilities derived from the tests have reduced validity. Significance between factors from *post-hoc* analyses displayed in figures are referred to as stars (*= P≤0.05; **= P≤0.005; ***= P≤0.001; **** P≤0.0001). The alpha level was set at P<0.05 for all statistical comparisons.

4.3 – Results

4.3.1 – No observed age-dependent neuronal loss in TgF344-AD model

Region of interest analysis was implemented over whole area counts as a more representative way to compare brain regions and understand the distributions of cells. Brains from all groups (wild type and Tg) were analysed in terms of cell counts and percentage field of view analyses. *NeuN*+ cell counts revealed no trend towards varying cell counts across all categories within brain regions (Figure 4.1). Cell counts demonstrated that 6-month-old wild type striatum had the highest number of *NeuN*+ cells, reaching 171±30 per 0.138mm^2. Fimbria had the lowest number of cells, with 1 cell per 0.138mm^2 in the 12-month-old Tg category, indicative of negligible *NeuN*+ labelling.

Percentage field of view analyses demonstrated similar trends across categories to cell counts (Figure 4.2), however, the CA3 region demonstrated much higher levels of *NeuN*+ labelling reaching 21.42% per 0.138mm^2 in the 6-month-old wild type category. As a result of the densely packed neurons found in CA3, percentage field of view was a better measurement to quantify fluorescent *NeuN*+ labelling. *NeuN* labelling in fimbria covered 0.08% per 0.138mm^2, which was the lowest across the 12-month-old wild type groups.

Closer inspection of fluorescent *NeuN*+ labelling revealed noticeable increases in *NeuN*+ labelling between 12 and 18 months Tg groups that did not resemble neuronal morphology (Figure 4.3). Labelling in Figure 4.3E resembled *NeuN*+ neuronal cell bodies (Panzanelli *et al.*, 2007), compared to labelling in Figure 4.3F, which looks like damaged neurons with surrounding cellular debris as observed by Streit and Kreutzberg (1988). By implementing fluorescent labelling made it impossible to disentangle neurons from cellular debris. Therefore, to better represent the number of neurons chromogenic *NeuN* labelling was implemented and subjected to manual cell counts.

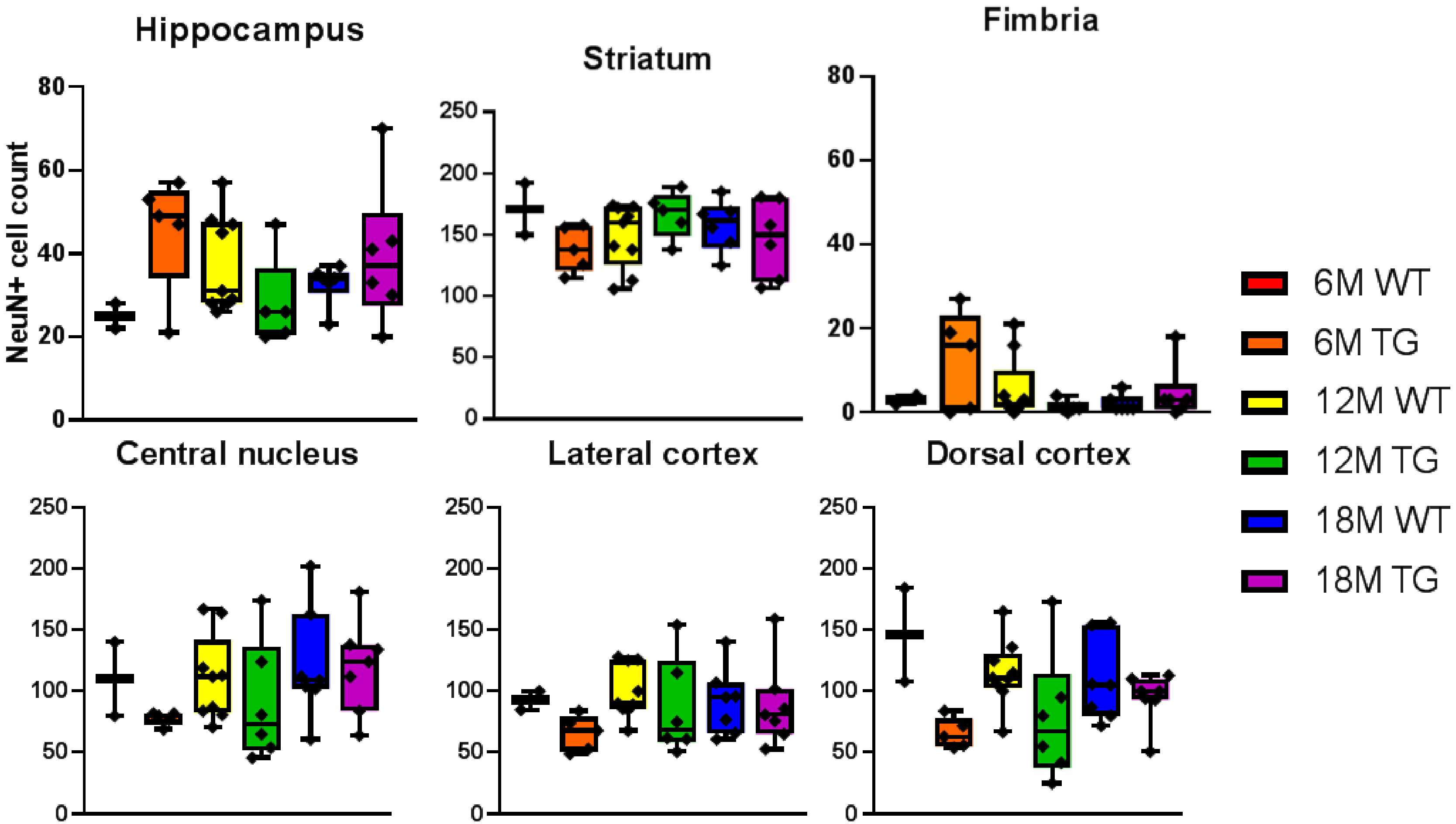

Figure 4.1. Boxplots displaying *NeuN*+ cell counts from 303x455x10μm regions of interest**.** Striatum had consistently the highest density of *NeuN*+ cells. The 6-month Tg group has the highest number of neurons in CA3 hippocampus. The white matter tract region fimbria had low levels of labelling throughout. All regions of IC demonstrated similar trends in neuronal numbers across groups. There was no observed *NeuN*+ neuronal loss up to 18-months of age in the Tg model using this approach – however, this could be as a result of non-specific labelling of cellular debris.

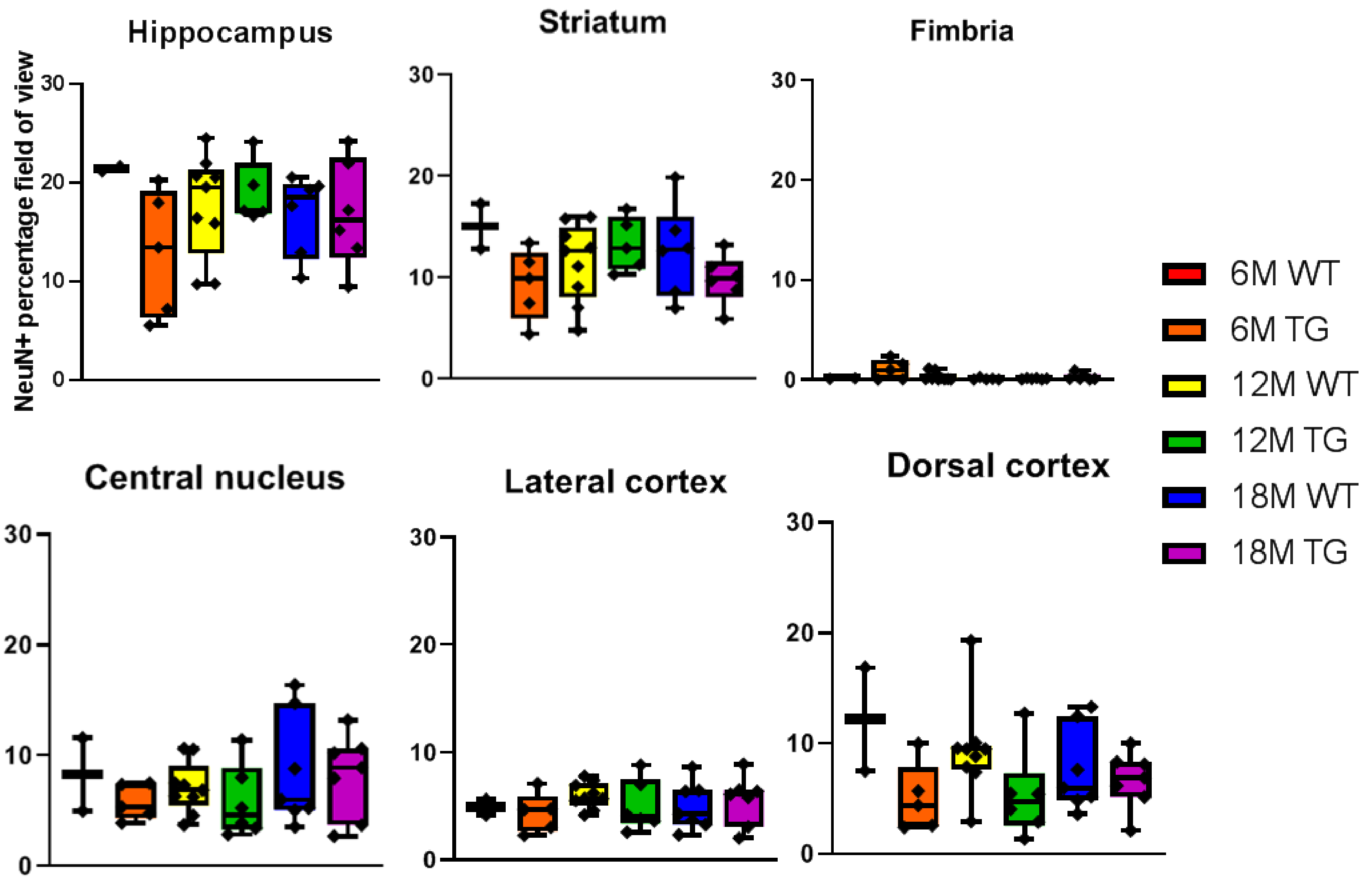

Figure 4.2. Boxplots displaying the percentage field of view covered by *NeuN*+ cells across 303x455x10µm regions of interest. CA3 had the overall highest neuronal labelling. Similar to cell counts, fimbria demonstrated negligible labelling across all groups, with the most labelling in the 6-month Tg group reaching 1%. All IC regions displayed similar trends across all categories. There was no observed significant change in *NeuN*+ labelling up to 18-months of age in the Tg model.

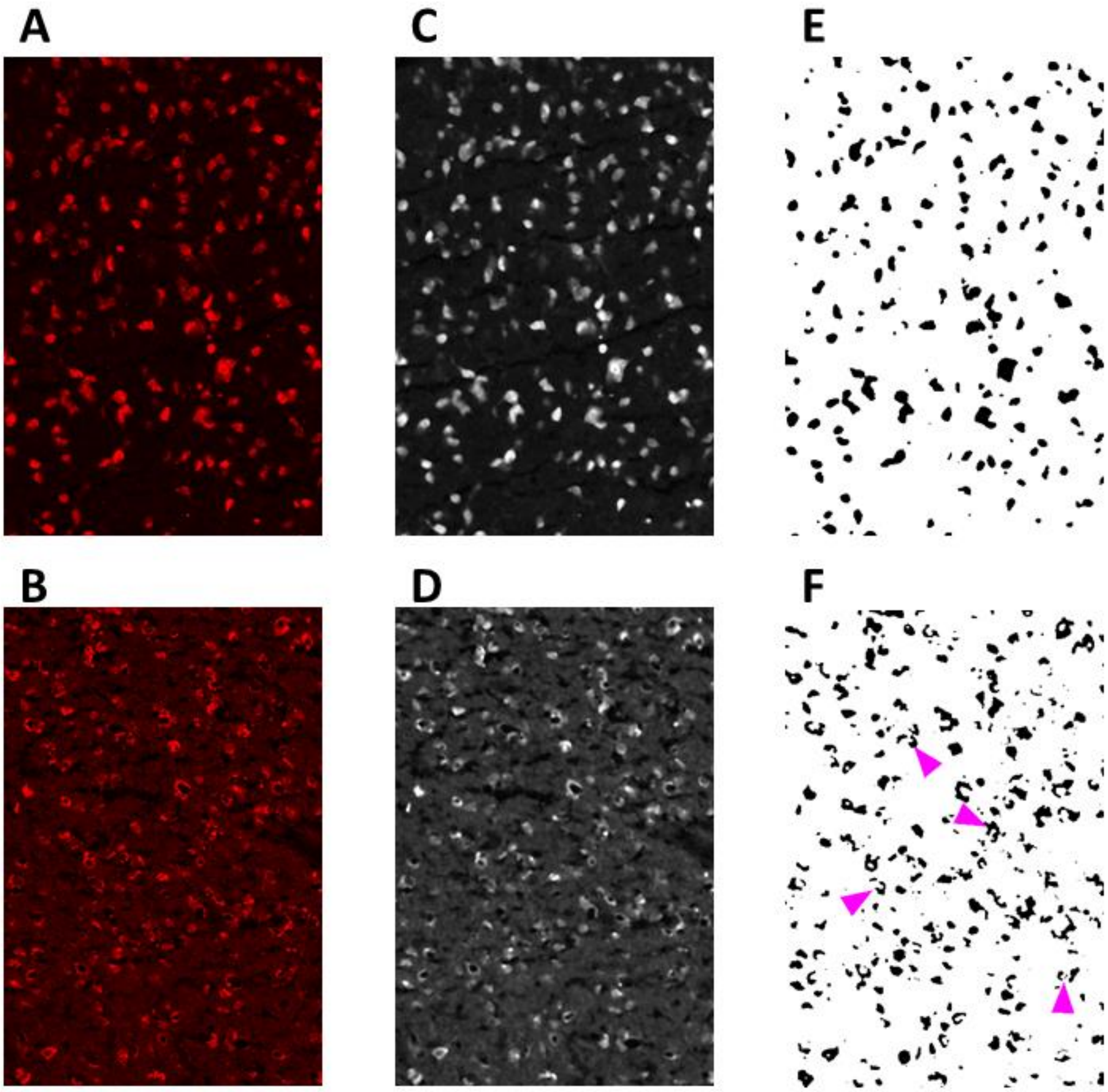

Figure 4.3. Example micrographs of *NeuN*+ labelling from CNIC. (A)**,** 12-month wild type. (B) 18-month Tg. (C&D)**,** median filtered monochrome examples of (A)&(B). (E&F)**,** masks of cells counted after (B)&(D) were thresholded using the IsoData algorithm. Of note, differences in neuronal morphology between wild-type (E) and Tg (F) was evident. Labelling in (F) resembles damaged neurons and the surrounding labelling is similar to the cellular debris described by Streit and Kreutzberg (1988) (magenta arrows). To compensate for this, parameters in the analyse particles plugin were set to exclude labelling under 30μm^2. This did not compensate for the increases observed at the 18-month time point, so chromogenic labelling was implemented to enable differentiation of neurons from debris (Figure 4.4).

A drawback to fluorescent labelling is that it merged debris with cell bodies and resulted in unrepresentative images. To combat this, chromogenic immunohistochemical labelling of *NeuN* was implemented and this enabled the differentiation of debris from cell bodies. To best encapsulate the number of neurons present, the positive cells were subjected to manual cell counts. 303x455x10μm regions of interest from CA3, striatum, CNIC, LCIC and DCIC (excluding fimbria due to negligible labelling) at 6- (wild type n=3, Tg n=8), 12- (wild type n=9, Tg n=12) and 18-month-old (wild type n=12, Tg n=11) rats were analysed. Figure 4.4 displays an example micrograph taken from around the lateral ventricle and demonstrates the demarcation of bounding regions of interest in CA3 and striatum. The same process was used to isolate sub regions of IC for cell counts.

Cell counts revealed that the highest density of *NeuN*+ cells were in the CNIC and striatum across all categories with the maximum in the 12-month CNIC Tg group, which contained a mean of 215 neurons per 0.138mm^2 (Figure 4.5). The CA3 had consistently lower counts than the other regions reaching a maximum of 79 neurons per 0.138mm^2 in the 6-month wild type group, although this was due to the inherent different anatomical distribution of neurons in CA3.

Similar to fluorescent *NeuN*+ cell counts and percentage field of view, chromogenic cell counts revealed that age and genotype did not affect cell density. These results confirm that up to 18-months in the Tg model, that there is no *NeuN*+ cell loss observed across the CA3, striatum, CNIC, DCIC and LCIC between 6- and 18-months of age.

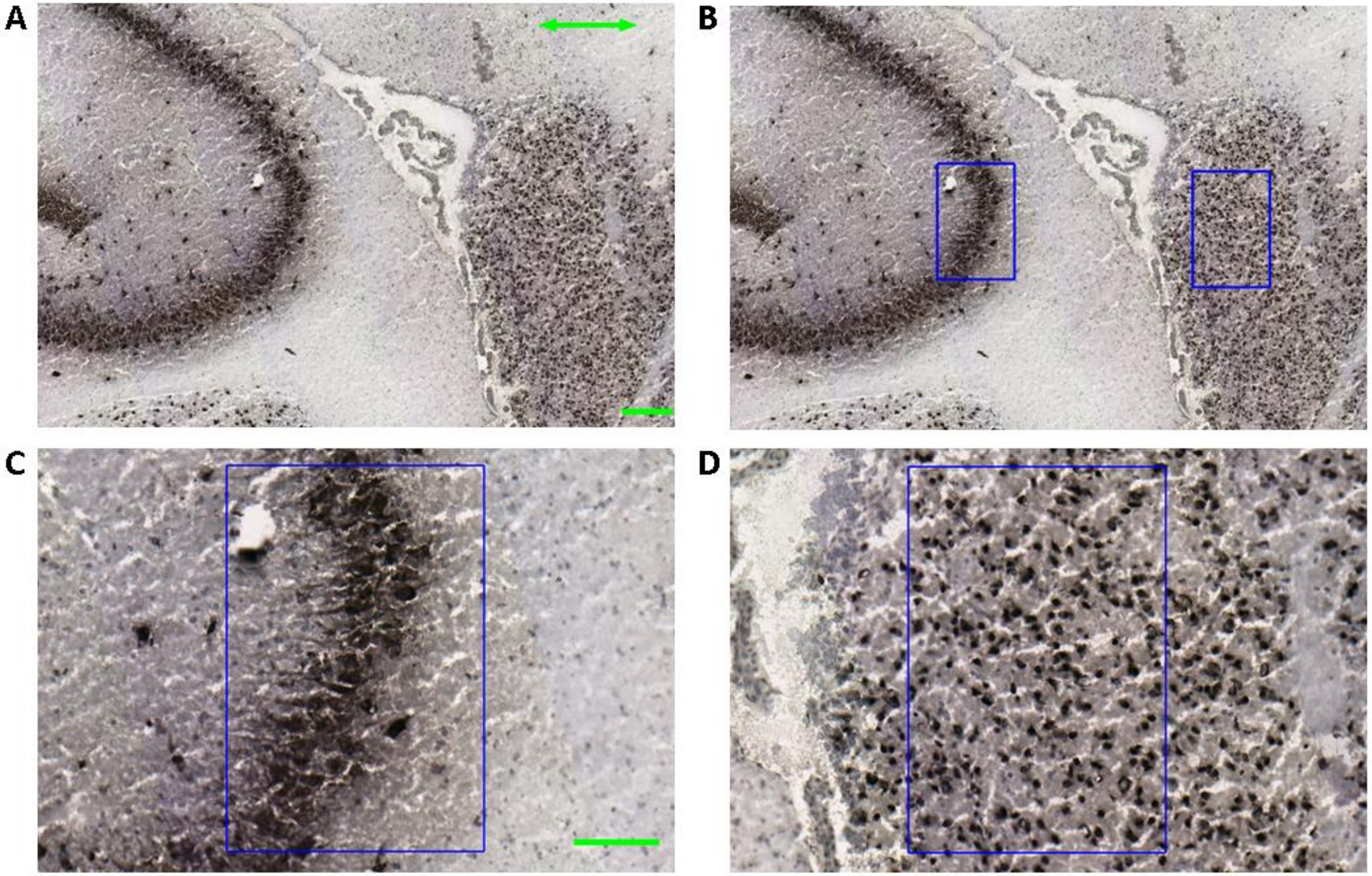

Figure 4.4. (A) Representative micrograph taken of chromogenic *NeuN*+ labelling from around the lateral ventricle. 5x magnification. Scale bar 200µm in (A) same in (B). Rostral (left), caudal (right), same orientation across all images. (B) 303x455x10µm regions of interest demarked by blue rectangles as examples of bounding boxes. Neurons within the blue boxes, CA3 hippocampus (left) and striatum (right), were subjected to manual cell counts. (C) Higher magnification (14x) example of CA3 hippocampus. Notice the difference to fluorescent *NeuN*+ labelling in Figure 4.3C. Scale bar 100µm in (C) same in (D). (D) example of striatum. By implementing chromogenic labelling and manual cell counts enabled the discrimination of neurons from debris.

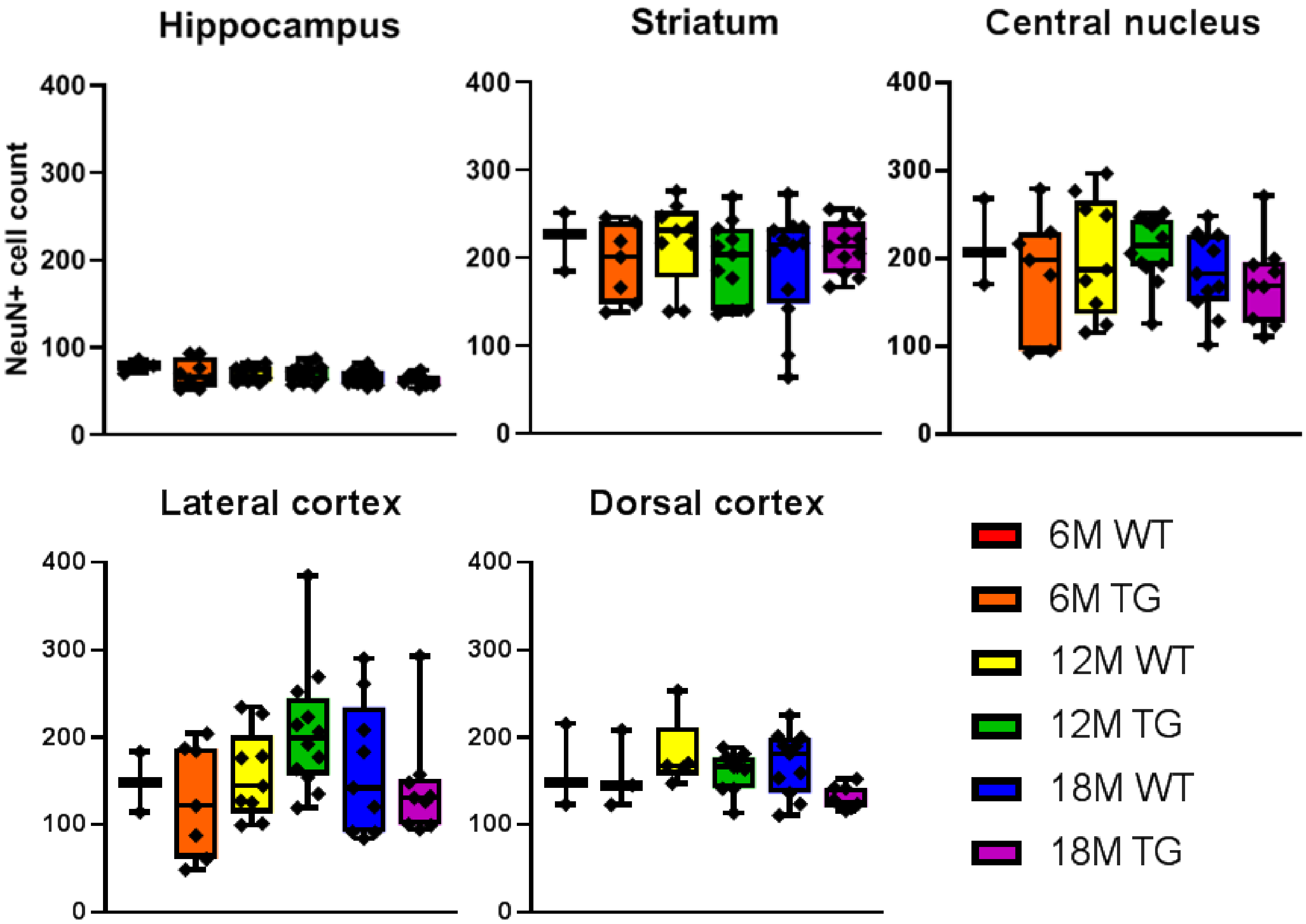

Figure 4.5. Boxplots displaying chromogenic *NeuN+* cell counts from 303x455x10μm regions of interest. The highest number of neurons were found in the striatum. 6-month wild type had the highest number of cells in CA3 hippocampus. Similar to fluorescent labelling, all regions of IC demonstrated similar trends in neuronal counts. There was no neuronal loss observed up to 18-months old in the Tg model.

4.3.2 – *CD11b*+ and *GFAP*+ labelling is elevated at 12- and 18-months in the TgF344-AD model

The level of *CD11b*+ and *GFAP*+ labelling was investigated comparing age-related changes in wild type and Tg rats. Example regions of interest are demarked in Figure 4.6. Labelling from these regions of interest were used throughout the whole Chapter. Micrographs were taken around the lateral ventricle adjacent to the hippocampus and striatum labelled with *CD11b* and *GFAP* antibodies (Figure 4.7). All sections showed a high density of *GFAP*+ labelling of the *glia-limitans externa* border surrounding the ventricle, which demonstrated increased density of labelling adjacent to the striatum in Tg 12- and 18-month sections (Figure 4.7D&F respectively). Myelinated white matter fibre tracts adjacent to the somatosensory cortex (dorsal to ventricle) and CA3 demonstrated elevated numbers of *CD11b*+ labelled cells in contrast to the grey matter regions in the 12- and 18-months-old Tg sections. Striatum was devoid of *CD11b*+ cells across all sections. In contrast, CA3 *CD11b*+ labelled cells became apparent in the 18-month wild-type and 12-month and 18-month Tg groups. *GFAP*+ labelled cells were visible in CA3 and striatum throughout all sections. Fimbria and corpus callosum demonstrated sparse *GFAP*+ labelling throughout. The most densely labelled *GFAP*+ regions were observed in the 12-month and 18-month Tg CA3 and striatum (Figure 4.7D&F respectively). *CD11b*+ and *GFAP*+ labelled cells increased in density in the aged Tg groups.

Micrographs were also taken of the IC (Figure 4.8). A similar *GFAP*+ glial response detected around the lateral ventricle was observed encompassing the *glia-limitans externa* surrounding the dorsal border of the IC in Tg sections. *CD11b*+ labelled cells were minimal in the IC of the 6-month wild type group (Figure 4.8A) in contrast to all other groups, which demonstrated a higher density of *CD11b*+ labelling, with increased cell numbers in Tg groups. *GFAP*+ labelling was present throughout all sections. The Tg groups demonstrated a higher density of *GFAP*+ labelling in the neuropil than wild type, with a markedly higher number of cells in the centre of the 12- and 18-month groups (Figure 4.8D&F). Interestingly, glial labelling in IC, to some extent mirrored that observed in the CA3. To quantify glial responses in the IC, regions of interest outlining the CNIC, LCIC and DCIC were contrasted to the regions around the lateral ventricle outlined in Figure 4.6.

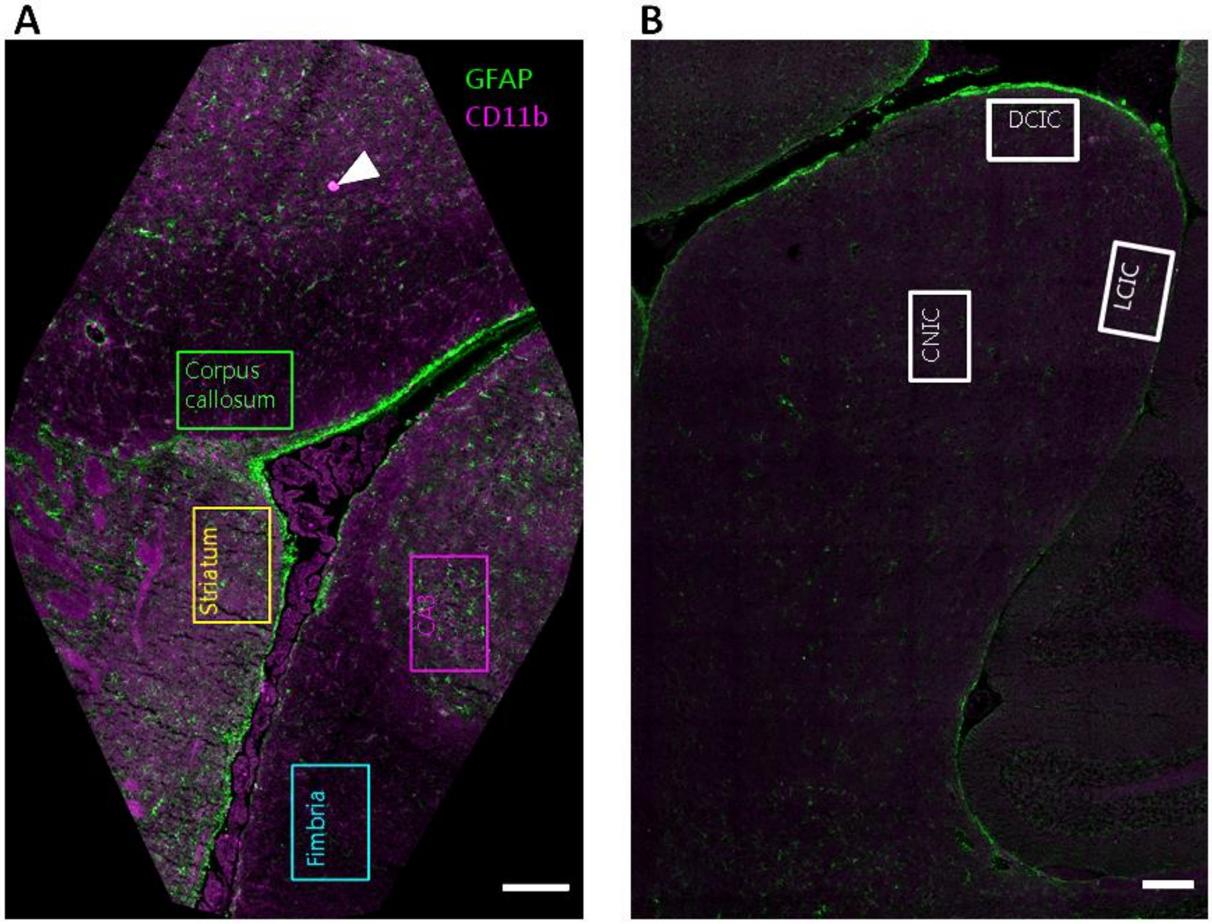

Figure 4.6. Example bounding 303x455x10µm regions of interest from each brain region that were used throughout the whole Chapter. Boxes in (A) represent regions from around the lateral ventricle, Green (corpus callosum), yellow (striatum), magenta (CA3 hippocampus), cyan (fimbria). Boxes in (B) represent regions from within the IC, white (DCIC), pink (CNIC and grey (LCIC). Scale bar 200µm in (A) and (B). White arrowhead in (A) points to putative artefact.

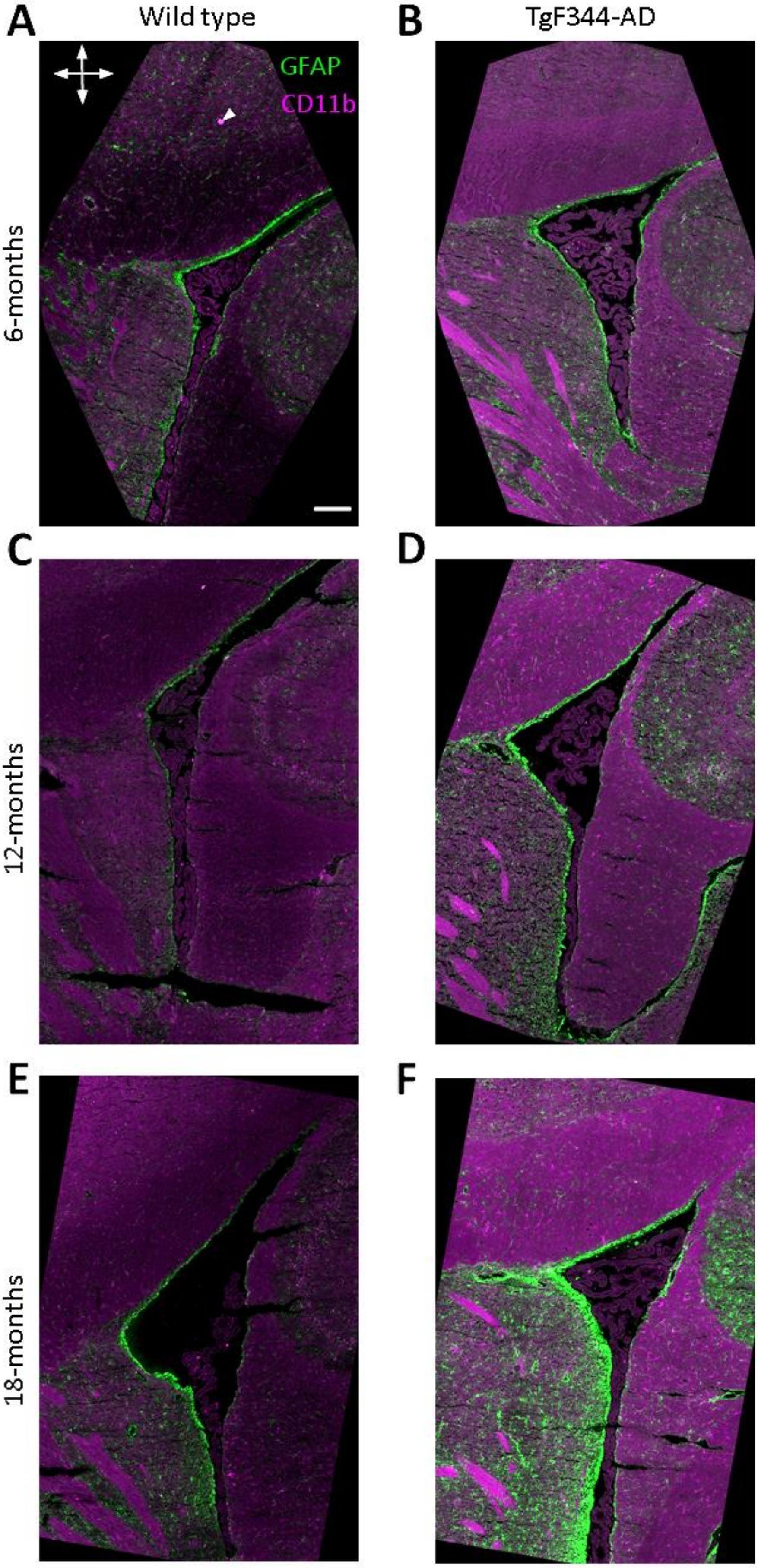
A
Wild type
B
TgF344-AD
GFAP
CD11b
6-months
C
D
12-months
E
F
18-months

Figure 4.7. Representative micrgraphs taken from around the lateral ventricle to quantify *CD11b*+ (magenta) and *GFAP*+ (green) labelling. 303x455x10µm *GFAP*+ and *CD11b*+ labelling in (A&C&E) wild type sections is noticably lower than in (B&D&F) Tg sections. Particularly notice the denser labelling in Tg 12- and 18-month groups. White arrowhead highlights an artifact in (A). Scale bar and axis in (A) 200µm; dorsal (up), ventral (down), rostral (right), caudal (left), applies to all panels. Specific regions were quantified across groups using the regions of interest demarked in Figure 4.6A.

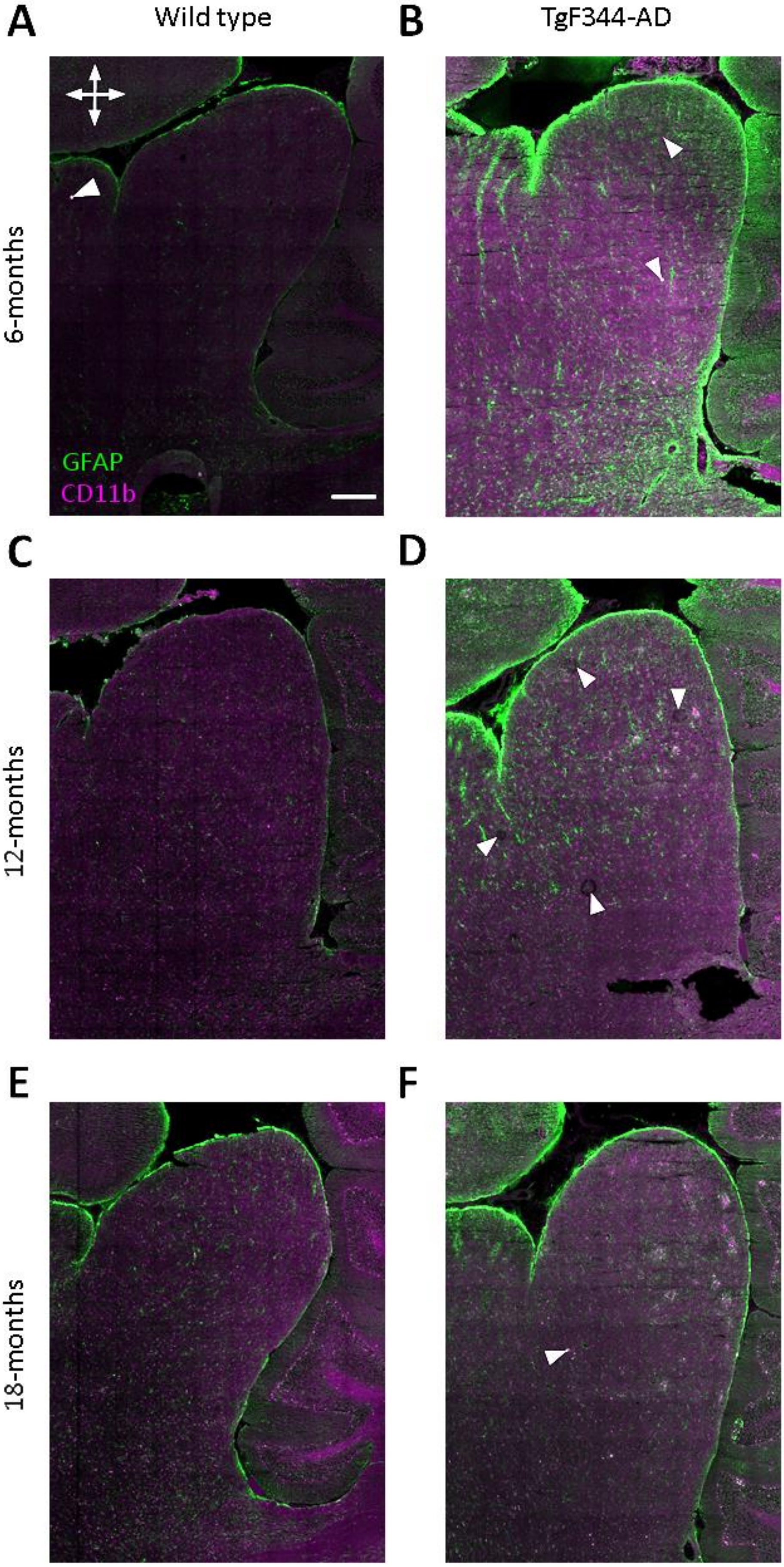
A
Wild type
B
TgF344-AD
6-months
GFAP
CD11b
C
D
12-months
E
F
18-months

Figure 4.8. Representative micrographs taken from the IC, summarising *CD11b*+ (magenta) and *GFAP*+ (green) labelling. Similar to the observed labelling in Figure 4.7, labelling in (A&C&E) wild type sections is noticeably lower than in (B&D&F) Tg sections. Particularly notice the denser labelling in the Tg groups. White arrowheads indicate putative artifacts. Scale bar in (A) 400µm scale bar applies to all panels and axis dorsal (up), ventral (down) rostral (left), caudal (right). Specific regions were quantified across groups using the regions of interest demarked in Figure 4.6A.

There was a higher level of *CD11b*+ and *GFAP*+ labelling in the Tg model, particularly from 6- to 12-months. Figure 4.9 demonstrates the increase in labelling observed from 6- to 12-months in the Tg groups CA3, fimbria, CNIC and DCIC. *CD11b*+ labelling substantially increased from 6- to 12-months in fimbria (Figure 4.9B&E respectively). There was also an increase in labelling in CA3, albeit less pronounced (Figure 4.9C&F). Oppositely, *GFAP*+ labelling in fimbria increased from 6- to 12-months (Figure 4.9B&E), but not as substantially as CA3 (Figure 4.9C&F). Notice, the increased size of *GFAP*+ cell ramifications from 6- to 12-months, this is quantified by Sholl analysis in section 4.4.5.

GFAP+ cell processes were larger and more ramified in CA3 than in fimbria, where they were less ramified, and had long axes, which is consistent with previous studies (Wolburg *et al.*, 2009). *GFAP*+ cells also increased in ramification density and soma size at 12-months. In the parenchyma of both CNIC and CA3 starting at 12-months, pockets of *GFAP*+ labelling increased in density with *CD11b*+ labelling (Figure 4.10) and resembled reactive gliosis surrounding putative amyloid plaques, similar to observations in studies of human post-morten tissue and other transgenic models (Orre *et al.*, 2013, Perez-Nievas and Serrano-Pozo, 2018, Sakakibara *et al.*, 2019). Labelling of both glial markers in IC demonstrated a similar increase in density from 6-months to 12-months. *GFAP*+ labelling also increased in density from 6- to 12-months and changed in morphology.

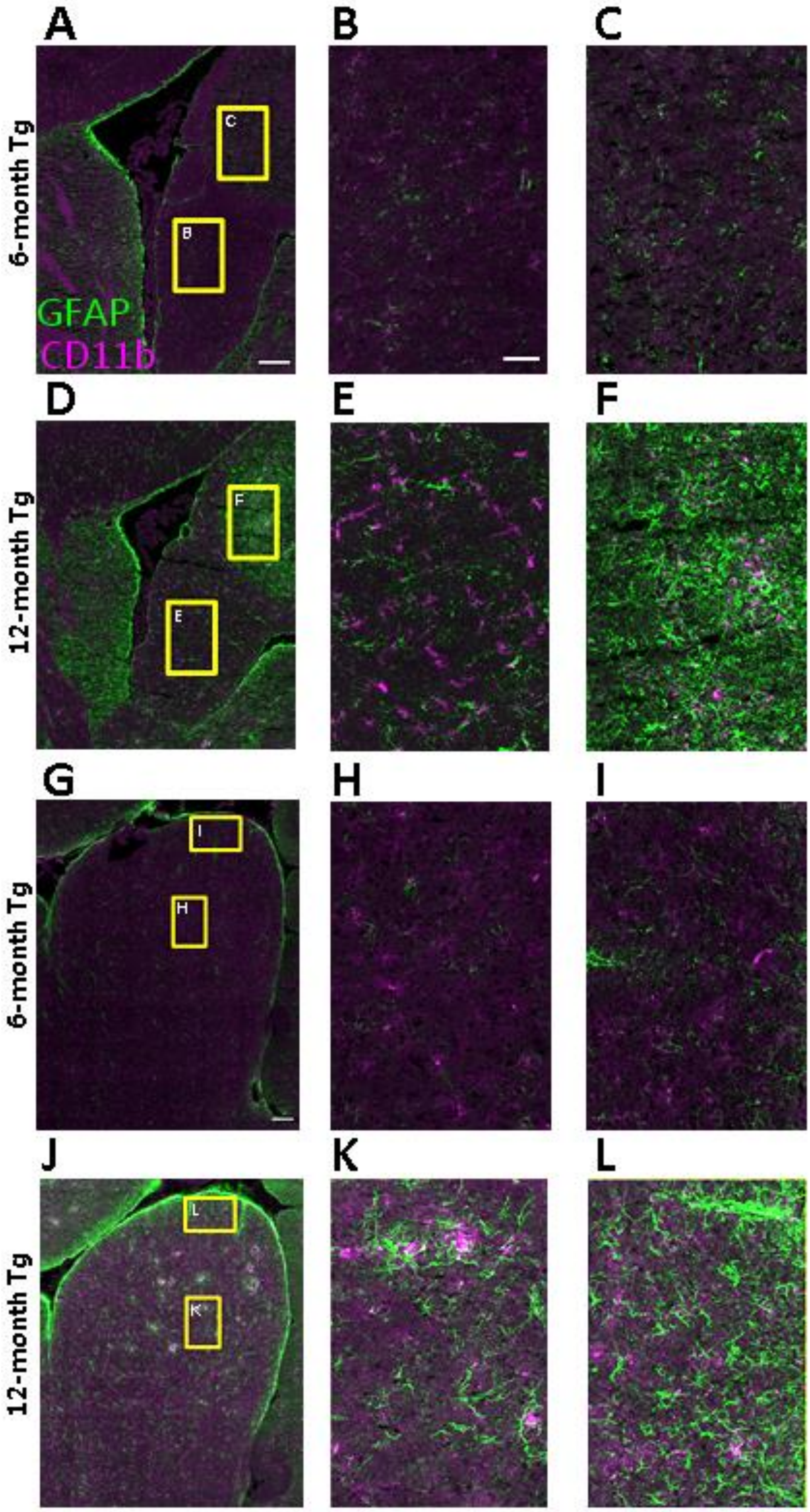
A
B
C
6-month Tg
C
B
GFAP
CD11b
D
E
F
12-month Tg
F
E
G
H
I
6-month Tg
I
H
J
K
L
12-month Tg
L
K

Figure 4.9. Micrographs contrasting *CD11b*+ activated microglia and *GFAP*+ reactive astrocytes in 6- and 12-month-old Tg sections. (A) 6-month-old Tg section around the lateral ventricle labelling the fimbria (B) and CA3 (C). (D) 12-month-old Tg section around the lateral ventricle labelling the fimbria (E) and CA3 (F). Scale bar 50µm. (G) 6-month-old Tg IC section, labelling CNIC (H) and DCIC (I). Scale bar 200µm. (L) 12-month-old Tg IC section, labelling CNIC (K) and DCIC (L). Both markers increase in density in the 12-month sections. Notice the localised pockets of increased *CD11b*+ and *GFAP*+ labelling resembling reactive gliosis (Kamphuis *et al.*, 2012, Rodriguez *et al.*, 2014). Scale bar in (A) 200µm applies to D, scale bar in G 200µm applies to J and scale bar in B 50µm applies to C, E, F, H, I, K and L.

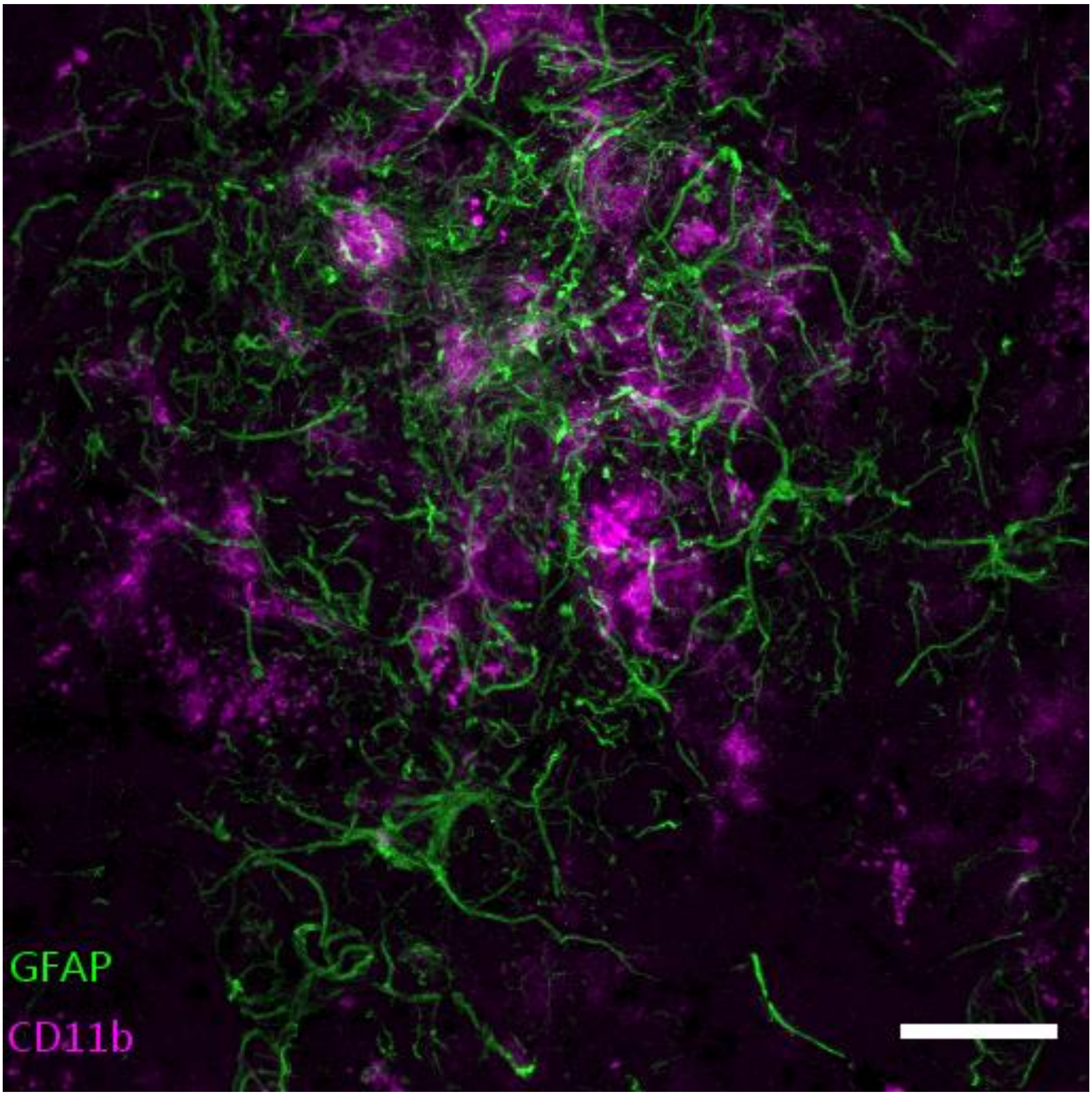

Figure 4.10 Maximum intensity projection of a confocal micrograph displaying reactive gliosis in CNIC. *CD11b*+ activated microglia (magenta) and *GFAP*+ reactive astrocyte (green) in a 12-month-old Tg IC section. Scale bar 20μm. This response appears at different points across the parenchyma from 12-months in the Tg rat model CNIC similar to hippocampus. The labelling appears to have similar anatomical charcteristics to reactive gliosis observed responding to amyloidosis seen in hippocampus (Sakakibara *et al*., 2019).

4.3.3 – *CD11b*+ microglial cell counts and percentage field of view increased in CA3 hippocampus

To investigate sub-region-specific differences in *CD11b*+ labelling, regions of interest were outlined, processed and analysed as in Figure 4.11. Figure 4.12 shows boxplots for every region of interest. The highest average number of *CD11b*+ cells were found in the 18-month-old Tg fimbria (mean=103, standard deviation±61 per 0.138mm^2) and corpus callosum (118±69). The lowest numbers were found in the 6-month Tg striatum (2±1). Cell counts in CA3 were highest in the 18-month Tg group (59±24) and lowest in 6-month Tg (6±7) and CNIC, LCIC and DCIC demonstrated similar numbers to each other.

A 3-factorial ANOVA of cell counts with brain region, age and genotype as factors identified no interactions (F(12,265) = 0.380, p = 0.970). A 2-factor ANOVA measuring age and genotype revealed that CA3 was the only region to demonstrate a two-way interaction (F(2,42) = 3.798, p=0.030). Partial eta squared uncovered a large effect size ($\eta p^2 > 0.25$) and *post-hoc* analysis revealed age differences between all categories (all p<0.001). However, 1-factor ANOVA of brain region (F(6,265) = 33.631, P = <0.001), age (F(2,265) = 5.651, P = 0.004) and genotype (F(1,265) = 9.634, P = 0.002) revealed independent effects on cell count and an eta squared demonstrated that the effect sizes were large (all $\eta p^2 > 0.25$). *Post-hoc* analyses via Tukey HSD tests showed fimbria and corpus callosum were different from all other regions (all p<0.001).

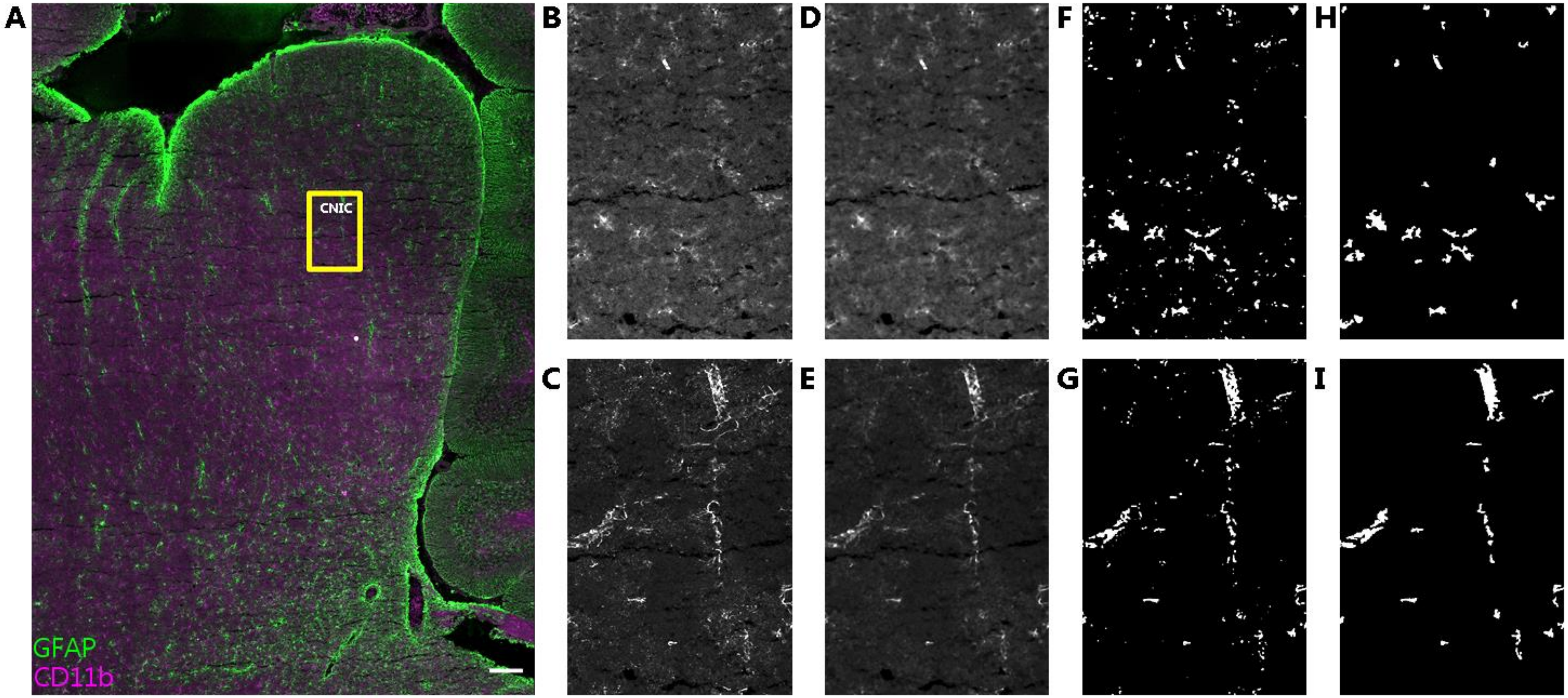

Figure 4.11. Micrographs demonstrating the methodology to process *CD11b*+ (magenta) and *GFAP*+ (green) labelling prior to cell count and percentage field of view analyses from a 6-month Tg section. (A) 6-month old Tg section from IC, yellow box outlines an example 303x455x10µm region of interest from the CNIC. (B&C) *CD11b*+ and *GFAP*+ labelling were isolated by splitting *CD11b*+ (B) and *GFAP*+ (C) into individual monochrome images. (D&E) Output from implementing a median filter to remove non-specific labelling. (F&G) Images threholded using the IsoData algorithm to binarise positive labelling. (H&I) Consequent masks of markers after setting parameters to exclude sizes under 30µm for the measurements.

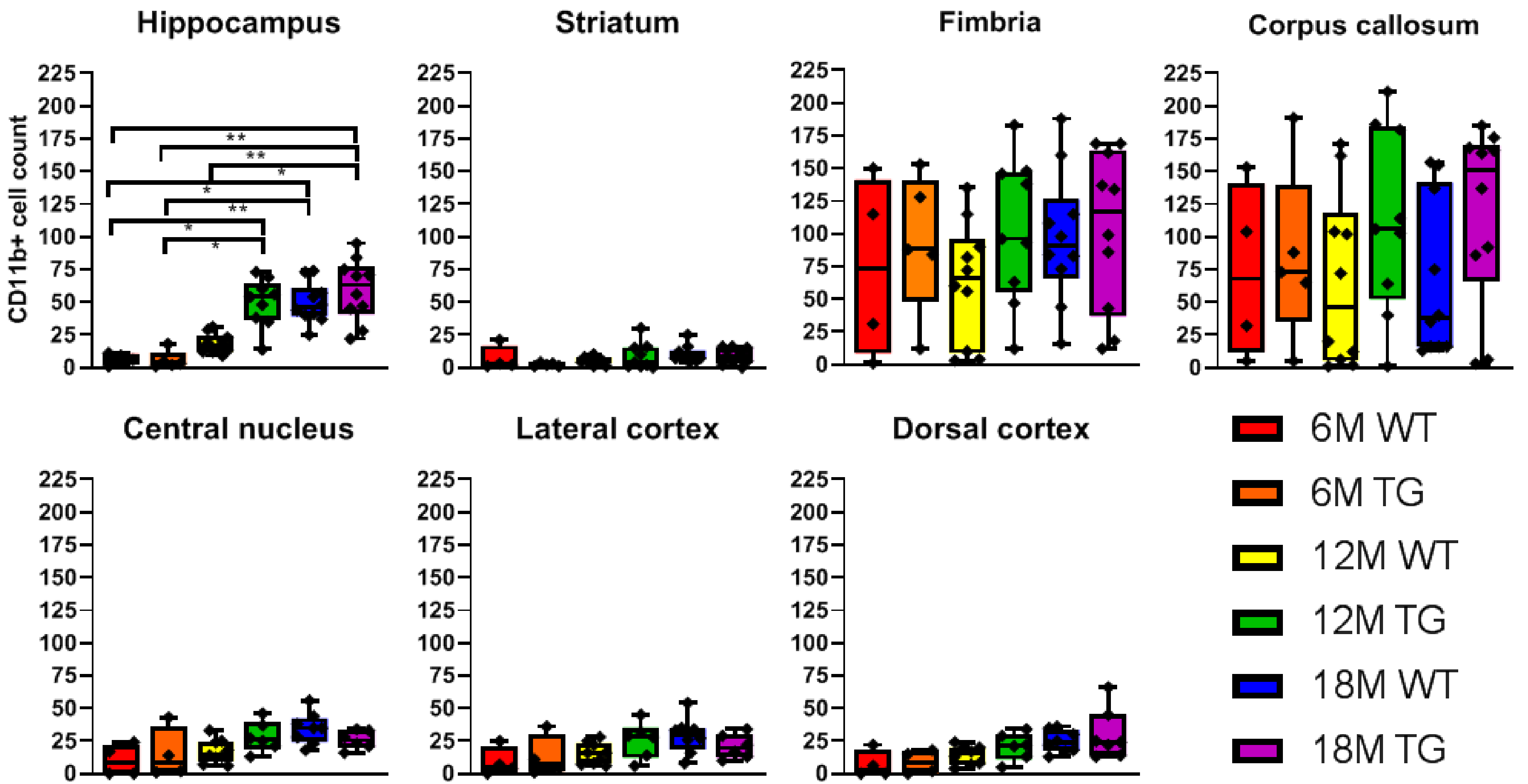

Figure 4.12. Boxplots displaying *CD11b*+ cell counts across 303x455x10μm regions of interest. CA3 hippocampus demonstrated age-dependent increases in the 12-month Tg, 18-month wild type and 18-month Tg groups, which were significantly higher than the other groups. Fimbria and corpus callosum showed the highest *CD11b*+ cell counts across all regions. CNIC flowed a similar trend to CA3, with the largest differences between 6- and 18-months, but these did not reach the criterion for significance. Striatum has the lowest *CD11b*+ labelling across all brain regions.

In addition to cell counts, percentage field of view analyses were used to measure *CD11b*+ labelling. Figure 4.13 illustrates boxplots for every region of interest. The highest percentage fields of view were found in the 18-month-old Tg fimbria (3.29%±2.65) and corpus callosum (3.55%±2.23) and the lowest in the 12-month wild type striatum (0.09%±0.07). CA3 and CNIC displayed similar trends in increased percentage field of view with age and genotype. LCIC and DCIC demonstrated similar percentage field of views across factors.

A 3-factorial ANOVA of percentage field of view contrasting brain region, age and genotype identified no interactions between factors (F(12,265) = 0.483, p = 0.924). Unlike cell counts, a 2-factor ANOVA of individual brain regions measuring age and genotype revealed that CA3 did not demonstrate a two-way interaction (F (2,42) = 2.067, p=0.139). Partial eta squared uncovered a large effect size ($\eta p^2 > 0.25$). However, a *post-hoc* analysis did reveal age differences between all categories (all p<0.001). However, similar to cell counts, 1-factor ANOVA of brain region (F(6,265) = 22.212, p = <0.001), age (F(2,265) = 6.230, p = 0.002) and genotype (F(1,265) = 13.650, p = <0.001) revealed independent effects on percentage field of view and a partial eta squared demonstrated that the effect sizes were large (all $\eta p^2 > 0.25$). *Post-hoc* analyses via Tukey HSD tests showed differences from fimbria and corpus callosum.

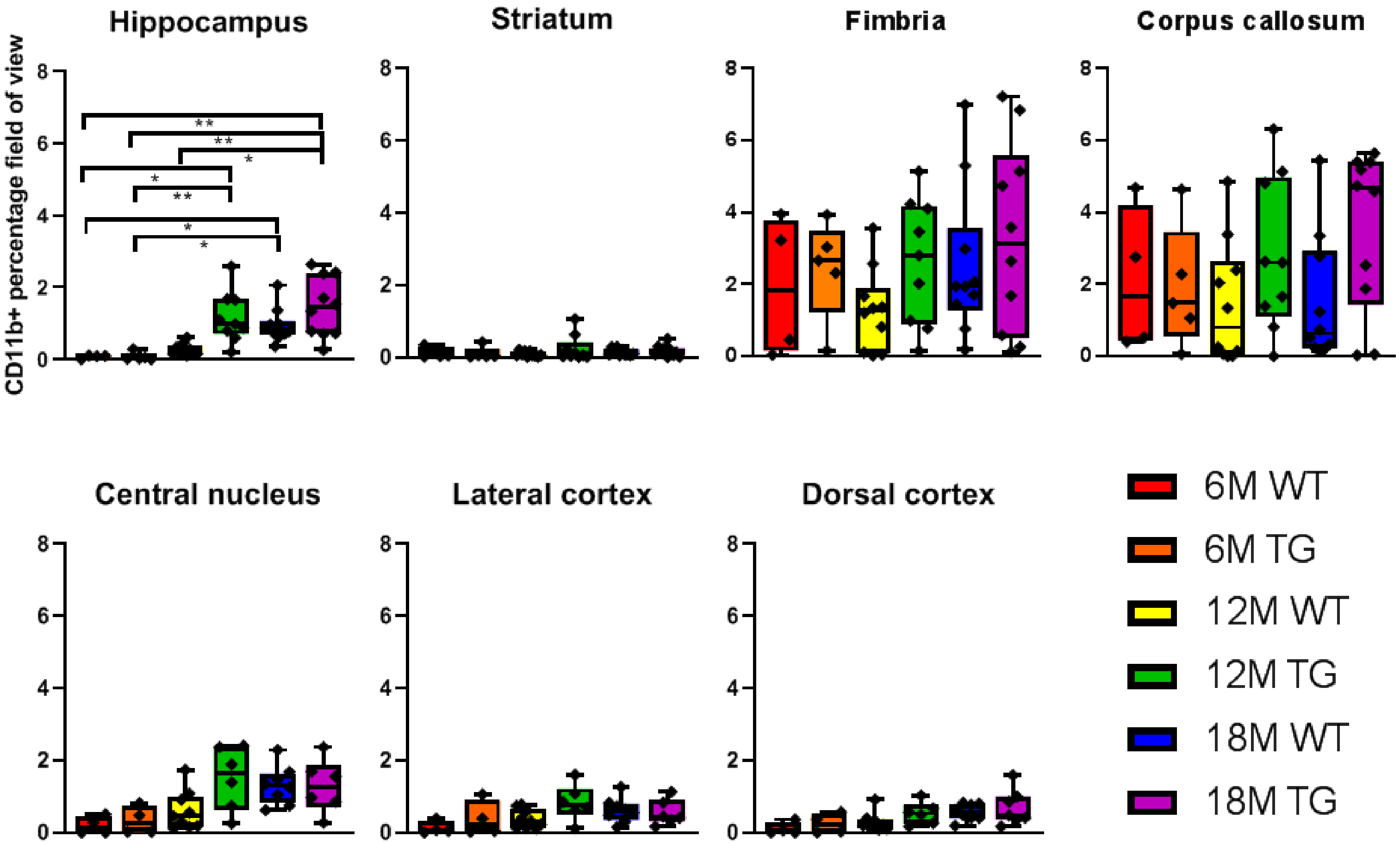

Figure 4.13. Boxplots displaying *CD11b*+ percentage field of view measurements across 303x455x10μm regions of interest. Similar to cell counts (Figure 4.12), CA3 hippocampus demonstrates age-dependent increases in the 12-month Tg, 18-month wild type and 18-month Tg groups. Fimbria and corpus callosum do not display age-dependent changes, but consistently have the highest level of *CD11b*+ labelling across groups. CNIC follows a similar trend to CA3, with a large increase in labelling in the 12-month Tg group. *CD11b*+ labelling in striatum is negligible. These results highlight the similarity in *CD11b* density between CA3 and CNIC and that the white matter tracts have a higher level of activated microglia independent of experimental factors.

4.3.4 – Hippocampus and central nucleus inferior colliculus display pronounced age dependent *GFAP*+ labelling, increasing at 12- and 18-months in the TgF344-AD model

To investigate sub-region-specific differences in *GFAP*+ labelling, regions of interest were outlined, processed and analysed by the same methods used in (Figure 4.11). Figure 4.14 shows boxplots for every region of interest. The highest number of *GFAP*+ cells were found in the 18-month-old Tg CA3 (219±61 per 0.138mm^2) and the lowest numbers were found in the 6-month wild type fimbria (18±10 per 0.138mm^2). Striatum demonstrated similar trends to CA3, with the highest numbers in the 18-month Tg group (203±82 per 0.138mm^2). All other regions showed little difference across the categories.

A 3-factorial ANOVA of cell counts contrasting brain region, age and genotype identified no interactions between factors (F(12,265) =0.395, p = 0.965). 2-factor ANOVA revealed that brain region and age influenced cell count (F(12,265) = 2.769, p = 0.001) and a partial eta squared demonstrated that the effect size was medium (ηp2 = 0.012). *Post-hoc* analyses showed that CA3 and striatum were similar in number (p=0.838), but different to all other regions (all p=<0.001) and CNIC was similar to fimbria and corpus callosum (p= 0.764 and 0.993 respectively).

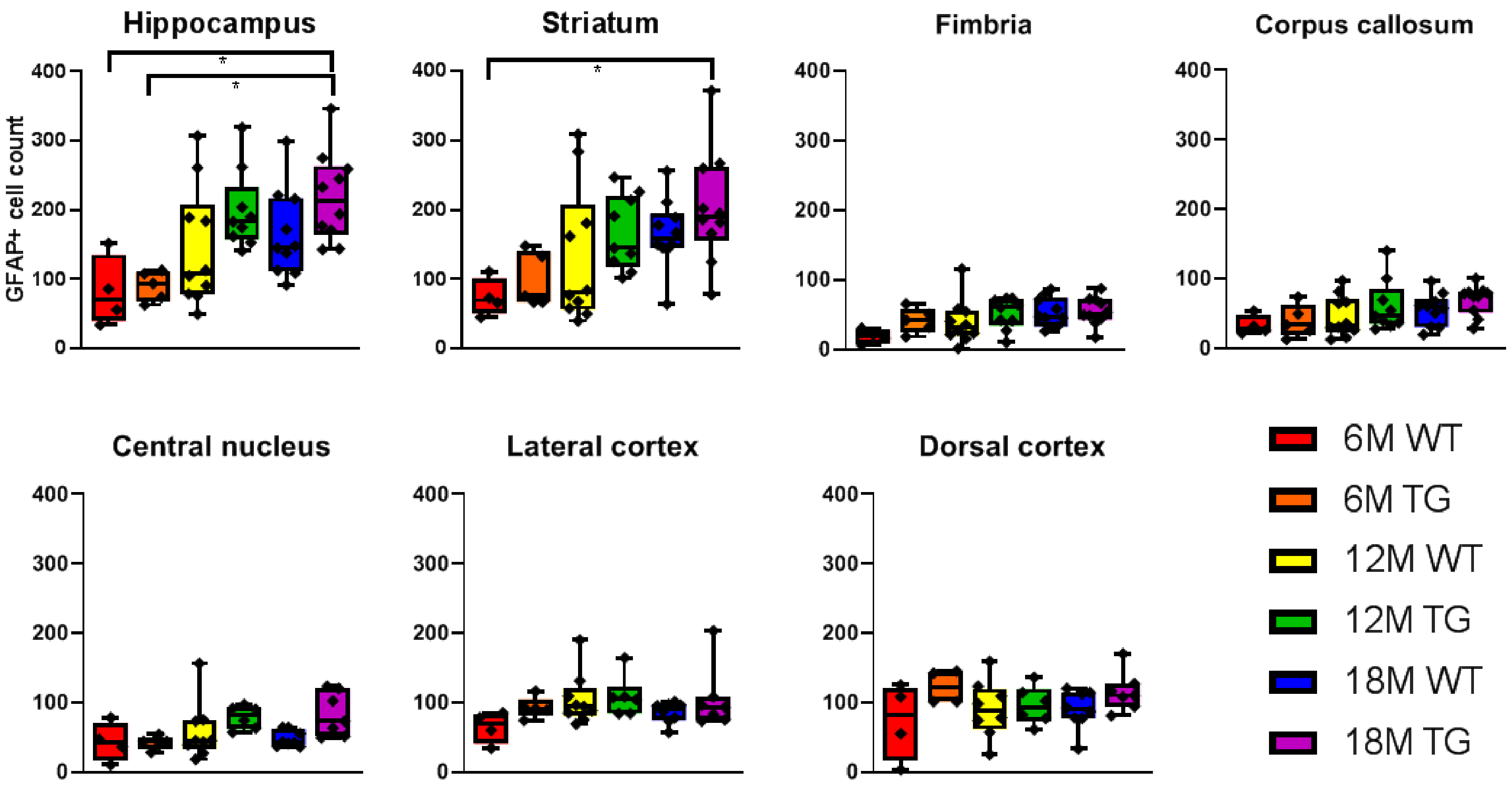

Figure 4.14. Boxplots displaying *GFAP*+ cell counts across 303x455x10µm regions of interest. CA3 region hippocampus demonstrated the most profound increases in *GFAP*+ cells between the 18-month Tg group and the 6-month wild type and Tg groups. Striatum counts followed a similar trend to CA3, with the highest numbers found in the 18-month Tg group and the lowest in the 6-month wild type. CNIC demonstrated a near doubling in cell number from 6-month groups to 12- and 18-month Tg groups, which is similar to CA3 and striatum, albeit less cells.

In addition to cell counts, percentage field of view analyses were used to measure *GFAP*+ labelling. Figure 4.15 depicts boxplots for every region of interest. The highest percentage fields of view were found in the 12-month-old Tg CNIC (8.27%±4.72 per 0.138mm^2) and DCIC (9.35%±8.47 per 0.138mm^2) and the lowest in the 6-month wild type fimbria (0.41%±0.22 per 0.138mm^2). CA3, striatum and CNIC displayed similar trends in increasing percentage field of views with age and genotype.

A 3-factorial ANOVA of percentage field of view contrasting brain region, age and genotype identified no interactions between factors (F(12,265) = 0.983, p = 0.466). *Post-hoc* analyses showed differences between 6 and 18 months (p=0.001) and similarities between CNIC, CA3, striatum and LCIC. 1-factor ANOVA of individual brain regions revealed that the CNIC was the only region to demonstrate effects, both age (F(2,33) = 6.447, p=0.004) and genotype (F(1,33) = 5.515, p=0.025) independently influenced the percentage field of view. Eta squared analysis showed that the effect size was large ($\eta p^2 > 0.25$), demonstrating the validity of the results.

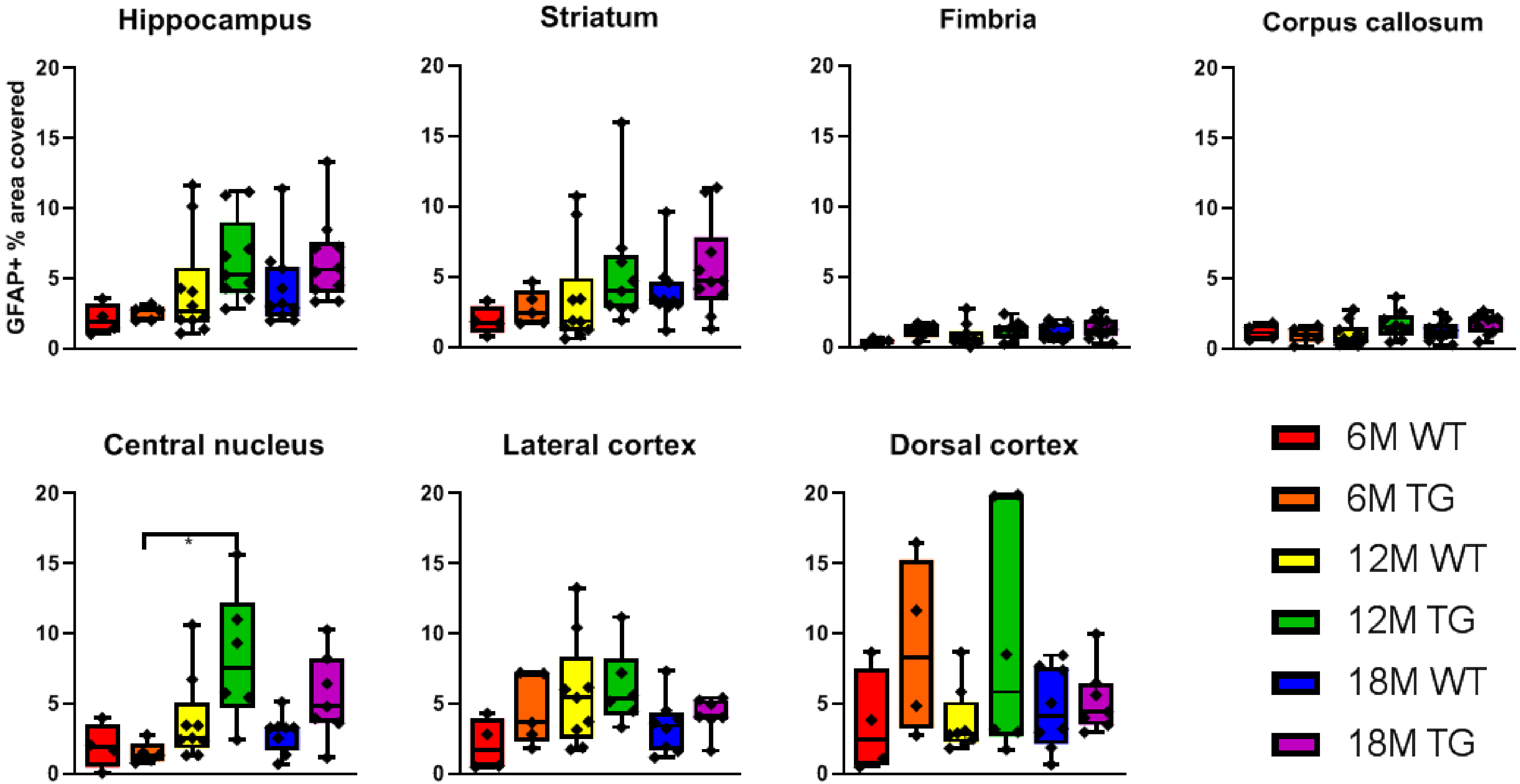

Figure 4.15. Boxplots displaying *GFAP*+ percentage field of view measurements across 303x455x10μm regions of interest. CNIC demonstrated the largest increase in levels of *GFAP*+ labelling between the 6-month Tg and the 12-month Tg groups. CA3 and striatum follow a similar trend to CNIC, albeit less pronounced. DCIC demonstrated high variability with the highest levels of labelling in the 6-month Tg group. The high variability is as a result of the dense layer of labelling adjacent to the ventricle, likely indicative of the protective nature to the circulating cerebrospinal fluid. These measurements with the results shown in Figure 4.13, highlight the similarity in *GFAP*+ labelling increases in the Tg model between CA3 and CNIC from 12-months. Differences in results between cell counts and percentage field of view, suggests astrocytes differ in morphology between regions.

4.3.5 –Sholl analyses reveals *GFAP*+ astrocytes in CA3 undergo age-dependent changes in the Tg model

Utilising the marker *GFAP*+ enabled the labelling of ramified astrocytes. Different brain regions were observed to display various astrocyte morphologies. Figure 4.16 demonstrates observed anatomical differences in *GFAP*+ labelled cells across CA3, striatum and CNIC. To quantify these observations, a Sholl analysis was undertaken as a measurement of astrocyte morphology. The CA3, striatum and CNIC were included in this analysis due to their contrastable level of cell bodies with ramified morphologies. Figure 4.17 illustrates the process undertaken to isolate and quantify the astrocytes. The analysis was implemented on a total of 545 astrocytes from CA3, striatum and CNIC at 6- (CA3 and striatum wild type n=20, Tg n=20 and CNIC n=10, n=25), 12- (CA3 and striatum wild type n=30, Tg n=35 and CNIC n=40, n=30) and 18-months old (CA3 and striatum wild type n=40, Tg n=35 and CNIC n=45, n=35) (Figure 4.18). This allowed the quantification of the total number of intersections, the farthest-ramified processes and the most ramified cells (Figure 4.19, 4.20&4.21 respectively).

Comparing the groups highlighted *GFAP*+ cells in striatum and CNIC were similar throughout, and the CA3 had consistently larger cells from 12-months with the largest separation apparent in 18-month Tg group, which reached a total number of 11 intersections. The smallest cells were found in the 6-month striatum Tg group were the cells reached 7 intersections. These changes uncover that the CA3 region demonstrates age-dependent increases in the number of intersections, particularly in the 18-month Tg group.

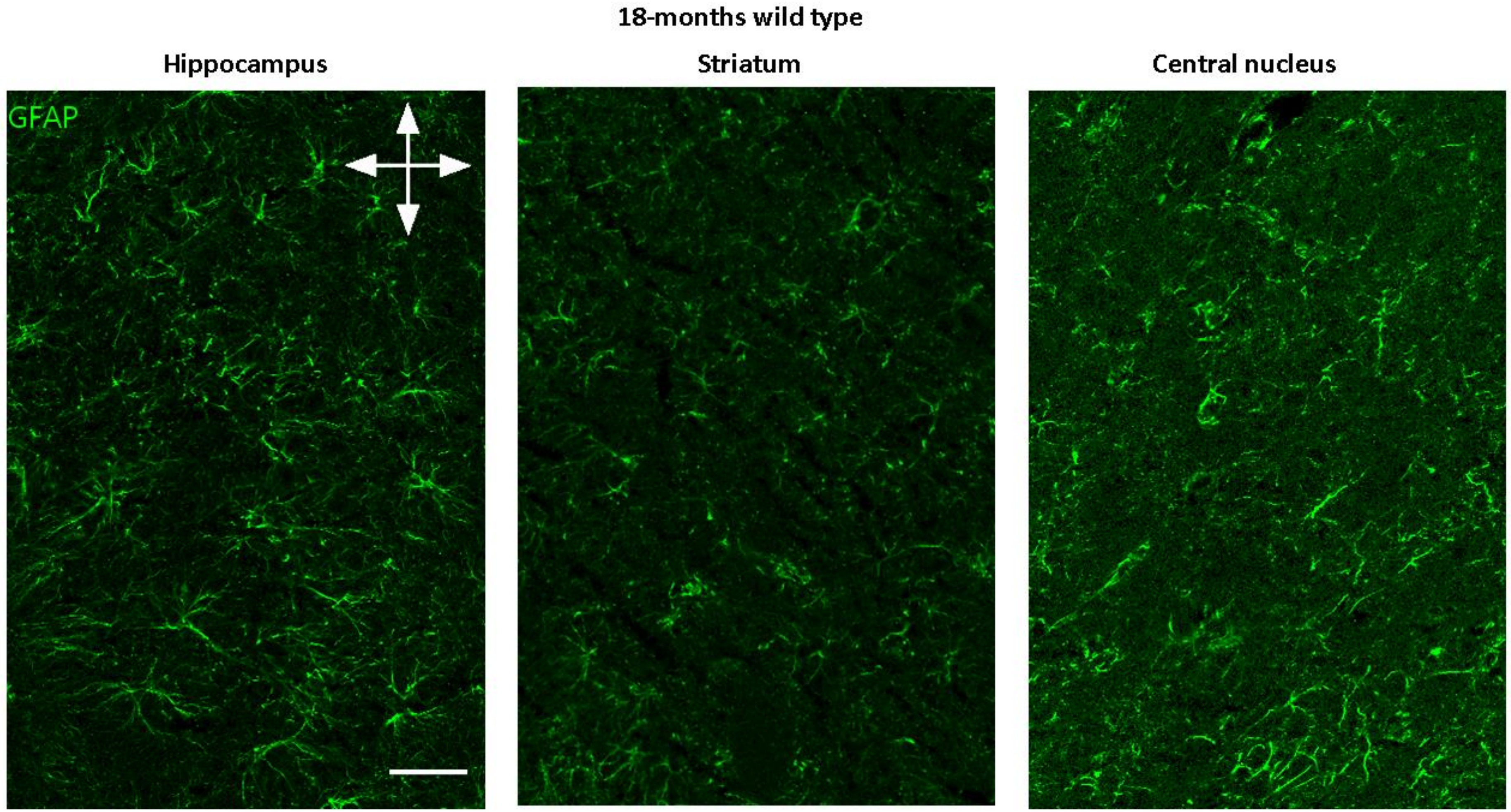

Figure 4.16. Representative example micrographs taken from 18-month-old wild type 303x45x10µm regions of interest to visualise *GFAP*+ labelled cellular morphologies across the CA3 hippocampus, striatum and CNIC. Notice the vast differences in *GFAP*+ morphologies across the categories. Cells in CA3 appear highly ramified in contrast to the other regions. Scale bar 50µm. Axis represents dorsal (up), ventral (down), caudal (right), rostral (left).

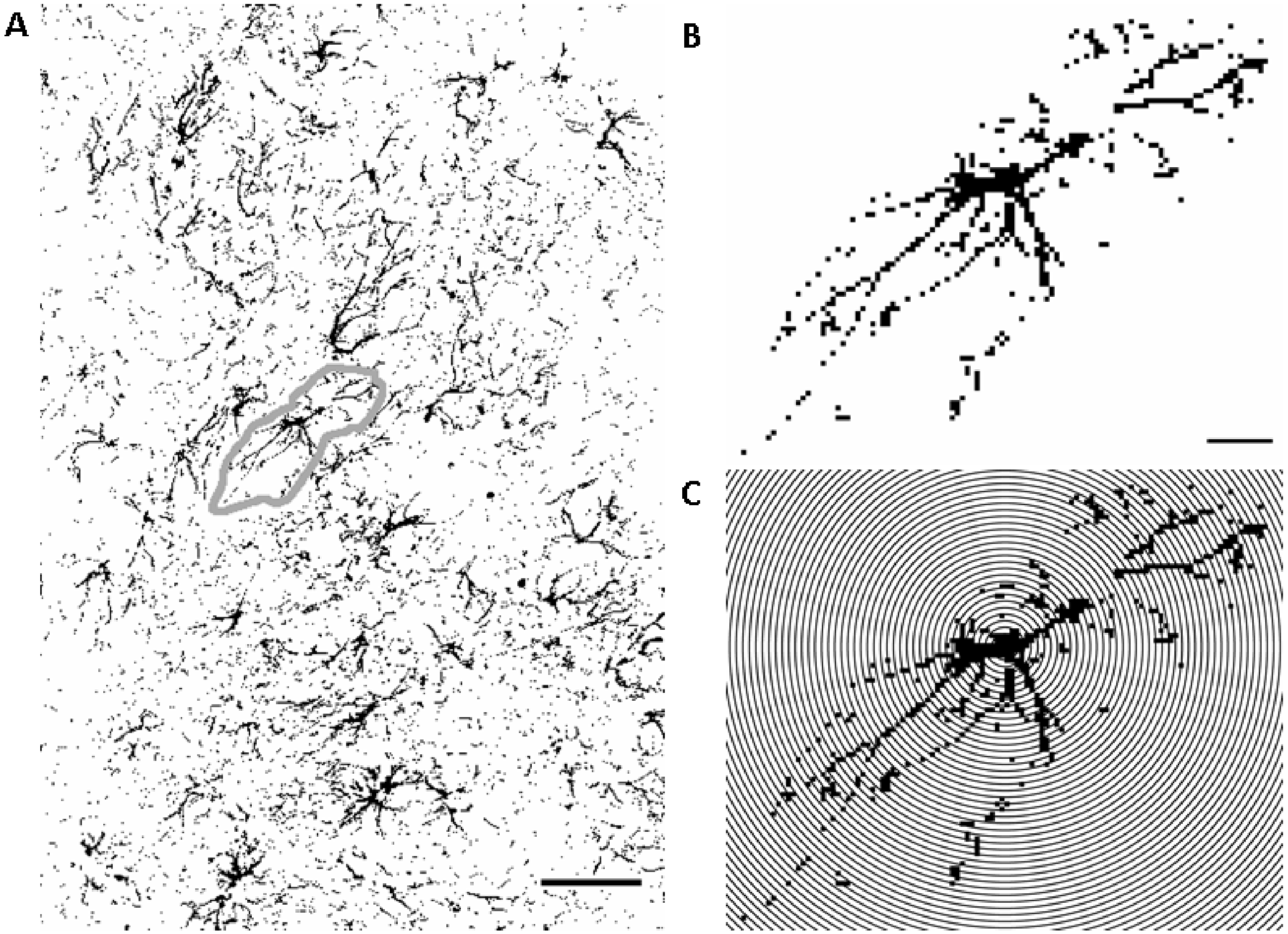

Figure 4.17. Cell isolation and Sholl analysis process. (A) Monochrome 303x455x10µm region of interest image outlining an individual *GFAP*+ cell in CA3 hippocampus. Scale bar 50µm (B) cropped cell. Scale bar 10µm same as in (C). (C) Centre of the soma marked, with radiating equidistant 0.76µm concentric circles from the point of origin. Each intersection with the binary representation of the cell is counted as an intersection. Notice the cell processes are not fully connected, due to the thinness of the sections (10µm), thicker sections (≥45µm) would provide a complete representation of the cell, however, this was beyond the scope of this study.

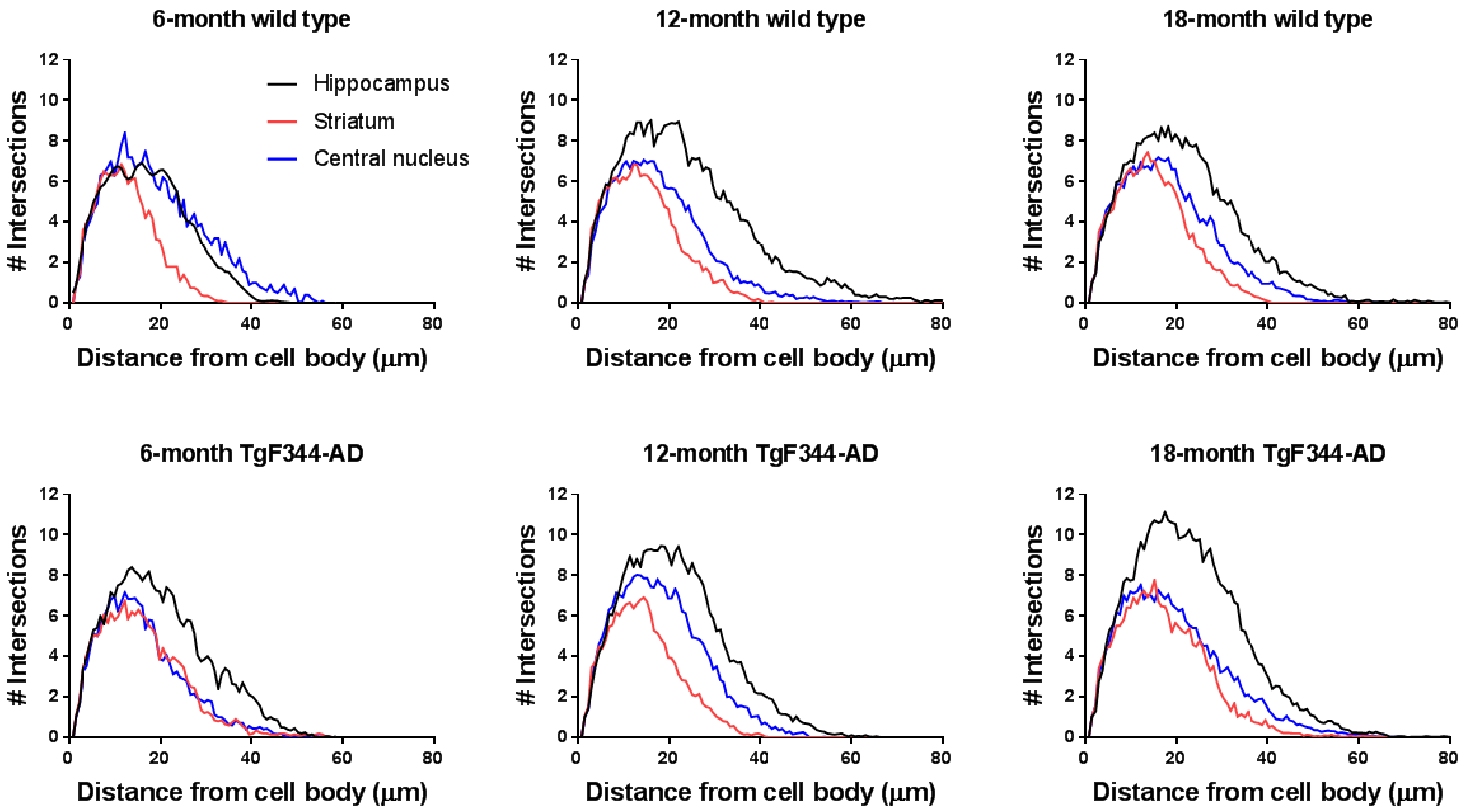

Figure 4.18 Line graphs contratsing the mean values of the age-dependent results from Sholl analysis in CA3, striatum and CNIC of wild type and Tg rats. The CA3 displays the highest number of intersections across categories. The striatum and CNIC display similar numbers, with the CNIC being marginally higher. The highest number and largest separation of intersections between groups is found between CA3 and other regions in the 18-month Tg category. CA3 is the only region to display an age-dependent and genotype influence on increasing the number of intersections in the Tg model.

To explore aspects of astrocyte morphology, the total number of intersections were quantified (Figure 4.19). Every intersection of *GFAP*+ labelling intersecting with the radiating concentric circles from the Sholl analysis were collated. The total number of intersections were then contrasted across the categories (Figure 4.19). Total intersection analysis revealed that the CA3 rangeD from a mean of 201±68 intersections per cell in the 6-month wild type group, to 415±170 intersections per cell in the 18-month Tg. Striatum ranged from 141±61 intersections per cell in the 6-month wild type group, to 214±92 intersections per cell in the 18-month Tg group. CNIC ranged from 187±80 intersections per cell in the 6-month Tg group to 247±90 intersections per cell in the 6-month wild type group.

A 3-factorial ANOVA revealed that age, genotype and brain region interacted and collectively influenced the total number of intersections (F(4,527) = 2.505, P=0.041). *Post hoc* analysis revealed the age-dependent increase in total number of intersections is between 6-months to 12- and 6- to 18-months (both P=<0.001) and that all brain regions were independent from each other (all P=<0.001). Interestingly, 1-factor ANOVA revealed that the CA3 was the only region to show an age-dependent increases with age (F(2,174) = 9.937, P=<0.001) and genotype (F(1,174) = 4.111, P=0.044) independently. The striatum demonstrated an age-dependent increase in total number of intersections with age (F(2,174) = 3.361, P=0.037), but not genotype and the CNIC displayed no influences across factors.

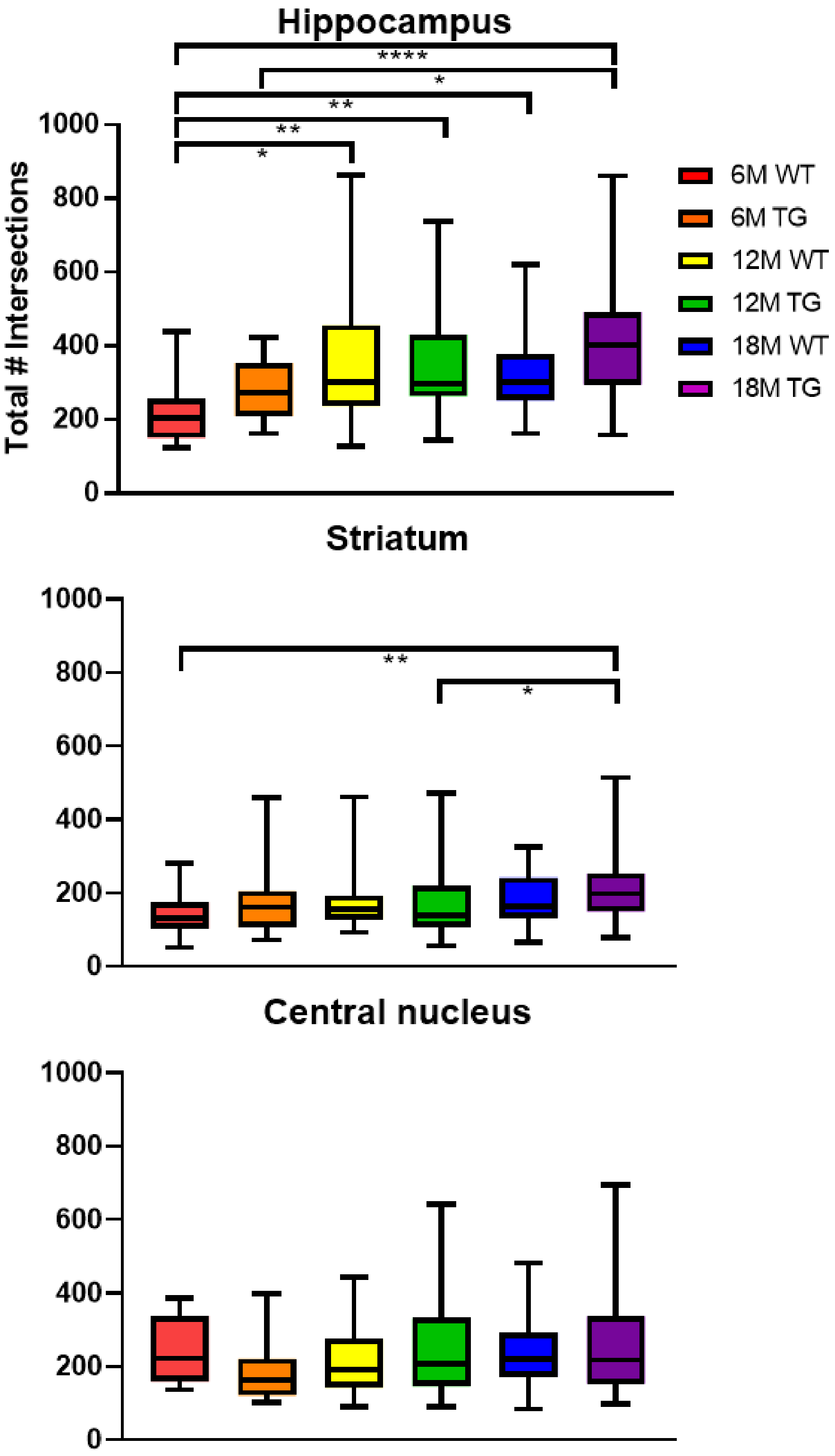

Figure 4.19. Boxplots displaying the total number of intersections recorded from Sholl analysis. CA3 had the highest total number of intersections in all groups. There were consistently higher numbers of intersections in the Tg groups compared to the wild type in CA3. Striatum 18-months Tg had a higher number of intersections than 6-month wild type and 12-month Tg. CNIC had marginally more intersections than the striatum, with no clear genotype or age-dependent influences. This figure displays that astrocytes demonstrate regional specific morphologies depending on brain region and genotype.

To address another aspect of astrocyte morphology, the furthest radiating processes were measured from the soma of each cell as a measure of astrocyte span, to determine whether astrocyte processes extended further across factors (Figure 4.20). In the CA3, the largest span was in the 12-months Tg, 18-months Tg and 12-months wild type, all with the same distance of 42.6μm in contrast to the 6-months wild type spanning 32.7μm. In striatum, the farthest span distance was much lower than in CA3, with the largest span reaching 31.2μm in the 18-months Tg groups, and the lowest in 6-months wild type at 23.6μm. The distances in CNIC were inbetween CA3 and striatum, with the highest span reaching 36.5μm in the 18-months Tg group and the lowest in 6-months Tg at 29.6μm.

A 3-factor ANOVA revealed that age, genotype and brain region interacted and influenced astrocyte branch length (F(4,527) = 2.642, P=0.033). *Post-hoc* analysis uncovered an age-dependent increase in branch length between 6- to 12- and 18-months across all groups (P=0.004 and P=<0.001 respectively) and that all regions were distinctly different in span from each other (all P=<0.001). Although astrocytes in the striatum displayed shorter branch lengths than in CA3, a 2-factor ANOVA highlighted that age and genotype interacted and influenced striatum astrocyte process span (F(2,174) = 3.824, P=0.024). *Post-hoc* analysis revealed age-dependent changes between 6- and 18-months (P=0.005) and 12- and 18-months (P=0.029). 1-factor ANOVA showed that only age influenced the CA3 astrocyte span (F(2,174) = 7.419, P=0.001) and *post-hoc* analysis revealed the difference is between 6- to 12- and 18-months (P=0.003 and P=<0.001 respectively). Interestingly, no factors influenced astrocyte process span in the CNIC.

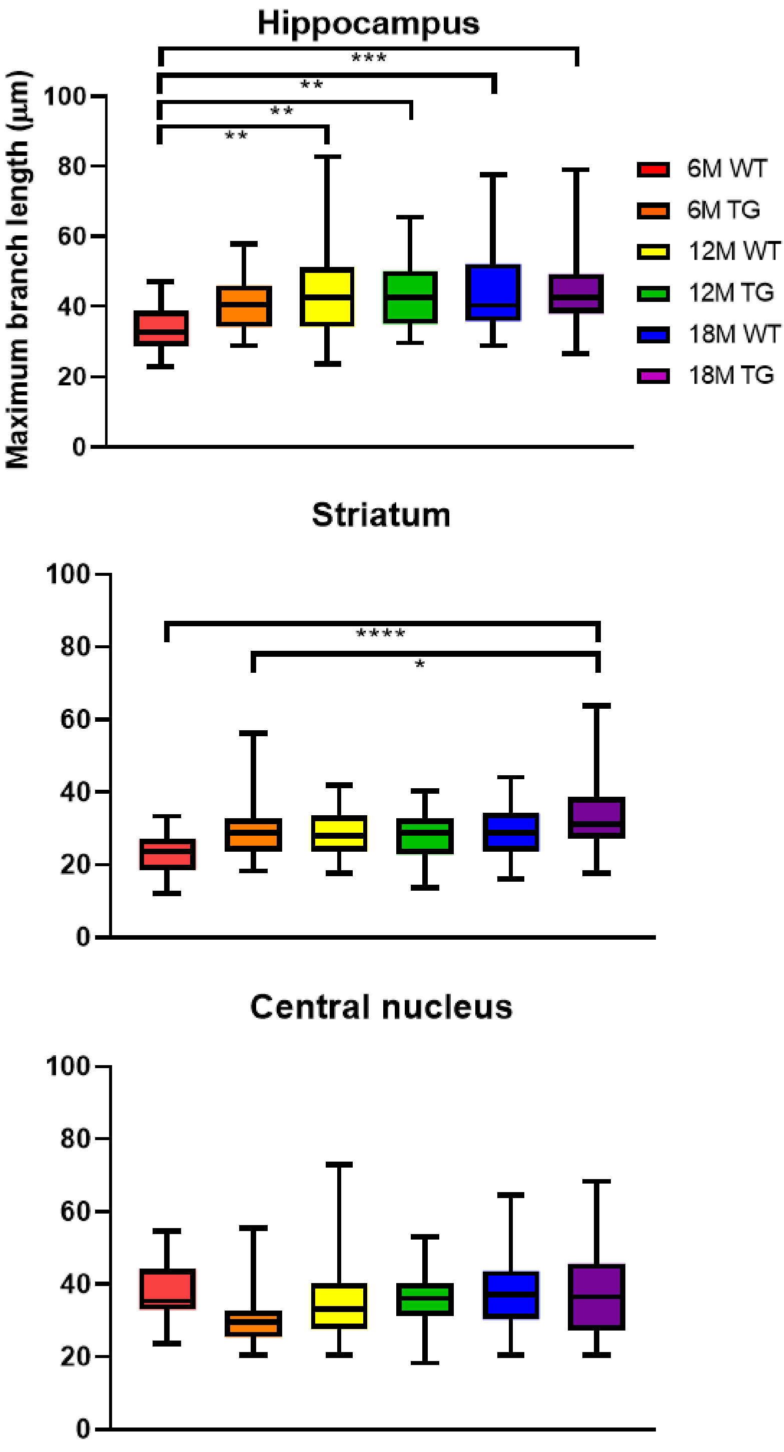

Figure 4.20 Boxplots displaying the maximum branch length recorded from the Sholl analysis. Results from *GFAP*+ cells in the CA3 demonstrated an age-dependent increase in wild type and Tg groups from 6- to 12- and 18-months, with the largest difference between 18-month TG and 6-month wild type. Striatum displayed significant increases in *GFAP*+ branch span from the 6-months wild type and Tg groups to the 18-month Tg group. CNIC decreased in process span from 6-month wild type to the 6-month Tg group, but overall does not reveal age-dependent or genotypic influences. CA3 underwent age-dependent and genotypic branch alterations, striatum also does at 18-months and CNIC span remains unaffected.

Another anatomical feature measured was the maximum number of intersections at any distance from the centre of the soma, which was an indirect measure of astrocyte ramification density (Figure 4.21). The most ramified astrocytes were found in the 18-months old Tg CA3 group, with a mean of 15±4 intersections per cell and the least in the 12-months old Tg striatum group with a mean of 10±4 intersections per cell. Unlike in CA3, the maximum intersections are comparatively similar in striatum and CNIC, both with a similar mean astrocyte ramification density of 11 intersections in 18-months transgenic and 6-months wild type respectively. Overall, the CA3 had a larger maximum number of intersections than the other regions across all factors.

In contrast to astrocyte total number of intersections and process span, a 3-factorial ANOVA demonstrated that age, genotype and brain region did not interact and affect ramification density (F(4,527) = 1.378, P=0.240). However, *post-hoc* analysis revealed that ramification density across CA3, striatum and CNIC were independent, with the strongest effect between CA3 and the other regions (both P=0.001), differences between striatum and CNIC was a smaller effect (P=0.039). 1-factor ANOVA revealed that only age influenced astrocyte ramification density in CA3 (F(2,174) = 7.145, P=0.001) and *post-hoc* analysis showed that the differences were between 6- to 12- and 18-months (P=0.004 and P=0.002 respectively). Astrocyte ramification density in both striatum and CNIC was not influenced by any experimental factors.

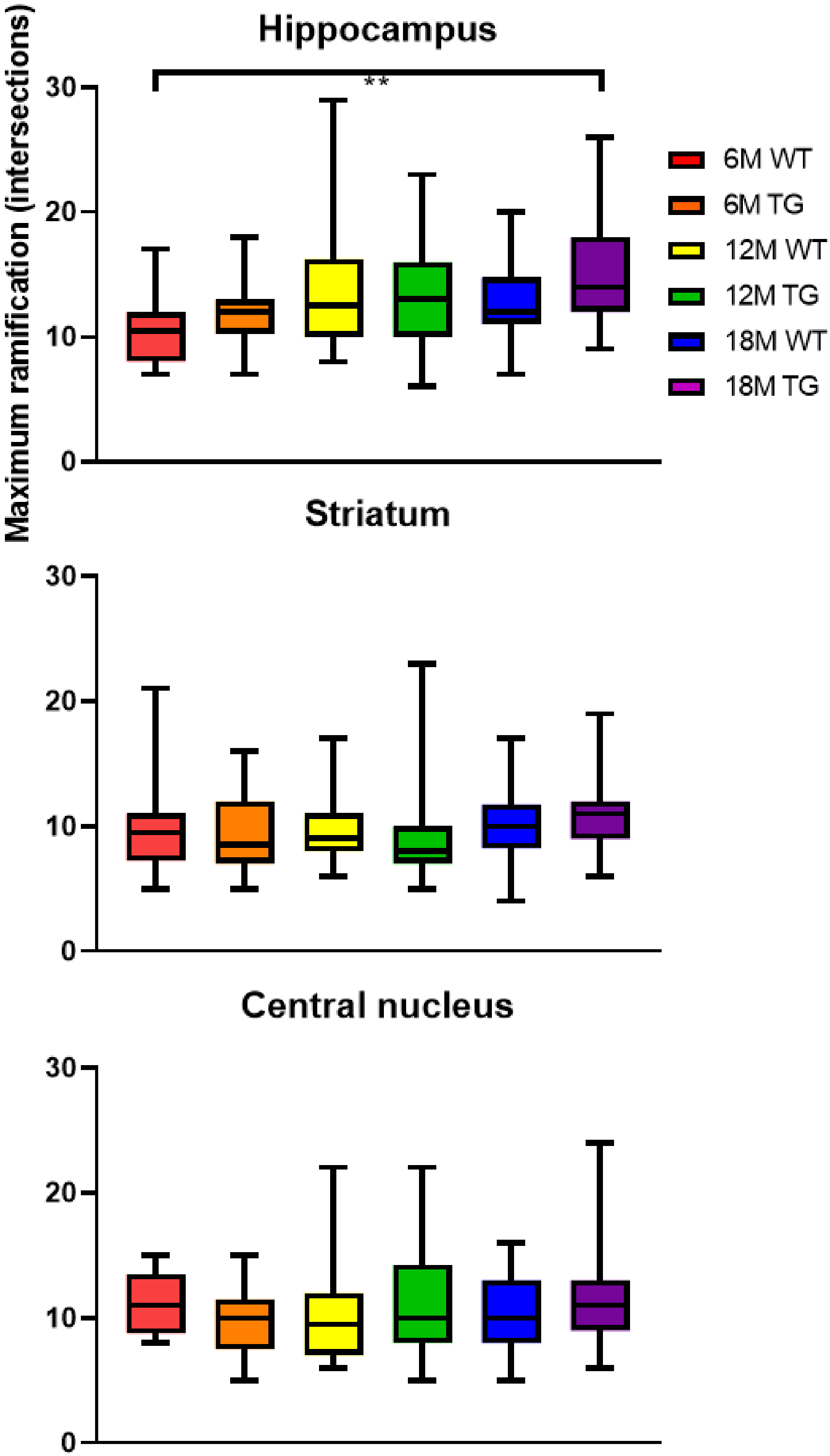

Figure 4.21. Boxplots displaying the maximum ramification of *GFAP*+ cells recorded from the Sholl analysis. Ramification density across the groups displayed similar numbers. Cells in CA3 hippocampus demonstrated in the 18-month Tg group significantly more ramified cells than in the 6-month Tg group. CNIC and striatum remained unaffected by age and genotype.

4.4 – Discussion

The main findings of this Chapter demonstrate in the Tg model that there is no evidence for neuronal loss across CA3, striatum, CNIC, LCIC and DCIC up to 18-months-old. Secondly, there is a similar trend in upregulated *CD11b*+ activated microglia and *GFAP*+ astrocyte labelling from 12-months-old in the CNIC and CA3. Finally, *GFAP*+ astrocytes display different morphologies across CNIC, striatum and CA3 and the astrocyte processes undergo age-dependent and genotype morphological adaptations in the CA3.

4.4.1 –Lack of neuronal loss in the Tg model up to 18-months-old

A critical component in the progression of AD is the atrophy of grey matter within the brain (Migliaccio *et al.*, 2015, Blanc *et al.*, 2016, Thompson *et al.*, 2003). This includes the widespread loss of neurons resulting in a reduction in brain volume and ultimately, cognitive disturbances (Kelley and Petersen, 2007). These symptoms only occur after a long prodromal stage of prior symptoms and surround the later stages of the condition (Wilson *et al.*, 2011). This highlights the importance of uncovering key elements of AD prior to neuronal loss that could prevent progression to this stage. Neuron loss in AD development is considered particularly to be induced by apoptosis under circumstances such as excessive Aβ, oxidative damage, and low energy metabolism (Cotman and Su, 1996). However, neuronal loss is not considered to surround the earlier stages of human AD patient development (Yang *et al.*, 2003). The exact stages of AD when neuronal loss becomes prominent in humans is currently unknown, which makes finding an animal model that can emulate the human stages of AD development crucial. Many transgenic mouse models have been developed over the years to try and recapitulate neuronal loss, but many have proven to be unsuccessful, including the APPSw (Irizarry *et al.*, 1997) and PDAPP (Ohno *et al.*, 2007) mouse models. Cohen *et al.* (2013), demonstrated profound neuronal loss at 16-months, which plateaus at 24-months in hippocampus and cingulate cortex in the Tg model. However, this Chapter demonstrates in hippocampus, striatum and all sub regions of IC of the Tg model up to 18-months of age, there is no observed loss of *NeuN*+ neurons. The results from Cohen *et al.* (2013) and this Chapter both utilised an approach sampling a large sample of neurons to estimate the population of neuronal loss. Considering these conflicting views, more sensitive approaches could be implemented in the future including investigating morphological changes of neurones or employing electron microscopy. These experiments would provide a clearer representation of what is happening to the neurons and a more firm conclusion could then be made about the model.

4.4.2 – Increased glial response in the Tg model

In 1992, the classification of the amyloid cascade was postulated, which hypothesised that AD was defined by the accumulation of Aβ followed by subsequent neurofibrillary tangles, neuronal loss and cognitive disturbances (Hardy and Higgins, 1992). Almost three decades later, there is extensive literature that has contributed to identifying the mechanisms that are involved in AD development surrounding the formation of Aβ deposits. Two of these mechanisms include microgliosis and astrogliosis, which are critical in development of amyloid plaque formation (Sakakibara *et al.*, 2019). Astrocytes and microglia become activated as a neuroinflammatory response to Aβ and it is uncertain whether this response is positive or negative (Pekny and Pekna, 2016, Burda and Sofroniew, 2014). Activated microglia have been found to phagocytose Aβ in the early stages of AD and if the microglia become chronically activated, can lead to neuronal damage (Solito and Sastre, 2012). The role of reactive astrocytes is mainly thought to be neuroprotective, yet, astrocytes have been observed releasing neurotoxic chemokines and pro-inflammatory cytokines that are detrimental to neurons (Choi *et al.*, 2014). The fact that microglia and astrocytes have both been found to display heterogeneous morphologies depending on brain region (Lawson *et al.*, 1990, Salter and Stevens, 2017, Oberheim *et al.*, 2012), throughout aging and pathology (Dossi *et al.*, 2018, Koellhoffer *et al.*, 2017) infers that brain regions will be affected differently throughout AD development. Results from this Chapter show a clear upregulation of glial responses in the CA3 region and CNIC demonstrates a similar increase in *GFAP*+ labelling to the CA3 from 12-months in the Tg model, which is more profound than other regions of the brain. Yuan *et al.* (2016) found that triggering receptor expressed on myeloid cells 2 mutations in mice and humans disrupted the neuroprotective effects of microglia, hence the formation of less refined amyloid plaques, which highlights the contribution of microglia in preventing plaque formation. The research of Yuan *et al.* (2016) into the role of microglia in synaptic regulation in a transgenic mouse model of AD shows that if microglia are chronically activated, this can result in synapse loss. The results in Figures 4.12&13 show that there is an increased level of activated microglia in CA3, which could render the hippocampus more susceptible to synaptic loss.

Astrocytes have been found to play a crucial role in regulating neuronal activity through the formation of tripartite synapse, which is constituted by the bidirectional communication between neurons and astrocytes (Perea et al 2009; Fields et al 2014). Therefore, if astrocytes exhibit dysfunction, one would suggest that this connection would be affected. Hence, Forman *et al.* (2005) utilised a transgenic mouse model expressing human tau protein driven by the *GFAP* promoter, which enabled the measurement of astrocytic tau expression. They found that dysfunction of astrocytes contributes to the degeneration of neurons. Astrocytes have also been found to increase the levels of Aβ in the presence of inflammatory cytokines such as IFNγ in combination with TNFα or IL-1β (Blasko *et al.*, 2000), which are important inflammatory components in AD progression (Zheng *et al.*, 2016). Figures 4.14&15 show that in the Tg model that astrocyte labelling undergoes age-dependent increases in CA3 and CNIC, which could render these regions more susceptible to the pressure of the Tg model and could explain why these were two of the regions to exhibit plaque like structures (Figure 4.10) from 12-months.

4.4.3 – Hippocampal CA3 astrocytes undergo age-dependent adaptations in morphology in the Tg model

The emerging evidence supporting that hearing loss contributes to the early development of dementia (Lin *et al.*, 2011a, Livingston *et al.*, 2017) emphasises the need to identify a mechanistic link in a region of central auditory processing. This Chapter provides evidence, in IC, that glial labelling prior to neuronal loss follows a similar trend to that of the CA3, albeit to a reduced extent. Pyapali and Turner (1996) measured age-dependent neuronal dendritic alterations in Fischer344 rat CA1 hippocampus and found that that they became more ramified. This most likely transfers to the age-dependent increase in astrocyte ramifications observed in CA3 in this Chapter (Figure 4.18) as a mechanism to accommodate for denervation because of reduced afferent input and the fact that this response was exemplified in the Tg model, suggests that this denervation is accelerated in AD. Due to the highly dynamic plastic nature and rapid memory storage capability of the CA3 region (Rebola *et al.*, 2017) it is not surprising that there is an increased glial response. The main findings of this Chapter demonstrate that astrocyte morphologies undergo age-dependent modifications in the CA3 of the Tg model (Figure 4.18) prior to neuronal loss (Figure 4.5). Contrastingly, CNIC and striatum do not undergo any adaptations in astrocyte morphology (Figures 4.18 & 19 & 20 & 21), even though there was a significant increase in labelling similar to CA3 (Figures 4.13&14).

Therefore, why do astrocytes in hippocampus adapt their morphology with ageing and to a greater extent in the Tg model, but not in striatum or CNIC? Matias *et al.* (2019) suggest that the functions of astrocytes include modulating neuronal activity, maintaining pH, homeostasis of synapses, provide nutrients to neurons, blood brain barrier formation and function, glymphatic system regulation and homeostasis of ions and water. Research by Wilhelmsson *et al.* (2006) suggest that *GFAP*+ astrocytes under stress in hippocampus do not increase in number, but increase in size and number of processes, which is commensurate with the findings in Figure 4.18-20. However, the fact that astrocyte morphology was unchanged in CNIC and striatum, suggests differences in the underlying neuroprotective roles of astrocytes across the brain that requires further investigation. Taking these factors into account, it is more than likely that astrocytes in IC are different morphologically due to their differences in function, which is likely a result of the inherent auditory anatomy and physiology. Hippocampal astrocytes are larger and have more ramified processes, which is more likely to be due to their high number of neuronal and synaptic interactions, perhaps reflecting the distinct cytoarchitecture of these subcortical structures. Therefore, one could suggest that the changes in hippocampus are as a result of age- and genotype-dependent stress on the resident astrocytes and perhaps in the Tg model are primed to respond in a more active manner, causing cells to remodel. In contrast, the increase in *GFAP*+ labelling observed in the aged Tg model of the IC could represent a different mechanism in response to the stress causing not an adaptation of resident cells, but an increase in number. The methodology employed in this Chapter opens up a new avenue of investigation into understanding AD and could be used as a basis for physiological experiments investigating changes in astrocyte functionality across the brain.

4.4.4 – Limitations

When quantifying neuronal and glial numbers, region of interest analysis was an appropriate measurement to provide insight into the differences of labelling across brain regions. This method was implemented to provide a large representative sample size across many regions of the brain, that would have been impossible in the same time frame implementing stereology. It also provided consistent easy to replicate measurements with less margin of error that may arise in other approaches. However, this method of analysis did not produce the total representation across all three dimensions of the total density of cells throughout the whole brain region and contrasting the differences in distinct brain regions such as the primary cell layer in hippocampus, to the evenly distributed cells in striatum hampers the interpretability. Future work could utilise the stereological approach as a more rigorous measurement of whole brain regions, which may uncover a more representative quantification of neurons, but may not produce the same sample size. In addition, more specific markers of sub types of neuronal markers could be implemented as a more sensitive method of labelling, but as a starting point, this would not have provided a good basis for future work as the above methods.

Also, *GFAP+* astrocytes in rodents differ substantially to the astrocytes found in humans (Vasile *et al.*, 2017), which hampers the interpretability of changes in astrocyte morphologies to human studies. However, one could argue that transferability to measuring age-dependent AD development in humans, may lead to more substantial morphological astrocytic changes. Fundamentally, rodent models are never going to recapitulate AD, but finding the closest possible option is paramount. By using rats opposed to mice has underlying issues such as the time it takes to mimic human aging is much slower, but rats have more similar synteny blocks to humans than mice (Bourque *et al.*, 2004), which demonstrates they are more evolutionarily like humans. This means that the underlying physiology of rats is more comparable to humans than mice. The Tg model has been characterised to undergo amyloidosis, tauopathy, gliosis, neuronal loss and cognitive disturbances (Cohen *et al.*, 2013), which is unattainable in most transgenic mouse models.

In addition, the thickness of the sections were 10µms, which is much smaller than the extensity of astrocytic process length (~40µm). Therefore, using thicker sections would have better represented astrocyte morphology across the x, y and z planes. However, as the sections were cut on the sagittal plane, it is difficult obtain a high number of sections to quantify, therefore it was beyond the scope of this study to implement this.

4.4.5 – Chapter conclusions

This Chapter provides anatomical evidence in the TgF344-AD rat model of AD of an age-dependent upregulated, activated *CD11b*+ microglial response in the CA3 hippocampus. An age-dependent upregulation of *GFAP*+ astrocyte labelling in the CA3 and CNIC in the TgF344-AD model. Astrocytes undergo age-dependent morphological adaptations in the CA3 of the TgF344-AD model, but do not demonstrate changes in CNIC. In addition, there was no observed neuronal loss up to 18-month of age in the TgF344-AD rat model. These results demonstrate differences in glial responses across different regions of the brain, with a particular response in CA3 hippocampus and to a lesser extent the CNIC. Together the results from this Chapter highlight that these glial responses are upregulated heavily but vary in morphology from 15-months in the Tg rats (~30 years humans), and the cells responses differ across the regions of the brain as a result of Alzheimer's disease. Therefore, this Chapter provides evidence for age-related gliosis that could be used as a basis for better understanding the progression of Alzheimer’s disease in humans. Chapter 5 further investigates the age-dependent effects of the TgF344-AD model by measuring synaptic mitochondrial dysfunction.

Chapter 5 – Age-dependent synaptic dysfunction in the inferior colliculus and hippocampus of Tg-F344AD rats

5.1 – Introduction

This Chapter focuses on physiological and molecular approaches to identify putative mechanisms of synaptic mitochondrial dysfunction in the Tg rat model. Fundamental hallmarks in the progression of AD are synaptic dysfunction and an overall reduction in metabolic rates (Jack and Holtzman, 2013). Synaptic loss and a reduction in metabolism are products of amyloidosis and tauopathy (Gouras, 2019). Amyloid beta (Aβ) regulates synaptic function by evoking the release of soluble Aβ, making synapses a key target in understanding subsequent dysfunction (Parihar and Brewer, 2010). The initiation of synaptic loss precedes cognitive impairment and is a critical component in the progression of AD (Kashyap *et al.*, 2019). The Tg model used in this study has been characterised to undergo amyloidosis and tauopathy (Cohen *et al.*, 2013), making it a potential platform to better understand synaptic dysfunction. This Chapter investigates presynaptic terminals where mitochondria are present, using *ex vivo* synaptosomes as an approach (see Whittaker (1993)) across different regions of the brain.

5.1.1 –Metabolic studies of brain function

Numerous techniques enable quantification of metabolic function within the brain. (Sokoloff *et al.*, 1977b) utilised the [14C]deoxyglucose autoradiography method which allowed the measurement of local cerebral glucose consumption across different sub-regions of the brain, *ex vivo*. Another approach involves injecting a subject with a radioactive tracer, most commonly fludeoxyglucose (FDG), and implementing Positron Emission Tomography (PET) to identify regional glucose uptake. This method is used in assessing gross synaptic loss in AD (e.g. (Mosconi *et al.*, 2010)).

Post-mortem analysis of markers associated with metabolism, include histochemical labelling of mitochondrial enzymes. Cant and Benson (2005) described strong labelling of the mitochondrial enzyme cytochrome oxidase in gerbil IC compared to other regions of the brain. Measuring cytochrome oxidase has been found to correlate with functional measures of metabolic activity (Wong-Riley, 1989). Another approach to identify mechanisms of metabolic functioning, include measuring the enzyme citrate synthase, which is an indirect measurement mitochondrial density. The primary focus of this Chapter measures oxygen consumption rate (OCR) and subsequent mitochondrial function/dysfunction by implementing mitochondrial stress analysis using a Seahorse XFP flux analyser (Seahorse) across IC, hippocampus, auditory cortex, frontal cortex, superior colliculus and cerebellum

5.1.2 – Parameters used in Seahorse analysis

Mitochondrial dysfunction is a fundamental hallmark in many diseases and mitochondrial respiration is consequently an indicator of mitochondrial health. Methods commonly used to quantify mitochondrial dysfunction in vivo include magnetic resonance imaging. However, magnetic resonance imaging does not provide precise measurements of individual isolated mitochondria. Therefore, using Seahorse analysis allows for the precise control and comparison of individual factors, which is unattainable using other methods.

Seahorse analysis manipulates the electron transport chain of mitochondria by introducing different compounds that interfere with electron flow. The first compound introduced is the antibiotic Oligomycin, which targets complex V on the mitochondrial electron transport chain and inhibits ATP synthase and prevents oxidative phosphorylation. This however, does not block all electron transport due to the passive transport of protons across the mitochondrial membrane (proton leak), which can be viewed as a measure of mitochondrial membrane dysfunction. The second compound introduced is the uncoupling agent FCCP that causes uninhibited electron flow through the mitochondrial electron transport chain and results in maximal oxidative respiration. By subtracting basal respiration from maximal respiration generates the measurement spare respiratory capacity. Varying levels of spare respiratory capacity are measures of reserve that mitochondria can utilise under stress. Finally, a combination of the pesticide Rotenone and the antibiotic Antimycin A are added to the sample, which together block the mitochondrial electron chain and prevent oxidative respiration *per se*. Any readings still present following this stage are as a result of non-mitochondrial oxygen consumption (Figure 5.15). The methods and animal model were chosen over other techniques due to the reliable and invasive measurement of metabolic function, which provides a direct metabolic measurement of synaptic populations that would be otherwise impossible to determine in human AD development.

5.1.3 – Chapter aims

After discovering that there was no observed loss of neurons in the Tg model up to 18-months in Chapter 4. This Chapter aimed to identify if synapses were affected prior to neuronal loss. Therefore, the time-points of the animals chosen in this Chapter were at 7- and 15-months to recapitulate key early time points of AD development. Using the IC as a model, due to it being the most metabolically active nucleus in the brain, makes it a prime candidate for targeting synaptic metabolic dysfunction. This Chapter is the first to utilise the physiological Seahorse mitochondrial stress analysis to analyse potential synaptosome dysfunction in the Tg rat model. In addition to physiological analysis, scanning electron microscopy (SEM) has been employed to validate the presence of synaptic structures in synaptosome samples and undertake subsequent morphological analyses of these. Further experiments included quantitative real-time PCR, investigating expression of genes in synaptosomes, hypothesised to be modified in the Tg model with ageing. These include the inhibitory presynaptic target *GAD65*, Synaptic vesicle glycoprotein 2A (*SV2A*), which is involved in neurotransmitter release, and the ubiquitous presynaptic gene *synaptophysin*. Finally, the gene *Iba1* was targeted to understand changes in this marker of microglial expression. This Chapter provides novel insight into age-dependent mitochondrial dysfunction in presynaptic terminals and the adaptations undergone in the Tg model of AD.

5.2 – Methodology

5.2.1 – Seahorse XFP Flux Mitochondrial Stress Analysis of Synaptosomes

Results are described from 7-month old Fischer344 wild type (n=7), 15-month old wild type Fischer344 (n=7), 7-month old Tg (n=7) and 15-month old Tg (n=7) rats (N=28). The night before each experiment, to calibrate the Seahorse XFp Extracellular Flux Cartridge, each well of the culture plate underneath the cartridge was filled with 200µl seahorse calibrant (Agilent #100840-000), surrounding wells with 400µls and incubated at 37°C until use. On the morning of each respective experiment, the Seahorse XFp Extracellular Flux Analzer (Seahorse; Agilent) was turned on and allowed to initialise.

Animals were culled at the University of Manchester in accordance with Schedule 1 (table A section 4) of the Animals (Scientific Procedures) Act 1986. Trial experiments comparing removing the brain pre- and post-transportation were undertaken to verify the most viable procedure. Methodology including taking the whole animal on ice and transporting to Manchester Metropolitan University (ca. 15 minutes) demonstrated the greatest sample viability. After transportation, the skull was removed with rongeurs (Micro Friedman, 0.8mm jaws, WPI) and a cut was made sagittally through the brain. The right hemisphere was placed in optimal cutting temperature (OCT) compound, snap-frozen using liquid nitrogen and placed in a -80°C freezer for molecular biology. The left hemisphere was analysed using Seahorse. From the left hemisphere, cerebellum, frontal cortex, auditory cortex, IC, superior colliculus and hippocampus were dissected and placed in 500µl of sucrose solution (320mM sucrose and 10mM Tris-HCl in deionised water). Samples were kept on ice throughout the dissection. Samples were then homogenised using an Ultra-Turrux T8 homogeniser (IKA) until all tissue was liquified. All steps of centrifugation to isolate synaptosomes were undertaken using the Refrigerated SIGMA 3-16KL centrifuge and kept at 4°C throughout. Each brain region was then centrifuged at 1,617G for 1 minute, to isolate cellular fractions, the supernatant was removed and the sediment resuspended in 500µls of sucrose solution and centrifuged again for 1 minute at 1,617G and further resuspended. Samples were then centrifuged at 15,973G for 4 minutes to separate synaptosomes from cellular fractions, cellular supernatants were collected and frozen at -80°C (process adopted from Gray and Whittaker (1962)). The synaptosome sediments were then resuspended in 500µls of sucrose solution and centrifuged again a further 4 minutes at 15,973G and resuspended in sucrose solution. The supernatant was then discarded and 5µl of synaptosome sample from each brain region was diluted with 45µl of sucrose solution. A Pierce bicinchoninic acid assay (BCA) protein assay kit (ThermoFisher) was used, according to the manufacturer's instructions, to determine the protein concentration from each brain region by measuring absorbance using a plate reader (Synergy HT microplate reader BioTek). Absorbances from unknown synaptosome samples were plotted against known standards at 562nm and the readings were calculated using linear regression (See example in Figure 5.1).

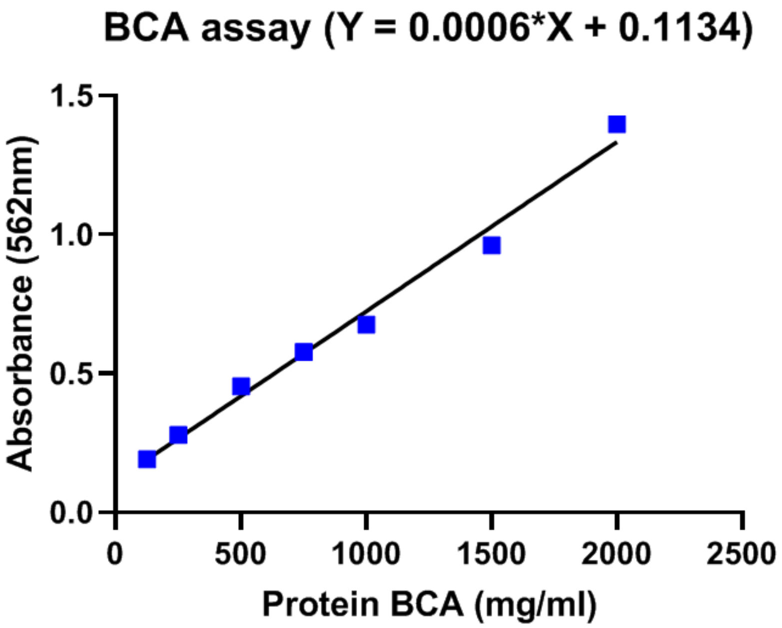

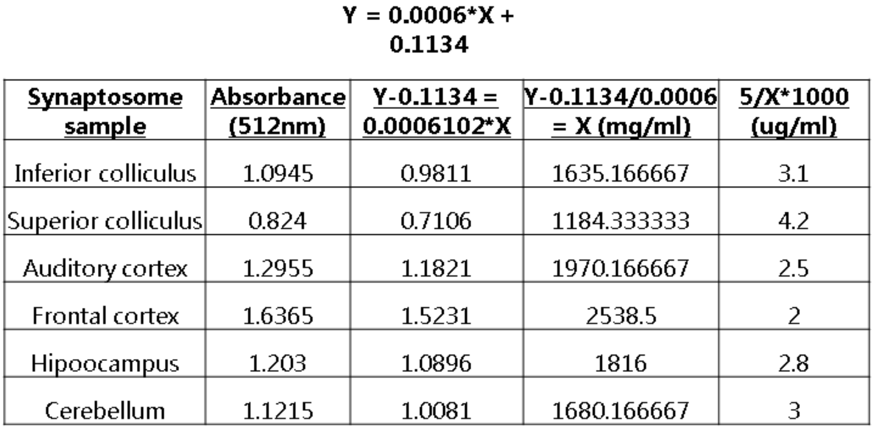
Y = 0.0006*X + 0.1134

Synaptosome sample	Absorbance (512nm)	Y-0.1134 = 0.0006102*X	Y-0.1134/0.0006 = X (mg/ml)	5/X*1000 (ug/ml)
Inferior colliculus	1.0945	0.9811	1635.166667	3.1
Superior colliculus	0.824	0.7106	1184.333333	4.2
Auditory cortex	1.2955	1.1821	1970.166667	2.5
Frontal cortex	1.6365	1.5231	2538.5	2
Hipoocampus	1.203	1.0896	1816	2.8
Cerebellum	1.1215	1.0081	1680.166667	3

Figure 5.1. Absorbances of standards from BCA assay were plotted for each brain region in each experiment, producing a linear increase in absorbance. Linear regression analysis was used to produce the resultant formula, and by rearranging the equation, the volume of solution required to include 5µg of protein was determined for each sample. The correct amount of liquid corresponding with 5µg of protein for each brain region was pipetted into a seahorse culture miniplate (Figure 5.2A).

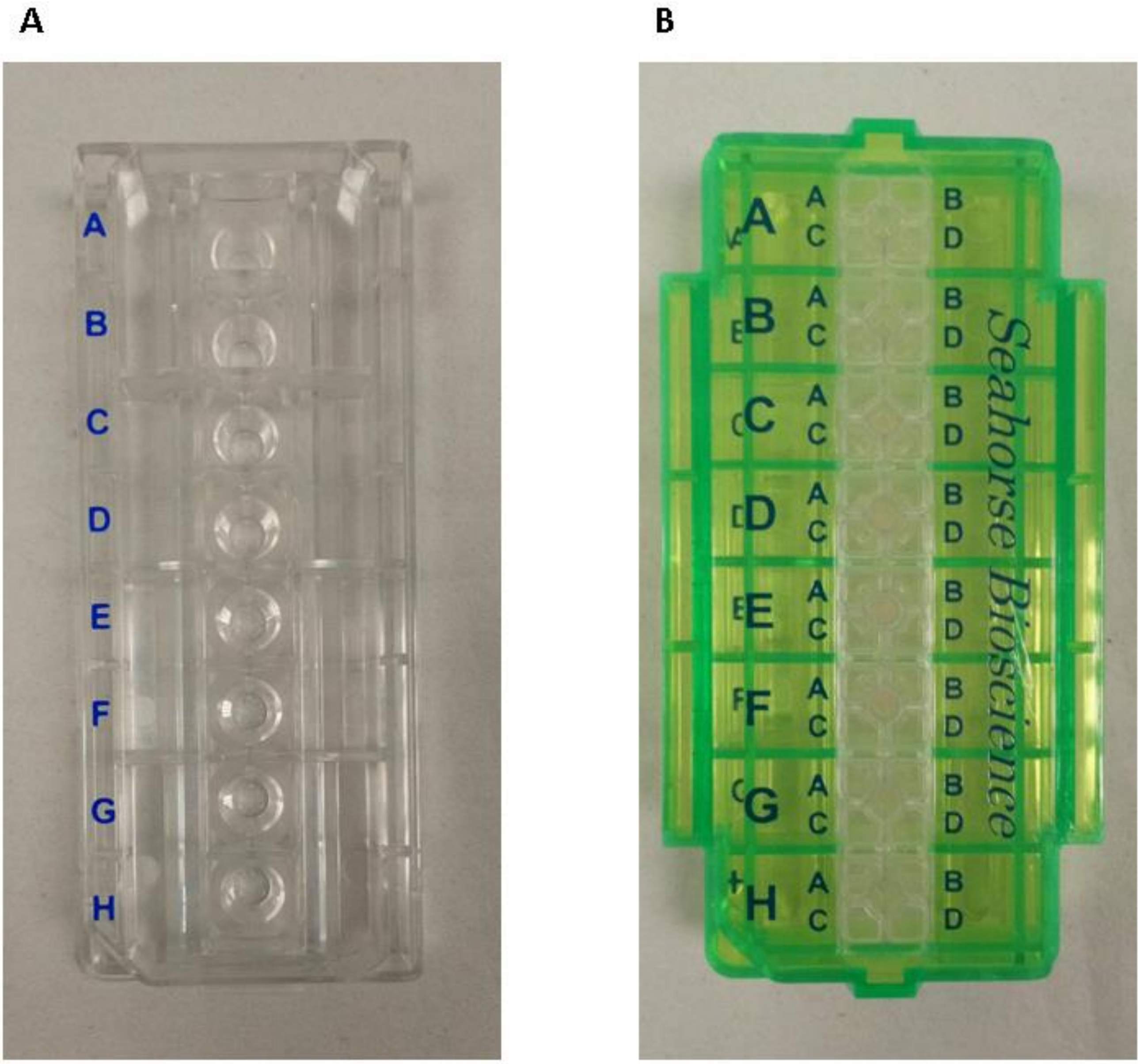

Figure 5.2. Example photographs taken of a Seahorse culture miniplate (A) and sensor cartridge (B). (A) Wells A and H were left blank for background measurements of culture solution. 5µg of protein from IC, superior colliculus, auditory cortex, frontal cortex, hippocampus and cerebellum were pipetted into wells B to G respectively. (B) 20µl of Oligomycin was pipetted into every sub-well A, FCCP into B and Rotenone and Antimycin A into C, all sub-wells D were left blank.

After protein concentrations were determined, 5µg of synaptosome sample from each brain region was pipetted into individual wells B to F of a seahorse culture miniplate (See Figure 5.2A), wells A and H were left blank to measure background levels. The miniplate was centrifuged at 2,129G for 40 minutes for samples to stick to the bottom of the plate using a

Sigma 3K10 centrifuge. The rest of the synaptosome samples were frozen for subsequent citrate synthase activity measurements. After centrifugation, 10ml of culture solution was made up (180µl glucose, 100µl sodium pyruvate and 100µl L-glutamine in 10ml of Seahorse XF RPMI medium pH 7.4) and 180µls was pipetted into every well, ensuring the synaptosome samples were not disrupted on the bottom of the miniplate. The plate was then incubated at 37°C for 45 minutes. In this period the compounds from the Seahorse XF Cell Mito Stress Test Kit (Agilent), which included eppendorfs of Oligomycin, FCCP and Rotenone and Antimycin A. Stock solutions of Oligomycin were made up with 252µl of culture solution, FCCP with 288µl and Rotenone and Antimycin A with 216µl. Oligomycin was then further diluted by introducing 60µl of stock solution to 240µl culture solution, FCCP 120µl to 180µl and Rotenone and Antimycin A 60µl to 240µl. Final stock solutions were then pipetted into a sensor cartridge (See Figure 5.2B). 20µl of final Oligomycin stock solution was pipetted into each sub-well labelled A, 22µl of FCCP into sub-wells labelled B and 25µl of Rotenone and Antimycin A into sub-wells C. The sensor cartridge was then calibrated in the Seahorse for 15 minutes. After calibration, incubated synaptosomes were entered into the Seahorse to initiate the measurement of OCRs of mitochondria per sample. The Seahorse initialised for 5 minutes, and then readings were taken every 7 minutes for 84 minutes. The first three 7-minute time points were measurements of basal respiration prior to compound injections. The first substrate introduced was Oligomycin, readings were taken at 7-miunte intervals for 21 minutes, then FCCP was introduced and measured three times over 21 minutes and finally, Rotenone and Antimycin A were injected onto the samples and measured at 7-minute intervals over 21 minutes (See figure 5.6 for an overview).

5.2.2 – Citrate Synthase Relative Quantity Analysis

Protein estimations were implemented to account for inconsistencies in protein concentrations across brain regions, however, this did not account for the varying levels of mitochondria in each sample. The measurement of citrate synthase an enzyme present in all mitochondria and is involved in catalysing initial reaction in the Krebs cycle, was used to provide estimates of mitochondrial abundance. These measurements were then used to normalise relative mitochondrial levels to account for heterogeneity across samples. Citrate synthase activity levels were calculated taking advantage of the formula $Acetyl\ CoA + Oxaloacetate + H20 \rightarrow Citrate + CoA - SH$ along with $CoA - SH + DTNB \rightarrow TNB + CoA - S - S - TNB$ to identify maximum absorbance at 412nm wavelength, which was identified by Srere (1969). Reagents used were purchased from Sigma-Aldrich (cat# CS0720). Initially, 15µg (5.1-15.3µl) of synaptosome samples were pipetted into individual wells of a 96-well plate, then 2µl of 30 mM Acetyl-CoA (cat#A2181) and 10 mM 5′, 5′-Dithiobis 2-nitrobenzoic acid (DTNB) (cat# D8130) and the difference was rounded up to 200µl with Assay Buffer for Citrate Synthase 1 (diluted from Assay Buffer for Citrate Synthase 5 cat# B6935). The plate was then placed into a plate reader (Synergy HT microplate reader). The protocol was set up to warm the samples to 25°C, then shake for 10 seconds to mix reagents and to read samples at 10 second intervals for 90 seconds at 412nm (subsequent level of baseline absorbance from reaction of DTNB with CoA-SH). Next, 10µl of oxaloacetate (cat# O4126) was introduced to each well to initiate the experiment to form 6-carbon citrate from two-carbon acetyl CoA with four-carbon oxaloacetate. The plate reader underwent the same protocol as above, which produced a linear plot of increasing absorbance for each sample (See figure 5.8 for examples). By subtracting the change in activity at baseline from the change in activity from the experiment, produced citrate synthase activity (CSA) levels. The formula enabled determination of citrate synthase/mitochondrial density in each sample:

$$\frac{CSA/min \times volume \times dilution\ factor}{Extinction\ coefficient(13.6) \times absorbance\ pathlength(0.552) \times volume\ of\ enzyme\ in\ sample} \times total\ protein$$

By doing this for every brain region from each experiment produced results that enabled the calculation of relative quantities and normalisation of synaptosomal mitochondrial densities across regions.

5.2.3 – Scanning Electron Microscopy of Synaptosomes

To validate the presence of synaptosomes isolated from the procedure outlined in section 5.2.1, SEM was implemented using a Zeiss Supra 40VP microscope. Images were taken of samples from IC and hippocampus from each animal (n=7; N=28). Samples were prepared by pipetting 1μl of synaptosome sample onto a 20mm circular coverslip (ThermoScientific) and distributed evenly by using another coverslip and gently pressing down until the whole coverslip was evenly covered in solution. The coverslip was then dried using a bench slide dryer (Elctrothermal) for 20 seconds at setting 6/10. To preserve the samples the coverslips were immersed in 150μls of 0.2% glutaraldehyde in 1M PBS and left at 4°C overnight to fix. The next day the coverslips were washed with 1M PBS twice for 2 minutes. Coverslips were immersed in 150μls of increasing concentrations of industrial methylated spirit in deionised water at 20, 40, 60 and 80% each for 30 minutes and twice at 100% for 30 minutes to dehydrate the samples. The samples were then left to dry in a closed case to minimise particle build-up. Once samples were dry, coverslips were placed, attached to 20mm aluminium pin stubs using a silver coating. The stubs were then coated with a thin layer of gold using gold splutter coating. This was improved by employing the silver-enhancement method, which involved enlarging the small diameter gold particles to optimise visualisation of the samples on the microscope (see

Scopsi *et al.* (1986)). The stubs were then placed into the Zeiss Supra 40VP. Initial images were taken at 1,000x along three 5mm increments across the diameter of the coverslip to develop an understanding of synaptosome density for each sample (Figure 5.3A-C). 10,000x images were then taken from each increment for region of interest analysis (Figure 5.3D-F). Image analyses were undertaken in FIJI (ImageJ) software (Abràmoff *et al.*, 2004). Three synaptosomes per image were subject to manual outlining using the contour tool in ImageJ for area, perimeter and circularity analyses using the measure plugin. Circularity measurements were calculated by using the formula: $\mathrm{Circularity} = 4\pi * \mathrm{area}/\mathrm{perimiter}^2$ (example $4\pi * 0.27\mu m^2/0.193^2 = 0.91$) with 1 being a perfect circle. A total of 236 synaptosomes in hippocampus (7- and 15-month wild type = 62 and 48 respectively, and Tg = 63 and 63 respectively) and 223 in IC (7- and 15-month wild type = 63 and 54 respectively and Tg = 52 and 54 respectively) were quantified.

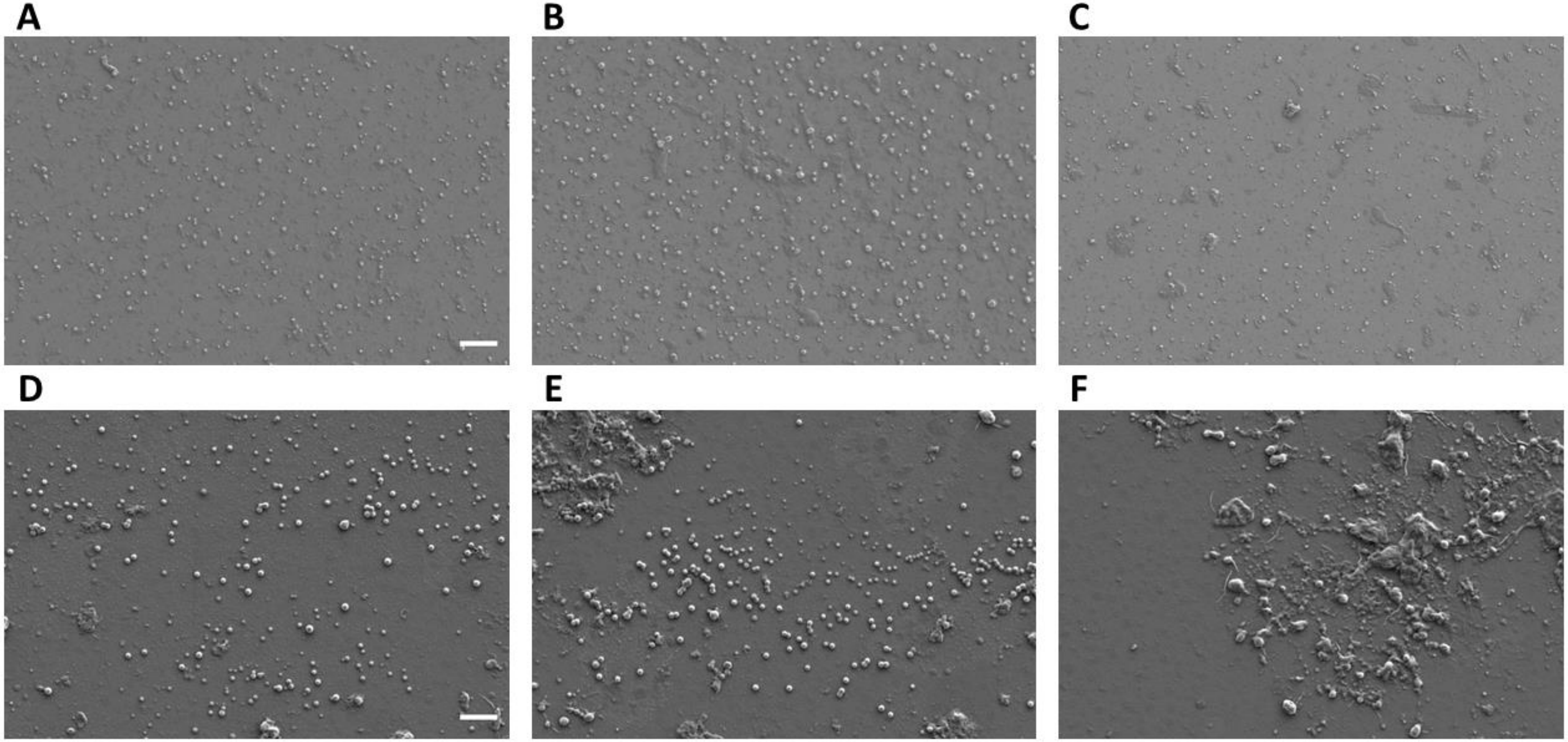

Figure 5.3. Example scanning electron micrographs from one brain region, validating synaptosome presence in samples. (A-C) 1,000x magnification images were taken of synaptosome densities at 5mm, equidistant distances from the centre to edge of the 20mm coverslip to estimate the quantity of synaptosomes presence within each sample. Scale bar in (A)_10µm, same in (B) and (C). (D-F – from A-C) 10,000x magnification images were then taken from regions of interest within each 1,000x image, to be used in individual synaptosome measurements of area, perimeter and circularity analyses. Scale bar in (D) 2µm, same in (E) and (F).

5.2.4 – Quantitative real time PCR analysis of *GAD65*, *SV2a*, *synaptophysin* and *Iba1*

Primers designed for quantitative real-time PCR (QRT-PCR) included four targets *GAD65*, *Iba1*, *SV2a* and *synaptophysin* and three housekeepers, *Cyc1*, *EIF4A2* and *GAPDH* (see Table 5.1 for design). Three animals per group (7- and 15-month wild type and Tg) were used in the experiments. Samples for molecular biology were obtained from the snap frozen right hemisphere obtained in section 5.2.1. The right hemisphere was taken out the -80°C freezer and placed in a cryostat (Leica CM3050 S) at a chamber temperature of -16°C and operating temperature of -18°C. The right hemisphere was frozen in the coronal plane, facing rostrally onto a specimen disc using OCT. Sections were then taken at 20μm intervals for immunohistochemistry (data not shown in this thesis), until the brain regions of interest were present. For brain region dissection for molecular biology, 200μm thick sections were taken on the cryostat and trimmed using a scalpel to dissect the regions of interest. To identify the regions of interest, initially the Paxinos and Watson rat atlas (2007) was used to identify (in order of first appearance in the rostro-caudal direction of sectioning) frontal cortex, hippocampus, auditory cortex, SC, IC and cerebellum. Photos were taken before each region of interest was cut to use as references for the remainder of experiments (Figure 5.4). All reagents used in the preparation of samples for QRT-PCR were from a Norgen Total RNA Purification Kit (Cat# 48400). Dissected brain regions were lysed in 2-mercaptoethanol in RL buffer (10:600) and homogenised by pipetting up and down until liquified, the samples were then stored at -80°C until RNA quantification. All steps undertaken for isolating RNA were followed using the protocol in the Norgen kit. The purity of RNA was quantified using a Nanodrop (Thermoscientific Nanodrop One^{c}). Equal amounts of RNA (5μg) from each brain region was then reverse transcribed (Quantinova SYBR green PCR kit cat# 208052) following the manufacturer's instructions. cDNA generated was then diluted 1:10 and specific primers were added to each brain region along with a no template control, then the experiment was initialised using a thermocycler (Bio-Rad CFX Connect Real Time System). After QRT-PCR, the samples were analysed using the Bio-Rad CFX Maestro software and quantified using double delta ct to identify the number of cycles needed to reach a fixed signal.

Gene	**Accession number**	**Forward primer**	**Reverse primer**
Synaptophysin	NM_012664.3	TCCCTCCACACTCCCGTTTG	GCAGAGGGTACAGGATCGGG
Glutamate decarboxylase 2 (*GAD65*)	NM_012563.1	CCAGGCTCATCGCATTCACG	TCTGTTCCGATCCCCAAGGC
Eukaryotic translation initiation factor 4A2 (*EIF4A2*)	NM_001008335.1	CCGCGGATTACAACAGAGAACAT	CTCTCTGCTGAATAGCTGAAGGC
Glyceraldehyde-3-phosphate dehydrogenase (*GAPDH*)	NM_017008.4	CAGTGCCAGCCTCGTCTCATA	CAAGAGAAGGCAGCCCTGGT
Cytochrome c-1 (*Cyc1*)	NM_001277194.1	GCCCCGGCATCTTCCATTAC	ACAGCATCACCTTTCGGCCT
Allograft inflammatory factor 1 (*Iba1*)	NM_017196.3	CTAAGGCCACCAGCGTCTGA	CCTGTTGGGCTTTCAGCAGT
Synaptic vesicle glycoprotein 2a (*SV2a*)	NM_057210.2	GAGTACCGGCGCATCACTCT	TCGGGCTGCATAGTCCACAG

Table 5.1. List of primers used for QRT-PCR analysis. Accession number correlates t exact gene from *rattus norvegicus.* Exact forward and reverse base sequences designed using NCBI nucleotide database https://www.ncbi.nlm.nih.gov/nucleotide/.

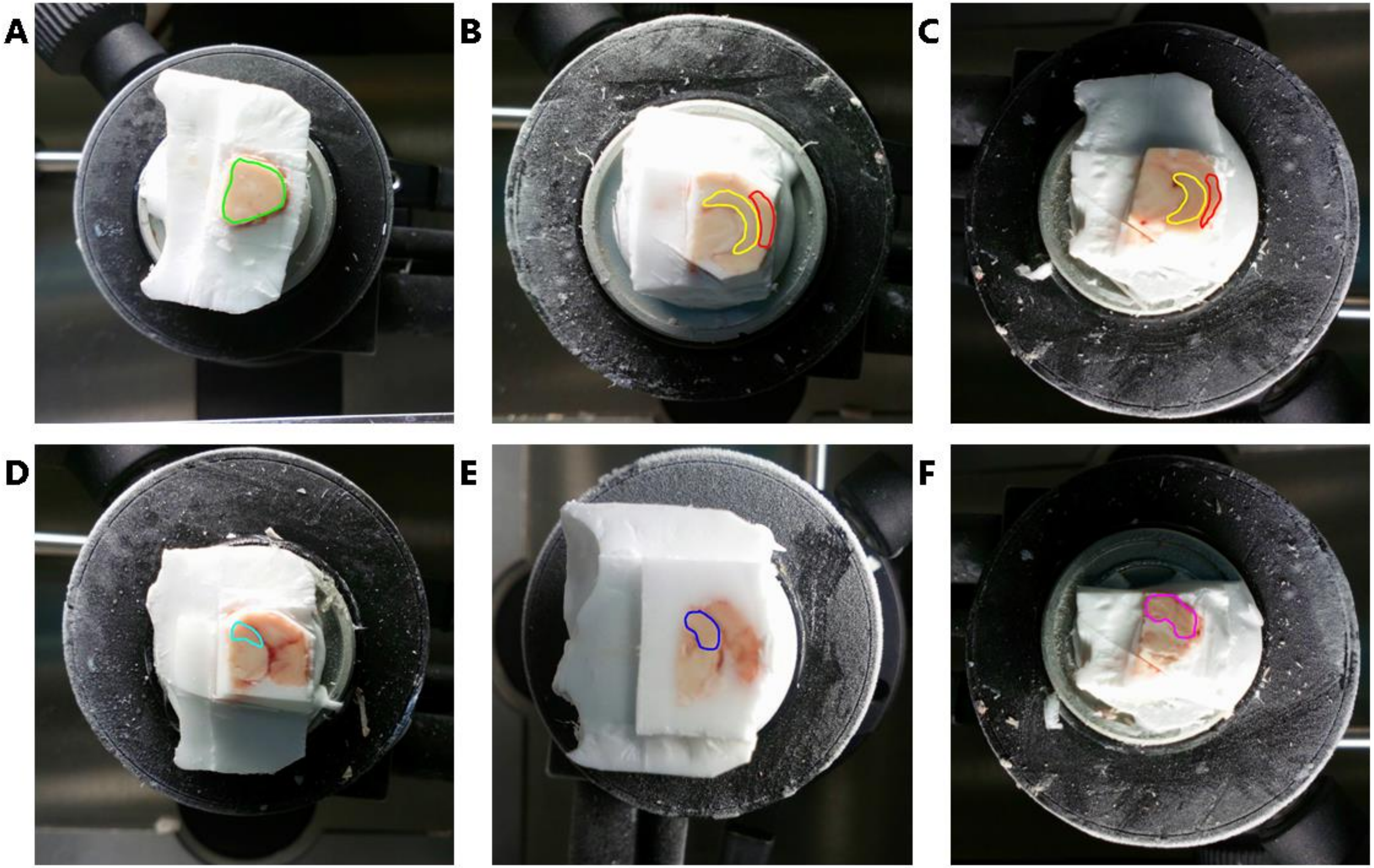

Figure 5.4. Reference images and respective contours outlining the specific regions dissected from (A) frontal cortex (green), (B&C) hippocampus (yellow)and auditory cortex (red), (D) superior colliculus (cyan), (E) IC (blue) and (F) cerebellum (magenta).

5.2.5 – Statistical analyses

Results from these analyses were recorded in Microsoft Excel and plotted using Prism (GraphPad) and statistically analysed using SPSS (v24, IBM). All line graph measurements are averaged, and the error presented as standard error of the mean and all box and whisker and violin plots are presented as median and standard deviation. For physiological Seahorse and molecular biology analyses, group sample size (n) in the text represents individual animals and in the anatomical SEM analyses represents individual synaptosomes. Significance was set to $p<0.05$ and determined using 3-, 2- and 1-factorial between groups ANOVA to measure the potential effects of brain region, age and genotype, as appropriate. *Post-hoc* Tukey HSD tests were undertaken where appropriate and effect sizes were determined by partial eta squared for 3- and 2- factor ANOVA and eta squared analyses for 1-factor ANOVA. Effect sizes were determined due to the nature of physiological analysis being more variable, to determine the validity of the significance found between results. The effect sizes were used to quantify the strength of the relationship between factors, small effect sizes refer to a weak relationship (<0.01), medium that there is a good relationship (<0.09) and large indicates a strong relationship (>0.25). Weak relationships between factors infer that the probabilities derived from the tests have reduced validity. Significance between factors from *post-hoc* analyses are either written in text above the figures or are displayed in figures as stars (*= $P\leq0.05$; **= $P\leq0.005$; ***= $P\leq0.001$; **** $P\leq0.0001$).

5.3 – Results

5.3.1 – Physiological Analysis of TgF344-AD Model

5.3.1.1 – Oxygen consumption rates are elevated in the TgF344-AD model compared to wild type controls

To understand age-dependent changes in synaptic metabolism across different regions of the brain in the Tg model, synaptosomal OCRs were manipulated and quantified by the addition of numerous substrates, which collectively enabled the measurement of different aspects of mitochondrial functioning (see Figure 5.5 for overview).

Overall, OCRs were consistently higher across all time points in the Tg 15-month-old groups (Figure 5.6). Oligomycin had the opposite effect to results observed in Figure 5.5 in the Tg 15-month old groups, whereby there was an increase in OCR, which correlates to a decrease in ATP production. Hippocampus, frontal cortex and IC followed similar trends across factors. OCRs were highest overall in the auditory cortex and frontal cortex and there were no differences between groups in the cerebellum.

Basal respiration was highest in the 15-month Tg auditory cortex, reaching 177.7±63.4 pmol/min, followed by the 15-month Tg superior colliculus with 157.7±70.8 pmol/min. All brain regions demonstrated a decrease in ATP production at the 15-month old time point, this was most prominent in hippocampus (21.6±29.8 pmol/min). Non-mitochondrial respiration was highest in the 15-month-old superior colliculus and auditory cortex (131.5±144.6 pmol/min and 124.5±85.5 pmol/min respectively). Maximal respiration displayed the largest OCR increase in the Tg 7-month old group frontal cortex, whereby the OCR more than doubled as a result (134±35 pmol/min).

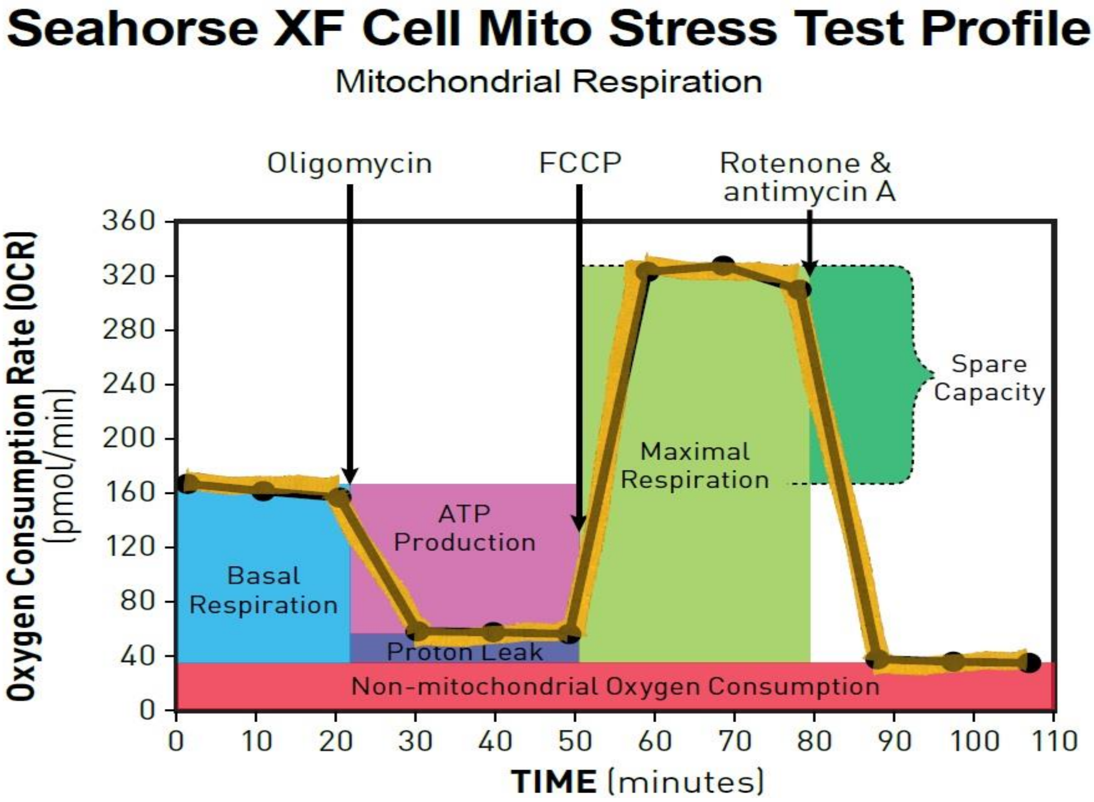

Figure 5.5. Model trace of OCRs taken from the Agilent Report Generator User Guide as an example to visualise how the different parameters of synaptosome mitochondrial functioning were measured. Basal respiration (cyan) is determined by averaging the initial three time points of OCRs. ATP production (magenta) is determined by the addition of the antibiotic Oligomycin, which inhibits ATP synthase resulting in the inability to convert ADP to ATP. The reduction in ATP production gives a measure of production. Next, adding the protonophore FCCP causes uncoupling of oxidative mitochondrial phosphorylation, by transporting protons across the mitochondrial membrane, resulting in the generation of the maximal oxygen consumption capacity (green). Finally, by together adding the pesticide Rotenone and the antibiotic antimycin A to the samples, both result in the inhibition of protons to cross the mitochondrial electron chain. Any OCRs still present must be as a result of non-mitochondrial oxygen consumption (red). In addition, by finding the difference between ATP production and non-mitochondrial oxygen consumption gives a measure of the protons leaking through the mitochondrial chain as a quantification of mitochondrial inefficiency (proton leak (blue)). Also, by subtracting basal respiration from maximal respiration gives a measure of spare respiratory capacity (dark green).

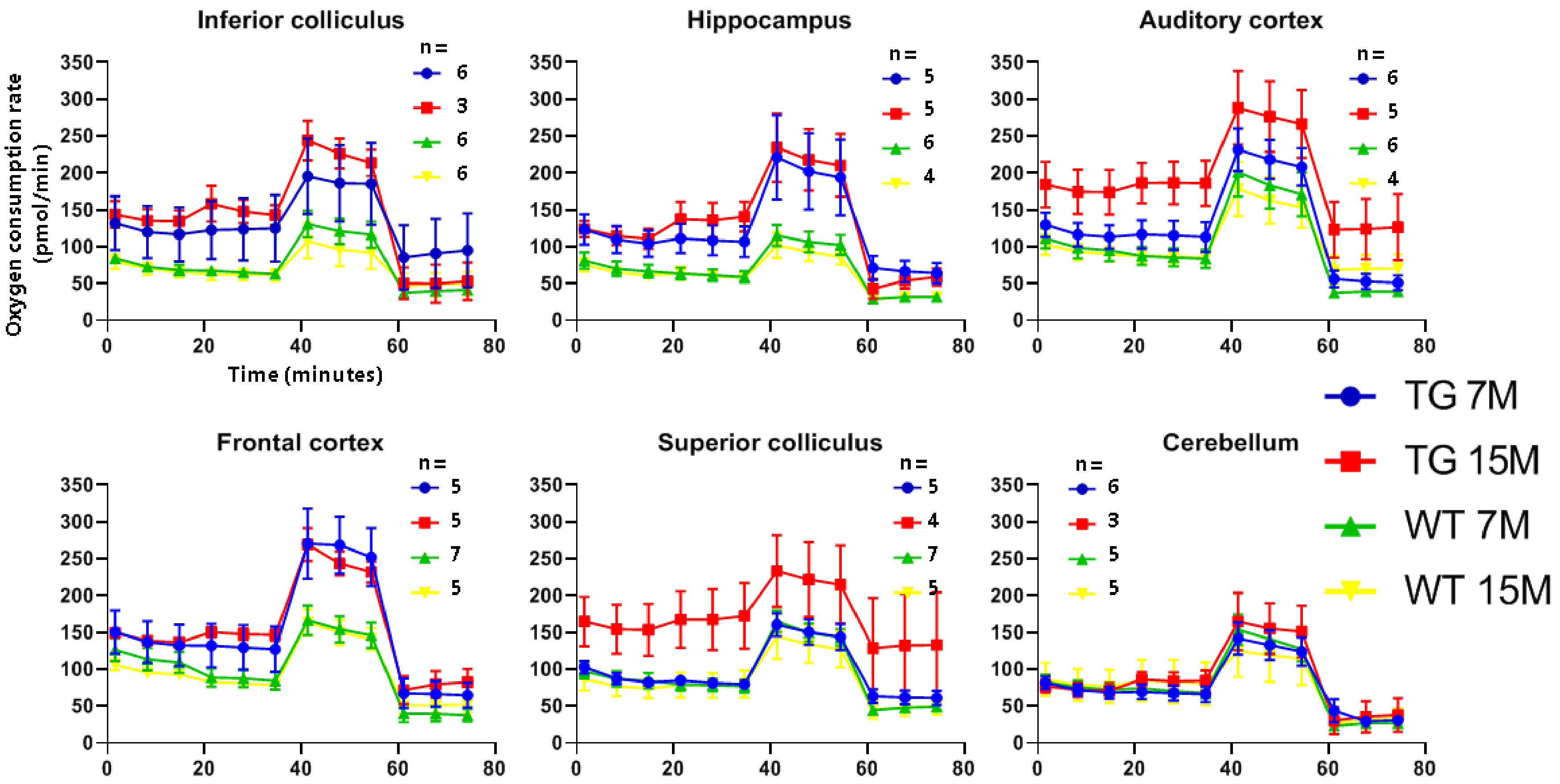

Figure 5.6. Seahorse mean OCR traces taken from 5µg synaptosomal fractions derived from each brain region. Notice that all traces do not demonstrate a profound decrease in OCR after the addition of Oligomycin, this trend is consistent with previous work investigating synaptosomal fractions (Flynn *et al.*, 2011); (Scott and Nicholls 1980). Across IC, hippocampus, auditory cortex and superior colliculus the Tg 15M group consistently has higher OCRs than the other groups, with the lowest readings in the wild type groups. Superior colliculus demonstrates a profound increase in OCR in the 15M Tg group compared to the other groups. IC, hippocampus and frontal cortex all share similar trends in OCR across all groups, with Tg groups being consistently higher than wild type. Cerebellum has the lowest OCRs across all brain regions and demonstrates similar responses across groups. Results presented as See figure 5.5 for reference on how to interpret mitochondrial function.

5.3.1.2 – Citrate synthase activity is highest in inferior colliculus, auditory cortex and cerebellum

When collecting different brain regions, there is substantial variability in tissue composition. A protein estimation was undertaken for each synaptosome sample to ensure that the level of protein was consistent, but this did not account for the underlying heterogenous synaptic densities found across brain regions. Therefore, citrate synthase activity experiments were undertaken on each sample to determine the level of mitochondria present (Figure 5.7&8).

Initially changes in baseline absorbance readings were taken from a cocktail of synaptosomes mixed with 1MTris-Cl (pH 7.4) and acetyl coenzyme-A to subtract from changes obtained from the catalytic reaction of the tricarboxylic acid cycle (Figure 5.7 baseline). The addition of oxaloacetic acid caused the catalytic reaction to occur resulting in a time dependent increase in absorbance (Figure 5.7 experiment). From the subtraction of baseline activity from the resultant absorbance of the catalytic reaction, measurements of citrate synthase activity were calculated (Figure 5.8). Citrate synthase activities were consistently highest in the IC, auditory cortex and cerebellum, with the highest levels reaching 57±55.4 nmols/min/μg in the 15-month Tg auditory cortex. Across groups, superior colliculus had the lowest citrate synthase activity, with the lowest level of 15.9± 7.9 nmols/min/μg found in the 15-month Tg group. The higher levels of citrate synthase activity observed in the 15-month Tg IC, auditory cortex and frontal cortex could be indicative of mitochondrial adaptation with age in the Tg model, but further investigation would need to be implemented to conclude this.

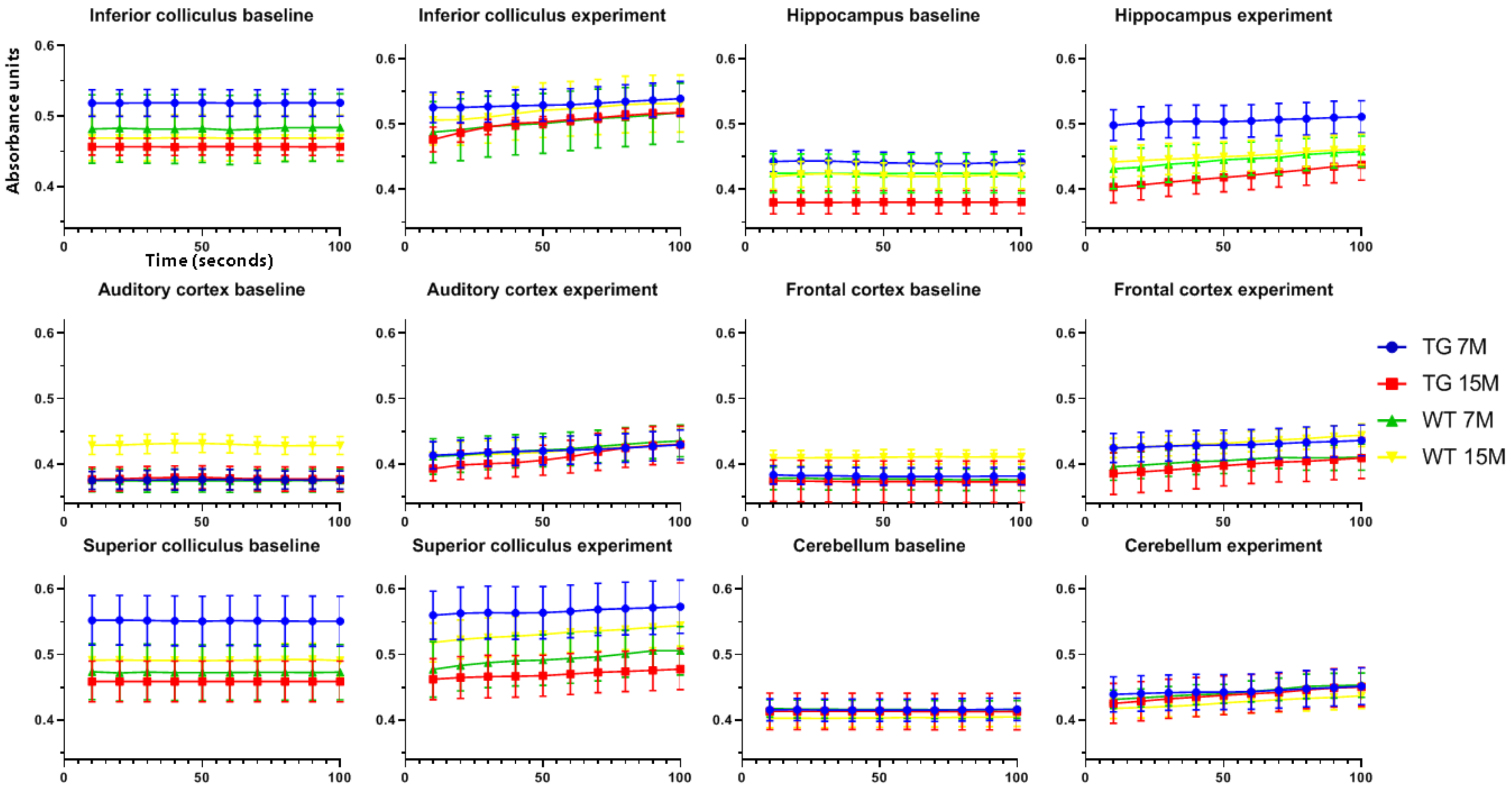

Figure 5.7. Process of measuring citrate synthase activity levels in synaptosome samples as a measure of mitochondrial density (n=7 each group). There was no statistical significance found between any groups. Each synaptosome sample was measured at baseline absorbance and then the experiment was initiated by the addition of oxaloacetic acid. To determine citrate synthase activity (CSA), the rate of change at baseline was subtracted from the rate of change of the experiment. To determine the amount of citrate synthase in the sample, the formula below was used. Across groups, IC, auditory cortex and cerebellum have highest levels of citrate synthase activity:

$$\frac{CSA/min \times volume \times dilution\ factor}{Extinction\ coefficient(13.6) \times absorbance\ pathlength(0.552) \times volume\ of\ enzyme\ in\ sample} \times total\ protein$$

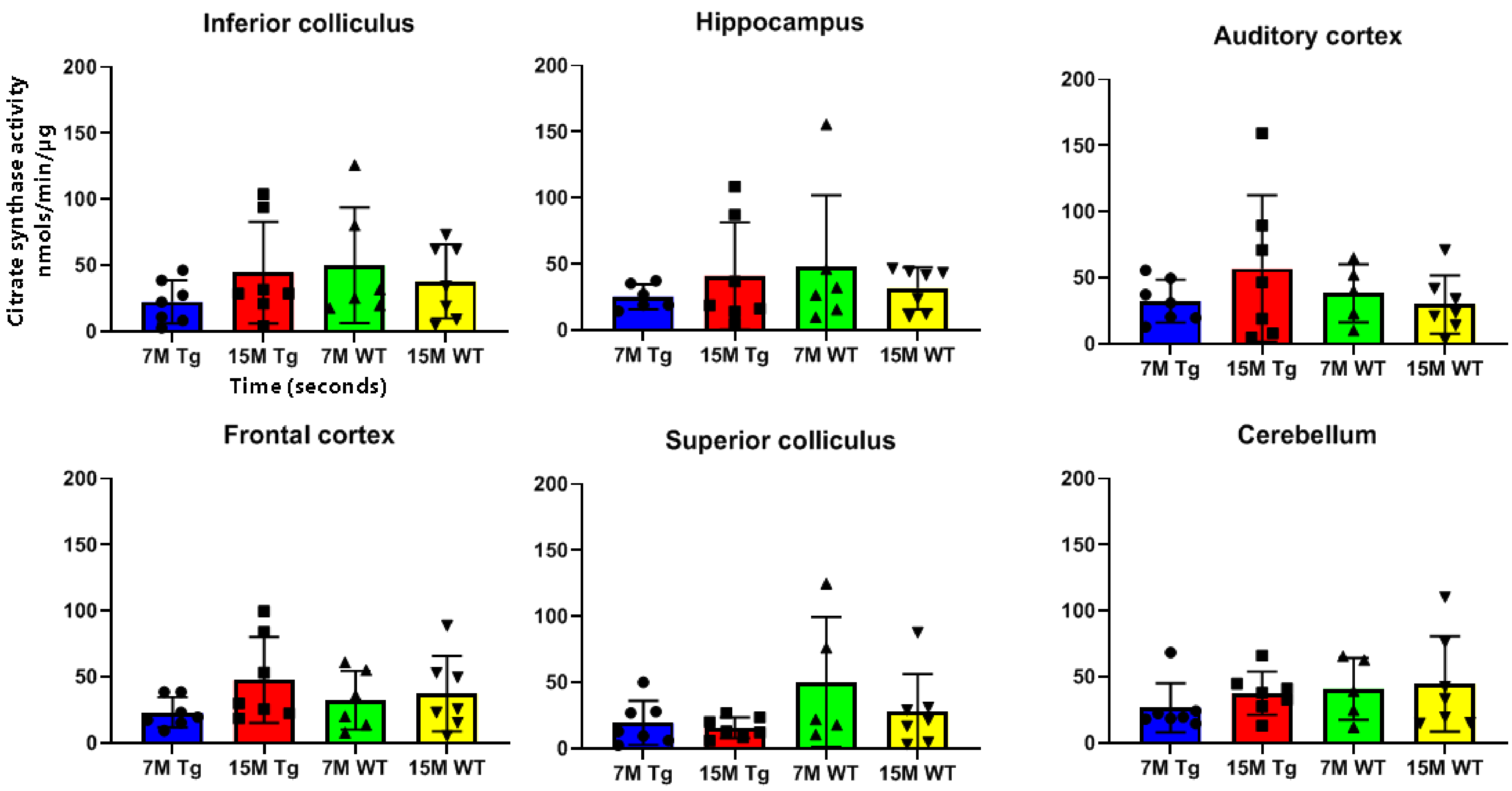

Figure 5.8. Calculated citrate synthase levels of protein across brain regions using the formula in Figure 5.7. Citrate synthase activity was highest in the 15-month Tg auditory cortex and lowest in 15-month Tg superior colliculus. Three-, two- and one-factor ANOVA uncovered no significant interactions or differences across groups. The calculated levels of citrate synthase activity from each brain region, from each experiment, were used to normalise the traces in Figure 5.6 accordingly to account for mitochondrial density variances between groups.

5.3.1.3 – Hippocampus demonstrated age-dependent increases in oxygen consumption rates in the TgF344-AD model

To account for possible differences in mitochondrial densities across brain regions, the raw OCRs were normalised by applying citrate synthase levels to produce rates relative to mitochondrial density, for each respective sample (Figure 5.9). These results show the normalised overall OCRs in the 15-month Tg groups are consistently highest in the hippocampus, auditory cortex and superior colliculus. The highest rates are found in the 15-month auditory cortex reaching 611.7±566.3 pmol/min. Hippocampus demonstrated an increase in OCR in response to the Oligomycin at 15-months in the Tg group. Area under the curve revealed that the total OCRs across the experiment were highest in the 15-month Tg group auditory cortex reaching 33,615±8182 pmol, followed by 15-month Tg superior colliculus with 32,006±3341 pmol.

Two-factor ANOVAs of OCRs across all brain regions revealed that together, genotype and age (F(1,264)=7.557, P=0.006), genotype and brain region (F(5,264)=3.962, P=0.002) and age and brain region (F(5,264)=4.768, P=<0.001) influenced OCRs. Partial eta squared analysis uncovered that the effect sizes were $p\eta^2=0.028$, $p\eta^2=0.070$ and $p\eta^2=0.083$ respectively, indicating that the effect sizes were modest. *Post-hoc* analysis revealed that hippocampus and IC were similar (P=1.000) and auditory cortex and frontal cortex were similar (P=0.972) and superior colliculus was different from all other regions (all P=<0.001). The most striking finding was found by an additional two-factor ANOVA hippocampus, which revealed an interaction between age and genotype influenced OCR (F(1,44)=14.768, P=<0.001) and a partial eta squared showed that the effect size was large ($p\eta^2=0.251$).

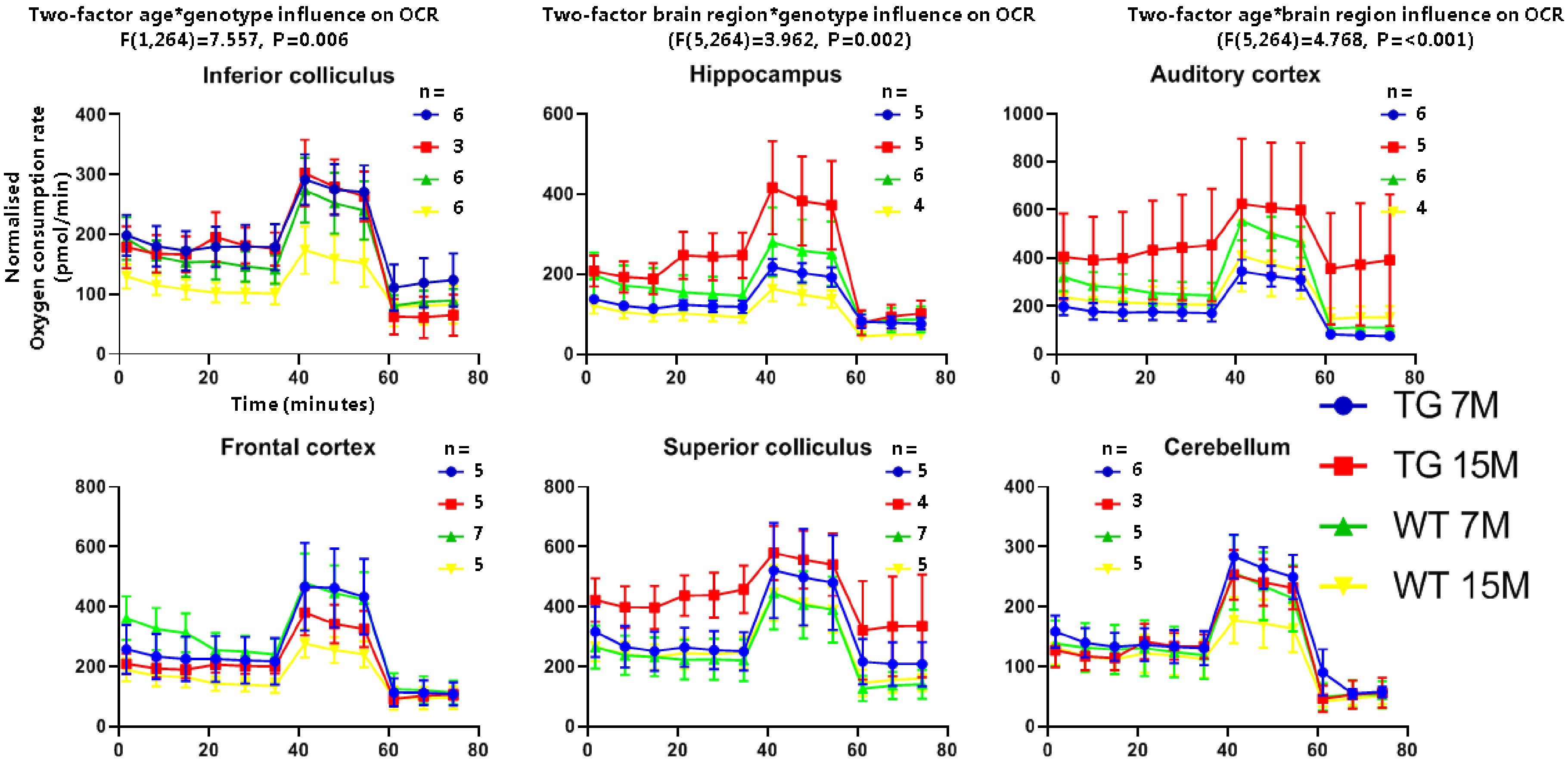

Figure 5.9. Traces of OCRs normalised to mitochondrial density from citrate synthase assays (Figure 5.7&8). Across hippocampus, auditory cortex and superior colliculus, the Tg-15-month groups have the highest OCRs. Superior colliculus has the highest OCRs across all brain regions in the Tg 15-month group. Both Tg groups are higher than the wild type in hippocampus and superior colliculus. Hippocampus demonstrates clear age-dependent differences in oxygen consumption. The wild type 15-month groups have the lowest OCRs in the IC, hippocampus, frontal cortex and cerebellum. In contrast to all other regions the 7-month wild type group is highest in cerebellum. See figure 5.5 for information on how to interpret mitochondrial function.

5.3.1.4 – Hippocampus undergoes compensatory age-dependent increases in basal respiration in the TgF344-AD model

In addition to the synaptosomal oxygen consumption readings, individual measures of mitochondrial function were calculated from the addition of different substrates and how they affected oxygen consumption (See figure 5.5 for an overview). The first readings across brain regions included quantifying and contrasting the oxygen consumption levels needed to maintain basal functioning before addition of any substrates that induced stress, this was the measure of basal respiration (Figure 5.10). Hippocampus and IC follow similar trends across all groups. In both superior and inferior colliculi and hippocampus, the highest levels of basal respiration were found Tg 15-month groups, which suggests increased demand to undertake basal functioning. This was in contrast to the cortical regions, where the 7-month wild type groups had the highest levels. Cerebellum rates remained consistent across cases. Superior colliculus had the highest overall basal respiration measurement of 270.1±219.4pmol/min OCR in the 15-month Tg group and had the lowest with 65.4±62.9pmol/min in the 7-month Tg group.

A two-factor ANOVA demonstrated age and genotype influenced basal respiration (F(1,103)=4.993, P=0.028) and a partial eta squared shows a medium effect size (η^2=0.046). Additional two-factor ANOVA of individual brain regions revealed an interaction between age and genotype influenced basal respiration in hippocampus (F(1,18)=5.844, P=0.027) and the effect size was large (pη^2=0.256). One-way ANOVA of individual regions, uncovered that frontal cortex was the only region to display an age-dependent decrease in basal respiration (F(1,18)=4.527, P=0.047) and an eta squared showed that the effect size was large (η^2=0.201),

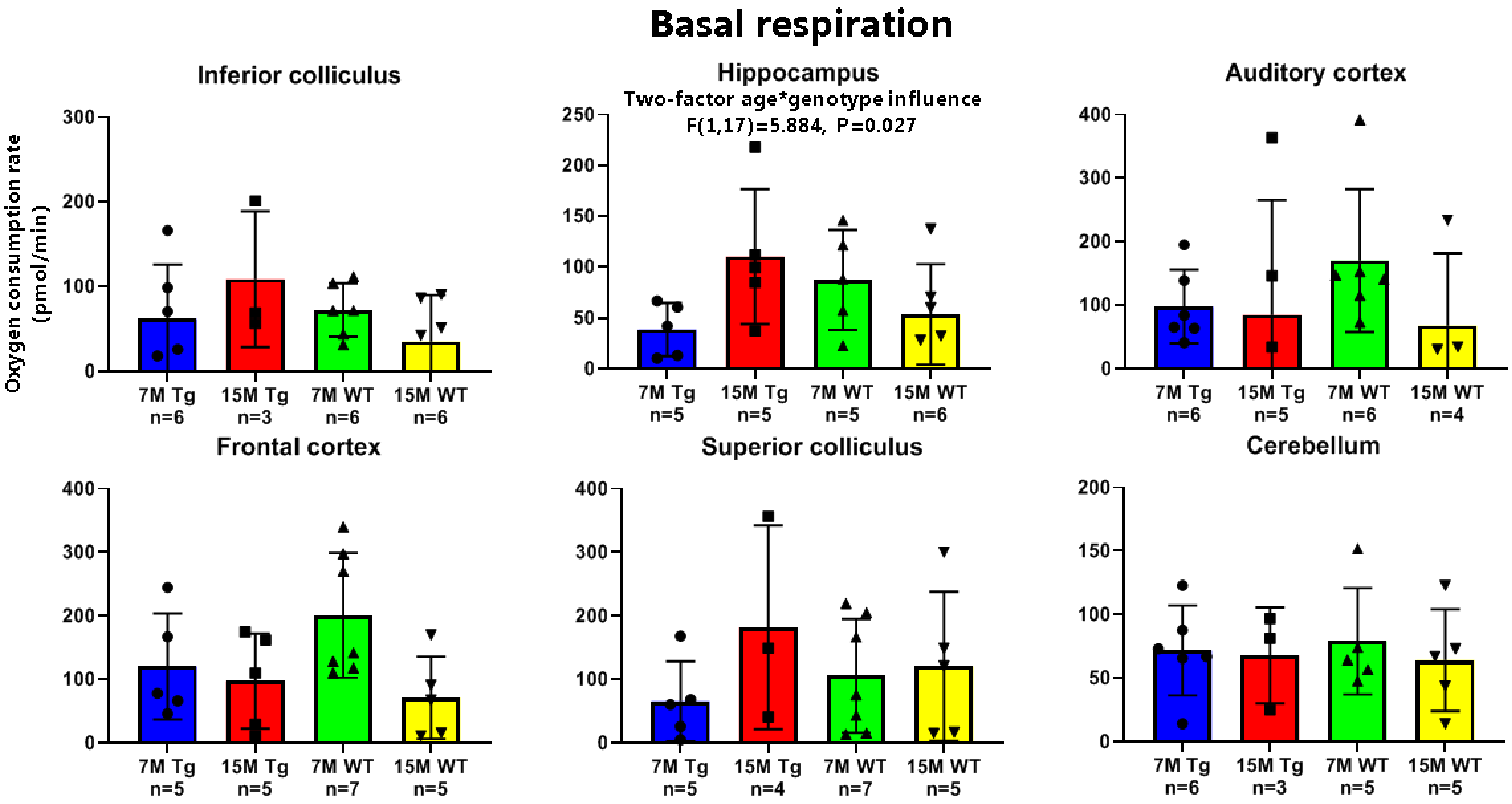

Figure 5.10. Basal respiration measurements derived from quantifying OCRs prior to addition of substrates as a measure of energy demand for basal activities. IC and hippocampus follow similar trends in basal respiration with the highest levels in Tg 15-month groups and the lowest in 15-month wild type. Superior colliculus has the highest overall basal rates in the 15-month Tg group and the lowest overall in the 7-month wild type. Auditory cortex and frontal cortex display similar trends across groups, both with the highest basal levels in the 7-month wild type. Cerebellum was unaffected by factors and remains consistent across all groups.

5.3.1.5 – Hippocampus undergoes an age-dependent increase in proton leak in the Tg model

Another measurement derived from the Seahorse mitochondrial stress analysis, includes the proton leak, which is a measurement of the inefficiency of the mitochondrial membrane to transport proteins across the matrix and the 'leaking' of protons outside the mitochondrial membrane (Figure 5.11).

The largest trends of increased proton leak are found in the IC, hippocampus, auditory cortex and superior colliculus, with the largest level of proton leak in the auditory cortex reaching 188.4±267.9 pmol/min. Proton leak in cerebellum was unaffected across factors. The lowest level of proton leak was found in the IC 15-month wild type group with an OCR of 38.1±32.8 pmol/min.

Statistical analysis of all brain regions demonstrated a two-factor interaction between age and genotype influencing proton leak (F(1,103)=9.113, P=0.003) and a partial eta squared showed that the effect size was small ($p\eta^2$=0.081). Two-factor ANOVA of individual brain regions revealed age-dependent increases in the Tg model hippocampus (F(1,17)=11.563, P=0.003) and the effect size was large ($p\eta^2$=0.405).

These results show that proton leak in the hippocampus of the Tg model is affected by age-dependent changes indicative of mitochondrial dysfunction.

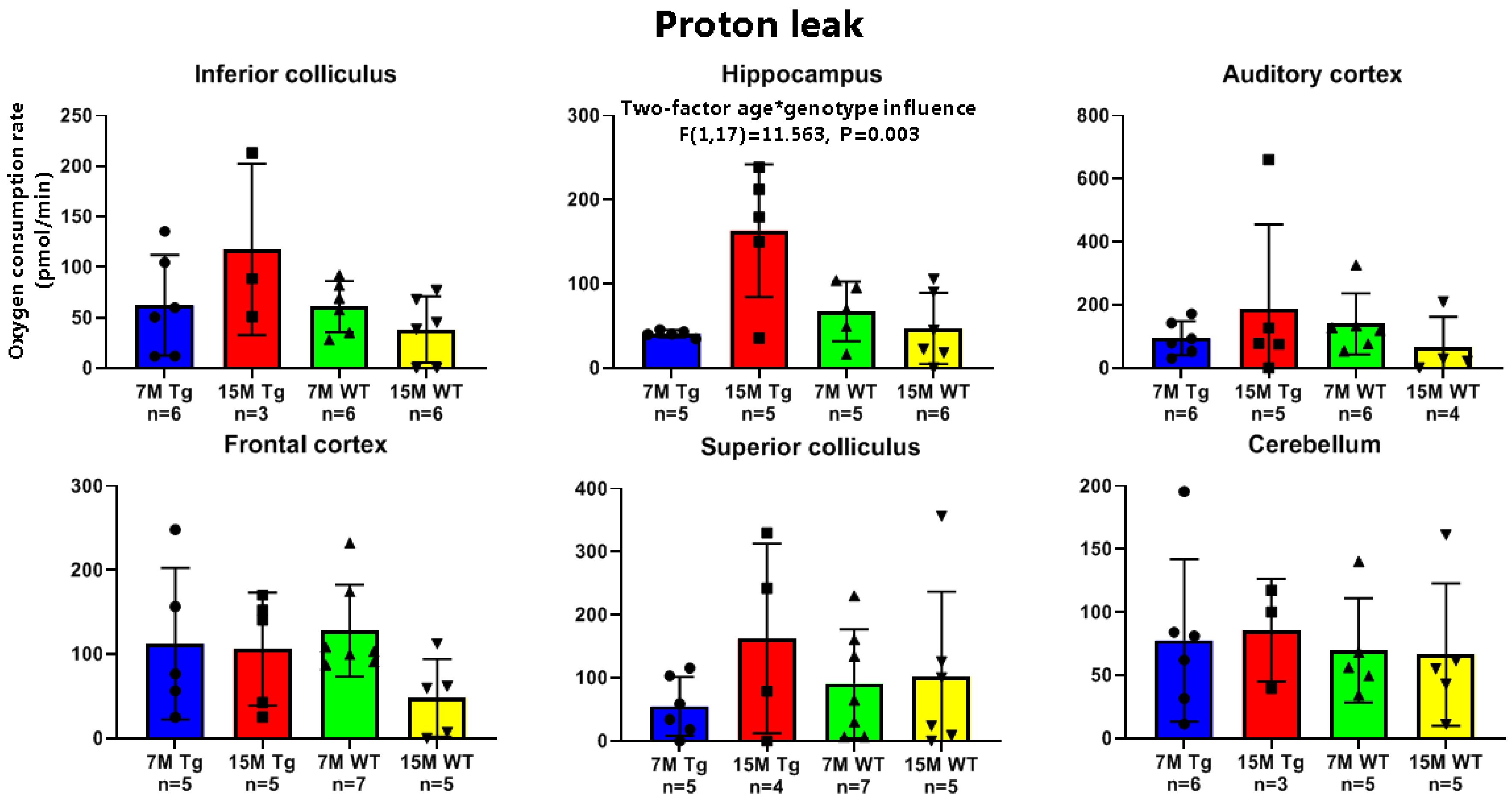

Figure 5.11. By subtracting the non-mitochondrial oxygen consumption from the basal respiration of synaptosomes, provides a measure of mitochondrial intactness. Any reading is as a result of protons leaking outside the mitochondrial membrane and mitochondrial membrane inefficiency. Proton leak is elevated in the 15-month Tg groups of IC, hippocampus, auditory cortex, superior colliculus and cerebellum. IC, hippocampus and auditory cortex share similar trends in proton leak, with hippocampus having the most profound increase in proton leak at 15-months in the Tg model. These results suggest that there are age-dependent decreases in mitochondrial membrane intactness of the IC, hippocampus and auditory cortex indicative of mitochondrial dysfunction within synaptosomes.

5.3.1.6 – ATP production is substantially reduced from 7-months wild type to 15-month Tg rats in auditory cortex and frontal cortex

To identify what constituted ATP production from the normalised OCR traces, the response of blocking ATP synthesis by the addition of the antibiotic Oligomycin was measured (Figure 5.12). In the IC, hippocampus, auditory cortex, frontal cortex and cerebellum, the 7-month wild type groups all had the highest levels of ATP production. Frontal cortex has the highest ATP production across all regions in the 7-month wild type group, producing 72.5±60.4 pmol/min oxygen. In contrast, across all groups the Tg 15-month groups had the lowest levels of ATP production, with diminished production found in the Tg-15-month cerebellum with 0±0 pmol/min production. These diminished readings more than likely do not emulate a real physiological response, however, they are indicative of mitochondrial dysfunction.

A two-factor ANOVA showed that genotype and brain region influenced ATP production (F(5,106)=3.943, P=0.003) and a partial eta squared demonstrated that the effect size was medium ($p\eta^2$=0.161). In auditory cortex and frontal cortex, one-factor ANOVAs revealed that genotype independently influenced ATP production (F(1,17)=6.630, P=0.022 and F(1,18)=8.089, P=0.011 respectively) and eta squared analysis demonstrated that the effect sizes were large (η^2=0.272 and 0.310 respectively).

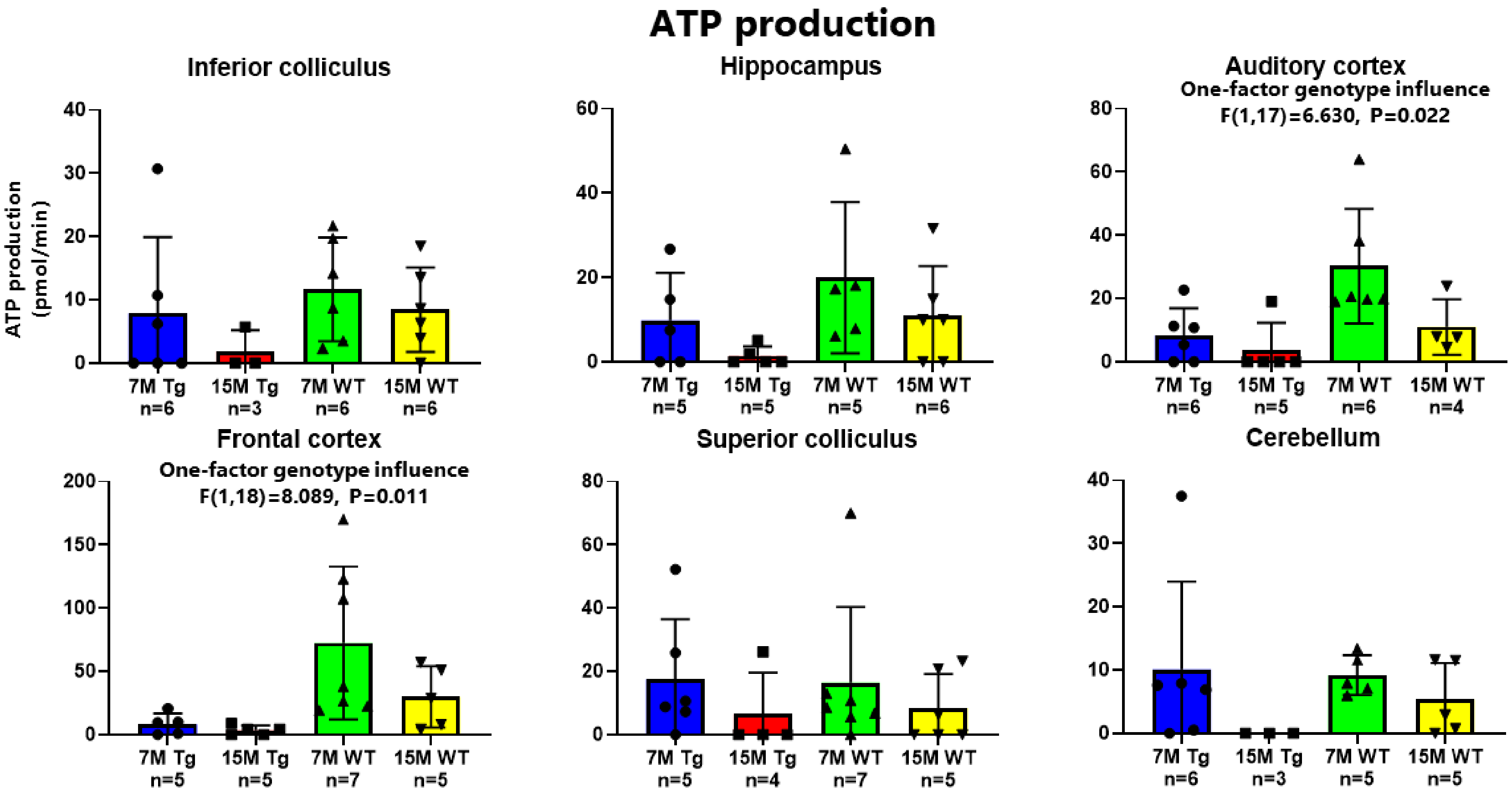

Figure 5.12. ATP production of synaptosomes derived from the inhibition of ADP conversion into ATP by the antibiotic Oligomycin. 7-month wild type groups across IC, hippocampus, auditory cortex, frontal cortex and cerebellum have the highest level of ATP production, in contrast to the 15-month TG groups. Frontal cortex has the highest level of ATP production in the 7-month wild type group. All groups, excluding superior colliculus demonstrate similar trends in ATP production across all groups. ATP production in superior colliculus follows the opposite trend to all other regions, which could provide insight into the much higher overall OCRs.

5.3.1.7 – The efficiency of synaptosomal mitochondria to couple oxidation to phosphorylation, decreased in the 15-month Tg group of all regions

To determine the ability of synaptosomes to couple oxidation to phosphorylation, the ATP production rate was divided by the basal rate of respiration, which was a measure of coupling efficiency (Figure 5.13). Interestingly, across all brain regions there was no heterogeneity in coupling efficiency, all regions displayed the lowest readings in the Tg 15-month and the highest efficiency in the 7-month wild type groups. Frontal cortex showed the highest coupling efficiency across all brain regions with 31.6±16.2% in the 7-month wild type group and cerebellum demonstrated diminished efficiency. These diminished readings more than likely do not emulate a real physiological response, however, they are indicative of mitochondrial dysfunction.

Two-factor ANOVA revealed an interaction between genotype and brain region that influenced coupling efficiency (F(1,106)=3.943, P=0003) and a partial eta squared showed that the effect size was medium ($p\eta^2$=0.161). In addition, a one-factor ANOVA of individual brain regions uncovered that auditory cortex and frontal cortex were the only regions to demonstrate a genotypic influence on coupling efficiency (F(1,17)=6.371, P=0.022 and F(1,18)=8.087, P=0.011 respectively) and an eta squared showed the effect sizes were medium and large (η^2=0.122 and η=0.310 respectively).

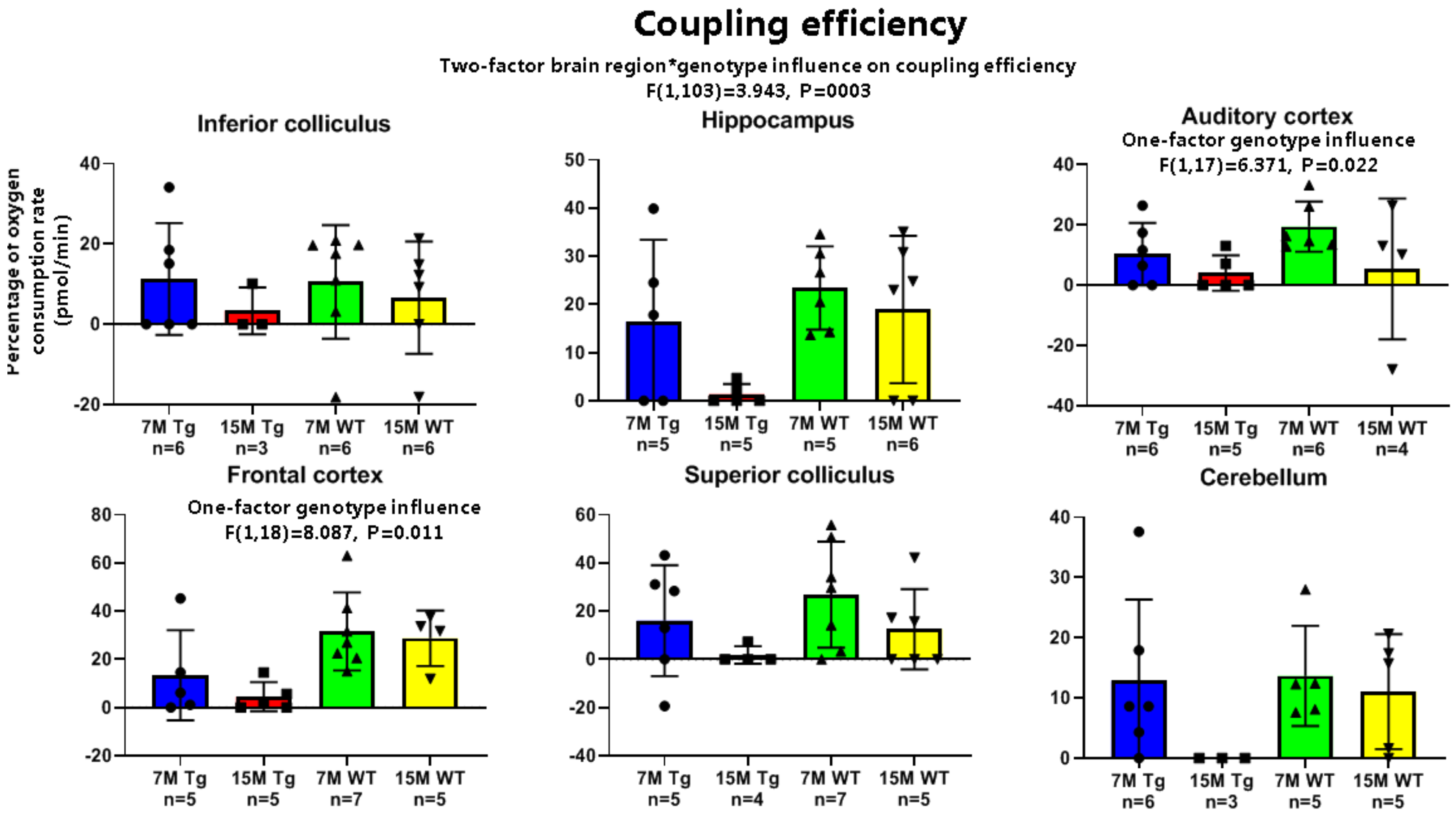

Figure 5.13. Dividing the rate of ATP production by the basal respiration rates provides an estimation of mitochondrial coupling oxidation to phosphorylation as a measure of synaptosomal coupling efficiency. The coupling efficiency of all measured regions of the brain was ubiquitously distributed across groups. 7-month wild type had the most efficient mitochondrial, which diminished in the 15-month Tg groups. The most efficient mitochondria were found in the 7-month wild type superior colliculi and in the 15-month Tg cerebellum group the efficiency was negligible. These results demonstrate that the efficiency of mitochondria in synaptosome is similarly affected across the brain. These results should be treated with caution as the equation that produces coupling efficiency responses does not incorporate negative values, however, these results do demonstrate that there is significant dysfunction of synaptosome mitochondria in the 15-month Tg group.

5.3.1.8 – Inferior colliculus and hippocampus demonstrate similar age-dependent increases in maximal respiration in the Tg model

Adding the ionophore FCCP to the synaptosome samples as a phosphorylation uncoupler, caused the uncoupling of ATP synthesis and resulted in hydrogen ions to traverse through the mitochondrial membrane. This caused the synaptosomes to respire at maximal oxidative capacity, enabling the measurement of maximal respiration (Figure 5.14).

Hippocampus and IC follow similar trends in maximal respiration across groups. Maximal respiration in IC and hippocampus was highest in the 15-month Tg groups. The highest overall respiration was found in the 7-month wild type auditory cortex reaching 450±156.5 pmol/min. In contrast, the lowest rate was found in the 15-month wild type auditory cortex, with 123±36.2 pmolmin.

ANOVA of all brain regions revealed a two-factor interaction of age and genotype that influenced maximal respiration (F(1,106)=5.125, P=0.025) and a partial eta squared showed that the effect was medium sized ($p\eta^2$=0.046). Two-factor ANOVA of individual brain regions uncovered that IC and hippocampus independently demonstrated age-dependent increases in maximal respiration in the Tg model (F(1,17)=5.088, P=0.038 and F(1,17)=5.864, P=0.027 respectively) and the effect sizes were large ($p\eta^2$=0.230 and 0.256 respectively). These results demonstrate that the mitochondria in IC and hippocampus undergo similar increases in the maximal oxidative capacity in the Tg model with age.

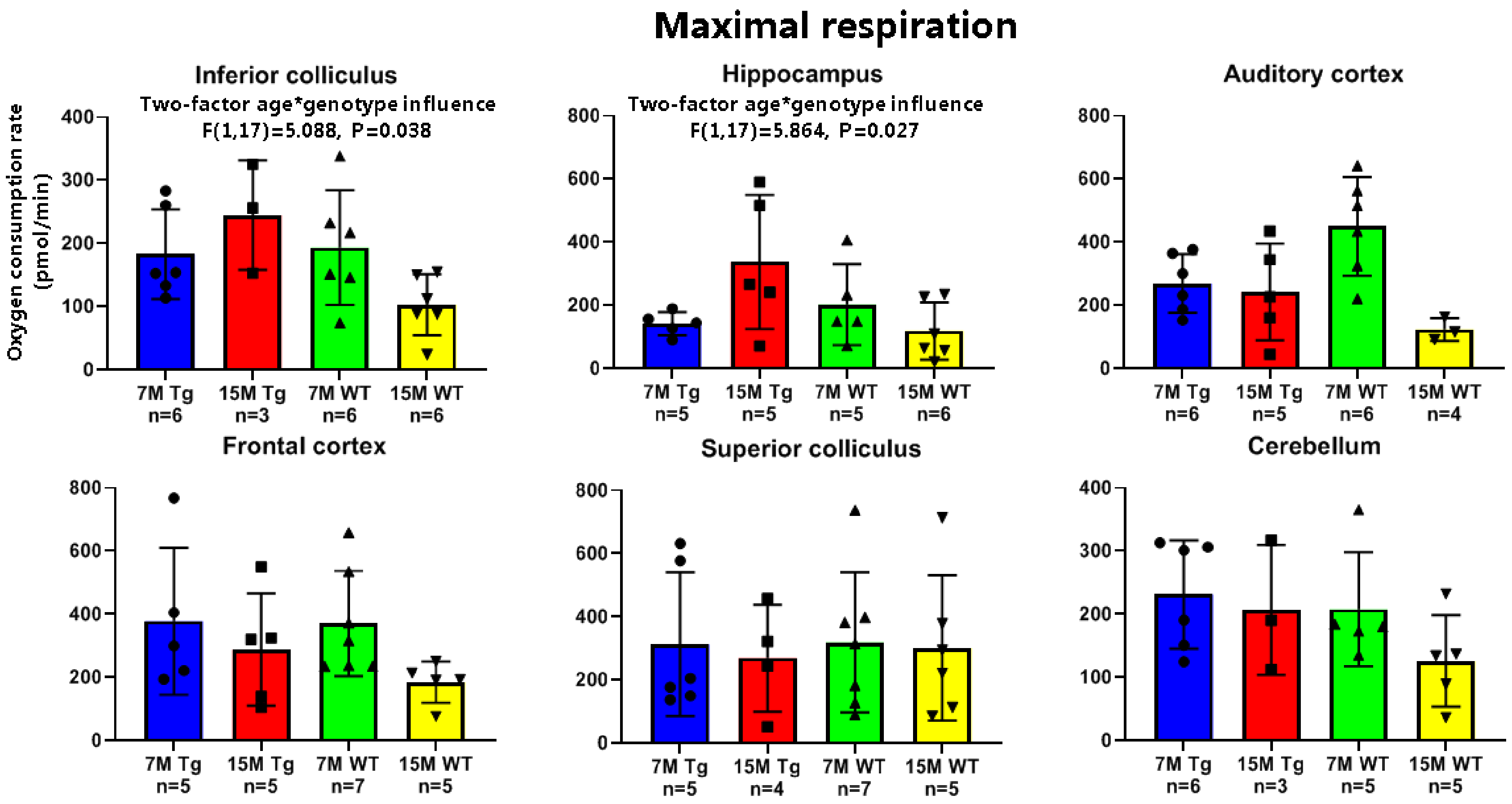

Figure 5.14. Boxplots displaying the culmination of adding FCCP to uncouple oxidative phosphorylation of the mitochondrial membrane of synaptosomes resulting in maximal oxidative respiration. Maximal respiration was highest and lowest in the auditory cortex 7-month wild type and 15-month wild type respectively. IC and hippocampus demonstrated similar trends in increasing maximal respiration at 15-months in the Tg groups. Interestingly, auditory cortex demonstrated the largest overall OCRs in the 15-month Tg model (see figure 5.5), however maximal respiration is an interdependent value and due to the high levels of non-mitochondrial respiration (see figure) hippocampus demonstrates the highest maximal respiration in the 15-month Tg group. These results suggest there is an increased mitochondrial maximal oxidative respiration present in the 15-month Tg rat model in IC and hippocampus.

5.3.1.9 – Non-mitochondrial respiration was unaffected by increasing age in the Tg model

From the traces of normalised OCRs (Figure 5.6) it can be noted that there are differences in trends across factors. By adding the pesticide rotenone and antibiotic antimycin A to mitochondrial samples, causes inhibition of mitochondria to respire, which results in any OCRs present are due to non-mitochondrial respiration. This approach enabled the identification of the influence of non-mitochondria to the overall results (Figure 5.15).

Surprisingly, non-mitochondrial rates were not significantly influenced by the different factors. The highest level of non-mitochondrial respiration reached 209.8±147 pmol/min OCR in the 15-month Tg superior colliculus. The cerebellum had the lowest levels of non-mitochondria across all regions and had the lowest overall consumption in the 15-month wild type group with 37.8±20.4 pmol/min OCR.

A one factor analysis across all brain regions revealed that brain region was the only factor to influence non-mitochondrial respiration (F(5,105)=3.647, P=0.004) and an eta squared analysis showed that the effect was medium sized (η^2=0.148). *Post-hoc* analysis contrasting the brain regions uncovered that the difference observed was between superior colliculus with hippocampus (P= 0.050) and cerebellum (P=0.020). This lack of influence that age and genotype have on non-mitochondrial levels across samples, suggests that effects of genotype and age are as a result of mitochondrial dysfunction, thus providing validity to all measures and claims of metabolic dysfunction.

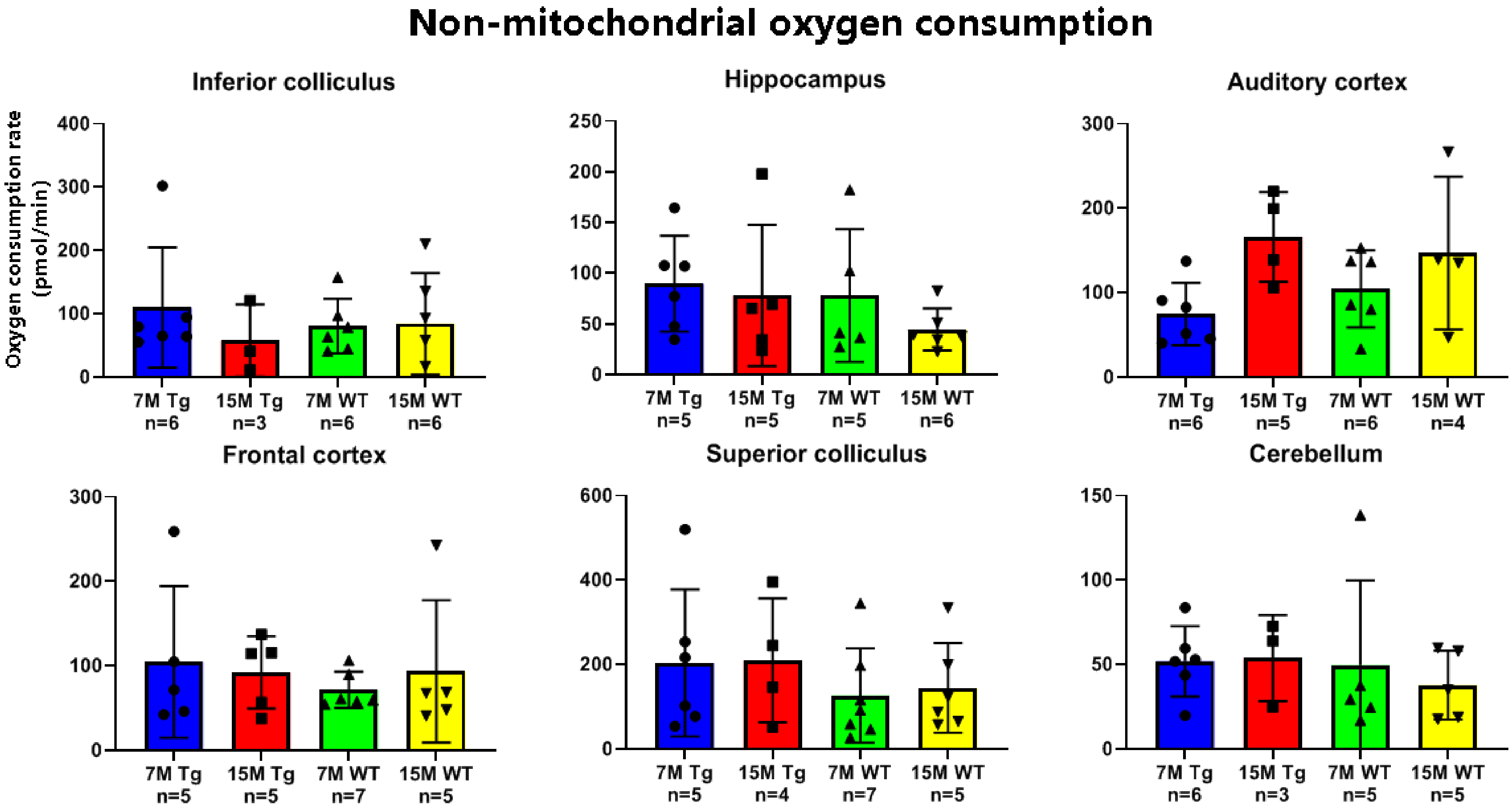

Figure 5.15. To measure the level of non-mitochondrial oxygen consumption of synaptosomes, the pesticide rotenone and antibiotic antimycin A were added, which together block mitochondrial oxygen production. Non-mitochondrial respiration was highest in the 15-month old Tg superior colliculus compared to the lowest in 15-month wild type cerebellum. Non-mitochondrial respiration did not vary substantially across all brain regions.

5.3.1.10 – Spare respiratory capacity differed across sub regions, but remained unaffected by age in the Tg model

To identify if the synaptosomal mitochondrial capacity changed across factors, analysis of spare respiratory capacity was implemented. The spare respiratory capacity is derived from subtracting the basal respiration rate from the maximal respiration (See figure 5.5). Spare respiratory capacities of groups varied across brain regions (Figure 5.16). The highest capacities were found in the 7-month wild type auditory cortex with 279.7±107.3 pmol/min followed by 257±159 pmol/min in the 7-month Tg frontal cortex. The smallest respiratory capacities were found in the 15-month wild type cerebellum with 61.6±32.1 pmol/min and 15-month wild type hippocampus reaching 65.3±53.5 pmol/min.

One-factor ANOVA across all brain regions revealed that brain region influenced spare respiratory capacity (F(5,103)=3.936, P=0.003) and an eta squared analysis showed that the effect size was small (η^2=0.160). *Post-hoc* analysis uncovered that the differences in brain region were attributed to superior colliculus differing from cerebellum (P=0.047) and IC (P=0.014). There are no statistical age or genotype influences on individual brain regions.

These results suggest, unlike the other mitochondrial analyses, that there are no age-dependent or genotype influences on spare respiratory capacity, which suggests that this measurement is maintained across brain regions in this model.

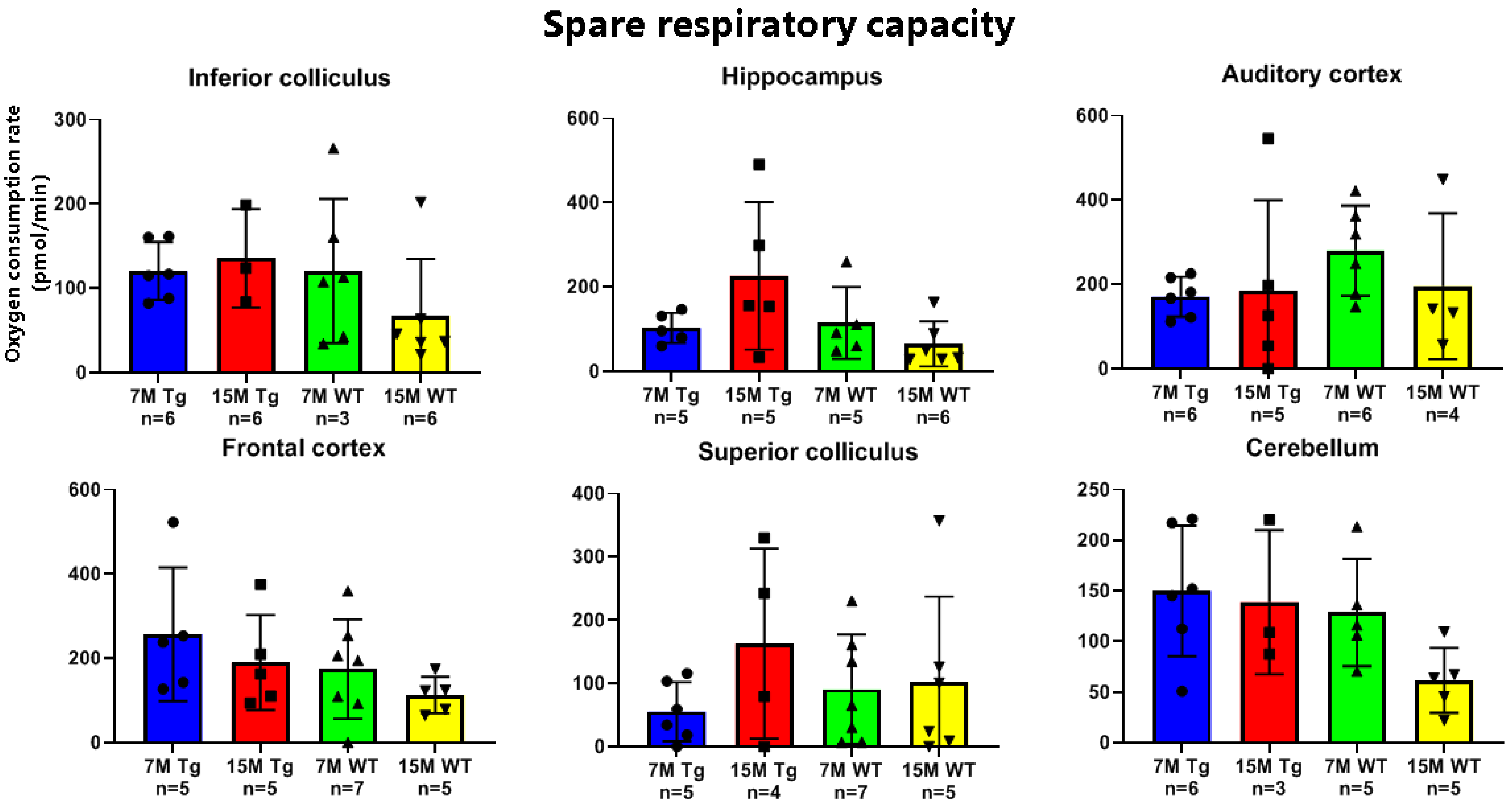

Figure 5.16. Subtracting basal respiration from maximal respiration provided a measure of the respiratory capacity of mitochondrial in synaptosomes. Spare respiratory capacity was highest in the 7-month wild type auditory cortex and lowest in the 15-month wild type cerebellum. There was increased capacity in the IC, hippocampus and superior colliculus, albeit not substantial. Respiratory capacity remained largely unaffected by age and genotype, which suggests that synaptosome mitochondrial dysfunction, is not attributed to an increased spare respiratory capacity.

5.3.2 – Anatomical Analysis of TgF344-AD Model

5.3.2.1 – Synaptosome area and perimeter substantially decreased with age in the Tg model inferior colliculus

There is currently a paucity of anatomical investigations into synaptosome structure in the literature, which is as a result of the difficulty of isolating synaptosomal fractions. This Chapter provides thorough anatomical quantification of individual synaptosomes through using SEM. Initially, SEM was used to visualise whether synaptosomes were present in the samples (Figure 5.17A). After identifying that synaptosomes were present, they were also identified to be heterogenous in morphology. To quantify these differences, region of interest analysis was undertaken on synaptosome samples from 7- and 15-month wild type and Tg IC and hippocampus. Analyses were taken using the measure function in ImageJ to produce area, perimeter and circularity measurements. Synaptosomes in micrographs were first isolated (Figure 5.17B) and cropped. Using pixel inspector in ImageJ produced a table of pixel intensities (Red box in Figure 5.17B), the borders of the synaptosomes were determined by using the formula in Figure 5.17C and then the perimeter was manually outlined using the contour tool (Figure 5.17D).

Interestingly, areas differed across groups and brain regions (Figure 5.18A&B), with the largest synaptosomes present in the 7-month Tg IC, reaching 0.400±0.204μm^2 opposed to the lowest with 0.216±0.124μm^2 in the 15-month Tg group. A three-factor ANOVA revealed that age, genotype and brain region interacted and influenced synaptosome area (F(1,453)=11.069, P=0.001) and a partial eta squared showed that the effect size was small (pη^2=0.024). A further two-factor ANOVA including both brain regions demonstrated an interaction between age and genotype influenced synaptosome area (F(1,453)=4.593, P=0.033) and a partial eta squared showed the effect size was below small ($p\eta^2$=0.002). Statistical analysis of IC uncovered a two-factor interaction between genotype and age on synaptosome area (F(1,220)=12.835, P=<0.001) with a medium effect size ($p\eta^2$=0.055). A two-factor ANOVA did not reveal a two-way influence on area in hippocampus, but a single-factor ANOVA demonstrated that genotype did (F(1,233)=10.665, P=0.001) and the effect size was medium (η^2=0.044).

When measuring circularity, readings range from 0 to 1, with a reading of 1 being a perfect circle and 0 a straight line. A lower value indirectly correlates to more appendages, which could be axonal input or from other cell types. Therefore, more circular synaptosomes corresponds with reduced input/weaker connections. The most circular synaptosomes were found in 7-month Tg hippocampus with a circularity reading of 0.901±0.068, opposed to the least circular synaptosomes in 7-month wild type IC with a reading of 0.853±0.076 (Figure 5.18C&D). A three-factor ANOVA uncovered age, genotype and brain region interacted and influenced circularity (F(1,453)=4.130, P=0.043) and a partial eta squared shows the effect size was less than small ($p\eta^2$=0.009) -circular results informed further analysing perimeter quantifications to identify if the measurements differed from area measurements (Figure 5.18E&F). Synaptosome perimeters were largest in the 7-month Tg IC, reaching 2.333±0.619µm around, in contrast to 1.694±0.463µm in 15-month Tg IC. Like area measurements, a three-factor ANOVA revealed age, genotype and brain region interacted and had a substantial influence on perimeter (F(1,453)=9.723, P=0.002) and a partial eta squared showed a medium effect ($p\eta^2$=0.021). Two-factor analysis of age and genotype demonstrated that the effects were mainly attributed to IC (F(1,220)=13.949, P=<0.001) and effect size was large ($p\eta^2$=0.60).

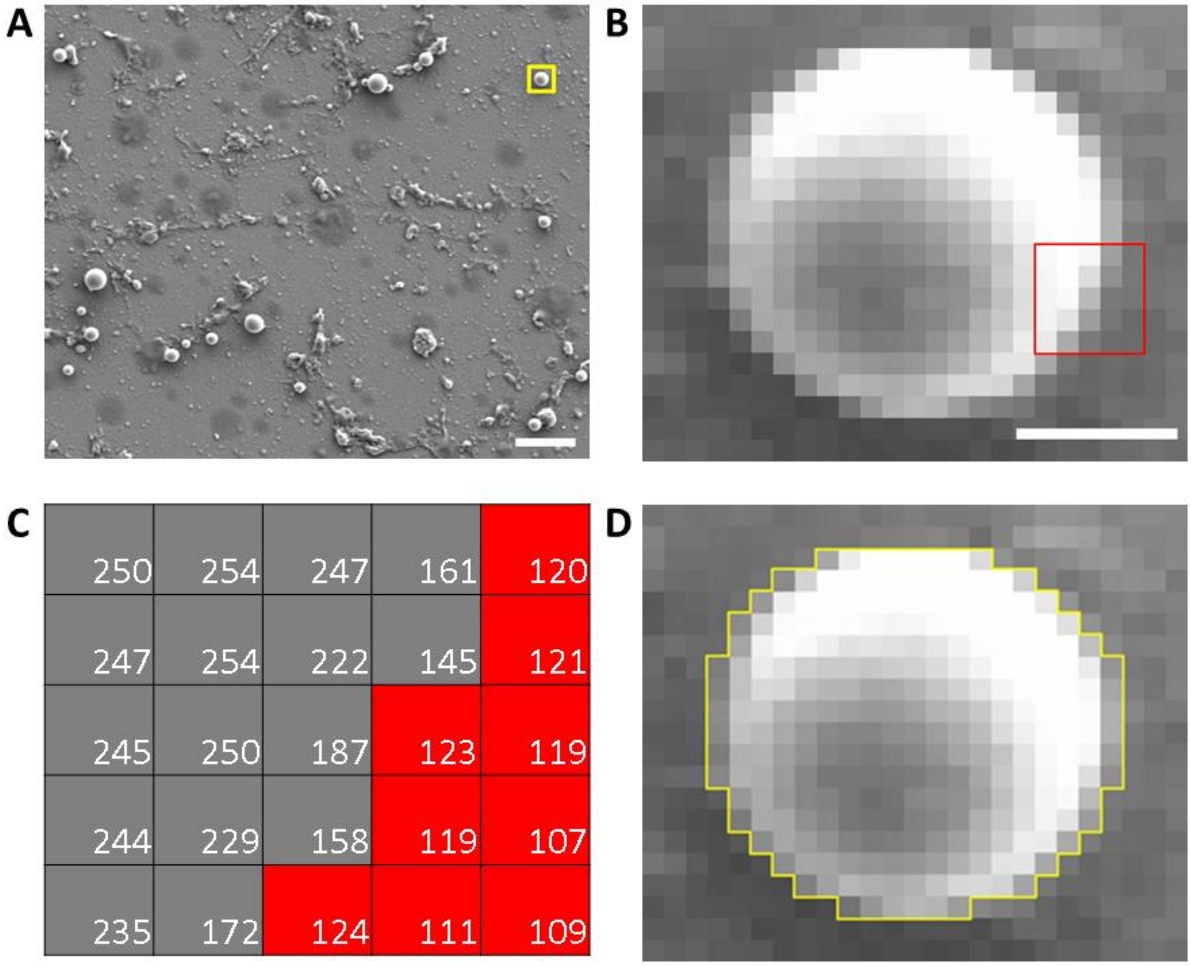

250	254	247	161	120
247	254	222	145	121
245	250	187	123	119
244	229	158	119	107
235	172	124	111	109

Figure 5.17. Process of isolating synaptosomes for area, perimeter and circularity analysis. (A) region of interest taken using a scanning electron microscope. Scale bar 50µm. (B) yellow box outlines the cropping region of a synaptosome. (C) Cropped region of interest from yellow box in (B), red box outlines an example region of interest from the pixel inspector tool used in ImageJ. Scale bar in (B) same in (D) 0.2µm. (D) Output of pixel intensities from pixel inspector plugin from red region in (C), the formula: $Max\ intensity\ (250) - STDEV * 2$ and any readings under were not included in the analysis. Definition of the borders of synaptosomes were determined by pixel intensities (in this example >132) and using these parameters, contours were manually drawn around synaptosomes. Regions of interest were quantified using the measure function in ImageJ to produce area, perimeter and circularity measurements.

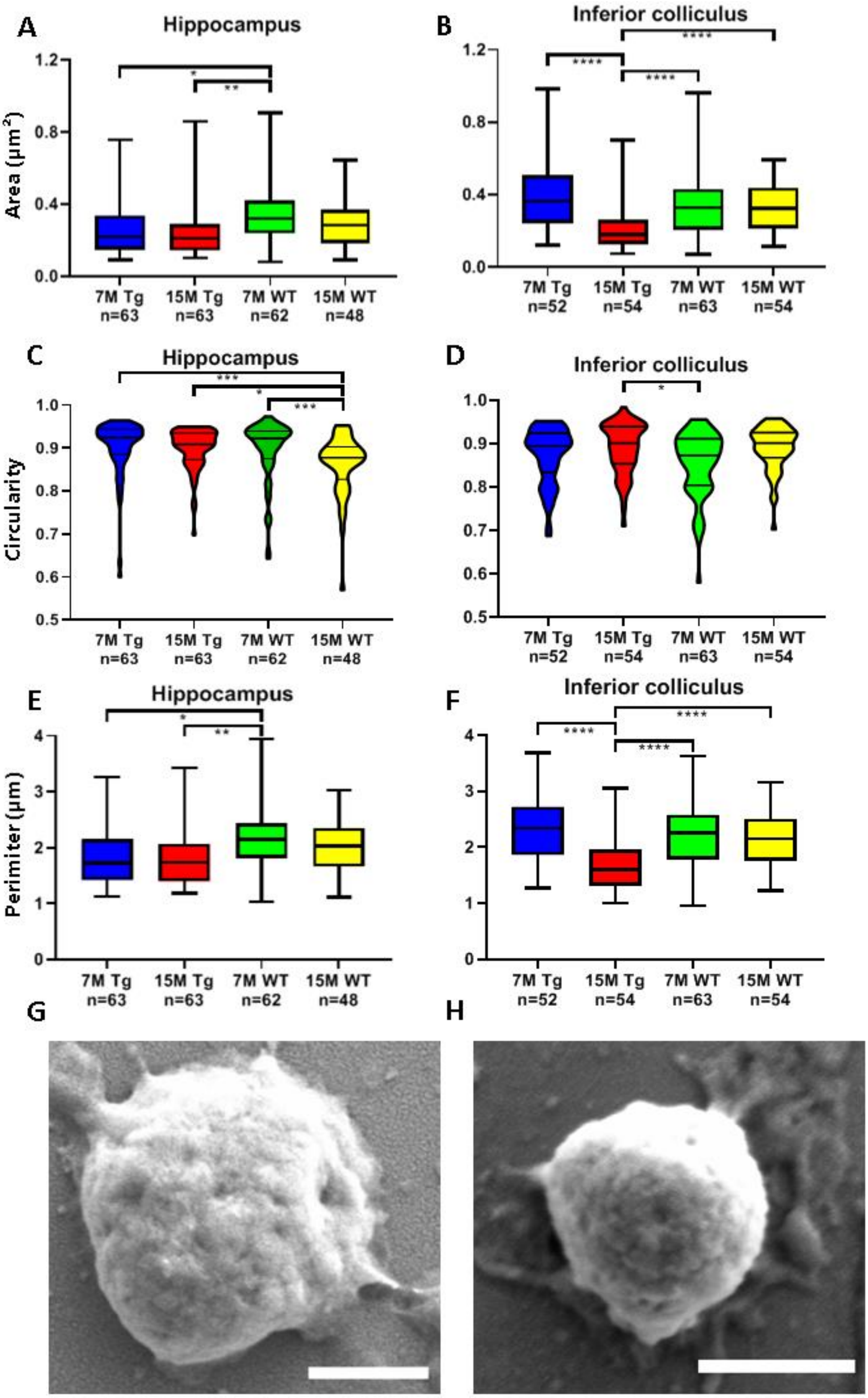
A
Hippocampus
Area (μm²)
1.2
0.8
0.4
0.0
*
**
7M Tg n=63
15M Tg n=63
7M WT n=62
15M WT n=48
B
Inferior colliculus
1.2
0.8
0.4
0.0
****
****
****
7M Tg n=52
15M Tg n=54
7M WT n=63
15M WT n=54
C
Hippocampus
Circularity
1.0
0.9
0.8
0.7
0.6
0.5
***
*
***
7M Tg n=63
15M Tg n=63
7M WT n=62
15M WT n=48
D
Inferior colliculus
1.0
0.9
0.8
0.7
0.6
0.5
*
7M Tg n=52
15M Tg n=54
7M WT n=63
15M WT n=54
E
Hippocampus
Perimiter (μm)
4
3
2
1
0
*
**
7M Tg n=63
15M Tg n=63
7M WT n=62
15M WT n=48
F
Inferior colliculus
4
3
2
1
0
****
****
****
7M Tg n=52
15M Tg n=54
7M WT n=63
15M WT n=54
G
H

Figure 5.18. Outputs from synaptosome measurements were taken using the process in Figure 5.17 to determine area, perimeter and circularity. Area and perimeter measurements were implemented to understand synaptosome sizes. n=individual synaptosomes. (A) Synaptosomes in hippocampus had the largest area in the 7-month wild type group and were significantly larger than both transgenic groups. The smallest synaptosomes in hippocampus were found in the 15-month Tg group. Synaptosome sizes were reduced in the Tg model. (B) Largest synaptosome areas were found in the 7-month Tg group, and the smallest were in the Tg-15-month group. Synaptosomes were significantly smaller in the 15-month Tg group compared to all other groups. (C) Hippocampus demonstrated significant levels of reduced circularity between the 15-month wild type with all other groups. (D) IC increased in circularity from 7-months wild type to the 15-month Tg group. (E&F) Perimeter measurements followed similar trends to area measurements. (G&H) Example high-power scanning electron micrographs demonstrating significance from parameter measurements of synaptosomes form 7-month wild type (G) and 15-month Tg (H) IC. Notice the smaller sized and more uniformed circular synaptosome in Tg IC. Scale bars 0.2µm in (G&H).

5.3.3 – Molecular Analysis of TgF344-AD model

5.3.3.1 – Inferior colliculus demonstrates an age-dependent reduction in *GAD65* mRNA abundance

To further understand age-dependent changes in the Tg model, QRT-PCR was conducted to identify whether strain affected specific mRNA abundance. Primers were optimised by determining the ideal melt temperature and in the experiment, only results that had similar cycles and melt curves were included (Figure 5.19). Housekeeping genes were referenced against each other (*Cyc1*, *GAPDH* and *EIF4A2*) to identify the most appropriate reference genes (Figure 5.20). This process identified that *EIF4A2* did not produce consistent mRNA abundance across cases, so was not included as a housekeeper. All target genes were contrasted across brain regions and normalised to the housekeeping genes *Cyc1*, *GAPDH*. The first gene targeted was *GAD65* as a marker of GABAergic synapses (Figure 5.21). mRNA abundance was highest in 7-month age groups across all brain regions, with the highest in 7-month wild type superior colliculus with more than double the levels of the housekeepers. There was a lower level of *GAD65* mRNA abundance expression across all groups in auditory cortex, frontal cortex and cerebellum in contrast to the colliculi, which suggests less inhibitory synapse activity. The lowest mRNA abundance was found in the 15-month Tg auditory cortex with a relative decrease to 0.6±0.08 normalised levels.

One-factor ANOVAs uncovered that age independently influenced *GAD65* mRNA abundance (F(1,48)=9.035, P=0.004) and an eta squared showed that this was a medium effect size (η^2=0.158). Additionally, mRNA abundance also was influenced differently depending on brain region (F(5,48)=15.474, P=<0.001) and the effect size was large (η^2=0.617). *Post-hoc* analysis revealed that superior colliculus was independent in *GAD65* mRNA abundance from all other groups (all P<0.005) and IC was much higher than in auditory cortex and cerebellum (P=0.015 and 0.036 respectively). One factor ANOVA of individual brain regions demonstrated that the only region that underwent an age-dependent decrease in *GAD65* mRNA abundance, was the IC (F(1,8)=8.336, P=0.020) and an eta squared showed that the effect size was large (η^2=0.510).

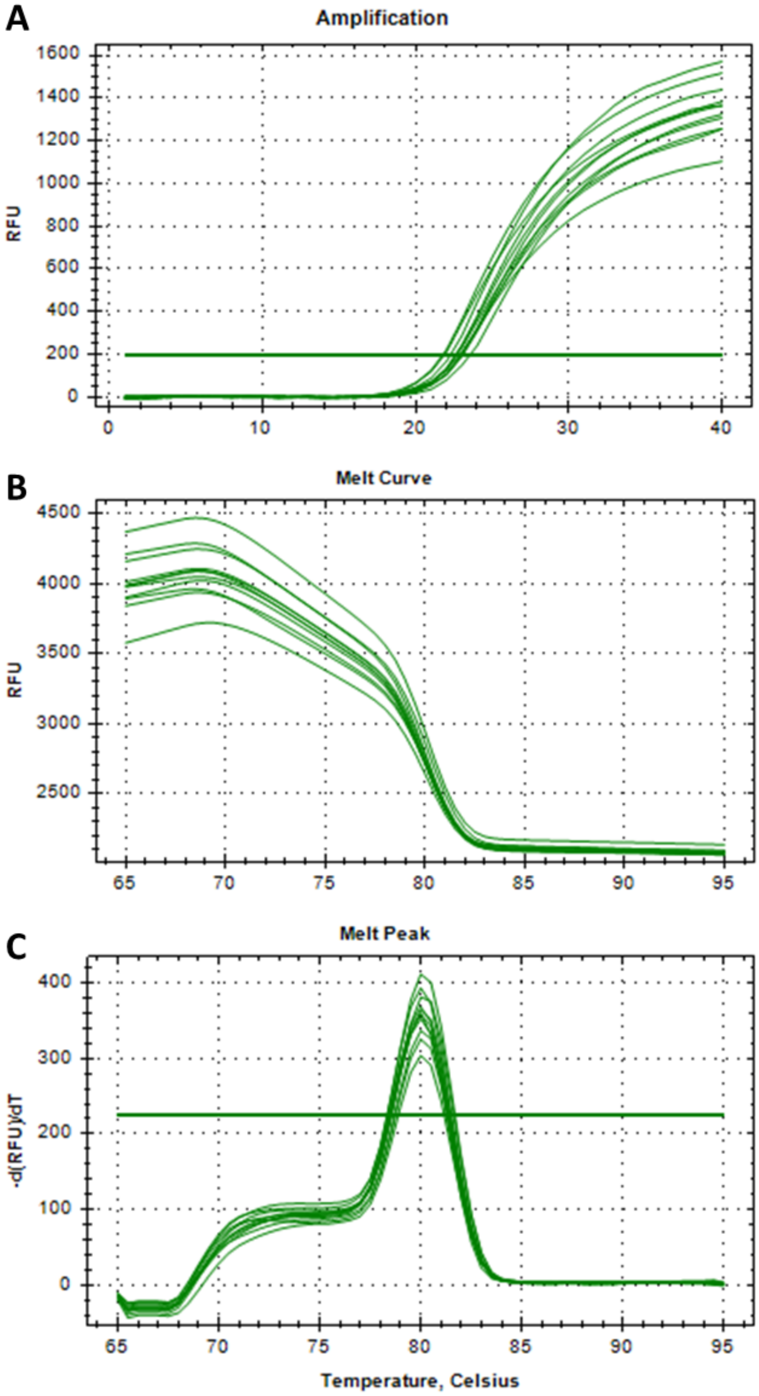

Figure 5.19. Example traces from one experiment including all genes across all brain regions. QRT-PCR experiment taken using the Bio-Rad CFX Maestro software, demonstrating the optimisation of primers to undergo consistent amplification and melting temperatures. (A) Cycles per relative fluorescent units. (B) Changes in relative fluorescent units with temperature. (C) Peak temperature for primer to reach maximum cycles of mRNA abundance. If results underwent abnormal cycles or melting temperatures, they were excluded from analyses.

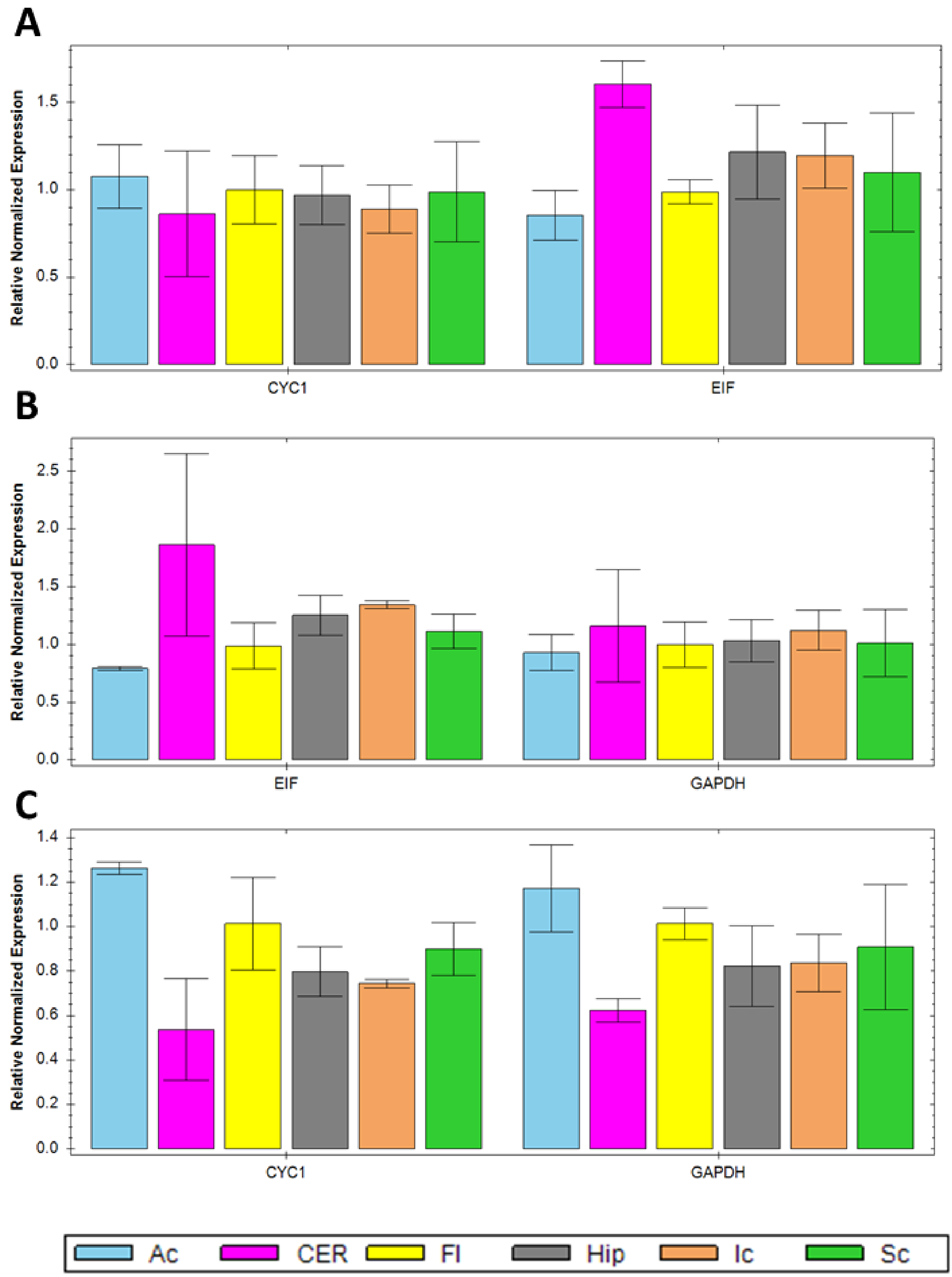

Figure 5.20. (A) Referenced housekeeping genes *Cyc1*and *EIF4A2* to *GAPDH* across the brain regions. Note the variability in *EIF4A2*. (B) Referenced housekeeping genes *EIF4A2* and *GAPDH* to *Cyc1*, notice again the high variability in *EIF4A2*. (C) *Cyc1* and *GAPDH* were referenced to *EIF4A2*. Not the variability across both. The housekeeper *EIF4A2* was excluded from normalising the mRNA abundance of target genes, due to high variability.

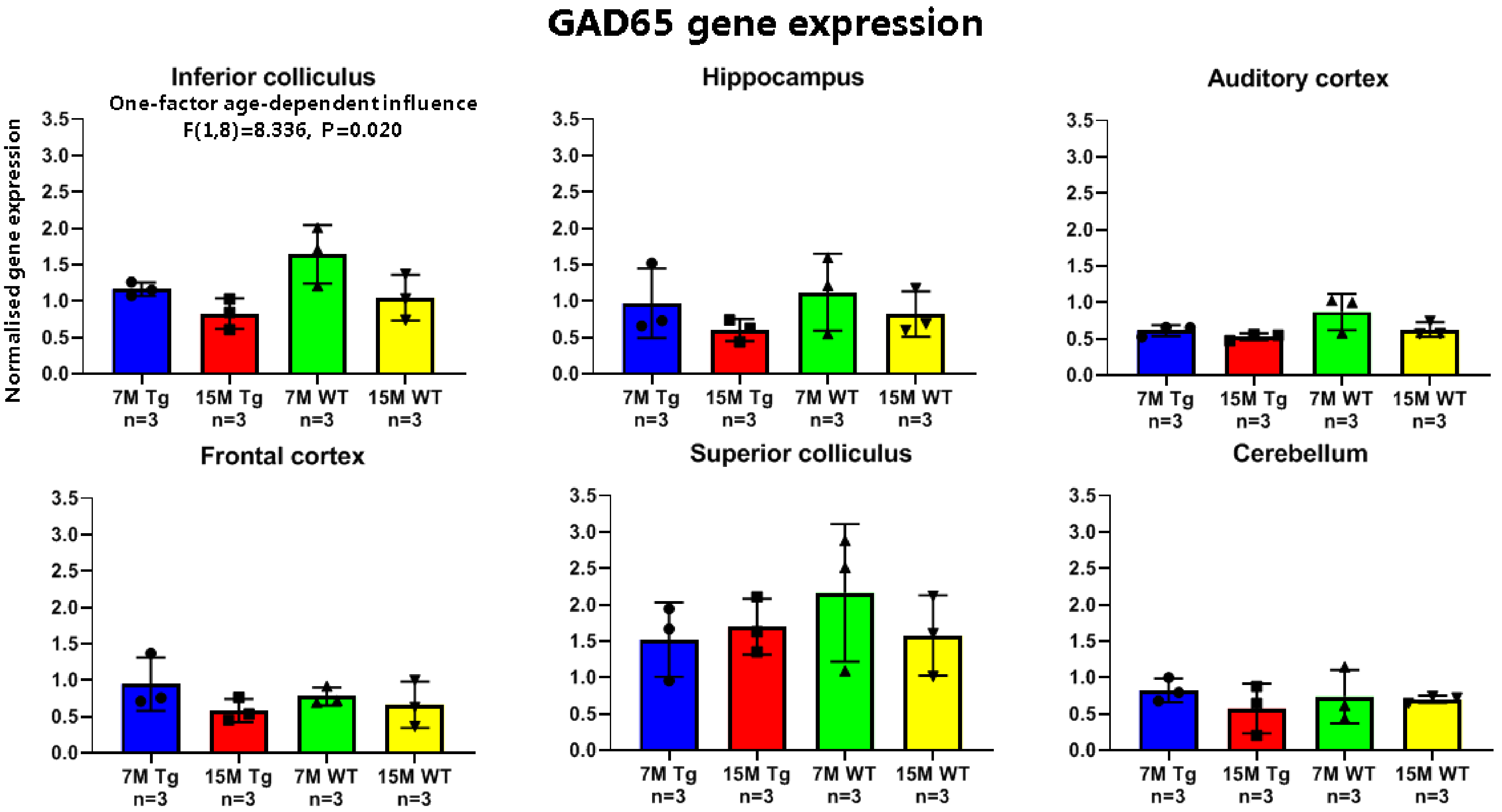

Figure 5.21. *GAD65* mRNA abundance was highest in the 7-month wild type IC, hippocampus, auditory cortex and superior colliculus, with the highest levels in superior colliculus. The lowest expression was found in the 15-month Tg cerebellum. Age influenced mRNA abundance in IC resulting in a reduction. Most markedly, there is a decrease between 7-month wild type and 15-month Tg IC and hippocampus, suggestive of selective pressure on GABAergic synapses.

5.3.3.2 – *Iba1* expression decreases with age across all brain regions

Next, *Iba1* was measured as a marker of microglia, to determine whether mRNA abundance increased across brain regions (Figure 5.22). mRNA abundance was lowest in the 15-month Tg group of all brain regions, except hippocampus where 15-month wild type was lowest. The highest levels of *Iba1* mRNA abundance were found in the 7-month wild type superior colliculus, with a 2±1 fold difference above housekeepers in expression. Cerebellum had the lowest levels of *Iba1* mRNA abundance across all groups, with the lowest overall of 0.5±0.1-fold change in the 15-month Tg group.

One-factor ANOVA of all brain regions shows an age-dependent influence on *Iba1* mRNA abundance (F(1,48)=4.126, P=0.048) and eta squared demonstrates that the effect size was medium (η^2=0.079). Moreover, ANOVA revealed that brain region influenced the levels of *Iba1* mRNA abundance (F(5,48)=6.429, P=<0.001), which had a large effect size (η^2=0.401). *Post-hoc* analysis revealed that the cerebellum was largely different from auditory cortex (P=0.011), hippocampus, IC and superior colliculus (all P=<0.001). All other regions displayed similar levels of mRNA abundance. Analysis of individual brain regions measuring different factors uncovered no significant influences. These results show that across all brain regions *Iba1* decreases with age but is not attributed to individual regions. Levels of *Iba1* mRNA abundance were substantially lower in cerebellum than other regions.

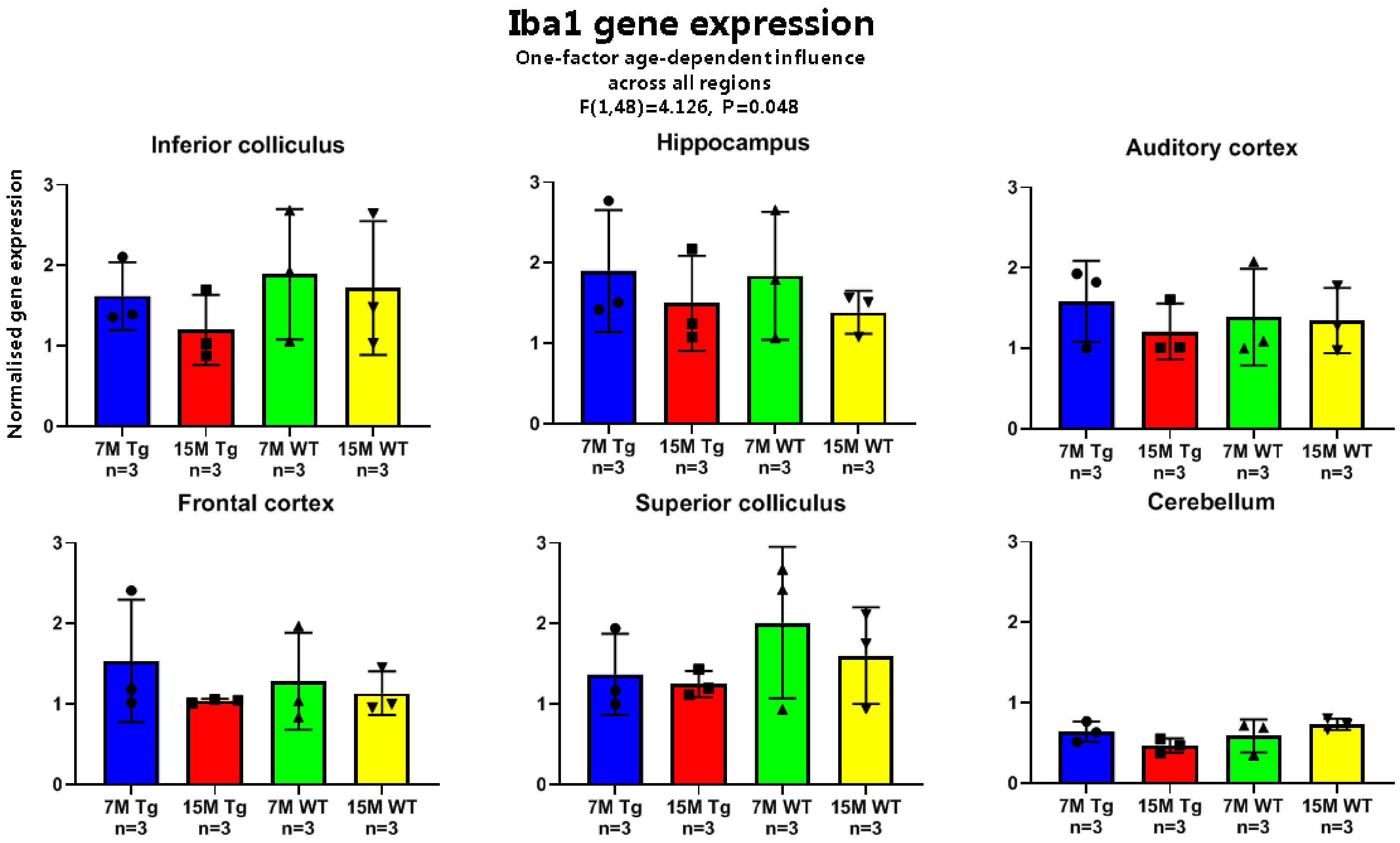

Figure 5.22. *Iba1* expression underwent age-dependent decreases across all brain regions, except for cerebellum. Highest expression was found in the 7-month wild type superior colliculus, followed by 7-month Tg hippocampus. Lowest readings were found in the 15-month Tg cerebellum. The most striking differences were found between 7-month wild type and 15-month Tg IC and superior colliculus. Similar to *GAD65* expression (Figure 5.22), there was a decrease between 7-month wild type and 15-month Tg, indicative of the deteriorative effects of the Tg model with age.

5.3.3.3 – *SV2a* expression across the brain undergoes age-dependent decreases

In addition to inhibitory *GAD65* synapses, excitatory synapses were targeted by implementing the marker *SV2a* (Figure 5.23). *SV2a* expression was marginally higher in the 7-month groups across all brain regions, except cerebellum, which remained unaffected. IC demonstrated the largest difference in *SV2a* mRNA abundance was between 1.5±0.3 fold above housekeepers in the 7-month wild type group, to 0.9±0.2 in the Tg 15-month group. Expression in cerebellum was consistently lower in all groups in contrast to other regions, with 0.7±0.3 in the 15-month wild type group.

One-factor ANOVA of all brain regions demonstrated an age-dependent decrease in *SV2a* expression (F(1,48)=5.045, P=0.029) and an eta squared showed a medium effect size (η^2=0.095). Additionally, brain region also influenced the levels of mRNA abundance (F(5,48)=15.065, P=<0.001) and the effect size was large (η^2=0.611). *Post-hoc* analysis that the IC and superior colliculus were similar in expression (P=>0.999) but were distinct from all other regions (all P=<0.002). Analysis of individual brain region revealed no significant influences. These results show that across all brains regions, there is age-dependent decrease in *SV2a* expression.

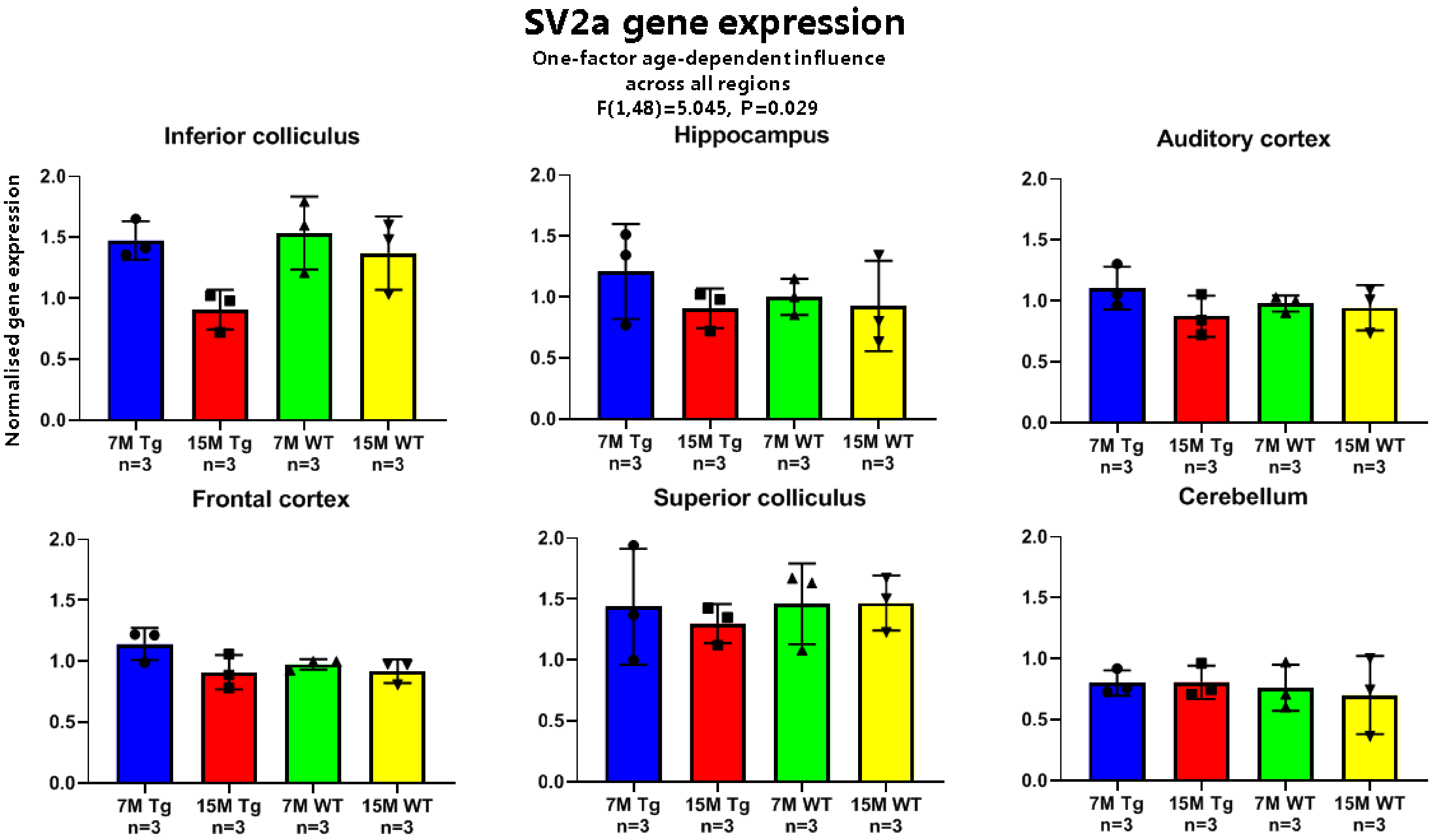

Figure 5.23. Like *Iba1* expression (Figure 5.23), there was an age dependent decrease in *SV2a* expression across all brain regions. The highest levels of expression were in 7-month wild type and Tg IC and superior colliculus. Lowest levels were found in the 15-month Tg group of IC, hippocampus, auditory cortex and frontal cortex, with similar numbers across regions. Cerebellum remained unaffected across groups. The largest effect was in IC between 7-month wild type and 15-month Tg groups. IC demonstrates an age-dependent decrease in *SV2a* expression in the Tg model.

5.3.3.4 – Across brain regions *synaptophysin* expression demonstrates an age-dependent decrease in the Tg model

To contrast with *GAD65* and *SV2a*, *synaptophysin* was measured as a marker of presynapses (Figure 5.24). *Synaptophysin* mRNA abundance was notably highest in the 7-month Tg group of the hippocampus, auditory cortex and frontal cortex, with the highest relative levels reaching 2.3±1.9 in frontal cortex. Consistent with *SV2a* results, *synaptophysin* expression in IC and superior colliculus followed similar trends across groups. The lowest overall relative *synaptophysin* mRNA abundance was found at 0.6±0.1 in the 15-month Tg IC group.

A two-factor ANOVA across all brain regions revealed age and genotype influenced *synaptophysin* mRNA abundance (F(1,48)=5.908, P=0.019) and a partial eta squared revealed a medium effect size ($p\eta^2=0.110$). *Post-hoc* analysis uncovered that the differences in brain region were attributed to between cerebellum with auditory cortex (P=0.033), frontal cortex (P=0.037) and hippocampus (P=0.024). A single-factor ANOVA of individual brain regions demonstrated that genotype influenced mRNA abundance in cerebellum (F(1,8)=7.491, P=0.026) and the effect size was small ($p\eta^2=0.026$).

These results demonstrate that across brain regions, *synaptophysin* expression is affected collectively by age and genotype. Also, expression in cerebellum is lower in the Tg model independent of age.

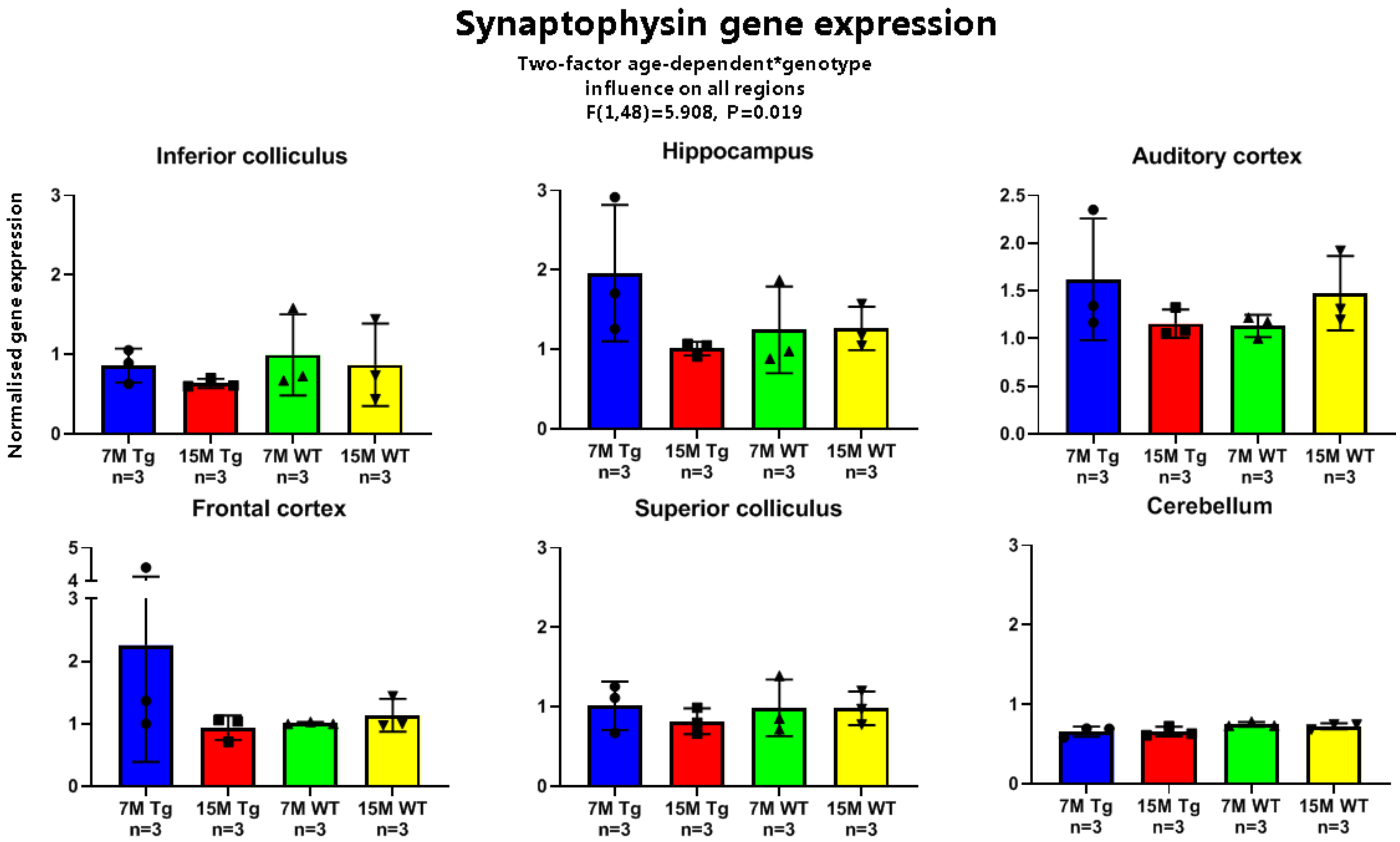

Figure 5.24. Across synaptic measurements of mRNA abundance, *synaptophysin* elicited the most profound effect, uncovering a two-factor interaction between age and genotype influencing expression across brain regions. Highest readings were found in 7-month Tg frontal cortex and hippocampus, although frontal cortex could be due to one outlier. The lowest expression was found in cerebellum but remained consistent across groups. The largest between-groups differences were found in IC, hippocampus, auditory cortex and frontal cortex.

5.4 – Discussion

The results from this chapter are the first to contrast age-dependent mitochondrial dysfunction in the Tg model, along with in-depth anatomical quantification of individual synaptosomes and molecular analysis. The main findings from this Chapter include i) age-dependent increases in proton leak found in hippocampus (Figure 5.1), ii) increases in basal respiration in hippocampus of the 15-month Tg model (Figure 5.10) and iii) age-dependent increases in maximal respiration of IC and hippocampus in the Tg groups (Figure 5.14). Similar levels of non-mitochondrial oxygen consumption (Figure 5.15) corroborate that changes in mitochondrial functioning are attributed to mitochondrial dysfunction and are not due to non-mitochondrial respiration. Additionally, consistent levels of spare respiratory capacity (Figure 5.16) suggest that the above parameters are dependent measures of mitochondrial dysfunction and not as a result of ancillary metabolic pathways. The other measures included are decreases in ATP-production (Figure 5.12) and coupling efficiency (Figure 5.13) in the 15-month Tg groups, but these results incorporated negative responses after the addition of Oligomycin, which led to negative readings and in turn hampers the interpretability of the findings. However, these negative responses do indirectly uncover possible aspects of mitochondrial dysfunction commensurate with the other parameters meriting further investigation.

Overall changes in OCRs across brain regions demonstrate that synaptosomes are physiologically dependent on where they are situated. The opposite response observed after the injection of Oligomycin (review Figure 5.9) onto the synaptosomes of the 15-month Tg groups, suggest age-dependent adaptations in mitochondrial physiology in the Tg model indicative of mitochondrial dysfunction. The process of measuring the mitochondrial parameters basal respiration, proton leak, maximal respiration, non-mitochondrial oxygen consumption, spare respiratory capacity, ATP-production and coupling efficiency using the Seahorse instrument is a well characterised model (Divakaruni *et al.*, 2014). By identifying specific changes in these inter-dependent parameters, highlight independent measures of mitochondrial function attributed to synaptosomal dysfunction.

5.4.1 – Identifying mechanisms behind synaptic dysfunction is in Alzheimer's disease is critical to understanding the condition

It is well established that synaptic dysfunction is a major contributor to AD (Marcello *et al.*, 2012, Davies *et al.*, 1987, Dekosky and Scheff, 1990, Selkoe, 2002). Jackson *et al.* (2019) focus on the early pathology of AD and suggest that synaptic neuroplasticity is a targetable mechanism that could restore cognitive function. They suggest that the brain adapts in response to damage and the synapse morphology changes accordingly. Hebb (1952) postulated the mechanism whereby synaptic plasticity is defined by the pre-synapses' repeated stimulation of the post-synapse, which suggests that dysfunction of pre-synapses would result in altered synaptic plasticity. This Chapter targeted the energy production that drives synaptic transmission by measuring aspects of synaptic mitochondrial functioning to identify changes in physiological synaptosome plasticity in the Tg model that could translate to potential targets in early onset AD.

5.4.2 – The efficiency of the mitochondrial membrane decreased in the 15-month Tg hippocampus

Proton leak is defined by protons that re-enter the mitochondrial matrix by other means than via complex V of the mitochondrial chain (Jastroch *et al.*, 2010). The direct mechanisms contributing to proton leak involve movement across the phospholipid bilayer, transport across integral membrane proteins or other protein-based sites located on the mitochondrial membrane.

Dysfunction of mitochondria and increased membrane inefficiency leading to proton leak, cause the production of reactive oxygen species furthering the damage to mitochondria. Generation of reactive oxygen species is more than likely generated at complex III of the mitochondrial chain during the oxidation of complex I substrates (Chen *et al.*, 2003). In contrast, the excess of reactive oxygen species accumulation can also promote damage to the mitochondrial membrane, causing proton leak (Cheng *et al.*, 2018). This makes interpreting what initiates proton leak difficult, but highlights the importance of the measurement in that dysfunction could result in a dialectic feedback loop that promotes progressive deterioration of the mitochondrial membrane. Therefore, if AD induces mitochondrial membrane inefficiency, could contribute to a progressive reduction in metabolism

When interpreting changes in proton leak, it is unclear which specific mechanisms are associated, but increased levels induced by the Tg model can be attributed to mitochondrial membrane dysfunction and the production of reactive oxygen species. This Chapter uncovered a selective increase in age-dependent proton leak in hippocampus of the Tg model (Figure 5.11), which suggests a high level of induced mitochondrial membrane injury impairing the efficiency of the mitochondrial chain. These regional-specific responses highlight the increased susceptibility of hippocampus to synaptic mitochondrial dysfunction in this model of AD.

5.4.3 – Age-dependent increases in basal metabolism within hippocampus of the Tg model is suggestive of increased pressure to maintain synaptic functioning

The minimal rate of rate of metabolism required to undertake basic functions, is basal respiration. Measuring OCRs of synaptosomes and contrasting across cases in a consistently metabolising environment, allows the detection of adaptations that mitochondria undergo to maintain basal synaptic functioning. Changes in basal respiration are indicative of synaptosome adaptations to the surrounding milieu. These are the first results to demonstrate an increase in age-dependent basal synaptic metabolism in the Tg model. The results show elevated pressure on synaptosomes in hippocampus, in contrast to other regions of the brain, to undergo increases in basal energy demand (Figure 5.10). Increases are found at 15-months in the Tg model, demonstrating the adaptations that the hippocampus experiences due to its environment. Rylett *et al.* (1983) demonstrated in synaptosomal fractions from hippocampus and frontal cortex from AD patients, sodium-dependent and hemicholinium-sensitive choline uptake into hippocampal fractions were twice as great as in frontal cortex fractions. These results are commensurate with the findings in Figure 5.10, that basal metabolism in hippocampal synaptosomes undergo a doubling in OCR. Similarly, Rylett *et al.* (1983) identified that choline transport into synaptosomes was reduced more markedly in frontal cortex than in hippocampus of AD patients compared to healthy controls. Contrastingly, their results suggest that although hippocampus choline uptake increases, frontal cortex has a reduced capacity to uptake choline. This could explain why basal and maximal respiration OCRs were substantially higher in young cortical regions, but lower in sub-cortical regions such as hippocampus and IC, and the Tg model causes an opposite compensatory effect, which could provide insight into how synapses are affected across the different regions of the brain. This increase in energy needed to maintain basal functioning in the Tg model could be a source of accelerated synaptic dysfunction that promotes early changes in plasticity in hippocampus.

5.4.4 – Elevated maximal respiration in 15-month Tg model in inferior colliculus similar to hippocampus

Yao *et al.* (2009) demonstrated a decrease in basal and maximal respiration in triple transgenic AD mice 14-day old embryo hippocampal neurons compared to age-matched non-transgenic controls. Contrastingly, in synaptosomes, the results from this Chapter show an increase in maximal respiration (Figure 5.14) of 15-month old Tg rat IC and hippocampus. Synaptosomal studies of AD patient post-mortem tissue identified a reduction in cortical acetylcholine (Nordberg and Winblad, 1986), which correlates with the age-dependent decreases in basal and maximal respiration observed in the Tg model of both cortical regions in this Chapter (Figure 5.10&14). Hardy *et al.* (1987) show in synaptosomes taken from AD patients and healthy controls, that there is approximately a 70% reduction of GABAergic terminals in hippocampus and cortices in the AD patients. They also suggest that although there may not be neuronal loss (Chapter 4), GABAergic terminals are substantially affected. This large effect on GABAergic terminals in AD, therefore, will more than likely have a substantial effect on the highly GABAergic IC (Merchán *et al.*, 2005), which is probably why the results in IC mirrored those of the hippocampus. Dekosky and Scheff (1990) correlated that a loss of synapses in human AD patients is associated with a reduction in mental ability, which more than likely translates the synaptosomal dysfunction observed in this Chapter to potential dysfunction in humans.

Spare respiratory capacity (Figure 5.16) remained similar across groups, which suggests that the increased levels of maximal respiration are interdependent with increases in basal respiration (Figure 5.10) and proton leak (Figure 5.11). An elevated maximal respiration corresponds with the maximal level of substrate utilisation and oxidation capacity of mitochondria (Divakaruni *et al.*, 2014). Therefore, the increases in maximal respiration of synaptosomes are more than likely a compensatory response to accommodate for the increasing stress of aging in the Tg model.

5.4.5 – Decreases in ATP production and coupling efficiency are indirectly suggestive of synaptic dysfunction in the aging Tg model

The production of ATP is determined by the addition of Oligomycin, by selectively blocking the synthesis of ATP, and coupling efficiency is calculated by dividing ATP production by basal respiration and multiplying by one-hundred. Figure 5.5 outlines the typical responses in OCR to added compounds. Across all cases, Oligomycin had little effect on synaptosome fractions, but interestingly at 15-months in the Tg groups there was an increase in OCR. The other substrates added to the synaptosomes elicited somewhat expected results, suggesting that the response to Oligomycin is a real effect. Scott and Nicholls (1980) found that Oligomycin had a similar response in guinea pig synaptosomes, where there was a slight increase in OCRs and Flynn *et al.* (2011) demonstrated in SOD2 null mice very minor changes in OCR similar to the results seen in 7-month wild type groups in Figure 5.9. Although the decreases in ATP production and coupling efficiency cannot be interpreted as real effects, the nature of the results are real physiological responses to Oligomycin. It appears that the uptake of Oligomycin does not have a profound effect on blocking ATP synthesis, which could suggest a more glycolytic role, but could also be as a result of a lack of blocking due to a insufficient concentration of Oligomycin introduced. However, measurements between groups demonstrated different responses, which highlights that here were effects. Therefore, the nature of increasing OCRs in the 15-month Tg group is more than likely suggestive of synaptic dysfunction which merits further investigation.

5.4.6 – Synaptosome size decreases in the 15-month Tg inferior colliculus

This Chapter is one of the first studies to provide in-depth anatomical quantification of individual synaptosomes and through the analysis identifies clear adaptations in the Tg model. The images were first taken on the SEM to validate the presence of synaptosomes in the samples (Figure 5.4). When contrasting with the literature, the high-power images seen in Figure 5.18 G&H are similar in size and shape to the examples imaged by (Ajito and Torimitsu, 2002) using SEM and in the transverse sections imaged by (DiGiovanni *et al.*, 2012) using transmission electron microscopy. Morphological analysis was then undertaken to identify if age and genotype caused remodelling of synaptosomal anatomy. Interestingly, synaptosomes were substantially reduced in size in the 15-month Tg groups of both hippocampus and IC, indicative of pressure on synapses to remodel. In addition, synaptosomes in IC were more circular in the 15-month Tg group, potentially suggestive of fewer synaptic inputs and integrated synapses, which has been observed as a key transitional point in transgenic AD mice development (Kashyap *et al.*, 2019).

The Tg model has been developed to express mutant human amyloid precursor protein and presenilin genes (Cohen *et al.*, 2013), which cause a substantial increase in Aβ production along with a reduced ability to cleave these proteins. This leads to considerable levels of Aβ being present throughout the brain. Koffie *et al.* (2012) demonstrate that oligomeric Aβ is elevated at synapses and results in synapse shrinkage, which is commensurate with the results from this Chapter. This age-dependent pressure observed for synapses to remodel in the presence of Aβ suggests that targeting synaptosomes at early stages of the disease to rectify changes in synaptosome size could be critical.

5.4.7 –Age-dependent *synaptophysin* decreases in the Tg model across brain regions, with the largest differences in inferior colliculus

The molecular biological approach of QRT-PCR was implemented to identify whether synaptic markers were affected on a transcriptional level that coincided with the physiological results. Other studies have identified decreases in *GAD65* (Schwab *et al.*, 2013), *synaptophysin* (Tampellini *et al.*, 2010) and *SV2a* (Chen *et al.*, 2018). In this Chapter, all synaptic markers demonstrated an age-dependent reduction in mRNA abundance (Figures 5.21, 23 & 24). Since all markers demonstrated a similar reduction suggests that there is likely to be a decrease in synapse density. Consistently, the 15-month Tg groups had the lowest levels of synaptic mRNA abundance, particularly in IC and hippocampus, which correlates with the mitochondrial dysfunction observed in the synaptosomes. This suggests that along with synaptic dysfunction, there is also a reduction in synaptic mRNA abundance. A study by Chen *et al.* (2018) showed that in patients with AD, there was a 41% reduction in *SV2a* binding sites compared to cognitively normal controls. These results are from patients at later stages of the disease, and when comparing with results from this section, it suggests that this begins at an earlier stage of the disease. Stockburger *et al.* (2016) show that *SV2a* is expressed in mitochondria and that the drug levetiracetam could be used to improve the symptoms of AD. This could be used as a future approach in line with the presented work to target potential metabolic mechanisms that could reverse observed synaptic dysfunction.

5.4.8 – Technical limitations

Inherent problems arise when studying the physiology of mitochondria, Brand and Nicholls (2011) summarised advantages and disadvantages of isolating mitochondria. Problems that had to be considered when isolating synaptosomes included, synaptosomes not operating collectively with surrounding structures, damage when isolating synaptosomes and adding substrates to synaptosomes out of physiological context could affect interpretability, such as explaining the lack of Oligomycin response. However, these considerations do not discredit that there were differences between groups and unusual responses in the 15-month Tg group, which more than likely is having a negative effect within the living animal.

Problems that arise when measuring proton leak include determining whether changes in membrane potential contribute to the changes detected in respiration. This observation therefore hampers the interpretability of the findings as the exact mechanism causing the excessive proton leak in the 15-month Tg model was not determined. Future work would seek to implement a mitochondrial membrane potential assay as a measurement of membrane potential, to confirm the levels of proton leak were attributed to membrane inefficiency. Basal respiration, proton leak and maximal respiration are inter-dependent values, therefore when measuring them as independent values does not incorporate whether it was a common mechanism that caused the similar trends across the groups. However, this does not disregard differences between groups and that there is synaptic dysfunction.

There were low numbers of viable samples in some of the physiological data and in all the molecular experiments, there was only time to perform experiments of three animals per group. These results will therefore be underpowered and hamper the interpretability of the findings. The low n numbers in the 15-month Tg IC and across molecular results are more than likely the reason why significant results have not been derived. Future experiments to increase the 'n' numbers for each experiment to improve the representability and the statistical power of the findings, may uncover further statistical significance.

Homogenising and undergoing high force centrifugation could have caused damage to synaptosome samples. In addition, synaptosomes separated from presynaptic nerve endings using centrifugation at high speeds will causes the synaptosomes to seal up and become particle like (Whittaker, 1969), which directly affects the interpretability of the morphological analysis of synaptosomes and the circularity measurements, but this could provide insight into why synaptosomes become smaller and more circular in the Tg groups. One could suggest that due to the lack of input, integration and induced stress causing damage to synaptosomes, would potentially render them more susceptible to separation from surrounding structures.

5.4.9 – Conclusions

This Chapter is the first research to provide molecular, anatomical and physiological evidence for age-dependent synaptic dysfunction in a transgenic rat model of AD. The pre-synaptic terminals (synaptosomes) undergo age-dependent dysfunction in the Tg model including an increased basal level of metabolism to accommodate normal functioning, increased maximal oxidative capacity and increased mitochondrial membrane inefficiency to undergo energy production. These results are supported by age-dependent anatomical changes in synaptosome morphology and molecular decreases in *GAD65*, *SV2a* and *synaptophysin* mRNA abundance in the Tg model. Taken together, these findings show for the first time that there is a level of synaptic dysfunction in the inferior colliculus, similar to that of the hippocampus in the TgF344-AD model that precedes neuronal loss. Overall, these findings demonstrate that the key auditory nucleus, the inferior colliculus, undergoes accelerated synaptic dysfunction in contrast to other regions of the brain. Therefore, the results provide a mechanistic link between hearing loss and early onset Alzheimer's disease. This research uncovers new avenues of investigation for future therapeutic tests, which could be instrumental in combatting the early development of the condition in humans.

Chapter 6 – General Discussion

6.1 – Summary of findings

This thesis has revealed that two types of *GAD67*+ (putative GABAergic) neuron in IC can be classified based on the extent of *Iba1* contacts on their soma. Furthermore, there are more *GAD67*+ somata present within the VCNIC than other sub-regions, and microglia have longer processes than other sub-regions. Moreover, microglia are more ramified in DCIC, and also colocalise with more putative glutamatergic synapses than other sub-regions. This suggests *Iba1*+ microglial processes are associated with IC synapses and the density of these is associated to the nature of local processing between sub-regions of IC. This means that in addition to what is known about neurons transmitting signals to the IC, that microglia influence the synaptic transmission differentially across the sub-regions, which could be informative to fundamental processing throughout different regions of the brain.

Using fluorescent and chromogenic approaches produced evidence that neurons across CNIC, DCIC, LCIC, hippocampus and striatum do not undergo age-dependent reductions in density in the Tg model up to 18-months. This is in direct conflict with the key paper that characterised the Tg model (Cohen *et al.*, 2013). This highlights a need for further research to characterise the Tg model before a concrete conclusion can be made. Activated microglial labelling was highest in white matter regions, but only demonstrated an age dependent increase in number in the Tg model, which broadly highlights that the Tg model systemic inflammatory response causes microglia to activate, and the fact that the response differed across subregions demonstrates that resident microglia respond differently. Astrocytic *GFAP*+ labelling substantially increased at 12-months in CNIC and hippocampus, while astrocyte morphology in hippocampus underwent age-dependent increases in total ramifications and ramification density.

Synaptic mitochondrial dysfunction was most prominent at 15-months in Tg hippocampus, with a similar trend of maximum respiratory capacity seen in IC. The morphology of synaptosomes decreased in size most markedly at 15-months in IC and hippocampus, indicating structural alterations to presynaptic proteins. Pre-synaptic markers *GAD65*, *SV2a* and *synaptophysin* all demonstrated trends in age-dependent reductions in the Tg model, similarly to *Iba1*, indicating general synaptic and microglial dysfunction at 15-months, that precedes loss of neurons.

6.2 – Discussion of glia in IC, in health and dysfunction

Before researchers can fully understand how microglia respond to pathology, an understanding must be developed regarding their function under healthy conditions. This thesis uses the sub regions of IC as a model for investigating microglial anatomy and their possible contributions to processing. The results from Chapter 3 demonstrate that microglia, under normal 'ongoing' conditions demonstrate profound sub regional differences. These findings therefore provide a basis for utilising physiological approaches to further understand the role microglia play in neuronal transmission, such as identifying differences in the types and composition of ion channels across the microglia. Following on from Chapter 3, Chapter 4 shows that putative microglial-associated plaques at 12- and 18-month in the Tg model form predominantly in the CNIC caudo-medially, which could be due to the specific afferent sources and local processing, plus high density of GABAergic neurons therein. This could also reflect a role for the less ramified microglia found in VCNIC. In addition, Chapter 5 revealed a reduction in *Iba1* gene expression at 15-months in the Tg model which could correlate with a reduced number of microglia connections that promotes plaque formation. Gomez-Nicola and Perry (2015) suggest that microglial processes are involved in regulating synaptic transmission and sensing the microenvironment. Therefore, this may correlate to a different role for microglia in DCIC than in CNIC, which could be why there is an enhanced susceptibility to plaque formation. On the dorsal border of IC in Tg rats there is a clearly higher level of activated astrocytes than elsewhere in IC, and chronic activation is considered to exacerbate plaque development (Phatnani and Maniatis, 2015). However, the activated glia around plaques that appear in sub-regions are less densely packed under normal conditions. Therefore, one could suggest that a lack of sufficient local resident glia to mediate an effective response to local damage, could contribute to plaque formation and subsequent pathology.

In Chapter 3, *GFAP*+ astrocytes were shown to be numerous around the borders of the IC, but lacking throughout the parenchyma. This labelling was also found around the borders of IC in Chapter 4, but was exacerbated in the Tg models, which suggests that the dense labelling of reactive *GFAP*+ astrocytes located at the borders may be exerting a neuroprotective role in 'ongoing' conditions. However, when pathological conditions cause increased stress on the borders adjacent to the ventricle, there is a response that caused activation of glia. Microglia and astrocytes are neuroprotective cells (Bylicky *et al.*, 2018) and suggests that a greater density of glia in normal conditions may also confer enhanced neuroprotection in these areas, such as DCIC and LCIC, thus decreasing the likelihood of developing plaques compared to other regions. From this position, one could suggest that underlying anatomical and functional differences of microglia and astrocytes in certain regions of the brain, renders them more susceptible to damage, as a result of not having the capability to produce the same level of neuroprotection as other regions, which could be an extremely important aspect to understand regional AD development, such as the link between hearing loss and dementia.

In Chapter 4, astrocytes were found to significantly increase in CNIC, but did not undergo age-dependent morphological modifications similar to the hippocampus in the Tg model. Although there was a substantial increase in *GFAP*+ astrocyte labelling, the morphology of astrocytes in CNIC did not become more ramified or lead to extended length of arbours in the ageing Tg model. Therefore, this could infer that while there are similarities between IC and hippocampus in the Tg model the astrocytes exhibit divergent responses, related to local processing and potentially disparate phenotypes.

6.3 – Suggestions for future investigations

Future work may look to implement real time monitoring of microglia in IC, to observe the interactions they make with synapses and inhibitory neurons across sub regions and implement physiological measures of microglial functioning. The use of multi-photon microscopy (Hierro-Bujalance *et al.*, 2018), and the accessible location of the IC in rodents, at the dorsal surface of the brain, between the cortex and cerebellum, may allow investigation of the highly ramified morphologies on *Iba1*+ microglia in DCIC and their putative contribution to synaptic processing. Measuring 'resting' microglia is a topic of particular interest, due to their activation in response to even minor stimuli (Guttenplan and Liddelow, 2019). Cell co-culture approaches may also be of interest in addressing these issues (Nistor *et al.*, 2011).

Future work may also look to contrast different astrocyte markers, across the IC, both in young adults during normal processing and under pathological conditions. Preliminary work (not shown in this thesis), demonstrated that using the marker Aldh1L1 also did not uncover astrocytes throughout the parenchyma. Hafidi and Galifianakis (2003) showed that the marker *S100B* revealed 'astrocytes' throughout the parenchyma, but *S100B* is a known marker of myelinated fibres (Steiner *et al.*, 2007) and the IC is constituted heavily of myelinated fibres, also hampering the interpretability of this marker.

Chapter 5 revealed a reduction in *GAD65* gene expression at 15-months in the Tg model in whole IC homogenates, but *GAD67*+ somata in Chapter 3 were found in high numbers in the VCNIC, with fewer in CNIC and fewer still in DCIC and LCIC. This demonstrates the necessity of approaches that retain morphometric detail of the sample. While a loss of *GAD65* in the 18-months Tg group is interesting – it is imperative to localise where that change is manifest in IC, as this has profound implications for the interpretation of this finding. Future work should therefore also include immunohistochemistry with microscopy.

Chapter 4 demonstrated no evidence for a loss of *NeuN* somata up to 18-months, which could be due to *NeuN* being a broad marker of post-mitotic neurons. Specifically targeting neuronal subtypes in the ageing Tg model could identify losses of certain subtypes and increases of others, potentially via phenotypic switching of gene expression. Inhibitory processing is more metabolically intensive than excitatory or neuromodulatory processing (Kann *et al.*, 2014), and the results from Chapter 5 demonstrated reductions in basal metabolic rate in aged Tg, along with a reduction in *GAD65* mRNA. This leads to the suggestion that altered inhibition, which is known to be reduced in aged Fisher 344 rats (Ouda and Syka, 2012) may be an interesting avenue of future investigations. This may be of particular interest in further understanding the sub-regional differences in glial response in IC.

6.4 – Overall summary

Overall, the results of this thesis demonstrate that glial cells are important in processing throughout the sub regions of IC. These different sub-regions all have distinct functions, and this is the first study to subsequently demonstrate that among these IC regions, there are different sub-types of microglial cells. The neuronal pathways are already well established in IC and these results provide evidence that microglia contribute to this network, uncovering new avenues for the field to investigate in more depth how auditory signals are processed.

In addition, the thesis provided evidence in IC and hippocampus of the Tg model up to 18-months that there is no neuronal loss. However, there was an increase in the labelling of reactive astrocytes similar to hippocampus, which provides evidence for this integral nucleus within the auditory system to undergo similar AD related astrogliosis. Contrastingly, the morphology of the astrocytes in IC did not mirror the hippocampus. Therefore, by utilising future physiological approaches in line with these results could unearth interesting new areas of research regarding AD related glial responses, which could help in better understanding the link between hearing loss and AD.

Finally, anatomical, physiological and molecular approaches corroborated results that demonstrated synaptic dysfunction between IC and hippocampus in the Tg rat model, at similar time-points to when human AD symptoms start to develop. Therefore, these results reveal potential targets for future therapeutics to try and prevent the early manifestation of mitochondrial dysfunction of synapses within the auditory pathway to slow down the development of AD symptoms.

References

ABE, K. & CHIBA, Y. 2019. A case of treatable dementia with Lewy bodies remarkably improved by immunotherapy. *J Neuroimmunol,* 330**,** 35-37.

ABRÀMOFF, M. D., MAGALHÃES, P. J. & RAM, S. J. 2004. Image processing with ImageJ. *Biophotonics International,* 11**,** 36-42.

ACHTEN, E., BOON, P., DEPOORTER, J., CALLIAUW, L., VANDEKERCKHOVE, T., DEREUCK, J. & KUNNEN, M. 1995. An Mr Protocol for Presurgical Evaluation of Patients with Complex Partial Seizures of Temporal-Lobe Origin. *American Journal of Neuroradiology,* 16**,** 1201-1213.

ADAMS, J. C. 1979. Ascending Projections to the Inferior Colliculus. *Journal of Comparative Neurology,* 183**,** 519-538.

ADAMS, J. C. & MUGNAINI, E. 1984. Dorsal Nucleus of the Lateral Lemniscus - a Nucleus of Gabaergic Projection Neurons. *Brain Research Bulletin,* 13**,** 585-590.

ADE, K. K., JANSSEN, M. J., ORTINSKI, P. I. & VICINI, S. 2008. Differential tonic GABA conductances in striatal medium spiny neurons. *Journal of Neuroscience,* 28**,** 1185-1197.

AITKIN, L. M., DICKHAUS, H., SCHULT, W. & ZIMMERMANN, M. 1978. External nucleus of inferior colliculus - auditory and spinal somatosensory afferents and their interactions. *Journal of Neurophysiology,* 41**,** 837-847.

AJITO, K. & TORIMITSU, K. 2002. Laser trapping and Raman spectroscopy of single cellular organelles in the nanometer range. *Lab on a Chip,* 2**,** 11-14.

ALVAREZ, J. I., KATAYAMA, T. & PRAT, A. 2013. Glial influence on the blood brain barrier. *Glia,* 61**,** 1939-1958.

ALVES, L., CORREIA, A. S., MIGUEL, R., ALEGRIA, P. & BUGALHO, P. 2012. Alzheimer's disease: a clinical practice-oriented review. *Front Neurol,* 3**,** 63.

AMARAL, D. G., SCHARFMAN, H. E. & LAVENEX, P. 2007. The dentate gyrus: fundamental neuroanatomical organization (dentate gyrus for dummies). *Dentate Gyrus: A Comphrehensive Guide to Structure, Function, and Clinical Implications,* 163**,** 3-790.

AMENTA, F., BRONZETTI, E., SABBATINI, M. & VEGA, J. A. 1998. Astrocyte changes in aging cerebral cortex and hippocampus: A quantitative immunohistochemical study. *Microscopy Research and Technique,* 43**,** 29-33.

AMIEVA, H., LE GOFF, M., MILLET, X., ORGOGOZO, J. M., PERES, K., BARBERGER-GATEAU, P., JACQMIN-GADDA, H. & DARTIGUES, J. F. 2008. Prodromal Alzheimer's Disease: Successive Emergence of the Clinical Symptoms. *Annals of Neurology,* 64**,** 492-498.

ANAND, K. S. & DHIKAV, V. 2012. Hippocampus in health and disease: An overview. *Ann Indian Acad Neurol,* 15**,** 239-46.

ANDREOLLO, N. A., SANTOS, E. F. D., ARAÚJO, M. R. & LOPES, L. R. 2012. Rat's age versus human's age: what is the relationship? *ABCD. Arquivos Brasileiros de Cirurgia Digestiva (São Paulo),* 25**,** 49-51.

ANGELAKI, D. E. & CULLEN, K. E. 2008. Vestibular system: The many facets of a multimodal sense. *Annual Review of Neuroscience,* 31**,** 125-150.

ANGULO, M. C., KOZLOV, A. S., CHARPAK, S. & AUDINAT, E. 2004. Glutamate released from glial cells synchronizes neuronal activity in the hippocampus. *Journal of Neuroscience,* 24**,** 6920-6927.

ARMANO, S., ROSSI, P., TAGLIETTI, V. & D'ANGELO, E. 2000. Long-term potentiation of intrinsic excitability at the Mossy fiber-granule cell synapse of rat cerebellum. *Journal of Neuroscience,* 20**,** 5208-5216.

ATCHERSON, S. R., NAGARAJ, N. K., KENNETT, S. E. & LEVISEE, M. 2015. Overview of Central Auditory Processing Deficits in Older Adults. *Semin Hear,* 36**,** 150-161.

AYALA, Y. & MALMIERCA, M. 2013. Stimulus-specific adaptation and deviance detection in the inferior colliculus. *Frontiers in Neural Circuits,* 6**,** 89.

BAJO, V. M., MERCHAN, M. A., LOPEZ, D. E. & ROUILLER, E. M. 1993. Neuronal Morphology and Efferent Projections of the Dorsal Nucleus of the Lateral Lemniscus in the Rat. *Journal of Comparative Neurology,* 334**,** 241-262.

BAJO, V. M. & MOORE, D. R. 2005. Descending projections from the auditory cortex to the inferior colliculus in the gerbil, Meriones unguiculatus. *Journal of Comparative Neurology,* 486**,** 101-116.

BAJO, V. M., NODAL, F. R., BIZLEY, J. K., MOORE, D. R. & KING, A. J. 2006. The ferret auditory cortex: descending projections to the inferior colliculus. *Cerebral Cortex,* 17**,** 475-491.

BAJO, V. M., NODAL, F. R., MOORE, D. R. & KING, A. J. 2010. The descending corticocollicular pathway mediates learning-induced auditory plasticity. *Nature Neuroscience,* 13**,** 253-260.

BALL, K. K., CRUZ, N. F., MRAK, R. E. & DIENEL, G. A. 2010. Trafficking of glucose, lactate, and amyloid-beta from the inferior colliculus through perivascular routes. *J Cereb Blood Flow Metab,* 30**,** 162-176.

BARRADAS, P. C., CAVALCANTE, L. A., MENDEZ-OTERO, R. & VIEIRA, A. M. 1989. Astroglial differentiation in the opossum superior colliculus. *Glia,* 2**,** 103-111.

BARTLETT, E. L. 2013. The organization and physiology of the auditory thalamus and its role in processing acoustic features important for speech perception. *Brain and Language,* 126**,** 29-48.

BAUER, C. A., WISNER, K. W., BAIZER, J. S. & BROZOSKI, T. J. 2013. Tinnitus, Unipolar Brush Cells, and Cerebellar Glutamatergic Function in an Animal Model. *Plos One,* 8.

BAUMANN, S., GRIFFITHS, T. D., SUN, L., PETKOV, C. I., THIELE, A. & REES, A. 2011. Orthogonal representation of sound dimensions in the primate midbrain. *Nature Neuroscience,* 14**,** 423-425.

BEEBE, N. L., YOUNG, J. W., MELLOTT, J. G. & SCHOFIELD, B. R. 2016. Extracellular molecular markers and soma size of inhibitory neurons: evidence for four subtypes of GABAergic cells in the inferior colliculus. *Journal of Neuroscience,* 36**,** 3988-3999.

BENSON, C. G. & CANT, N. B. 2008. The ventral nucleus of the lateral lemniscus of the gerbil (Meriones unguiculatus): Organization of connections with the cochlear nucleus and the inferior colliculus. *Journal of Comparative Neurology,* 510**,** 673-690.

BENSON, T. E. & BROWN, M. C. 2004. Postsynaptic targets of type II auditory nerve fibers in the cochlear nucleus. *Jaro-Journal of the Association for Research in Otolaryngology,* 5**,** 111-125.

BHAT, R., CROWE, E. P., BITTO, A., MOH, M., KATSETOS, C. D., GARCIA, F. U., JOHNSON, F. B., TROJANOWSKI, J. Q., SELL, C. & TORRES, C. 2012. Astrocyte Senescence as a Component of Alzheimer's Disease. *Plos One,* 7**,** e45069.

BIELEFELD, E. C., COLING, D., CHEN, G. D., LI, M., TANAKA, C., HU, B. H. & HENDERSON, D. 2008. Age-related hearing loss in the Fischer 344/NHsd rat substrain. *Hearing Research,* 241**,** 26-33.

BLACKBURN, C. C. & SACHS, M. B. 1990. The representations of the steady-state vowel sound/e/in the discharge patterns of cat anteroventral cochlear nucleus neurons. *Journal of neurophysiology,* 63**,** 1191-1212.

BLACKSTAD, T. W., OSEN, K. K. & MUGNAINI, E. 1984. Pyramidal neurones of the dorsal cochlear nucleus: a Golgi and computer reconstruction study in cat. *Neuroscience,* 13**,** 827-854.

BLANC, F., COLLOBY, S. J., CRETIN, B., DE SOUSA, P. L., DEMUYNCK, C., O'BRIEN, J. T., MARTIN-HUNYADI, C., MCKEITH, I., PHILIPPI, N. & TAYLOR, J. P. 2016. Grey matter atrophy in prodromal stage of dementia with Lewy bodies and Alzheimer's disease. *Alzheimers Research & Therapy,* 8**,** 1-11.

BLASKO, I., VEERHUIS, R., STAMPFER-KOUNTCHEV, M., SAURWEIN-TEISSL, M., EIKELENBOOM, P. & GRUBECK-LOEBENSTEIN, B. 2000. Costimulatory effects of interferon-gamma and interleukin-1beta or tumor necrosis factor alpha on the synthesis of Abeta1-40 and Abeta1-42 by human astrocytes. *Neurobiol Dis,* 7**,** 682-689.

BOURQUE, G., PEVZNER, P. A. & TESLER, G. 2004. Reconstructing the genomic architecture of ancestral mammals: Lessons from human, mouse, and rat genomes. *Genome Research,* 14**,** 507-516.

BRAKEMAN, P. R., LANAHAN, A. A., O'BRIEN, R., ROCHE, K., BARNES, C. A., HUGANIR, R. L. & WORLEY, P. F. 1997. Homer: A protein that selectively binds metabotropic glutamate receptors. *Nature,* 386**,** 284-288.

BRAND, M. D. & NICHOLLS, D. G. 2011. Assessing mitochondrial dysfunction in cells. *Biochem J,* 435**,** 297-312.

BROTHERTON, H., PLACK, C. J., MASLIN, M., SCHAETTE, R. & MUNRO, K. J. 2015. Pump Up the Volume: Could Excessive Neural Gain Explain Tinnitus and Hyperacusis? *Audiology and Neuro-Otology,* 20**,** 273-282.

BROWNELL, W. E. 1997. How the ear works: Nature's solutions for listening. *Volta Review,* 99**,** 9-28.

BRUNSO-BECHTOLD, J. K., THOMPSON, G. C. & MASTERTON, R. B. 1981. HRP study of the organization of auditory afferents ascending to central nucleus of inferior colliculus in cat. *J Comp Neurol,* 197**,** 705-722.

BULLOCH, K., MILLER, M. M., GAL-TOTH, J., MILNER, T. A., GOTTFRIED-BLACKMORE, A., WATERS, E. M., KAUNZNER, U. W., LIU, K., LINDQUIST, R., NUSSENZWEIG, M. C., STEINMAN, R. M. & MCEWEN, B. S. 2008. CD11c/EYFP transgene illuminates a discrete network of dendritic cells within the embryonic, neonatal, adult, and injured mouse brain. *Journal of Comparative Neurology,* 508**,** 687-710.

BURDA, J. E. & SOFRONIEW, M. V. 2014. Reactive Gliosis and the Multicellular Response to CNS Damage and Disease. *Neuron,* 81**,** 229-248.

BURKE, S. N. & BARNES, C. A. 2006. Neural plasticity in the ageing brain. *Nature Reviews Neuroscience,* 7**,** 30-40.

BUSCEMI, L., GINET, V., LOPATAR, J., MONTANA, V., PUCCI, L., SPAGNUOLO, P., ZEHNDER, T., GRUBIŠIĆ, V., TRUTTMAN, A., SALA, C., HIRT, L., PARPURA, V., PUYAL, J. & BEZZI, P. 2017. Homer1 scaffold proteins govern Ca2+ dynamics in normal and reactive astrocytes. *Cerebral Cortex,* 27**,** 2365-2384.

BYLICKY, M. A., MUELLER, G. P. & DAY, R. M. 2018. Mechanisms of Endogenous Neuroprotective Effects of Astrocytes in Brain Injury. *Oxid Med Cell Longev,* 2018**,** 6501031.

CANT, N. B. & BENSON, C. G. 2003. Parallel auditory pathways: projection patterns of the different neuronal populations in the dorsal and ventral cochlear nuclei. *Brain Res Bull,* 60**,** 457-474.

CANT, N. B. & BENSON, C. G. 2005. An atlas of the inferior colliculus of the gerbil in three dimensions. *Hearing Research,* 206**,** 12-27.

CENTONZE, D., PICCONI, B., GUBELLINI, P., BERNARDI, G. & CALABRESI, P. 2001. Dopaminergic control of synaptic plasticity in the dorsal striatum. *European Journal of Neuroscience,* 13**,** 1071-1077.

CHAI, H., DIAZ-CASTRO, B., SHIGETOMI, E., MONTE, E., OCTEAU, J. C., YU, X. Z., COHN, W., RAJENDRAN, P. S., VONDRISKA, T. M., WHITELEGGE, J. P., COPPOLA, G. & KHAKH, B. S. 2017. Neural Circuit-Specialized Astrocytes: Transcriptomic, Proteomic, Morphological, and Functional Evidence. *Neuron,* 95**,** 531-549.

CHAN-PALAY, V. & PALAY, S. L. 1972. The form of velate astrocytes in the cerebellar cortex of monkey and rat: high voltage electron microscopy of rapid Golgi preparations. *Z Anat Entwicklungsgesch,* 138**,** 1-19.

CHEN, C. G., CHENG, M. X., ITO, T. & SONG, S. 2018. Neuronal Organization in the Inferior Colliculus Revisited with Cell-Type-Dependent Monosynaptic Tracing. *Journal of Neuroscience,* 38**,** 3318-3332.

CHEN, H. C., DETMER, S. A., EWALD, A. J., GRIFFIN, E. E., FRASER, S. E. & CHAN, D. C. 2003. Mitofusins Mfn1 and Mfn2 coordinately regulate mitochondrial fusion and are essential for embryonic development. *Journal of Cell Biology,* 160**,** 189-200.

CHENG, G., ZIELONKA, M., DRANKA, B., KUMAR, S. N., MYERS, C. R., BENNETT, B., GARCES, A. M., MACHADO, L. G. D. D., THIEBAUT, D., OUARI, O., HARDY, M., ZIELONKA, J. & KALYANARAMAN, B. 2018. Detection of mitochondria-generated reactive oxygen species in cells using multiple probes and methods: Potentials, pitfalls, and the future. *Journal of Biological Chemistry,* 293**,** 10363-10380.

CHINTA, S. J., WOODS, G., RANE, A., DEMARIA, M., CAMPISI, J. & ANDERSEN, J. K. 2015. Cellular senescence and the aging brain. *Exp Gerontol,* 68**,** 3-7.

CHOI, S. S., LEE, H. J., LIM, I., SATOH, J. & KIM, S. U. 2014. Human Astrocytes: Secretome Profiles of Cytokines and Chemokines. *Plos One,* 9**,** e92325.

CHOLFIN, J. A. & RUBENSTEIN, J. L. R. 2008. Frontal cortex subdivision patterning is coordinately regulated by Fgf8, Fgf17, and Emx2. *Journal of Comparative Neurology,* 509**,** 144-155.

CHRISTENSEN, J. R., LARSEN, K. B., LISANBY, S. H., SCALIA, J., ARANGO, V., DWORK, A. J. & PAKKENBERG, B. 2007. Neocortical and hippocampal neuron and glial cell numbers in the rhesus monkey. *Anatomical Record-Advances in Integrative Anatomy and Evolutionary Biology,* 290**,** 330-340.

CIRUELA, F., SOLOVIEV, M. M., CHAN, W. Y. & MCILHINNEY, R. A. 2000. Homer-1c/Vesl-1L modulates the cell surface targeting of metabotropic glutamate receptor type 1alpha: evidence for an anchoring function. *Molecular and Cellular Neuroscience,* 15**,** 36-50.

CLERICI, W. J. & COLEMAN, J. R. 1987. Resting and Pure-Tone Evoked Metabolic Responses in the Inferior Colliculus of Young-Adult and Senescent Rats. *Neurobiology of Aging,* 8**,** 171-178.

CLERICI, W. J., MCDONALD, A. J., THOMPSON, R. & COLEMAN, J. R. 1990. Anatomy of the rat medial geniculate body: II. Dendritic morphology. *J Comp Neurol,* 297**,** 32-54.

CLIFTON, N. E., CAMERON, D., TRENT, S., SYKES, L. H., THOMAS, K. L. & HALL, J. 2017. Hippocampal regulation of postsynaptic density homer1 by associative learning. *Neural Plasticity,* 2017**,** 11.

COFFMAN, K. A., DUM, R. P. & STRICK, P. L. 2011. Cerebellar vermis is a target of projections from the motor areas in the cerebral cortex. *Proceedings of the National Academy of Sciences of the United States of America,* 108**,** 16068-16073.

COHEN, J. D. & SERVAN-SCHREIBER, D. 1992. Context, cortex, and dopamine: a connectionist approach to behavior and biology in schizophrenia. *Psychol Rev,* 99**,** 45-77.

COHEN, R. M., REZAI-ZADEH, K., WEITZ, T. M., RENTSENDORJ, A., GATE, D., SPIVAK, I., BHOLAT, Y., VASILEVKO, V., GLABE, C. G., BREUNIG, J. J., RAKIC, P., DAVTYAN, H., AGADJANYAN, M. G., KEPE, V., BARRIO, J. R., BANNYKH, S., SZEKELY, C. A., PECHNICK, R. N. & TOWN, T. 2013. A Transgenic Alzheimer Rat with Plaques, Tau Pathology, Behavioral Impairment, Oligomeric A beta, and Frank Neuronal Loss. *Journal of Neuroscience,* 33**,** 6245-6256.

COOTE, E. J. & REES, A. 2008. The distribution of nitric oxide synthase in the inferior colliculus of guinea pig. *Neuroscience,* 154**,** 218-225.

COTMAN, C. W. & SU, J. H. 1996. Mechanisms of neuronal death in Alzheimer's disease. *Brain Pathol,* 6**,** 493-506.

COVEY, E. & CASSEDAY, J. H. 1991. The Monaural Nuclei of the Lateral Lemniscus in an Echolocating Bat - Parallel Pathways for Analyzing Temporal Features of Sound. *Journal of Neuroscience,* 11**,** 3456-3470.

CREMER, J. E. & SEVILLE, M. P. 1983. Regional brain blood flow, blood volume, and haematocrit values in the adult rat. *J Cereb Blood Flow Metab,* 3**,** 254-256.

CREWS, L. & MASLIAH, E. 2010. Molecular mechanisms of neurodegeneration in Alzheimer's disease. *Hum Mol Genet,* 19**,** R12-20.

CUREOGLU, S., BAYLAN, M. Y. & PAPARELLA, M. M. 2010. Cochlear otosclerosis. *Curr Opin Otolaryngol Head Neck Surg,* 18**,** 357-362.

D'ANGELO, E. & CASALI, S. 2012. Seeking a unified framework for cerebellar function and dysfunction: from circuit operations to cognition. *Front Neural Circuits,* 6**,** 116.

DAVIES, C. A., MANN, D. M. A., SUMPTER, P. Q. & YATES, P. O. 1987. A Quantitative Morphometric Analysis of the Neuronal and Synaptic Content of the Frontal and Temporal Cortex in Patients with Alzheimers-Disease. *Journal of the Neurological Sciences,* 78**,** 151-164.

DE MARTINO, F., MOEREL, M., VAN DE MOORTELE, P. F., UGURBIL, K., GOEBEL, R., YACOUB, E. & FORMISANO, E. 2013. Spatial organization of frequency preference and selectivity in the human inferior colliculus. *Nature Communications,* 4**,** 1-8.

DE NO, R. L. 1981. *The primary acoustic nuclei*, Raven Press.

DE STROOPER, B. 2007. Loss-of-function presenilin mutations in Alzheimer disease - Talking Point on the role of presenilin mutations in Alzheimer disease. *Embo Reports,* 8**,** 141-146.

DE STROOPER, B. & KARRAN, E. 2016. The Cellular Phase of Alzheimer's Disease. *Cell,* 164**,** 603-615.

DEBUS, E., WEBER, K. & OSBORN, M. 1983. Monoclonal-antibodies specific for glial fibrillary acidic (GFA) protein and for each of the neurofilament triplet polypeptides. *Differentiation,* 25**,** 193-203.

DEKOSKY, S. T. & SCHEFF, S. W. 1990. Synapse Loss in Frontal-Cortex Biopsies in Alzheimers-Disease - Correlation with Cognitive Severity. *Annals of Neurology,* 27**,** 457-464.

DESTRIEUX, C., BOURRY, D. & VELUT, S. 2013. Surgical anatomy of the hippocampus. *Neurochirurgie,* 59**,** 149-158.

DIGIOVANNI, J., SUN, T. & SHENG, Z. H. 2012. Characterizing synaptic vesicle proteins using synaptosomal fractions and cultured hippocampal neurons. *Current protocols in neuroscience,* 59**,** 2.7. 1-2.7. 22.

DIVAKARUNI, A. S., PARADYSE, A., FERRICK, D. A., MURPHY, A. N. & JASTROCH, M. 2014. Analysis and Interpretation of Microplate-Based Oxygen Consumption and pH Data. *Mitochondrial Function,* 547**,** 309-354.

DOSSI, E., VASILE, F. & ROUACH, N. 2018. Human astrocytes in the diseased brain. *Brain Research Bulletin,* 136**,** 139-156.

EDELINE, J. M. 1999. Learning-induced physiological plasticity in the thalamo-cortical sensory systems: A critical evaluation of receptive field plasticity, map changes and their potential mechanisms. *Progress in Neurobiology,* 57**,** 165-224.

EKDALE, E. G. 2016. Form and function of the mammalian inner ear. *Journal of Anatomy,* 228**,** 324-337.

ELSTON, G. N., OGA, T., OKAMOTO, T. & FUJITA, I. 2010. Spinogenesis and Pruning from Early Visual Onset to Adulthood: An Intracellular Injection Study of Layer III Pyramidal Cells in the Ventral Visual Cortical Pathway of the Macaque Monkey. *Cerebral Cortex,* 20**,** 1398-1408.

ENG, L. F. & DEARMOND, S. J. 1982. Immunocytochemical studies of astrocytes in normal development and disease. *Advances in cellular neurobiology.* Elsevier.

ENGLE, J. R., GRAY, D. T., TURNER, H., UDELL, J. B. & RECANZONE, G. H. 2014. Age-related neurochemical changes in the rhesus macaque inferior colliculus. *Frontiers in Aging Neuroscience,* 6**,** 73.

ESHKOOR, S. A., HAMID, T. A., MUN, C. Y. & NG, C. K. 2015. Mild cognitive impairment and its management in older people. *Clin Interv Aging,* 10**,** 687-693.

EVANS, E. & NELSON, P. 1973. The responses of single neurones in the cochlear nucleus of the cat as a function of their location and the anaesthetic state. *Experimental Brain Research,* 17**,** 402-427.

EVERSFIELD, C. L. & ORTON, L. D. 2019. Auditory and visual hallucination prevalence in Parkinson's disease and dementia with Lewy bodies: a systematic review and meta-analysis. *Psychol Med,* 49**,** 2342-2353.

FAYE-LUND, H. & OSEN, K. K. 1985. Anatomy of the inferior colliculus in rat. *Anatomy and Embryology,* 171**,** 1-20.

FELICIANO, M. & POTASHNER, S. J. 1995. Evidence for a glutamatergic pathway from the guinea-pig auditory-cortex to the inferior colliculus. *Journal of Neurochemistry,* 65**,** 1348-1357.

FISCHER, N., WEBER, B. & RIECHELMANN, H. 2016. [Presbycusis - Age Related Hearing Loss]. *Laryngorhinootologie,* 95**,** 497-510.

FITZPATRICK, K. A. 1975. Cellular architecture and topographic organization of the inferior colliculus of the squirrel monkey. *J Comp Neurol,* 164**,** 185-207.

FLOOD, D. G. & COLEMAN, P. D. 1986. Failed Compensatory Dendritic Growth as a Pathophysiological Process in Alzheimers-Disease. *Canadian Journal of Neurological Sciences,* 13**,** 475-479.

FLYNN, J. M., CHOI, S. W., DAY, N. U., GERENCSER, A. A., HUBBARD, A. & MELOV, S. 2011. Impaired spare respiratory capacity in cortical synaptosomes from Sod2 null mice. *Free Radic Biol Med,* 50**,** 866-873.

FONG, A. Y., STORNETTA, R. L., FOLEY, C. M. & POTTS, J. T. 2005. Immunohistochemical localization of GAD67-expressing neurons and processes in the rat brainstem: subregional distribution in the nucleus tractus solitarius. *Journal of Comparative Neurology,* 493**,** 274-290.

FONNUM, F. 1984. Glutamate - a Neurotransmitter in Mammalian Brain. *Journal of Neurochemistry,* 42**,** 1-11.

FORMAN, M. S., LAL, D., ZHANG, B., DABIR, D. V., SWANSON, E., LEE, V. M. Y. & TROJANOWSKI, J. Q. 2005. Transgenic mouse model of tau pathology in astrocytes leading to nervous system degeneration. *Journal of Neuroscience,* 25**,** 3539-3550.

FOSTER, N. L., MELLOTT, J. G. & SCHOFIELD, B. R. 2014. Perineuronal nets and GABAergic cells in the inferior colliculus of guinea pigs. *Frontiers in Neuroanatomy,* 7**,** 53.

FREUND, T. F. & BUZSAKI, G. 1996. Interneurons of the hippocampus. *Hippocampus,* 6**,** 347-470.

FRISINA, R. D., SMITH, R. L. & CHAMBERLAIN, S. C. 1990. Encoding of amplitude modulation in the gerbil cochlear nucleus: I. A hierarchy of enhancement. *Hearing research,* 44**,** 99-122.

FUENTES-SANTAMARÍA, V., ALVARADO, J. C. & JUIZ, J. M. 2012. Long-term interaction between microglial cells and cochlear nucleus neurons after bilateral cochlear ablation. *Journal of Comparative Neurology,* 520**,** 2974-2990.

FUJITA, I. & KONISHI, M. 1991. The role of GABAergic inhibition in processing of interaural time difference in the owl's auditory system. *J Neurosci,* 11**,** 722-739.

GAMES, K. D. & WINER, J. A. 1988. Layer V in rat auditory: cortex projections to the inferior colliculus and contralateral cortex. *Hearing Research,* 34**,** 1-26.

GATES, G. A. & MILLS, J. H. 2005. Presbycusis. *Lancet,* 366**,** 1111-1120.

GAVRILOVICI, C., D'ALFONSO, S. & POULTER, M. O. 2010. Diverse interneuron populations have highly specific interconnectivity in the rat piriform cortex. *Journal of Comparative Neurology,* 518**,** 1570-1588.

GEIS, H. R. A. P. & BORST, J. G. G. 2013. Intracellular responses to frequency modulated tones in the dorsal cortex of the mouse inferior colliculus. *Frontiers in Neural Circuits,* 7**,** 7.

GHIRARDINI, E., WADLE, S. L., AUGUSTIN, V., BECKER, J., BRILL, S., HAMMERICH, J., SEIFERT, G. & STEPHAN, J. 2018. Expression of functional inhibitory neurotransmitter transporters GlyT1, GAT-1, and GAT-3 by astrocytes of inferior colliculus and hippocampus. *Molecular Brain,* 11**,** 4.

GIBBS, R. A., WEINSTOCK, G. M., METZKER, M. L., MUZNY, D. M., SODERGREN, E. J., SCHERER, S., SCOTT, G., STEFFEN, D., WORLEY, K. C., BURCH, P. E., OKWUONU, G., HINES, S., LEWIS, L., DERAMO, C., DELGADO, O., DUGAN-ROCHA, S., MINER, G., MORGAN, M., HAWES, A., GILL, R., CELERA, HOLT, R. A., ADAMS, M. D., AMANATIDES, P. G., BADEN-TILLSON, H., BARNSTEAD, M., CHIN, S., EVANS, C. A., FERRIERA, S., FOSLER, C., GLODEK, A., GU, Z., JENNINGS, D., KRAFT, C. L., NGUYEN, T., PFANNKOCH, C. M., SITTER, C., SUTTON, G. G., VENTER, J. C., WOODAGE, T., SMITH, D., LEE, H. M., GUSTAFSON, E., CAHILL, P., KANA, A., DOUCETTE-STAMM, L., WEINSTOCK, K., FECHTEL, K., WEISS, R. B., DUNN, D. M., GREEN, E. D., BLAKESLEY, R. W., BOUFFARD, G. G., DE JONG, P. J., OSOEGAWA, K., ZHU, B., MARRA, M., SCHEIN, J., BOSDET, I., FJELL, C., JONES, S.,

KRZYWINSKI, M., MATHEWSON, C., SIDDIQUI, A., WYE, N., MCPHERSON, J., ZHAO, S., FRASER, C. M., SHETTY, J., SHATSMAN, S., GEER, K., CHEN, Y., ABRAMZON, S., NIERMAN, W. C., HAVLAK, P. H., CHEN, R., DURBIN, K. J., EGAN, A., REN, Y., SONG, X. Z., LI, B., LIU, Y., QIN, X., CAWLEY, S., WORLEY, K. C., COONEY, A. J., D'SOUZA, L. M., MARTIN, K., WU, J. Q., GONZALEZ-GARAY, M. L., JACKSON, A. R., KALAFUS, K. J., MCLEOD, M. P., MILOSAVLJEVIC, A., VIRK, D., VOLKOV, A., WHEELER, D. A., ZHANG, Z., BAILEY, J. A., EICHLER, E. E., et al. 2004. Genome sequence of the Brown Norway rat yields insights into mammalian evolution. *Nature,* 428**,** 493-521.

GIMSE, K., GORZEK, R. C., OLIN, A., OSTING, S. & BURGER, C. 2018. Hippocampal Homer1b/c is necessary for contextual fear conditioning and group I metabotropic glutamate receptor mediated long-term depression. *Neurobiology of Learning and Memory,* 156**,** 17-23.

GIRARD, S. D., JACQUET, M., BARANGER, K., MIGLIORATI, M., ESCOFFIER, G., BERNARD, A., KHRESTCHATISKY, M., FERON, F., RIVERA, S., ROMAN, F. S. & MARCHETTI, E. 2014. Onset of hippocampus-dependent memory impairments in 5XFAD transgenic mouse model of Alzheimer's disease. *Hippocampus,* 24**,** 762-772.

GLEICH, O., NETZ, J. & STRUTZ, J. 2014. Comparing the inferior colliculus of young and old gerbils (Meriones unguiculatus) with an emphasis on GABA. *Experimental Gerontology,* 57**,** 155-162.

GLENDENNING, K., BRUSNO-BECHTOLD, J., THOMPSON, G. & MASTERTON, R. 1981. Ascending auditory afferents to the nuclei of the lateral leminscus. *Journal of Comparative Neurology,* 197**,** 673-703.

GLUECKERT, R., BITSCHE, M., MILLER, J. M., ZHU, Y. Y., PRIESKORN, D. M., ALTSCHULER, R. A. & SCHROTT-FISCHER, A. 2008. Deafferentiation-associated changes in afferent and efferent processes in the guinea pig cochlea and afferent regeneration with chronic intrascalar brain-derived neurotrophic factor and acidic fibroblast growth factor. *Journal of Comparative Neurology,* 507**,** 1602-1621.

GOATE, A. & HARDY, J. 2012. Twenty years of Alzheimer's disease-causing mutations. *J Neurochem,* 120 Suppl 1**,** 3-8.

GOLDBERG, J. M. & BROWN, P. B. 1968. Functional organization of the dog superior olivary complex: an anatomical and electrophysiological study. *J Neurophysiol,* 31**,** 639-656.

GOMEZ-NICOLA, D. & PERRY, V. H. 2015. Microglial dynamics and role in the healthy and diseased brain: a paradigm of functional plasticity. *Neuroscientist,* 21**,** 169-184.

GOURAS, G. K. 2019. Aging, Metabolism, Synaptic Activity, and A beta in Alzheimer's Disease. *Frontiers in Aging Neuroscience,* 11**,** 185.

GOVONI, S., AMADIO, M., BATTAINI, F. & PASCALE, A. 2010. Senescence of the brain: focus on cognitive kinases. *Curr Pharm Des,* 16**,** 660-671.

GRAY, E. G. & WHITTAKER, V. P. 1962. The isolation of nerve endings from brain: an electron-microscopic study of cell fragments derived by homogenization and centrifugation. *J Anat,* 96**,** 79-88.

GREENE, N. T., ANBUHL, K. L., FERBER, A. T., DEGUZMAN, M., ALLEN, P. D. & TOLLIN, D. J. 2018. Spatial hearing ability of the pigmented Guinea pig (Cavia porcellus): Minimum audible angle and spatial release from masking in azimuth. *Hearing Research,* 365**,** 62-76.

GRIFFIN, W. S. T., STANLEY, L. C., LING, C., WHITE, L., MACLEOD, V., PERROT, L. J., WHITE, C. L. & ARAOZ, C. 1989. Brain Interleukin-1 and S-100 Immunoreactivity Are Elevated in down Syndrome and Alzheimer-Disease. *Proceedings of the National Academy of Sciences of the United States of America,* 86**,** 7611-7615.

GROSCHE, J., KETTENMANN, H. & REICHENBACH, A. 2002. Bergmann glial cells form distinct morphological structures to interact with cerebellar neurons. *J Neurosci Res,* 68**,** 138-149.

GROSS, P. M., SPOSITO, N. M., PETTERSEN, S. E., PANTON, D. G. & FENSTERMACHER, J. D. 1987. Topography of Capillary Density, Glucose-Metabolism, and Microvascular Function within the Rat Inferior Colliculus. *Journal of Cerebral Blood Flow and Metabolism,* 7**,** 154-160.

GUINAN, J. J., NORRIS, B. E. & GUINAN, S. S. 1972. Single auditory units in the superior olivary complex: II: locations of unit categories and tonotopic organization. *International Journal of Neuroscience,* 4**,** 147-166.

GUTTENPLAN, K. A. & LIDDELOW, S. A. 2019. Astrocytes and microglia: Models and tools. *J Exp Med,* 216**,** 71-83.

HAFIDI, A. & GALIFIANAKIS, D. 2003. Macroglia distribution in the developing and adult inferior colliculus. *Developmental Brain Research,* 143**,** 167-177.

HALL, A. M. & ROBERSON, E. D. 2012. Mouse models of Alzheimer's disease. *Brain Res Bull,* 88**,** 3-12.

HANSEL, C., LINDEN, D. J. & D'ANGELO, E. 2001. Beyond parallel fiber LTD: the diversity of synaptic and non-synaptic plasticity in the cerebellum. *Nat Neurosci,* 4**,** 467-475.

HARADA, C. N., NATELSON LOVE, M. C. & TRIEBEL, K. L. 2013. Normal cognitive aging. *Clin Geriatr Med,* 29**,** 737-752.

HARDY, J., COWBURN, R., BARTON, A., REYNOLDS, G., DODD, P., WESTER, P., OCARROLL, A. M., LOFDAHL, E. & WINBLAD, B. 1987. A Disorder of Cortical Gabaergic Innervation in Alzheimers-Disease. *Neuroscience Letters,* 73**,** 192-196.

HARDY, J. A. & HIGGINS, G. A. 1992. Alzheimer's disease: the amyloid cascade hypothesis. *Science,* 256**,** 184-186.

HARRISON, J. M. & IRVING, R. 1966. The organization of the posterior ventral cochlear nucleus in the rat. *J Comp Neurol,* 126**,** 391-401.

HAYASHI, Y., ISHIBASHI, H., HASHIMOTO, K. & NAKANISHI, H. 2006. Potentiation of the NMDA receptor-mediated responses through the activation of the glycine site by microglia secreting soluble factors. *Glia,* 53**,** 660-668.

HEBB, D. O. 1952. *The organisation of behaviour: a neuropsychological theory*, Wiley.

HELFER, J. L., GOODLETT, C. R., GREENOUGH, W. T. & KLINTSOVA, A. Y. 2009. The effects of exercise on adolescent hippocampal neurogenesis in a rat model of binge alcohol exposure during the brain growth spurt. *Brain Research,* 1294**,** 1-11.

HEQUEMBOURG, S. & LIBERMAN, M. C. 2001. Spiral ligament pathology: A major aspect of age-related cochlear degeneration in C57BL/6 mice. *Jaro,* 2**,** 118-129.

HERBERT, H., ASCHOFF, A. & OSTWALD, J. 1991. Topography of projections from the auditory cortex to the inferior colliculus in the rat. *Journal of Comparative Neurology,* 304**,** 103-122.

HIERRO-BUJALANCE, C., BACSKAI, B. J. & GARCIA-ALLOZA, M. 2018. In Vivo Imaging of Microglia With Multiphoton Microscopy. *Front Aging Neurosci,* 10**,** 218.

HILL, R. A. & GRUTZENDLER, J. 2014. In vivo imaging of oligodendrocytes with sulforhodamine 101. *Nature Methods,* 11**,** 1081-1082.

HUANG, Q. & TANG, J. 2010. Age-related hearing loss or presbycusis. *Eur Arch Otorhinolaryngol,* 267**,** 1179-91.

HUBER, G. C. & CROSBY, E. C. 1943. A comparison of the mammalian and reptilian tecta. *Journal of Comparative Neurology,* 78**,** 133-168.

HUCHON, D., MADSEN, O., SIBBALD, M. J., AMENT, K., STANHOPE, M. J., CATZEFLIS, F., DE JONG, W. W. & DOUZERY, E. J. 2002. Rodent phylogeny and a timescale for the evolution of Glires: evidence from an extensive taxon sampling using three nuclear genes. *Mol Biol Evol,* 19**,** 1053-65.

HUDSPETH, A. J. 1989. How the Ears Works Work. *Nature,* 341**,** 397-404.

HUMES, L. E., DUBNO, J. R., GORDON-SALANT, S., LISTER, J. J., CACACE, A. T., CRUICKSHANKS, K. J., GATES, G. A., WILSON, R. H. & WINGFIELD, A. 2012. Central presbycusis: a review and evaluation of the evidence. *J Am Acad Audiol,* 23**,** 635-66.

HUYNH, D. P., FIGUEROA, K., HOANG, N. & PULST, S. M. 2000. Nuclear localization or inclusion body formation of ataxin-2 are not necessary for SCA2 pathogenesis in mouse or human. *Nature Genetics,* 26**,** 44-50.

IDRIZBEGOVIC, E., HEDERSTIERNA, C., DAHLQUIST, M., KAMPFE NORDSTROM, C., JELIC, V. & ROSENHALL, U. 2011. Central auditory function in early Alzheimer's disease and in mild cognitive impairment. *Age Ageing,* 40**,** 249-254.

IMAI, Y., IBATA, I., ITO, D., OHSAWA, K. & KOHSAKA, S. 1996. A novel gene iba1 in the major histocompatibility complex class III region encoding an EF hand protein expressed in a monocytic lineage. *Biochemical and Biophysical Research Communications,* 224**,** 855-862.

INGHAM, N. J. & MCALPINE, D. 2005. GABAergic inhibition controls neural gain in inferior colliculus neurons sensitive to interaural time differences. *J Neurosci,* 25**,** 6187-6198.

IQBAL, K. & GRUNDKE-IQBAL, I. 2010. Alzheimer's disease, a multifactorial disorder seeking multitherapies. *Alzheimers Dement,* 6**,** 420-424.

IRIZARRY, M. C., MCNAMARA, M., FEDORCHAK, K., HSIAO, K. & HYMAN, B. T. 1997. APP(Sw) transgenic mice develop age-related A beta deposits and neuropil abnormalities, but no neuronal loss in CA1. *Journal of Neuropathology and Experimental Neurology,* 56**,** 965-973.

ITO, M. 1989. Long-term depression. *Annu Rev Neurosci,* 12**,** 85-102.

ITO, T., BISHOP, D. C. & OLIVER, D. L. 2009. Two classes of GABAergic neurons in the inferior colliculus. *Journal of Neuroscience,* 29**,** 13860-13869.

JAAFARI, N., KHOMITCH-BAUD, A., GILHODES, J. C., HUA, G. & JULÉ, Y. 2008. Qualitative and quantitative analysis of tachykinin NK2 receptors in chemically defined human colonic neuronal pathways. *Journal of Comparative Neurology,* 507**,** 1542-1558.

JACK, C. R. & HOLTZMAN, D. M. 2013. Biomarker Modeling of Alzheimer's Disease. *Neuron,* 80**,** 1347-1358.

JACKSON, J., JAMBRINA, E., LI, J., MARSTON, H., MENZIES, F., PHILLIPS, K. & GILMOUR, G. 2019. Targeting the Synapse in Alzheimer's Disease. *Frontiers in Neuroscience,* 13**,** 735.

JANKOVIC, J. & AGUILAR, L. G. 2008. Current approaches to the treatment of Parkinson's disease. *Neuropsychiatr Dis Treat,* 4**,** 743-757.

JANKOWSKY, J. L. & ZHENG, H. 2017. Practical considerations for choosing a mouse model of Alzheimer's disease. *Mol Neurodegener,* 12**,** 89.

JASTROCH, M., DIVAKARUNI, A. S., MOOKERJEE, S., TREBERG, J. R. & BRAND, M. D. 2010. Mitochondrial proton and electron leaks. *Essays in Biochemistry: Mitochondrial Function,* 47**,** 53-67.

JAY, M. F. & SPARKS, D. L. 1987. Sensorimotor integration in the primate superior colliculus. I. Motor convergence. *J Neurophysiol,* 57**,** 22-34.

JOHNSON, N. A., JAHNG, G. H., WEINER, M. W., MILLER, B. L., CHUI, H. C., JAGUST, W. J., GORNO-TEMPINI, M. L. & SCHUFF, N. 2005. Pattern of cerebral hypoperfusion in Alzheimer disease and mild cognitive impairment measured with arterial spin-labeling MR imaging: initial experience. *Radiology,* 234**,** 851-859.

JORIS, P. X., SMITH, P. H. & YIN, T. C. 1994. Enhancement of neural synchronization in the anteroventral cochlear nucleus. II. Responses in the tuning curve tail. *J Neurophysiol,* 71**,** 1037-1051.

KAAS, J. H. 2010. The evolution of neocortex from early mammals to humans. *International Journal of Developmental Neuroscience,* 28**,** 648-648.

KAAS, J. H. & HACKETT, T. A. 1999. 'What' and 'where' processing in auditory cortex. *Nature Neuroscience,* 2**,** 1045-1047.

KALINICHENKO, S. G. & OKHOTIN, V. E. 2005. Unipolar brush cells--a new type of excitatory interneuron in the cerebellar cortex and cochlear nuclei of the brainstem. *Neurosci Behav Physiol,* 35**,** 21-36.

KAMPHUIS, W., MAMBER, C., MOETON, M., KOOIJMAN, L., SLUIJS, J. A., JANSEN, A. H. P., VERVEER, M., DE GROOT, L. R., SMITH, V. D., RANGARAJAN, S., RODRIGUEZ, J. J., ORRE, M. & HOL, E. M. 2012. GFAP Isoforms in Adult Mouse Brain with a Focus on Neurogenic Astrocytes and Reactive Astrogliosis in Mouse Models of Alzheimer Disease. *Plos One,* 7**,** e42823.

KANN, O., PAPAGEORGIOU, I. E. & DRAGUHN, A. 2014. Highly energized inhibitory interneurons are a central element for information processing in cortical networks. *J Cereb Blood Flow Metab,* 34**,** 1270-1282.

KARANTZOULIS, S. & GALVIN, J. E. 2011. Distinguishing Alzheimer's disease from other major forms of dementia. *Expert Rev Neurother,* 11**,** 1579-1591.

KARTEN, H. J. 2015. Vertebrate brains and evolutionary connectomics: on the origins of the mammalian 'neocortex'. *Philosophical Transactions of the Royal Society B-Biological Sciences,* 370**,** 20150060.

KASHYAP, G., BAPAT, D., DAS, D., GOWAIKAR, R., AMRITKAR, R. E., RANGARAJAN, G., RAVINDRANATH, V. & AMBIKA, G. 2019. Synapse loss and progress of Alzheimer's disease - A network model. *Scientific Reports,* 9**,** 1-9.

KAZEE, A. M., HAN, L. Y., SPONGR, V. P., WALTON, J. P., SALVI, R. J. & FLOOD, D. G. 1995. Synaptic Loss in the Central Nucleus of the Inferior Colliculus Correlates with Sensorineural Hearing-Loss in the C57bl/6 Mouse Model of Presbycusis. *Hearing Research,* 89**,** 109-120.

KEATING, P., DAHMEN, J. C. & KING, A. J. 2013. Context-specific reweighting of auditory spatial cues following altered experience during development. *Current Biology,* 23**,** 1291-1299.

KELLEHER, M. A., HIRST, J. J. & PALLISER, H. K. 2013. Changes in neuroactive steroid concentrations after preterm delivery in the guinea pig. *Reproductive Sciences,* 20**,** 1365-1375.

KELLEHER, M. A., PALLISER, H. K., WALKER, D. W. & HIRST, J. J. 2011. Sex-dependent effect of a low neurosteroid environment and intrauterine growth restriction on foetal guinea pig brain development. *Journal of Endocrinology,* 208**,** 301-309.

KELLEY, B. J. & PETERSEN, R. C. 2007. Alzheimer's disease and mild cognitive impairment. *Neurol Clin,* 25**,** 577-609.

KELLY, J. B., VAN ADEL, B. A. & ITO, M. 2009. Anatomical projections of the nuclei of the lateral lemniscus in the albino rat (Rattus norvegicus). *J Comp Neurol,* 512**,** 573-593.

KESSLAK, J. P., NALCIOGLU, O. & COTMAN, C. W. 1991. Quantification of magnetic resonance scans for hippocampal and parahippocampal atrophy in Alzheimer's disease. *Neurology,* 41**,** 51-54.

KETTENMANN, H., HANISCH, U. K., NODA, M. & VERKHRATSKY, A. 2011. Physiology of Microglia. *Physiological Reviews,* 91**,** 461-553.

KIVIPELTO, M., NGANDU, T., FRATIGLIONI, L., VIITANEN, M., KAREHOLT, I., WINBLAD, B., HELKALA, E. L., TUOMILEHTO, J., SOININEN, H. & NISSINEN, A. 2005. Obesity and vascular risk factors at midlife and the risk of dementia and Alzheimer disease. *Archives of Neurology,* 62**,** 1556-1560.

KNABE, W., WASHAUSEN, S., HAPPEL, N. & KUHN, H. J. 2008. Diversity in mammalian chiasmatic architecture: ipsilateral axons are deflected at glial arches in the prechiasmatic optic nerve of the eutherian Tupaia belangeri. *Journal of Comparative Neurology,* 508**,** 437-457.

KNOPMAN, D. S. & PETERSEN, R. C. 2014. Mild cognitive impairment and mild dementia: a clinical perspective. *Mayo Clin Proc,* 89**,** 1452-1459.

KOCH, U. & GROTHE, B. 1998. GABAergic and glycinergic inhibition sharpens tuning for frequency modulations in the inferior colliculus of the big brown bat. *Journal of Neurophysiology,* 80**,** 71-82.

KOELLHOFFER, E. C., MCCULLOUGH, L. D. & RITZEL, R. M. 2017. Old Maids: Aging and Its Impact on Microglia Function. *Int J Mol Sci,* 18**,** 769.

KOFFIE, R. M., HASHIMOTO, T., TAI, H. C., KAY, K. R., SERRANO-POZO, A., JOYNER, D., HOU, S., KOPEIKINA, K. J., FROSCH, M. P., LEE, V. M., HOLTZMAN, D. M., HYMAN, B. T. & SPIRES-JONES, T. L. 2012. Apolipoprotein E4 effects in Alzheimer's disease are mediated by synaptotoxic oligomeric amyloid-beta. *Brain,* 135**,** 2155-2168.

KOLB, B., MYCHASIUK, R., MUHAMMAD, A., LI, Y. L., FROST, D. O. & GIBB, R. 2012. Experience and the developing prefrontal cortex. *Proceedings of the National Academy of Sciences of the United States of America,* 109**,** 17186-17193.

KOMITOVA, M., ZHAO, L. R., GIDÖ, G., JOHANSSON, B. B. & ERIKSSON, P. 2005. Postischemic exercise attenuates whereas enriched environment has certain enhancing effects on lesion-induced subventricular zone activation in the adult rat. *European Journal of Neuroscience,* 21**,** 2397-2405.

KOTANI, T., MURATA, Y., OHNISHI, H., MORI, M., KUSAKARI, S., SAITO, Y., OKAZAWA, H., BIXBY, J. L. & MATOZAKI, T. 2010. Expression of PTPRO in the interneurons of adult mouse olfactory bulb. *Journal of Comparative Neurology,* 518**,** 119-136.

KOTTI, T. J., RAMIREZ, D. M. O., PFEIFFER, B. E., HUBER, K. M. & RUSSELL, D. W. 2006. Brain cholesterol turnover required for geranylgeraniol production and learning in mice. *Proceedings of the National Academy of Sciences of the United States of America,* 103**,** 3869-3874.

KUHN, M., HEMAN-ACKAH, S. E., SHAIKH, J. A. & ROEHM, P. C. 2011. Sudden sensorineural hearing loss: a review of diagnosis, treatment, and prognosis. *Trends Amplif,* 15**,** 91-105.

KULESZA, R. J. & BERREBI, A. S. 2000. Superior paraolivary nucleus of the rat is a GABAergic nucleus. *Jaro,* 1**,** 255-269.

KUMPIK, D. P. & KING, A. J. 2019. A review of the effects of unilateral hearing loss on spatial hearing. *Hearing Research,* 372**,** 17-28.

KUWABARA, N. & ZOOK, J. M. 2000. Geniculo-collicular descending projections in the gerbil. *Brain Research,* 878**,** 79-87.

LANDAU, R. L., BERGENSTAL, D. M., LUGIBIHL, K. & KASCHT, M. E. 1955. The metabolic effects of progesterone in man. *J Clin Endocrinol Metab,* 15**,** 1194-1215.

LANGA, K. M. & LEVINE, D. A. 2014. The Diagnosis and Management of Mild Cognitive Impairment A Clinical Review. *Jama-Journal of the American Medical Association,* 312**,** 2551-2561.

LATOV, N., NILAVER, G., ZIMMERMAN, E. A., JOHNSON, W. G., SILVERMAN, A. J., DEFENDINI, R. & COTE, L. 1979. Fibrillary astrocytes proliferate in response to brain injury - study combining immunoperoxidase technique for glial fibrillary acidic protein and autoradiography of tritiated-thymidine. *Developmental Biology,* 72**,** 381-384.

LAURIN, D., VERREAULT, R., LINDSAY, J., MACPHERSON, K. & ROCKWOOD, K. 2001. Physical activity and risk of cognitive impairment and dementia in elderly persons. *Archives of Neurology,* 58**,** 498-504.

LAUWEREYNS, J., WATANABE, K., COE, B. & HIKOSAKA, O. 2002. A neural correlate of response bias in monkey caudate nucleus. *Nature,* 418**,** 413-417.

LAWSON, L. J., PERRY, V. H., DRI, P. & GORDON, S. 1990. Heterogeneity in the distribution and morphology of microglia in the normal adult-mouse brain. *Neuroscience,* 39**,** 151-170.

LE, T. N., STRAATMAN, L. V., LEA, J. & WESTERBERG, B. 2017. Current insights in noise-induced hearing loss: a literature review of the underlying mechanism, pathophysiology, asymmetry, and management options. *J Otolaryngol Head Neck Surg,* 46**,** 41.

LEE, K. S., VANDEMARK, K., MEZEY, D., SHULTZ, N. & FITZPATRICK, D. 2019. Functional synaptic architecture of callosal inputs in mouse primary visual cortex. *Neuron,* 101**,** 421-428.

LEE, K. Y. 2013. Pathophysiology of age-related hearing loss (peripheral and central). *Korean J Audiol,* 17**,** 45-49.

LENNERZ, J. K., RÜHLE, V., CEPPA, E. P., NEUHUBER, W. L., BUNNETT, N. W., GRADY, E. F. & MESSLINGER, K. 2008. Calcitonin receptor-like receptor (CLR), receptor activity-modifying protein 1 (RAMP1), and calcitonin gene-related peptide (CGRP) immunoreactlivity in the rat trigeminovascular system: Differences between peripheral and central CGRP receptor distribution. *Journal of Comparative Neurology,* 507**,** 1277-1299.

LEVY-LAHAD, E., WASCO, W., POORKAJ, P., ROMANO, D. M., OSHIMA, J., PETTINGELL, W. H., YU, C. E., JONDRO, P. D., SCHMIDT, S. D., WANG, K. & ET AL. 1995. Candidate gene for the chromosome 1 familial Alzheimer's disease locus. *Science,* 269**,** 973-977.

LIN, F. R., METTER, E. J., O'BRIEN, R. J., RESNICK, S. M., ZONDERMAN, A. B. & FERRUCCI, L. 2011a. Hearing loss and incident dementia. *Arch Neurol,* 68**,** 214-220.

LIN, F. R., METTER, E. J., O'BRIEN, R. J., RESNICK, S. M., ZONDERMAN, A. B. & FERRUCCI, L. 2011b. Hearing Loss and Incident Dementia. *Archives of Neurology,* 68**,** 214-220.

LIU, S., GAO, X., GAO, N., WANG, X., FANG, X., HU, H. Z., WANG, G. D., XIA, Y. & WOOD, J. D. 2005. Expression of type 1 corticotropin-releasing factor receptor in the guinea pig enteric nervous system. *Journal of Comparative Neurology,* 481**,** 284-98.

LIU, X. Z. & YAN, D. 2007. Ageing and hearing loss. *J Pathol,* 211**,** 188-197.

LIVINGSTON, G., SOMMERLAD, A., ORGETA, V., COSTAFREDA, S. G., HUNTLEY, J., AMES, D., BALLARD, C., BANERJEE, S., BURNS, A., COHEN-MANSFIELD, J., COOPER, C., FOX, N., GITLIN, L. N., HOWARD, R., KALES, H. C., LARSON, E. B., RITCHIE, K., ROCKWOOD, K., SAMPSON, E. L., SAMUS, Q., SCHNEIDER, L. S., SELBAEK, G., TERI, L. & MUKADAM, N. 2017. Dementia prevention, intervention, and care. *Lancet,* 390**,** 2673-2734.

LOPEZ-OTIN, C., BLASCO, M. A., PARTRIDGE, L., SERRANO, M. & KROEMER, G. 2013. The hallmarks of aging. *Cell,* 153**,** 1194-1217.

LORENTE DE NÓ, R. 1979. Central representation of the eighth nerve. *Ear Diseases, Deafness and Dizziness***,** 64-86.

LORENZ, B., GARCIA-SEGURA, L. M. & DONCARLOS, L. L. 2005. Cellular phenotype of androgen receptor-immunoreactive nuclei in the developing and adult rat brain. *Journal of Comparative Neurology,* 492**,** 456-468.

LOVINGER, D. M. 2010. Neurotransmitter roles in synaptic modulation, plasticity and learning in the dorsal striatum. *Neuropharmacology,* 58**,** 951-961.

LYNCH, M. A. 2009. The multifaceted profile of activated microglia. *Mol Neurobiol,* 40**,** 139-156.

MALMIERCA, M. S. & HACKETT, T. A. 2010. *Structural organization of the ascending auditory pathway,* NewYork, NY, Oxford University Press.

MANDELKOW, E. M. & MANDELKOW, E. 1998. Tau in Alzheimer's disease. *Trends Cell Biol,* 8**,** 425-427.

MARCELLO, E., EPIS, R., SARACENO, C. & DI LUCA, M. 2012. Synaptic Dysfunction in Alzheimer's Disease. *Synaptic Plasticity: Dynamics, Development and Disease,* 970**,** 573-601.

MARINO, R. A., LEVY, R. & MUNOZ, D. P. 2015. Linking express saccade occurance to stimulus properties and sensorimotor integration in the superior colliculus. *J Neurophysiol,* 114**,** 879-892.

MARQUARDT, T., HENSEL, J., MROWINSKI, D. & SCHOLZ, G. 2007. Low-frequency characteristics of human and guinea pig cochleae. *Journal of the Acoustical Society of America,* 121**,** 3628-3638.

MARTIN, R., BAJO-GRANERAS, R., MORATALLA, R., PEREA, G. & ARAQUE, A. 2015. Circuit-specific signaling in astrocyte-neuron networks in basal ganglia pathways. *Glia,* 63**,** E214-E215.

MASON, M. J. 2016. Structure and function of the mammalian middle ear. II: Inferring function from structure. *Journal of Anatomy,* 228**,** 300-312.

MATIAS, I., MORGADO, J. & GOMES, F. C. A. 2019. Astrocyte Heterogeneity: Impact to Brain Aging and Disease. *Front Aging Neurosci,* 11**,** 59.

MERCHÁN, M., AGUILAR, L. A., LOPEZ-POVEDA, E. A. & MALMIERCA, M. S. 2005. The inferior colliculus of the rat: quantitative immunocytochemical study of GABA and glycine. *Neuroscience,* 136**,** 907-925.

MIGLIACCIO, R., AGOSTA, F., POSSIN, K. L., CANU, E., FILIPPI, M., RABINOVICI, G. D., ROSEN, H. J., MILLER, B. L. & GORNO-TEMPINI, M. L. 2015. Mapping the Progression of Atrophy in Early- and Late-Onset Alzheimer's Disease. *Journal of Alzheimers Disease,* 46**,** 351-364.

MILAZZO, M., FALLAH, E., CARAPEZZA, M., KUMAR, N. S., LEI, J. H. & OLSON, E. S. 2017. The path of a click stimulus from ear canal to umbo. *Hearing Research,* 346**,** 1-13.

MILLER, R. H. & RAFF, M. C. 1984. Fibrous and protoplasmic astrocytes are biochemically and developmentally distinct. *J Neurosci,* 4**,** 585-592.

MILLER, S. J. 2018. Astrocyte Heterogeneity in the Adult Central Nervous System. *Frontiers in Cellular Neuroscience,* 12**,** 401.

MIYAMOTO, A., WAKE, H., ISHIKAWA, A. W., ETO, K., SHIBATA, K., MURAKOSHI, H., KOIZUMI, S., MOORHOUSE, A. J., YOSHIMURA, Y. & NABEKURA, J. 2016. Microglia contact induces synapse formation in developing somatosensory cortex. *Nature Communications,* 7**,** 1-12.

MONTGOMERY, E. B. & BUCHHOLZ, S. R. 1991. The Striatum and Motor Cortex in Motor Initiation and Execution. *Brain Research,* 549**,** 222-229.

MOREST, D. K. 1964. The Neuronal Architecture of the Medial Geniculate Body of the Cat. *J Anat,* 98**,** 611-630.

MOREST, D. K. 1968. The collateral system of the medial nucleus of the trapezoid body of the cat, its neuronal architecture and relation to the olivo-cochlear bundle. *Brain Res,* 9**,** 288-311.

MOREST, D. K. & OLIVER, D. L. 1984. The Neuronal Architecture of the Inferior Colliculus in the Cat - Defining the Functional-Anatomy of the Auditory Midbrain. *Journal of Comparative Neurology,* 222**,** 209-236.

MORRISON, J. H. & BAXTER, M. G. 2012. The ageing cortical synapse: hallmarks and implications for cognitive decline. *Nature Reviews Neuroscience,* 13**,** 240-250.

MOSCONI, L., BERTI, V., GLODZIK, L., PUPI, A., DE SANTI, S. & DE LEON, M. J. 2010. Pre-Clinical Detection of Alzheimer's Disease Using FDG-PET, with or without Amyloid Imaging. *Journal of Alzheimers Disease,* 20**,** 843-854.

MOURIEC, K. & BALTHAZART, J. 2013. Peripubertal proliferation of progenitor cells in the preoptic area of Japanese quail (Coturnix japonica). *Brain Research,* 1516**,** 20-32.

NAKAMOTO, K. T., SOWICK, C. S. & SCHOFIELD, B. R. 2013. Auditory cortical axons contact commissural cells throughout the guinea pig inferior colliculus. *Hearing Research,* 306**,** 131-144.

NAVARRO, V., SANCHEZ-MEJIAS, E., JIMENEZ, S., MUNOZ-CASTRO, C., SANCHEZ-VARO, R., DAVILA, J. C., VIZUETE, M., GUTIERREZ, A. & VITORICA, J. 2018. Microglia in Alzheimer's Disease: Activated, Dysfunctional or Degenerative. *Frontiers in Aging Neuroscience,* 10**,** 140.

NAYAK, D., ROTH, T. L. & MCGAVERN, D. B. 2014. Microglia Development and Function. *Annual Review of Immunology, Vol 32,* 32**,** 367-402.

NIMMERJAHN, A., KIRCHHOFF, F. & HELMCHEN, F. 2005. Resting microglial cells are highly dynamic surveillants of brain parenchyma in vivo. *Science,* 308**,** 1314-1318.

NISTOR, G., SIEGENTHALER, M. M., POIRIER, S. N., ROSSI, S., POOLE, A. J., CHARLTON, M. E., MCNEISH, J. D., AIRRIESS, C. N. & KEIRSTEAD, H. S. 2011. Derivation of high purity neuronal progenitors from human embryonic stem cells. *PLoS One,* 6**,** e20692.

NORDBERG, A. 2004. PET imaging of amyloid in Alzheimer's disease. *Lancet Neurol,* 3**,** 519-527.

NORDBERG, A. & WINBLAD, B. 1986. Reduced Number of [H-3] Nicotine and [H-3] Acetylcholine Binding-Sites in the Frontal-Cortex of Alzheimer Brains. *Neuroscience Letters,* 72**,** 115-119.

O'BRIEN, R. J. & WONG, P. C. 2011. Amyloid Precursor Protein Processing and Alzheimer's Disease. *Annual Review of Neuroscience, Vol 34,* 34**,** 185-204.

OBERHEIM, N. A., GOLDMAN, S. A. & NEDERGAARD, M. 2012. Heterogeneity of astrocytic form and function. *Methods Mol Biol,* 814**,** 23-45.

OERTEL, D., WU, S. H., GARB, M. W. & DIZACK, C. 1990. Morphology and Physiology of Cells in Slice Preparations of the Posteroventral Cochlear Nucleus of Mice. *Journal of Comparative Neurology,* 295**,** 136-154.

OHNO, M., COLE, S. L., YASVOINA, M., ZHAO, J., CITRON, M., BERRY, R., DISTERHOFT, J. F. & VASSAR, R. 2007. BACE1 gene deletion prevents neuron loss and memory deficits in 5XFAD APP/PS1 transgenic mice. *Neurobiol Dis,* 26**,** 134-145.

OLAH, M., BIBER, K., VINET, J. & BODDEKE, H. W. G. M. 2011. Microglia phenotype diversity. *CNS & Neurological Disorders-Drug Targets,* 10**,** 108-118.

OLIVER, D. L., BECKIUS, G. E. & SHNEIDERMAN, A. 1995. Axonal Projections from the Lateral and Medial Superior Olive to the Inferior Colliculus of the Cat - a Study Using Electron-Microscopic Autoradiography. *Journal of Comparative Neurology,* 360**,** 17-32.

OLIVER, D. L., WINER, J. A., BECKIUS, G. E. & SAINTMARIE, R. L. 1994. Morphology of GABAergic neurons in the inferior colliculus of the cat. *Journal of Comparative Neurology,* 340**,** 27-42.

OLIVIERI, F., RECCHIONI, R., MARCHESELLI, F., ABBATECOLA, A. M., SANTINI, G., BORGHETTI, G., ANTONICELLI, R. & PROCOPIO, A. D. 2013. Cellular senescence in cardiovascular diseases: potential age-related mechanisms and implications for treatment. *Curr Pharm Des,* 19**,** 1710-1719.

OMATA, Y., THARASEGARAN, S., LIM, Y. M., YAMASAKI, Y., ISHIGAKI, Y., TATSUNO, T., MARUYAMA, M. & TSUDA, L. 2016. Expression of amyloid-beta in mouse cochlear hair cells causes an early-onset auditory defect in high-frequency sound perception. *Aging (Albany NY),* 8**,** 427-439.

ONGUR, D. & PRICE, J. L. 2000. The organization of networks within the orbital and medial prefrontal cortex of rats, monkeys and humans. *Cerebral Cortex,* 10**,** 206-219.

ONO, M., YANAGAWA, Y. & KOYANO, K. 2005. GABAergic neurons in inferior colliculus of the GAD67-GFP knock-in mouse: electrophysiological and morphological properties. *Neuroscience Research,* 51**,** 475-492.

ORRE, M., KAMPHUIS, W., DOOVES, S., KOOIJMAN, L., CHAN, E. T., KIRK, C. J., SMITH, V. D., KOOT, S., MAMBER, C., JANSEN, A. H., OVAA, H. & HOL, E. M. 2013. Reactive glia show increased immunoproteasome activity in Alzheimer's disease. *Brain,* 136**,** 1415-1431.

ORTON, L. D., PAPASAVVAS, C. A. & REES, A. 2016. Commissural gain control enhances the midbrain representation of sound location. *Journal of Neuroscience,* 36**,** 4470-4481.

ORTON, L. D. & REES, A. 2014. Intercollicular commissural connections refine the representation of sound frequency and level in the auditory midbrain. *Elife,* 3**,** e03764.

OSEN, K. K. & ROTH, K. 1969. Histochemical localization of cholinesterases in the cochlear nuclei of the cat, with notes on the origin of acetylcholinesterase-positive afferents and the superior olive. *Brain Res,* 16**,** 165-185.

OUDA, L., BURIANOVA, J. & SYKA, J. 2012. Age-related changes in calbindin and calretinin immunoreactivity in the central auditory system of the rat. *Experimental gerontology,* 47**,** 497-506.

OUDA, L. & SYKA, J. 2012. Immunocytochemical profiles of inferior colliculus neurons in the rat and their changes with aging. *Frontiers in Neural Circuits,* 6**,** 68.

PADURARIU, M., CIOBICA, A., MAVROUDIS, I., FOTIOU, D. & BALOYANNIS, S. 2012. Hippocampal Neuronal Loss in the Ca1 and Ca3 Areas of Alzheimer's Disease Patients. *Psychiatria Danubina,* 24**,** 152-158.

PALMER, A. R. & BERGER, J. I. 2018. Changes in the Inferior Colliculus Associated with Hearing Loss. *The Oxford Handbook of the Auditory Brainstem.*

PANZANELLI, P., FRITSCHY, J. M., YANAGAWA, Y., OBATA, K. & SASSOE-POGNETTO, M. 2007. GABAergic phenotype of periglomerular cells in the rodent olfactory bulb. *Journal of Comparative Neurology,* 502**,** 990-1002.

PAREKH, M. B., RUTT, B. K., PURCELL, R., CHEN, Y. X. & ZEINEH, M. M. 2015. Ultra-high resolution in-vivo 7.0 T structural imaging of the human hippocampus reveals the endfolial pathway. *Neuroimage,* 112**,** 1-6.

PARIHAR, M. S. & BREWER, G. J. 2010. Amyloid-beta as a Modulator of Synaptic Plasticity. *Journal of Alzheimers Disease,* 22**,** 741-763.

PARK, S. Y., KIM, M. J., SIKANDANER, H., KIM, D. K., YEO, S. W. & PARK, S. N. 2016. A causal relationship between hearing loss and cognitive impairment. *Acta Oto-Laryngologica,* 136**,** 480-483.

PARKHURST, C. N., YANG, G., NINAN, I., SAVAS, J. N., YATES, J. R., LAFAILLE, J. J., HEMPSTEAD, B. L., LITTMAN, D. R. & GAN, W. B. 2013. Microglia Promote Learning-Dependent Synapse Formation through Brain-Derived Neurotrophic Factor. *Cell,* 155**,** 1596-1609.

PAXINOS, G. & FRANKLIN, K. B. 2019. *Paxinos and Franklin's the mouse brain in stereotaxic coordinates*, Academic press.

PEKNY, M. & PEKNA, M. 2004. Astrocyte intermediate filaments in CNS pathologies and regeneration. *J Pathol,* 204**,** 428-437.

PEKNY, M. & PEKNA, M. 2014. Astrocyte Reactivity and Reactive Astrogliosis: Costs and Benefits. *Physiological Reviews,* 94**,** 1077-1098.

PEKNY, M. & PEKNA, M. 2016. Reactive gliosis in the pathogenesis of CNS diseases. *Biochimica Et Biophysica Acta-Molecular Basis of Disease,* 1862**,** 483-491.

PELKEY, K. A., CHITTAJALLU, R., CRAIG, M. T., TRICOIRE, L., WESTER, J. C. & MCBAIN, C. J. 2017. Hippocampal Gabaergic Inhibitory Interneurons. *Physiological Reviews,* 97**,** 1619-1747.

PEREA, G., NAVARRETE, M. & ARAQUE, A. 2009. Tripartite synapses: astrocytes process and control synaptic information. *Trends Neurosci,* 32**,** 421-431.

PEREZ-NIEVAS, B. G. & SERRANO-POZO, A. 2018. Deciphering the Astrocyte Reaction in Alzheimer's Disease. *Frontiers in Aging Neuroscience,* 10**,** 114.

PERRET, E. 1974. The left frontal lobe of man and the suppression of habitual responses in verbal categorical behaviour. *Neuropsychologia,* 12**,** 323-330.

PERRY, V. H., NICOLL, J. A. & HOLMES, C. 2010. Microglia in neurodegenerative disease. *Nat Rev Neurol,* 6**,** 193-201.

PETERS, R. 2006. Ageing and the brain. *Postgrad Med J,* 82**,** 84-88.

PETERSEN, R. C., ROBERTS, R. O., KNOPMAN, D. S., BOEVE, B. F., GEDA, Y. E., IVNIK, R. J., SMITH, G. E. & JACK, C. R., JR. 2009. Mild cognitive impairment: ten years later. *Arch Neurol,* 66**,** 1447-1455.

PHATNANI, H. & MANIATIS, T. 2015. Astrocytes in neurodegenerative disease. *Cold Spring Harb Perspect Biol,* 7**,** a020628.

POCOCK, J. M. & KETTENMANN, H. 2007. Neurotransmitter receptors on microglia. *Trends in neurosciences,* 30**,** 527-535.

PREUSS, T. M. 1995. Do Rats Have Prefrontal Cortex - the Rose-Woolsey-Akert Program Reconsidered. *Journal of Cognitive Neuroscience,* 7**,** 1-24.

PRINCE, M., BRYCE, R., ALBANESE, E., WIMO, A., RIBEIRO, W. & FERRI, C. P. 2013. The global prevalence of dementia: A systematic review and metaanalysis. *Alzheimers & Dementia,* 9**,** 63-75.

PYAPALI, G. K. & TURNER, D. A. 1996. Increased dendritic extent in hippocampal CA1 neurons from aged F344 rats. *Neurobiology of Aging,* 17**,** 601-611.

QIU, C., KIVIPELTO, M. & VON STRAUSS, E. 2009. Epidemiology of Alzheimer's disease: occurrence, determinants, and strategies toward intervention. *Dialogues Clin Neurosci,* 11**,** 111-128.

RAJMOHAN, V. & MOHANDAS, E. 2007. The limbic system. *Indian journal of psychiatry,* 49**,** 132.

RAKIC, P. 1971. Neuron-glia relationship during granule cell migration in developing cerebellar cortex. A Golgi and electronmicroscopic study in Macacus Rhesus. *J Comp Neurol,* 141**,** 283-312.

RAKIC, P. 2009. Evolution of the neocortex: a perspective from developmental biology. *Nature Reviews Neuroscience,* 10**,** 724-735.

RAMIREZ, D. M. O., ANDERSSON, S. & RUSSELL, D. W. 2008. Neuronal expression and subcellular localization of cholesterol 24-hydroxylase in the mouse brain. *Journal of Comparative Neurology,* 507**,** 1676-1693.

REBOLA, N., CARTA, M. & MULLE, C. 2017. Operation and plasticity of hippocampal CA3 circuits: implications for memory encoding. *Nature Reviews Neuroscience,* 18**,** 209-221.

REZAIE, P. & MALE, D. 2002. Mesoglia & microglia--a historical review of the concept of mononuclear phagocytes within the central nervous system. *J Hist Neurosci,* 11**,** 325-374.

RIAZI, K., GALIC, M. A., KENTNER, A. C., REID, A. Y., SHARKEY, K. A. & PITTMAN, Q. J. 2015. Microglia-dependent alteration of glutamatergic synaptic transmission and plasticity in the hippocampus during peripheral inflammation. *Journal of Neuroscience,* 35**,** 4942-4952.

RICHARDSON, M. P., REID, A., TARLOW, M. J. & RUDD, P. T. 1997. Hearing loss during bacterial meningitis. *Arch Dis Child,* 76**,** 134-138.

RIQUELME, R., SALDANA, E., OSEN, K. K., OTTERSEN, O. P. & MERCHAN, M. A. 2001. Colocalization of GABA and glycine in the ventral nucleus of the lateral lemniscus in rat: An in situ hybridization and semiquantitative immunocytochemical study. *Journal of Comparative Neurology,* 432**,** 409-424.

RIZZI, L., ROSSET, I. & RORIZ-CRUZ, M. 2014. Global epidemiology of dementia: Alzheimer's and vascular types. *Biomed Res Int,* 2014**,** 908915.

ROBERTS, R. C. & RIBAK, C. E. 1987a. GABAergic neurons and axon terminals in the brainstem auditory nuclei of the gerbil. *Journal of Comparative Neurology,* 258**,** 267-280.

ROBERTS, R. C. & RIBAK, C. E. 1987b. An electron microscopic study of GABAergic neurons and terminals in the central nucleus of the inferior colliculus of the rat. *Journal of Neurocytology,* 16**,** 333-345.

ROCK, R. B., GEKKER, G., HU, S. X., SHENG, W. S., CHEERAN, M., LOKENSGARD, J. R. & PETERSON, P. K. 2004. Role of microglia in central nervous system infections. *Clinical Microbiology Reviews,* 17**,** 942-964.

ROCKEL, A. J. & JONES, E. G. 1973. The neuronal organization of the inferior colliculus of the adult cat. II. The pericentral nucleus. *J Comp Neurol,* 149**,** 301-334.

RODRIGUEZ-ARELLANO, J. J., PARPURA, V., ZOREC, R. & VERKHRATSKY, A. 2016. Astrocytes in physiological aging and Alzheimer's disease. *Neuroscience,* 323**,** 170-182.

RODRIGUEZ-RODERO, S., FERNANDEZ-MORERA, J. L., MENENDEZ-TORRE, E., CALVANESE, V., FERNANDEZ, A. F. & FRAGA, M. F. 2011. Aging Genetics and Aging. *Aging and Disease,* 2**,** 186-195.

RODRIGUEZ, G. A., TAI, L. M., LADU, M. J. & REBECK, G. W. 2014. Human APOE4 increases microglia reactivity at A beta plaques in a mouse model of A beta deposition. *Journal of Neuroinflammation,* 11**,** 111.

ROSE, J., GALAMBOS, R. & HUGHES, J. 1959. Microelectrode studies of the cochlear nuclei of the cat. *Bulletin of the Johns Hopkins Hospital,* 104**,** 211.

ROSEN, R. F., FARBERG, A. S., GEARING, M., DOOYEMA, J., LONG, P. M., ANDERSON, D. C., DAVIS-TURAK, J., COPPOLA, G., GESCHWIND, D. H., PARÉ, J. F., DUONG, T. Q., HOPKINS, W. D., PREUSS, T. M. & WALKER, L. C. 2008. Tauopathy with paired helical filaments in an aged chimpanzee. *Journal of Comparative Neurology,* 509**,** 259-270.

ROSSKOTHEN-KUHL, N., HILDEBRANDT, H., BIRKENHAGER, R. & ILLING, R. B. 2018. Astrocyte Hypertrophy and Microglia Activation in the Rat Auditory Midbrain Is Induced by Electrical Intracochlear Stimulation. *Frontiers in Cellular Neuroscience,* 12.

ROTHSTEIN, J. D., DYKES-HOBERG, M., PARDO, C. A., BRISTOL, L. A., JIN, L., KUNCL, R. W., KANAI, Y., HEDIGER, M. A., WANG, Y., SCHIELKE, J. P. & WELTY, D. F. 1996. Knockout of glutamate transporters reveals a major role for astroglial transport in excitotoxicity and clearance of glutamate. *Neuron,* 16**,** 675-686.

ROUILLER, E. M. & WELKER, E. 1991. Morphology of corticothalamic terminals arising from the auditory cortex of the rat: a Phaseolus vulgaris-leucoagglutinin (PHA-L) tracing study. *Hear Res,* 56**,** 179-190.

RYLETT, R. J., BALL, M. J. & COLHOUN, E. H. 1983. Evidence for High-Affinity Choline Transport in Synaptosomes Prepared from Hippocampus and Neocortex of Patients with Alzheimers-Disease. *Brain Research,* 289**,** 169-175.

RYUGO, D. K. & WILLARD, F. H. 1985. The Dorsal Cochlear Nucleus of the Mouse - a Light Microscopic Analysis of Neurons That Project to the Inferior Colliculus. *Journal of Comparative Neurology,* 242**,** 381-396.

SABIA, S., FAYOSSE, A., DUMURGIER, J., DUGRAVOT, A., AKBARALY, T., BRITTON, A., KIVIMAKI, M. & SINGH-MANOUX, A. 2018. Alcohol consumption and risk of dementia: 23 year follow-up of Whitehall II cohort study. *Bmj-British Medical Journal,* 362**,** k2927.

SADE, J., LUNTZ, M. & LEVY, D. 1995. Middle-Ear Gas-Composition and Middle-Ear Aeration. *Annals of Otology Rhinology and Laryngology,* 104**,** 369-373.

SAINT MARIE, R. L. & BAKER, R. A. 1990. Neurotransmitter-specific uptake and retrograde transport of [3H]glycine from the inferior colliculus by ipsilateral projections of the superior olivary complex and nuclei of the lateral lemniscus. *Brain Res,* 524**,** 244-253.

SAKAKIBARA, Y., SEKIYA, M., SAITO, T., SAIDO, T. C. & IIJIMA, K. M. 2019. Amyloid-beta plaque formation and reactive gliosis are required for induction of cognitive deficits in App knock-in mouse models of Alzheimer's disease. *Bmc Neuroscience,* 20**,** 13.

SAKURADA, O., KENNEDY, C., JEHLE, J., BROWN, J. D., CARBIN, G. L. & SOKOLOFF, L. 1978. Measurement of local cerebral blood flow with iodo [14C] antipyrine. *Am J Physiol,* 234**,** 59-66.

SALA, C., PIËCH, V., WILSON, N. R., PASSAFARO, M., LIU, G. & SHENG, M. 2001. Regulation of dendritic spine morphology and synaptic function by Shank and Homer. *Neuron,* 31**,** 115-130.

SALAT, D. H., CHEN, J. J., VAN DER KOUWE, A. J., GREVE, D. N., FISCHL, B. & ROSAS, H. D. 2011. Hippocampal degeneration is associated with temporal and limbic gray matter/white matter tissue contrast in Alzheimer's disease. *Neuroimage,* 54**,** 1795-1802.

SALTER, M. W. & STEVENS, B. 2017. Microglia emerge as central players in brain disease. *Nature Medicine,* 23**,** 1018-1027.

SALVI, R., SUN, W., DING, D. L., CHEN, G. D., LOBARINAS, E., WANG, J., RADZIWON, K. & AUERBACH, B. D. 2017. Inner Hair Cell Loss Disrupts Hearing and Cochlear Function Leading to Sensory Deprivation and Enhanced Central Auditory Gain. *Frontiers in Neuroscience,* 10**,** 621.

SAMPATH, D., SATHYANESAN, M. & NEWTON, S. S. 2017. Cognitive dysfunction in major depression and Alzheimer's disease is associated with hippocampal-prefrontal cortex dysconnectivity. *Neuropsychiatr Dis Treat,* 13**,** 1509-1519.

SANCHEZ, P. E., NAVARRO, F. P., FARES, R. P., NADAM, J., GEORGES, B., MOULIN, C., LE CAVORSIN, M., BONNET, C., RYVLIN, P., BELMEGUENAI, A., BODENNEC, J., MORALES, A. & BEZIN, L. 2009. Erythropoietin receptor expression is concordant with erythropoietin but not with common beta chain expression in the rat brain throughout the life span. *Journal of Comparative Neurology,* 514**,** 403-414.

SARLUS, H. & HENEKA, M. T. 2017. Microglia in Alzheimer's disease. *Journal of Clinical Investigation,* 127**,** 3240-3249.

SCHAFER, D. P., LEHRMAN, E. K., KAUTZMAN, A. G., KOYAMA, R., MARDINLY, A. R., YAMASAKI, R., RANSOHOFF, R. M., GREENBERG, M. E., BARRES, B. A. & STEVENS, B. 2012. Microglia sculpt postnatal neural circuits in an activity and complement-dependent manner. *Neuron,* 74**,** 691-705.

SCHOFIELD, B. R. 2010. *Structural organization of the descending auditory pathway,* New York, NY, Oxford University Press.

SCHOFIELD, B. R. & CANT, N. B. 1991. Organization of the superior olivary complex in the guinea pig. I. Cytoarchitecture, cytochrome oxidase histochemistry, and dendritic morphology. *J Comp Neurol,* 314**,** 645-670.

SCHONBRUNN, A. 2014. Editorial: antibody can get it right: confronting poblems of antibody specificity and irreproducibility. *Molecular Endocrinology,* 28**,** 1403-1407.

SCHWAB, C., YU, S., WONG, W. N., MCGEER, E. G. & MCGEER, P. L. 2013. GAD65, GAD67, and GABAT Immunostaining in Human Brain and Apparent GAD65 Loss in Alzheimer's Disease. *Journal of Alzheimers Disease,* 33**,** 1073-1088.

SCHWARTZ, I. R. 1977. Dendritic arrangements in the cat medial superior olive. *Neuroscience,* 2**,** 81-101.

SCOPSI, L., LARSSON, L. I., BASTHOLM, L. & NIELSEN, M. H. 1986. Silver-Enhanced Colloidal Gold Probes as Markers for Scanning Electron-Microscopy. *Histochemistry,* 86**,** 35-41.

SCOTT, I. D. & NICHOLLS, D. G. 1980. Energy transduction in intact synaptosomes. Influence of plasma-membrane depolarization on the respiration and membrane potential of internal mitochondria determined in situ. *Biochem J,* 186**,** 21-33.

SCOTT, K. R. & BARRETT, A. M. 2007. Dementia syndromes: evaluation and treatment. *Expert Rev Neurother,* 7**,** 407-422.

SELKOE, D. J. 2002. Alzheimer's disease is a synaptic failure. *Science,* 298**,** 789-791.

SERRANO-POZO, A., FROSCH, M. P., MASLIAH, E. & HYMAN, B. T. 2011. Neuropathological Alterations in Alzheimer Disease. *Cold Spring Harbor Perspectives in Medicine,* 1**,** a006189.

SHARAF, A., KRIEGLSTEIN, K. & SPITTAU, B. 2013. Distribution of microglia in the postnatal murine nigrostriatal system. *Cell Tissue Res,* 351**,** 373-382.

SHEN, Y., YE, B., CHEN, P., WANG, Q., FAN, C., SHU, Y. & XIANG, M. 2018. Cognitive Decline, Dementia, Alzheimer's Disease and Presbycusis: Examination of the Possible Molecular Mechanism. *Front Neurosci,* 12**,** 394.

SHERA, C. A., GUINAN, J. J. & OXENHAM, A. J. 2002. Revised estimates of human cochlear tuning from otoacoustic and behavioral measurements. *Proceedings of the National Academy of Sciences of the United States of America,* 99**,** 3318-3323.

SIMPSON, J. E., INCE, P. G., LACE, G., FORSTER, G., SHAW, P. J., MATTHEWS, F., SAVVA, G., BRAYNE, C., WHARTON, S. B. & NE, M. C. F. A. 2010. Astrocyte phenotype in relation to Alzheimer-type pathology in the ageing brain. *Neurobiology of Aging,* 31**,** 578-590.

SINGER, W. 1977. Control of thalamic transmission by corticofugal and ascending reticular pathways in the visual system. *Physiol Rev,* 57**,** 386-420.

SINGLA, S., DEMPSEY, C., WARREN, R., ENIKOLOPOV, A. G. & SAWTELL, N. B. 2017. A cerebellum-like circuit in the auditory system cancels responses to self-generated sounds. *Nature Neuroscience,* 20**,** 943-950.

SINHA, U. K., HOLLEN, K. M., RODRIGUEZ, R. & MILLER, C. A. 1993. Auditory system degeneration in Alzheimer's disease. *Neurology,* 43**,** 779-785.

SMITH, R. J. H., SHEARER, A. E., HILDEBRAND, M. S. & VAN CAMP, G. 1993. Deafness and Hereditary Hearing Loss Overview. *In:* PAGON, R. A., ADAM, M. P., ARDINGER, H. H., WALLACE, S. E., AMEMIYA, A., BEAN, L. J. H., BIRD, T. D., LEDBETTER, N., MEFFORD, H. C., SMITH, R. J. H. & STEPHENS, K. (eds.) *GeneReviews(R).* Seattle (WA).

SOFRONIEW, M. V. & VINTERS, H. V. 2010. Astrocytes: biology and pathology. *Acta Neuropathologica,* 119**,** 7-35.

SOKOLOFF, L., REIVICH, M., KENNEDY, C., DES ROSIERS, M. H., PATLAK, C. S., PETTIGREW, K. D., SAKURADA, O. & SHINOHARA, M. 1977a. The [14C] deoxyglucose method for the measurement of local cerebral glucose utilization: theory, procedure, and normal values in the conscious and anesthetized albino rat. *Journal of Neurochemistry,* 28**,** 897-916.

SOKOLOFF, L., REIVICH, M., KENNEDY, C., ROSIERS, M. D., PATLAK, C., PETTIGREW, K., ET AL., SAKURADA, O. & SHINOHARA, M. 1977b. The [14C] deoxyglucose method for the measurement of local cerebral glucose utilization: theory, procedure, and normal values in the conscious and anesthetized albino rat 1. *Journal of neurochemistry,* 28**,** 897-916.

SOLITO, E. & SASTRE, M. 2012. Microglia function in Alzheimer's disease. *Frontiers in Pharmacology,* 3.

SOLOVIEV, M. M., CIRUELA, F., CHAN, W. Y. & MCILHINNEY, R. A. J. 2000. Mouse brain and muscle tissues constitutively express high levels of Homer proteins. *European Journal of Biochemistry,* 267**,** 634-639.

SPIRES, T. L. & HYMAN, B. T. 2005. Transgenic models of Alzheimer's disease: learning from animals. *NeuroRx,* 2**,** 423-437.

SRERE, P. 1969. [1] Citrate synthase:[EC 4.1. 3.7. Citrate oxaloacetate-lyase (CoA-acetylating)]. *Methods in enzymology.* Elsevier.

STANTON, G. B., KOHLER, S. J., BOKLWESKI, J., CAMERON, J. L. & GREENOUGH, W. T. 2015. Cytogenesis in the adult monkey motor cortex: perivascular NG2 cells are the major adult born cell type. *Journal of Comparative Neurology,* 523**,** 849-868.

STEINER, J., BERNSTEIN, H. G., BIELAU, H., BERNDT, A., BRISCH, R., MAWRIN, C., KEILHOFF, G. & BOGERTS, B. 2007. Evidence for a wide extra-astrocytic distribution of S100B in human brain. *Bmc Neuroscience,* 8**,** 2.

STENFORS, L. E., SALEN, B. & WINBLAD, B. 1979. Role of the Pars Flaccida in the Mechanics of the Middle-Ear. *Acta Oto-Laryngologica,* 88**,** 395-400.

STOCKBURGER, C., MIANO, D., BAEUMLISBERGER, M., PALLAS, T., ARREY, T. N., KARAS, M., FRIEDLAND, K. & MULLER, W. E. 2016. A Mitochondrial Role of SV2a Protein in Aging and Alzheimer's Disease: Studies with Levetiracetam. *J Alzheimers Dis,* 50**,** 201-215.

STOWELL, R. D., WONG, E. L., BATCHELOR, H. N., MENDES, M. S., LAMANTIA, C. E., WHITELAW, B. S. & MAJEWSKA, A. K. 2018. Cerebellar microglia are dynamically unique and survey Purkinje neurons in vivo. *Dev Neurobiol,* 78**,** 627-644.

STREIT, W. J. 2001. Microglia and macrophages in the developing CNS. *Neurotoxicology,* 22**,** 619-624.

STREIT, W. J. & KREUTZBERG, G. W. 1988. Response of Endogenous Glial-Cells to Motor Neuron Degeneration Induced by Toxic Ricin. *Journal of Comparative Neurology,* 268**,** 248-263.

STREITBURGER, D. P., ARELIN, K., KRATZSCH, J., THIERY, J., STEINER, J., VILLRINGER, A., MUELLER, K. & SCHROETER, M. L. 2012. Validating Serum S100B and Neuron-Specific Enolase as Biomarkers for the Human Brain - A Combined Serum, Gene Expression and MRI Study. *Plos One,* 7**,** e43284.

SULTAN, F. & GLICKSTEIN, M. 2007. The cerebellum: Comparative and animal studies. *Cerebellum,* 6**,** 168-176.

SVENNINGSSON, P. 2019. Corticobasal degeneration: advances in clinicopathology and biomarkers. *Curr Opin Neurol,* 32**,** 597-603.

SYKA, J., POPELÁŘ, J., KVAŠŇÁK, E. & ASTL, J. 2000. Response properties of neurons in the central nucleus and external and dorsal cortices of the inferior colliculus in guinea pig. *Experimental Brain Research,* 133**,** 254-266.

TAKAKUSAKI, K. 2017. Functional Neuroanatomy for Posture and Gait Control. *Journal of Movement Disorders,* 10**,** 1-17.

TAMPELLINI, D., CAPETILLO-ZARATE, E., DUMONT, M., HUANG, Z., YU, F., LIN, M. T. & GOURAS, G. K. 2010. Effects of synaptic modulation on beta-amyloid, synaptophysin, and memory performance in Alzheimer's disease transgenic mice. *J Neurosci,* 30**,** 14299-14304.

TANAKA, K., OTANI, K., TOKUNAGA, A. & SUGITA, S. 1985. The Organization of Neurons in the Nucleus of the Lateral Lemniscus Projecting to the Superior and Inferior Colliculi in the Rat. *Brain Research,* 341**,** 252-260.

TARDIF, E., CHIRY, O., PROBST, A., MAGISTRETTI, P. J. & CLARKE, S. 2003. Patterns of calcium-binding proteins in human inferior colliculus: identification of subdivisions and evidence for putative parallel systems. *Neuroscience,* 116**,** 1111-1121.

TCHKONIA, T., ZHU, Y., VAN DEURSEN, J., CAMPISI, J. & KIRKLAND, J. L. 2013. Cellular senescence and the senescent secretory phenotype: therapeutic opportunities. *J Clin Invest,* 123**,** 966-972.

TEFFER, K. & SEMENDEFERI, K. 2012. Human prefrontal cortex: Evolution, development, and pathology. *Evolution of the Primate Brain: From Neuron to Behavior,* 195**,** 191-218.

THOMPSON, P. M., HAYASHI, K. M., DE ZUBICARAY, G., JANKE, A. L., ROSE, S. E., SEMPLE, J., HERMAN, D., HONG, M. S., DITTMER, S. S., DODDRELL, D. M. & TOGA, A. W. 2003. Dynamics of gray matter loss in Alzheimer's disease. *Journal of Neuroscience,* 23**,** 994-1005.

TORO, C. T., HALLAK, J. E. C., DUNHAM, J. S. & DEAKIN, J. F. W. 2006. Glial fibrillary acidic protein and glutamine synthetase in subregions of prefrontal cortex in schizophrenia and mood disorder. *Neuroscience Letters,* 404**,** 276-281.

TRAPP, B. D., WUJEK, J. R., CRISTE, G. A., JALABI, W., YIN, X., KIDD, G. J., STOHLMAN, S. & RANSOHOFF, R. 2007. Evidence for synaptic stripping by cortical microglia. *Glia,* 55**,** 360-368.

TREMBLAY, M. È., LOWERY, R. L. & MAJEWSKA, A. K. 2010. Microglial interactions with synapses are modulated by visual experience. *PLoS biology,* 8**,** e1000527.

TREMBLAY, R., LEE, S. & RUDY, B. 2016. GABAergic interneurons in the neocortex: from cellular properties to circuits. *Neuron,* 91**,** 260-292.

TSUDA, M., TOZAKI-SAITOH, H. & INOUE, K. 2010. Pain and purinergic signaling. *Brain Research Reviews,* 63**,** 222-232.

TULVING, E. & MARKOWITSCH, H. J. 1998. Episodic and declarative memory: Role of the hippocampus. *Hippocampus,* 8**,** 198-204.

UCHIDA, Y., SUGIURA, S., NISHITA, Y., SAJI, N., SONE, M. & UEDA, H. 2019. Age-related hearing loss and cognitive decline - The potential mechanisms linking the two. *Auris Nasus Larynx,* 46**,** 1-9.

UCHIHARA, T., KONDO, H., AKIYAMA, H. & IKEDA, K. 1995. White matter amyloid in Alzheimer's disease brain. *Acta Neuropathol,* 90**,** 51-56.

UGOLINI, F., LANA, D., NARDIELLO, P., NOSI, D., PANTANO, D., CASAMENTI, F. & GIOVANNINI, M. G. 2018. Different Patterns of Neurodegeneration and Glia Activation in CA1 and CA3 Hippocampal Regions of TgCRND8 Mice. *Frontiers in Aging Neuroscience,* 10**,** 372.

VAN ROSSUM, D. & HANISCH, U. K. 2004. Microglia. *Metabolic Brain Disease,* 19**,** 393-411.

VANGUILDER, H. D. & FREEMAN, W. M. 2011. The hippocampal neuroproteome with aging and cognitive decline: past progress and future directions. *Front Aging Neurosci,* 3**,** 8.

VASILE, F., DOSSI, E. & ROUACH, N. 2017. Human astrocytes: structure and functions in the healthy brain. *Brain Structure & Function,* 222**,** 2017-2029.

VOITENKO, L. P. & MARLINSKY, V. V. 1993. Stereotaxic atlas of the guinea pig brainstem. *Neurophysiology,* 25**,** 52-77.

VOSKUIL, J. L. 2017. The challenges with the validation of research antibodies. *F1000Research,* 6**,** 161.

WAGNER, K. V., HÄUSL, A. S., PÖHLMANN, M. L., HARTMANN, J., LABERMAIER, C., MÜLLER, M. B. & SCHMIDT, M. V. 2014. Hippocampal Homer1 levels influence motivational behavior in an operant conditioning task. *Plos one,* 9**,** e85975.

WAKE, H., MOORHOUSE, A. J., JINNO, S., KOHSAKA, S. & NABEKURA, J. 2009. Resting microglia directly monitor the functional state of synapses in vivo and determine the fate of ischemic terminals. *Journal of Neuroscience,* 29**,** 3974-3980.

WANG, S. E. & WU, C. H. 2015. Physiological and Histological Evaluations of the Cochlea between 3xTg-AD Mouse Model of Alzheimer's Diseases and R6/2 Mouse Model of Huntington's Diseases. *Chinese Journal of Physiology,* 58**,** 359-366.

WARREN, J. D., ROHRER, J. D. & ROSSOR, M. N. 2013. Clinical review. Frontotemporal dementia. *BMJ,* 347**,** f4827.

WEBSTER, D. B. 1992. An overview of mammalian auditory pathways with an emphasis on humans. *The mammalian auditory pathway: Neuroanatomy.* Springer.

WHALLEY, L. J. 2002. Brain ageing and dementia: what makes the difference? *British Journal of Psychiatry,* 181**,** 369-371.

WHITLEY, J. M. & HENKEL, C. K. 1984. Topographical Organization of the Inferior Collicular Projection and Other Connections of the Ventral Nucleus of the Lateral Lemniscus in the Cat. *Journal of Comparative Neurology,* 229**,** 257-270.

WHITTAKER, V. 1969. The synaptosome. *Structural neurochemistry.* Springer.

WHITTAKER, V. P. 1993. Thirty years of synaptosome research. *J Neurocytol,* 22**,** 735-742.

WIEDENMANN, B. & FRANKE, W. W. 1985. Identification and localization of synaptophysin, an integral membrane glycoprotein of Mr 38,000 characteristic of presynaptic vesicles. *Cell,* 41**,** 1017-1028.

WILHELMSSON, U., BUSHONGT, E. A., PRICE, D. L., SMARR, B. L., PHUNG, V., TERADA, M., ELLISMAN, M. H. & PEKNY, M. 2006. Redefining the concept of reactive astrocytes as cells that remain within their unique domains upon reaction to injury. *Proceedings of the National Academy of Sciences of the United States of America,* 103**,** 17513-17518.

WILLARD, F. & MARTIN, G. 1983. The auditory brainstem nuclei and some of their projections to the inferior colliculus in the North American opossum. *Neuroscience,* 10**,** 1203-1232.

WILLIS, C. L., LEACH, L., CLARKE, G. J., NOLAN, C. C. & RAY, D. E. 2004. Reversible disruption of tight junction complexes in the rat blood-brain barrier, following transitory focal astrocyte loss. *Glia,* 48**,** 1-13.

WILLIS, C. L., NOLAN, C. C., REITH, S. N., LISTER, T., PRIOR, M. J., GUERIN, C. J., MAVROUDIS, G. & RAY, D. E. 2003. Focal astrocyte loss is followed by microvascular damage, with subsequent repair of the blood-brain barrier in the apparent absence of direct astrocytic contact. *Glia,* 45**,** 325-337.

WILLOTT, J. F. 1986. Effects of Aging, Hearing-Loss, and Anatomical Location on Thresholds of Inferior Colliculus Neurons in C57bl/6 and Cba Mice. *Journal of Neurophysiology,* 56**,** 391-408.

WILSON, R. S., LEURGANS, S. E., BOYLE, P. A. & BENNETT, D. A. 2011. Cognitive decline in prodromal Alzheimer disease and mild cognitive impairment. *Arch Neurol,* 68**,** 351-356.

WINER, J. A. 1984. Anatomy of Layer-Iv in Cat Primary Auditory-Cortex (Ai). *Journal of Comparative Neurology,* 224**,** 535-567.

WINER, J. A., LARUE, D. T., DIEHL, J. J. & HEFTI, B. J. 1998. Auditory cortical projections to the cat inferior colliculus. *Journal of Comparative Neurology,* 400**,** 147-174.

WINER, J. A. & MOREST, D. K. 1983. The Neuronal Architecture of the Dorsal Division of the Medial Geniculate-Body of the Cat - a Study with the Rapid Golgi Method. *Journal of Comparative Neurology,* 221**,** 1-30.

WINER, J. A. & PRIETO, J. J. 2001. Layer V in cat primary auditory cortex (AI): Cellular architecture and identification of projection neurons. *Journal of Comparative Neurology,* 434**,** 379-412.

WINER, J. A. & WENSTRUP, J. J. 1994. The neurons of the medial geniculate body in the mustached bat (Pteronotus parnellii). *J Comp Neurol,* 346**,** 183-206.

WOLBURG, H., NOELL, S., WOLBURG-BUCHHOLZ, K., MACK, A. & FALLIER-BECKER, P. 2009. Agrin, Aquaporin-4, and Astrocyte Polarity as an Important Feature of the Blood-Brain Barrier. *Neuroscientist,* 15**,** 180-193.

WONG-RILEY, M. T. T. 1989. Cytochrome-Oxidase - an Endogenous Metabolic Marker for Neuronal-Activity. *Trends in Neurosciences,* 12**,** 94-101.

WONG, A. C. & RYAN, A. F. 2015. Mechanisms of sensorineural cell damage, death and survival in the cochlea. *Front Aging Neurosci,* 7**,** 58.

YAN, D. & LIU, X. Z. 2010. Genetics and pathological mechanisms of Usher syndrome. *J Hum Genet,* 55**,** 327-335.

YANG, Y., MUFSON, E. J. & HERRUP, K. 2003. Neuronal cell death is preceded by cell cycle events at all stages of Alzheimer's disease. *Journal of Neuroscience,* 23**,** 2557-2563.

YAO, J., IRWIN, R. W., ZHAO, L. Q., NILSEN, J., HAMILTON, R. T. & BRINTON, R. D. 2009. Mitochondrial bioenergetic deficit precedes Alzheimer's pathology in female mouse model of Alzheimer's disease. *Proceedings of the National Academy of Sciences of the United States of America,* 106**,** 14670-14675.

YECKEL, M. F. & BERGER, T. W. 1990. Feedforward Excitation of the Hippocampus by Afferents from the Entorhinal Cortex - Redefinition of the Role of the Trisynaptic Pathway. *Proceedings of the National Academy of Sciences of the United States of America,* 87**,** 5832-5836.

YU, C. X., DERDIKMAN, D., HAIDARLIU, S. & AHISSAR, E. 2006. Parallel thalamic pathways for whisking and touch signals in the rat. *Plos Biology,* 4**,** e124.

YUAN, P., CONDELLO, C., KEENE, C. D., WANG, Y. M., BIRD, T. D., PAUL, S. M., LUO, W. J., COLONNA, M., BADDELEY, D. & GRUTZENDLER, J. 2016. TREM2 Haplodeficiency in Mice and Humans Impairs the Microglia Barrier Function Leading to Decreased Amyloid Compaction and Severe Axonal Dystrophy (vol 90, pg 724, 2016). *Neuron,* 92**,** 252-264.

ZAHNERT, T. 2011. The differential diagnosis of hearing loss. *Dtsch Arztebl Int,* 108**,** 433-444.

ZELANO, J., BERG, A., THAMS, S., HAILER, N. P. & CULLHEIM, S. 2009. SynCAM1 expression correlates with restoration of central synapses on spinal motoneurons after two different models of peripheral nerve injury. *Journal of Comparative Neurology,* 517**,** 670-682.

ZETTEL, M. L., FRISINA, R. D., HAIDER, S. E. & O'NEILL, W. E. 1997. Age-related changes in calbindin D-28k and calretinin immunoreactivity in the inferior colliculus of CBA/CaJ and C57Bl/6 mice. *Journal of Comparative Neurology,* 386**,** 92-110.

ZHANG, J., MALIK, A., CHOI, H. B., KO, R. W., DISSING-OLESEN, L. & MACVICAR, B. A. 2014. Microglial CR3 activation triggers long-term synaptic depression in the hippocampus via NADPH oxidase. *Neuron,* 82**,** 195-207.

ZHENG, C., ZHOU, X. W. & WANG, J. Z. 2016. The dual roles of cytokines in Alzheimer's disease: update on interleukins, TNF-alpha, TGF-beta and IFN-gamma. *Translational Neurodegeneration,* 5**,** 7.

ZHONG, G., WANG, Y., ZHANG, Y., GUO, J. J. & ZHAO, Y. 2015. Smoking Is Associated with an Increased Risk of Dementia: A Meta-Analysis of Prospective Cohort Studies with Investigation of Potential Effect Modifiers (vol 10, e0118333, 2015). *Plos One,* 10**,** e0126169.

ZOOK, J. M. & CASSEDAY, J. H. 1982. Cytoarchitecture of auditory system in lower brainstem of the mustache bat, Pteronotus parnellii. *J Comp Neurol,* 207**,** 1-13.